University of Bergen

Master Thesis in Petroleum Technology - Reservoir Chemistry

Application of MRI in studies of tetrahydrofuran hydrates in quartz sand at atmospheric pressure

Author:

Emilie Sørfonden Tetlie

Supervisors:

Tanja Barth

Per Fotland

Faculty of Mathematics and Natural Sciences

Department of Chemistry

November 2017

Abstract

Natural gas hydrates form under low temperatures and high pressures. They can be found in abundance in permafrost environments and under the sea floor, where the temperature and pressure conditions ensure their stability. The conditions within petroleum transporting pipelines can enter the range of the hydrate stability zone which can result in formation of plugs. The understanding of formation and dissolution of hydrates is crucial for future production of hydrates and for hydrate inhibition within pipelines. At present there are no simple methods for examining hydrates within a porous medium. For further characterization of the formation and dissociation of hydrates within a porous medium, better methods are required.

Magnetic resonance imaging (MRI) is applied as a tool for studying hydrates within porous media in this master thesis. The porous media used for this thesis was unconsolidated quartz sand. Magnetic resonance imaging detects the signals sent out by hydrogen nuclei after exposure of radio frequency waves. This technique provides the opportunity to create images from the inside of a porous medium, without cutting it open. The intensity response from hydrogen nuclei within THF hydrate samples has been used to estimate the hydrate saturation of these samples. The estimation of hydrate saturation has been performed both for the total sample and on a local scale simultaneously, by dividing the sample into several slices. The intensity response from the THF hydrate samples was also used to determine formation and dissociation patterns. The T_2 relaxation process was studied during the dissociation and reforming of THF hydrates, both on a local scale and for the total sample. The possible effect of wettability preferences of a porous medium on the T_2 relaxation process has also been considered.

Acknowledgements

First, I would like to express my gratitude towards my supervisors Professor Tanja Barth and Professor Per Fotland. Thank you for exceptional guidance and encouragement during my time as your master student. I am very grateful for being given the opportunity to work on such an interesting topic. Thanks to you it has been a great and enlightening experience.

Further, I would like to thank Associate Professor John Georg Seland for contributing with his knowledge about MRI in several group meetings and discussions. Thanks to PhD candidate Henrik Nicolay Sørgård for assisting me in parts of my lab work, and further contributions regarding MRI. I would like to thank Gry Lien Aastvedt at Statoil for helping me get started on my work with the MRI instrument, for helpful tips and for fixing almost every problem I stumbled upon.

Finally, I would like to thank my supporting family and friends. Your encouragement has kept me motivated through my years as a student at the University of Bergen. Thank you to all fellow students for great years throughout our studies. A special thanks to Cathrine, Eirik, Kristian and Veronica. Without you, these past years would not be the same. To my dearest Sondre, thank you for always believing in me.

Table of Content

1 Introduction

Figure 1.1 - Natural gas hydrates burning. [2]

Estimates of the US Energy Information agency show that fossil fuels will still be the top energy source in 2040 [1]. As these sources are limited and non-renewable, they will eventually run out. Natural gas hydrates can be a potential source to fill the increasing energy demand. Figure 1.1 shows a picture of gas hydrates burning [2]. When a cubic meter of methane hydrates is dissociated at standard temperature and pressure, it can yield up to 164 cubic meters of methane gas [3]. The estimated amount of the methane hydrate reserves on a global scale range from 14 to 34000 trillion cubic meters for permafrost areas and from 3100 to 7600000 trillion cubic meters for oceanic sediments [4]. Though these estimates are uncertain the amount of organic carbon stored within natural gas hydrates is expected to exceed the reserves of fossil fuels, see figure 1.2 [5].

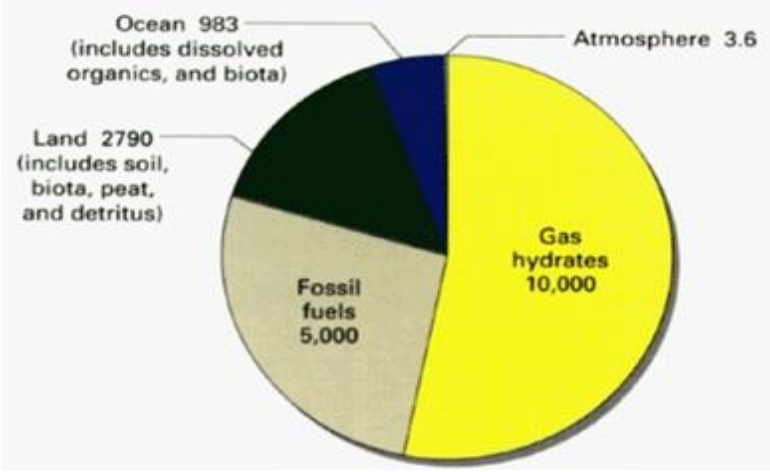

Figure 1.2 -The distribution of organic carbon within different reserves. The amount of carbon dispersed in rocks and sediments are excluded from this diagram. The numbers are given as gigatons of carbon [5].

For the conventional oil and gas industry, the formation of gas hydrates can be a problem. Formation and dissociation of hydrates are an important part of the flow-assurance strategy for each field. The conditions in multi-phase pipelines that transport the well-stream must be kept outside the hydrate stability zone, otherwise there is a risk of plugging the pipeline. Removal of hydrate plugs, figure 1.3 [6], is time consuming and delays the production. Hydrate research in the petroleum industry has therefore focused on how to prevent the formation of hydrates. In addition to the newer interest for gas hydrates as an energy source, the potential for storing gas within hydrates has also attracted interest in later years [3].

Figure 1.3 – Hydrate plug [6].

There are still unanswered fundamental questions about hydrates that require further studies to be performed. There are however no simple methods to study hydrates within a porous medium. The hydrate saturation within a porous medium will affect its permeability. The permeability of a porous medium is an important property for production strategies for oil and gas reservoir and for hydrate production. Methods to monitor hydrate saturation are hence crucial.

Application of magnetic resonance imagining has proven to be a useful tool for monitoring hydrate formation and dissociation [7]. Hydrogen nuclei within free water respond with a high signal intensity when exposed to radio frequency waves. When the hydrogen nuclei are in a solid state, like in natural gas hydrates, the signal intensity is not detectable above the background noise. As hydrate saturation increases, the signal intensity recorded by MRI will decrease. Studies has found that hydrate saturation can be monitored by MRI signals [8, 9] . Several studies have looked at hydrates in porous media. Baldwin et.al. found that a porous sandstone does not affect the dissociation temperature of hydrates [8]. Glass beads has been used to study the way hydrates form, finding that the interaction between the guest molecules and the host molecules, will affect whether the formation takes place after the cementing model, or the free flowing model [10].

1.1 Clathrate gas hydrates

1.1.1 Characteristics

A clathrate is defined as a compound formed by the inclusion of guests molecules within cavities in a crystal lattice of host molecules [4]. The host and guest molecules display no chemical bonding between each other. The clathrate compound is rather bound together by van der Waals interaction between the guest and the host molecules, and the hydrogen bonds between the water/host molecules. There are several types of clathrates where hydrates are a subgroup. Hydrates are clathrates in which the host molecules, i.e. the structural molecules, are water, and the cavities are occupied mainly by gas molecules[4]. Figure 1.4 illustrates a clathrate gas hydrate and the different shapes that can be formed [11].

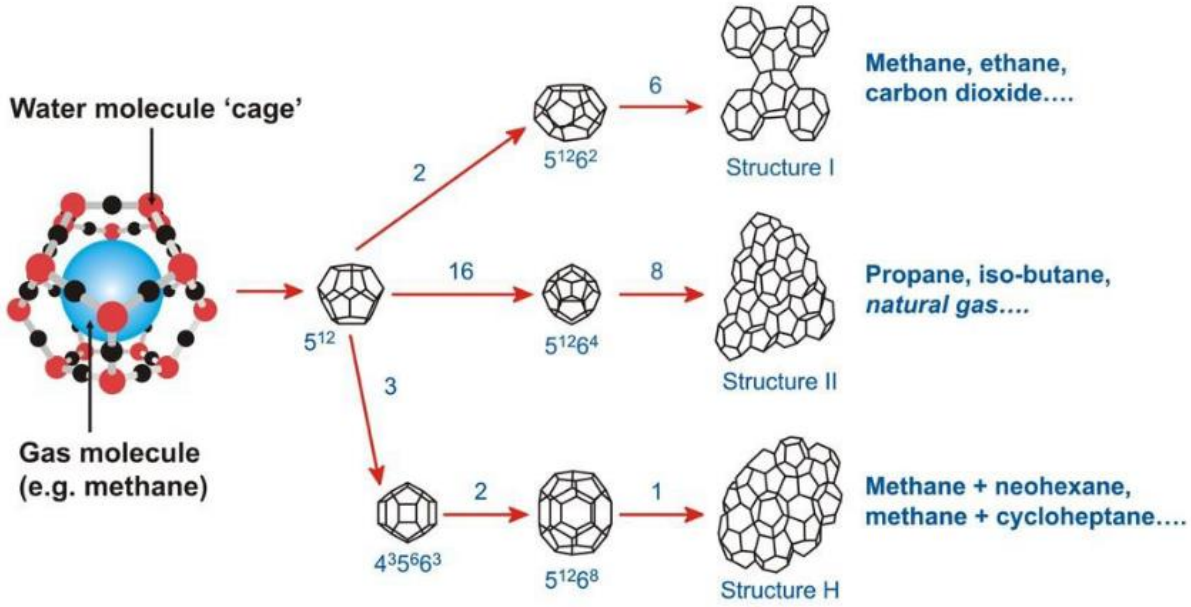

Figure 1.4 - Illustration of a clathrate lattice structure with a guest molecule, as well as the different types of structures that a hydrate can form. The structures that are illustrated are the five types of polyhedra used as bulding blocks in the three main hydrate structures. 5^{12} is called pentagonal dodehedron, $5^{12}6^2$ is called tetrakaidecahedron, $5^{12}6^4$ is called exakaidecahedron, $4^35^66^3$ is called irregular dodecahedron, and $5^{12}6^8$ is called icosahedron [11].

Clathrate gas hydrates can be formed with different lattice structures depending on the guest molecules that are present. There are mainly three types of structures called sI, sII and sH. These different hydrate structures are composed of the five different types of polyhedras, illustrated in figure 1.4. The nomenclature description $n_i{}^{m_i}$, describes the composition of the hydrate structure, e.g. 5^{12}, signifies that this structure consists of 12 pentagons. The number of edges that the face type consists of is then specified by n_i. The number of faces with this specific amount of edges is defined by m_i. Structure I crystals consist of primitive cubic lattice, structure II of face-centered cubic lattice, and structure H consists of hexagonal crystals[6]. The three kinds of structures will have different guest-molecules depending on the size of the cavities. Table 1.1 shows examples of which guest molecules that can be found within the different structures [6].

Clathrate gas hydrates form spontaneously under a definite pressure and temperature, depending on the guest molecule present. The host molecules will crystallize first, forming an open lattice structure, before guest molecules of suitable size and molecular composition completes the clathrate crystalline structure. The formation of hydrates is an exothermic reaction and the dissociation of hydrates is an endothermic reaction [4] [6]. Clathrate gas hydrates are therefore the most stable form for water and guest molecules to interact, upon favorable conditions.

Table 1.1 – Examples of guest molecules within the three main hydrate structures.

Structure	Diameter of guest molecule	Example of guest molecule
I	(0,42 - 0,6) nm	Methane, ethane, carbon dioxide, hydrogen sulfide
II	<0,42 nm (0,6 - 0,7) nm	Nitrogen, hydrogen Propane, iso-butane
H	(0,7 - 0,9) nm	Iso-pentane, neohexene When accompanied by smaller guests such as methane, hydrogen sulfide or nitrogen

The formation of natural gas hydrates develops through two major stages; hydrate nucleation and hydrate growth [12]. The process in which small clusters of hydrate nuclei grow and disperse to achieve critical size for continued growth, is known as hydrate nucleation [6]. The time between cooling, and hydrate growth, until hydrate nucleation is accomplished is called induction time. The hydrate nucleation is a stochastic process, meaning it does not necessarily occur at the same conditions for each experiment [6]. Figure 1.5 illustrates the full cycle of methane hydrate formation and dissociation. Point A to B displays the induction time for the hydrate formation, where cooling and nucleation takes place. After hydrate nuclei reaches the critical size, hydrate growth continues. This is illustrated from point B to C in the figure. As natural gas hydrates form, the gas and water molecules are packed in such a way that saves a significant amount of space. This will result in a major decrease in pressure as illustrated from B to C. From point C to point D, the hydrates are heated, leaving them to dissociate. As the temperature rises as the lattice structures fades, the molecules will occupy a larger space again and the pressure increases. For hydrates to decompose the hydrogen bonds between water molecules and the van der Waals interaction forces between the guest and the host molecules must be broken and heat must be applied.

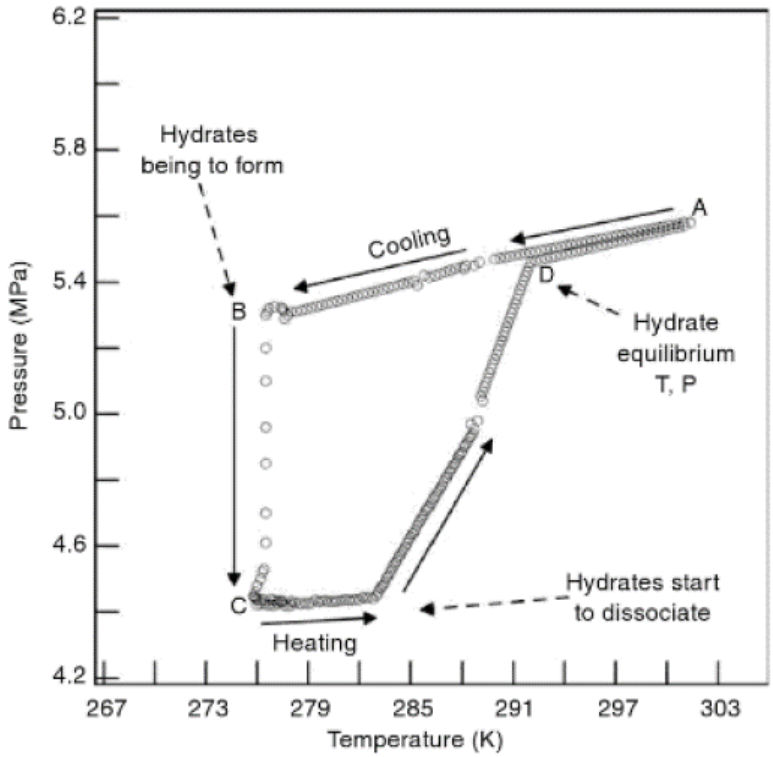

Figure 1.5 - Pressure and Temperature map for formation and dissociation of methane hydrates. The induction time is found between point A and B as cooling is performed. Between B and C hydrate growth occurs, and the pressure decreases. Heating occurs from C to D causing the hydrates to dissociate and the pressure to increase [6].

The methane hydrate is the most distributed and studied natural gas hydrate. The stability field of methane hydrate is illustrated in figure 1.6 [13]. This illustration shows the effect that temperature and pressure have on methane hydrates, for an arctic environment as well as for the marine environment. The dashed linear lines show the geothermal gradient, the increase in temperature recorded as one travels further away from the earth's surface. The lines are discontinuous due to a change in thermal conductivity [6]. To the left in figure 1.6, the arctic environment is displayed. The depth on this scale is here given in meters of overburden sediments. Due to the weight of the overlying mass the pressure will increase with the depth. From this figure, it becomes clear that the hydrate stability zone follows this geothermal gradient as a lower boundary for the temperature and as an upper boundary for the pressure. The hydrate stability zone is within the pink shaded area on the figure, and defines the temperature and depth where one can expect to find natural occurring methane hydrates. The marine environment is shown to the right in figure 1.6. For marine environments, the depth on the y-axis describes the distance the sea surface. The weight of overlying water will create an increase in pressure, as one travels further from the surface. The hydrothermal gradient describes the development of the temperature in the ocean as a function of position. As one approach the seabed the temperature will decrease, before it will increase as one travels into the crust. The methane hydrate stability zone is found below the ocean floor and follows the geothermal gradient as a lower boundary for temperature and upper boundary for pressure.

Methane hydrates cannot accumulate above the seafloor as water is denser than the methane hydrates [6].

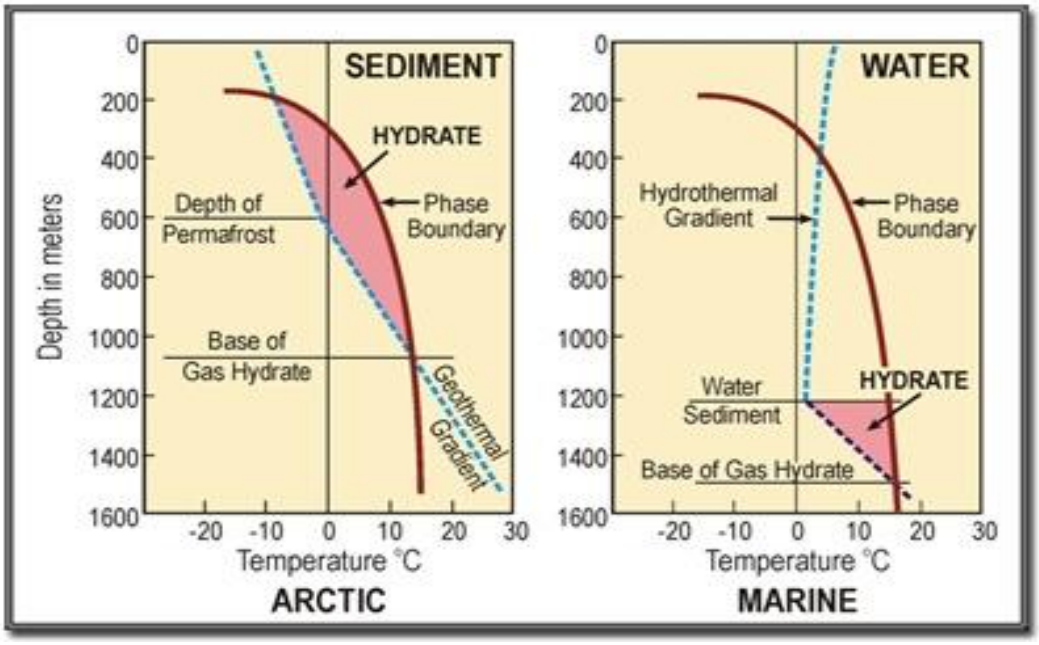

Figure 1.6 – Illustration of the stability zone for naturally occurring methane hydrates. The pink shaded area displays where one can expect to find naturally occurring methane hydrates, in both arctic and marine environments. The stability conditions follow the geothermal gradient as a lower boundary for the temperature and an upper boundary for pressures [13].

From figure 1.6 it becomes clear that the methane hydrate needs high pressures to enter the stability zone. For experiments performed at atmospheric pressure a different guest molecule is needed to successfully create hydrates.

1.1.2 Tetrahydrofuran hydrate

Tetrahydrofuran, from now on referred to as THF, is a water-soluble, polar organic compound. THF has the formula $(CH_2)_4O$, see figure 1.7. THF can be classified as a cyclic ether [6]. Table 1.2 displays the properties of THF.

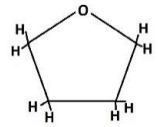

Figure 1.7 – Illustration of THF.

Table 1.2 - Properties of THF

Property	**Value**
Molecular weight [g/mol]	72,11
Boiling point [°C]	66,11
Freezing point [°C]	-108,33

Cyclic ethers can form hydrates at atmospheric pressure, if the temperature is low. THF is completely miscible with water and will therefore form a uniform hydrate, while most other hydrates are formed at the surface of the water face. The THF hydrate is of structure II, giving it the hydrate composition $THF{\cdot}17H_2O$, as the ideal hydration number [14]. The THF compound will only occupy the biggest cavities of structure II, leaving room for other guest molecules, if they are present.

Figure 1.8 shows the connection between the mass percentage of THF in water, and the corresponding melting point of the THF hydrate [14]. The figure shows a decrease in melting temperature for the lowest mass %, before an increase as the mass % of THF reaches 20. The maximum melting temperature is slightly below 5°C at approximately 20 mass % THF. For higher concentrations of THF, the melting temperature decreses. The hydrate composition $THF{\cdot}17H_2O$ corresponds to a mass % of 19, and a melting temperature of 4,5°C [6].

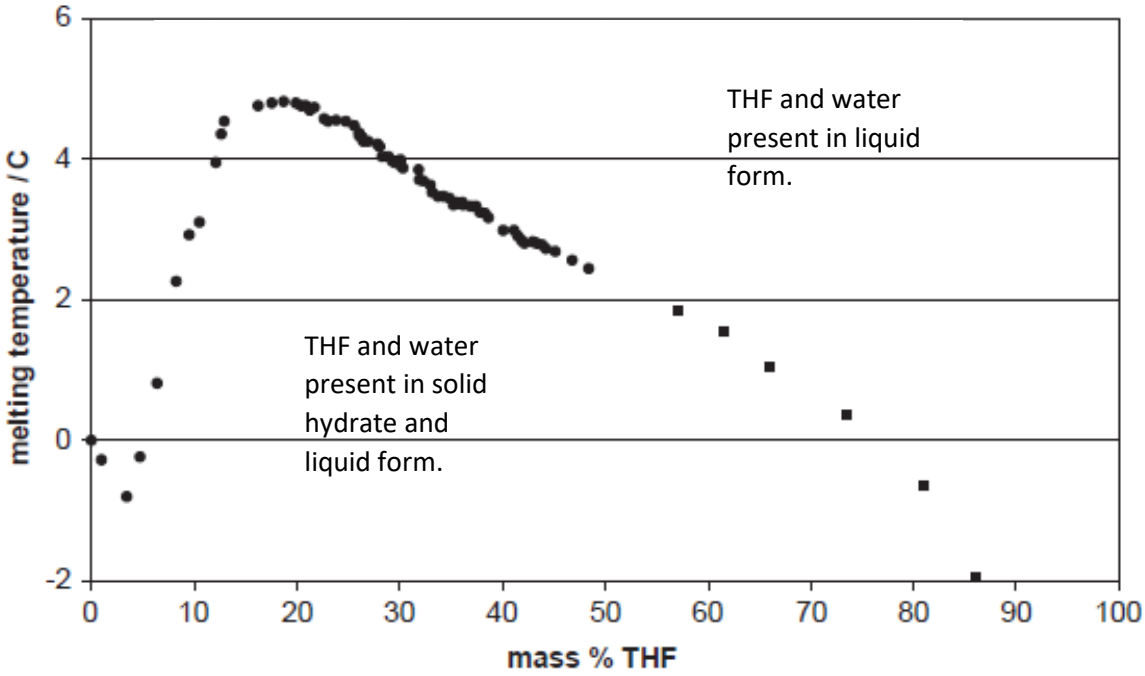

Figure 1.8 – The connection between mass % of THF in water and the resulting melting temperature of the THF hydrate, at atmospheric pressure. The recorded melting temperature shows a decreasing value for the lowest mass % of THF, before a significant increase in melting temperature as the mass % of THF reaches 20. For higher mass % of THF the melting temperature will decrease as the THF becomes more dominant. (The figure is adapted from the figure found in "Heterogenous nucleation of clathrates from supercooled tetrahydrofuran(THF)/water mixtures, and the effect of an added catalyst [14].

1.2 Magnetic Resonance Imaging

Magnetic resonance imaging is an imaging technique mostly associated with the field of medicine, but the interest within the petroleum technology field is increasing. The technique is based on the interaction between an applied magnetic field and a nucleus that possesses spin [15].

1.2.1 Basics nuclear magnetic resonance

All stable atoms are made up of electrons, protons, and neutrons (apart from hydrogen, which only contains one proton and one electron). These particles are used to define the different atoms and to separate them into different groups. The number of protons an atom contains corresponds directly to the atomic number, and defines the atom. The atomic mass of an atom is the sum of both the protons and the neutrons in its core, as well as the electrons that are bound to the atom. These two definitions can be used to divide natural occurring nuclei into three groups, based on a physical property called intrinsic spin angular momentum, often referred to as spin, I. The three groups of values for spin are; zero, half-integrals values, and integral values [15]. An even numbered atomic mass and odd atomic number will give intrinsic spin angular momentum the integral values, 1, 2, or 3 and so on. An odd numbered atomic mass will give the half-integral values, ½, 3/2, or 5/2 and so on. An even numbered atomic mass and even atomic number will not give any signal, the intrinsic spin angular momentum will therefore be zero [15]. In conclusion, for a nucleus to possess spin, it needs to have either an odd number of protons, an odd number of neutrons, or an odd number of both [16]. Table 1.3 shows a schematic overview of the atomic mass and atomic number values, and the resulting intrinsic spin angular momentum.

Table 1.3 - Overview of values for atomic number and mass and the following result for intrinsic spin angular momentum.

Atomic number	Atomic mass	Intrinsic spin angular momentum
Even	Even	Zero
Even	Odd	½, 3/2, 5/2, etc
Odd	Even	1, 2, 3, etc
Odd	Odd	½, 3/2, 5/2, etc

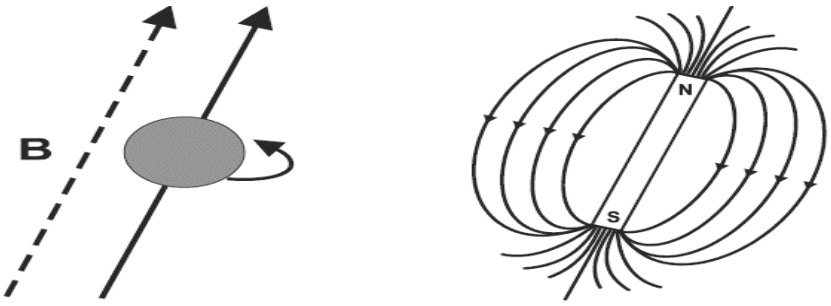

Figure 1.9 - Magnetic momentum of a nucleus. A rotating nucleus produces a magnetic field oriented parallel to the axis of rotation. This magnetic momentum can be compared to the magnetic field around a bar magnet and is given an axis of rotation, much like the orientation of the bar magnets magnetic field from the south pole to the north pole [15].

The spin angular momentum creates a magnetic field around the rotating nucleus called magnetic momentum. This magnetic field is parallel to the axis of rotation and can be compared to the field around a bar magnet, as illustrated in figure 1.9 [15]. In absence of an external magnetic field, the magnetic momentums of spinning nuclei will align randomly and the sum of these different spin vectors will equal to zero, this is illustrated in figure 1.10 [15]. A sum of spin vectors equal to zero means that there is no net magnetization present for the nuclei.

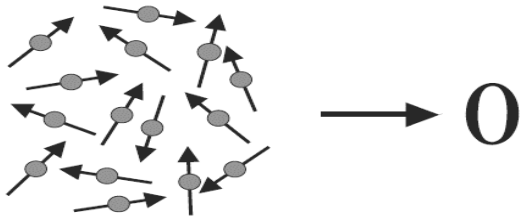

Figure 1.10 – Without the influence of an external magnetic field the magnetic momentums of nuclei are randomly oriented. The sum of these magnetic momentums will equal to zero, i.e. no net magnetization [15].

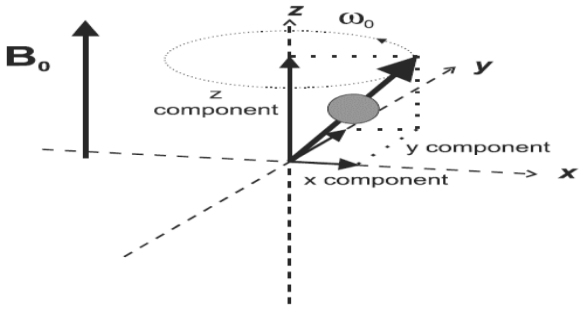

Figure 1.11 – A nucleus exposed to an external magnetic field, B_0, will align to the field and precess about it, with the frequency ω_0 [15].

When nuclei are exposed to an external magnetic field, B_O, they will align with the field, either parallel or anti-parallel, and precess about it. This is illustrated in figure 1.11 [15]. The frequency of precession is proportional to the strength of B_O and can be expressed by the Larmor Frequency:

$$\omega_0 = \frac{\gamma B_O}{2\pi} \tag{1.1}$$

Where ω_0 is the Larmor frequency given in Hz,

γ is the gyromagnetic ratio, a constant for each nucleus given in $\frac{1}{sT}$, T the magnetic strength in Tesla.

B_O is the Magnetic field given in T, Tesla.

Nuclei exposed to B_0, will to some extent favor the parallel spin, which has a lower energy state, see figure 1.12 [15]. The distribution of parallel spin and anti-parallel spin will consequently be slightly uneven. For a field of 0,5 T, 3 excess protons per one million protons will favor the lower energy state [17]. The excess of protons is proportional to B_0 and will increase as the field strength increases, explaining why stronger fields, will give better images [17]. The following formula display the distribution of the number of nuclei in the lower energy state, N^+, and the number of nuclei in the higher energy state, N^-:

$$\frac{N^-}{N^+} = e^{\frac{-\Delta E}{kT}} \tag{1.2}$$

Where ΔE is the energy difference between the two nuclei states

k is Boltzmann's constant $1{,}3805 \times 10^{-23}$ J/K and

T is the temperature in Kelvin.

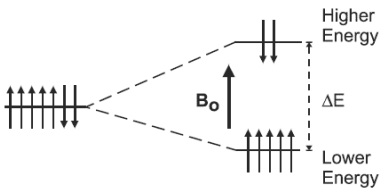

Figure 1.12 - The Zeeman Diagram displays the energy difference between the nuclei with parallel- and anti-parallel spin [15].

The unevenly distributed spin will give a net sum of magnetic momentum unequal to zero, hence a net magnetization, M_0. Manipulation of this M_0 is the foundation of MRI techniques. The orientation of M_0 will be in the same direction as B_0. The connection between M_0 and B_0 is given by formula (1.3), with the magnetic susceptibility, χ, as the slope. The magnetic susceptibility is a measure of how easily the material is magnetized.

$$M_0 = \chi B_0 \tag{1.3}$$

Like in the field of medicine, the nucleus of special interest for the petroleum industry is the hydrogen atom, ^{1}H. Hydrogen consist of a single proton and electron, giving it an odd atomic number as well as an odd numbered atomic mass. The intrinsic angular momentum of hydrogen is ½, and the gyromagnetic ratio which for hydrogen is 42,58MHz/T×2π. When hydrogen is exposed to an external magnetic field it gives one of the largest responses found in nature[15].

1.2.2 Excitation and relaxation

A nucleus exposed to a radio frequency pulse will only respond to the pulse if it carries the same frequency as the nuclei, allowing for excitation of only this one type of nuclei. To acquire data with MRI, nuclei in the sample are exposed to radio frequency pulses matching their Larmor frequencies, thus exciting the nuclei. The net magnetization will rotate into a plane perpendicular to the Z-axis; the X-Y plane. Hence the orientation of the net magnetization will flip 90°, this is illustrated in figure 1.13. When a proton is excited, it enters a higher energy level, which is «exhausting» for the proton. The proton will re-emit the energy to fall back to the normal energy state. This process is called relaxation. Relaxation is in principle the reverse of excitation. To fall back to the original energy state, the energy is released in the shape of a small amount of heat and radio frequency waves. There are two relaxation mechanisms of importance, spin-lattice and spin-spin relaxation with their respective time constants of T_1 relaxation time and T_2 relaxation time [15].

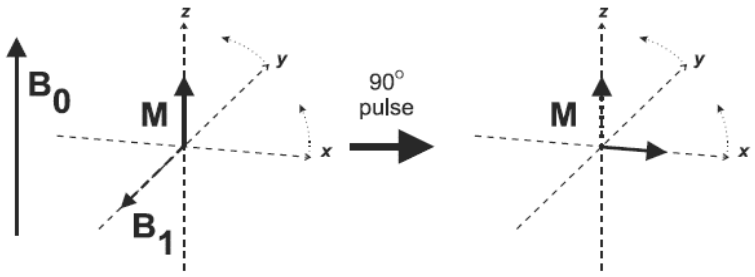

Figure 1.13 A nucleus aligned to a magnetic field B_O will when exposed to a 90° radiofrequency pulse flip its magnetization from the z-direction into the x-y plane [15].

1.2.3 T_1 and T_2 relaxation times

The T_1 relaxation time describes the spin-lattice relaxation, also called longitudinal relaxation. The excited proton transfers its energy to the surroundings, or the lattice, instead of to another spin, hence spin-lattice relaxation. It describes the time needed for the z-component of magnetization to return to 63% of its original value after exposure of an excitation pulse [15]. T_1 relaxation describes the magnetization in the z-direction. The return of the magnetization follows an exponential growth process, with T_1 as the time constant describing the rate of growth:

$$M(\tau) = M_0\left(1 - e^{(-\tau/T_1)}\right) \quad (1.4)$$

Where $M(\tau)$ is the magnetization as a function of τ
τ is the time development
T_1 is the longitudinal relaxation time

When nuclei are exposed to a 90° radiofrequency pulse, the longitudinal magnetization completely shifts into the X-Y plane. As the protons release their energy through T_1 relaxation, the longitudinal magnetization increases gradually. A larger fraction of the longitudinal magnetization M_z is reestablished until M_0 is completely restored, as illustrated in figure 1.14. The y-axis, $\frac{M_z}{M_0}$, describes how the longitudinal magnetization, gradually returns to the original M_0, over time τ. The rate of relaxation depends on how the atom of interest is bound to other atoms around it. The more tightly bound the hydrogen molecules are the faster they will release their energy [17].

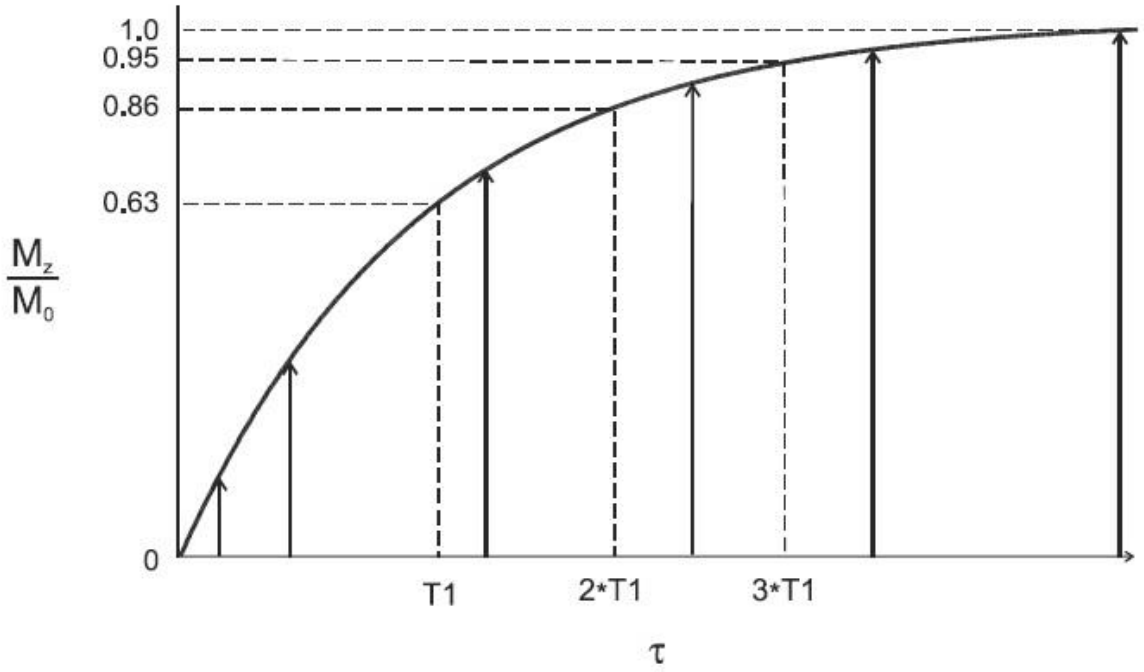

Figure 1.14 The T_1 relaxation curve displays how the longitudinal magnetization is reestablished as a function of time τ [15].

The T_2 relaxation time describes the spin-spin relaxation, also called transverse relaxation. The term spin-spin refers to the energy being transferred from one excited proton to another nearby proton, i.e. from one spin to another spin. T_1 and T_2 relaxations are two independent processes that only have one thing in common, they occur simultaneously [17]. The T_2 relaxation time represents the time needed for the transverse component of the magnetization to decay to 37% of its value after excitation [15]. It describes the magnetization in the X-Y plane. Decay of the transverse component of the magnetization is described by formula (1.5) where the time constant is T_2^* rather than T_2:

$$M_{XY}(t) = M_{XY_{max}} e^{(-t/T_2^*)} \tag{1.5}$$

Where $M_{XY}(t)$ represents the magnetization in the XY-plane as a function of t

t represents the time

$M_{XY_{max}}$ represents the maximum value of the magnetization in the XY-plane

T_2^* is given by formula (1.6):

$$1/T_2^* = 1/T_2 + 1/T_{2_M} + 1/T_{2_{MS}} \tag{1.6}$$

Where T_2 represents the transverse relaxation time
$T_{2_{MS}}$ is the dephasing time due to the magnetic susceptibility differences
T_{2_M} is the dephasing time due caused by the main fields inhomogeneity.

$M_{XY_{max}}$ is the transverse magnetization immediately following the excitation pulse. As M_{XY} decreases, the relation $\frac{M_{XY}}{M_{XY_{max}}}$ will decrease as illustrated in figure 1.15.

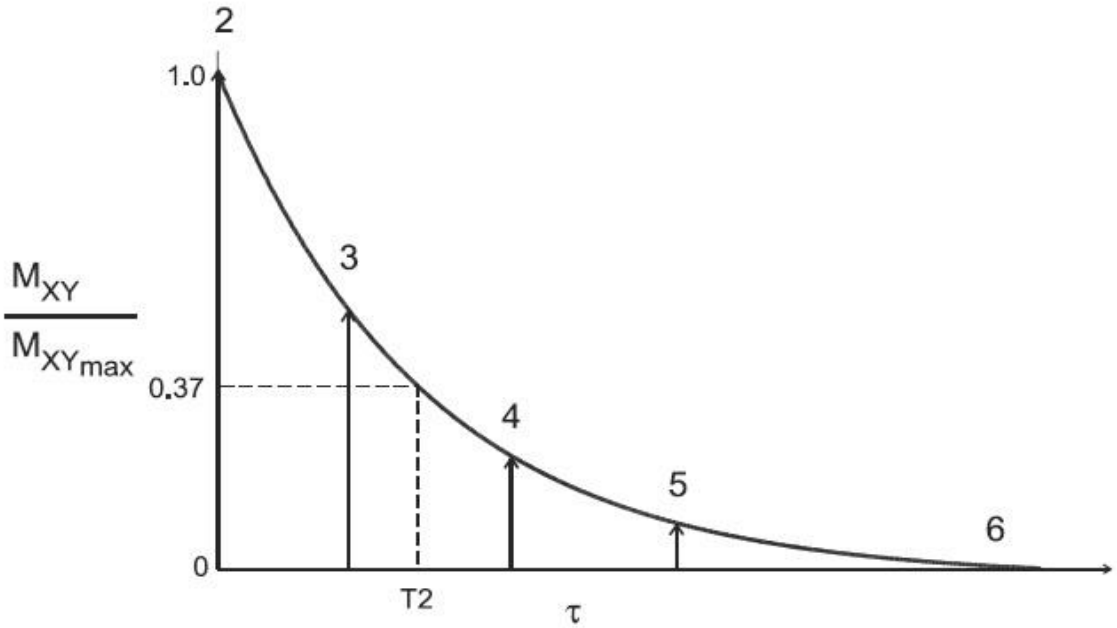

Figure 1.15 This curve displays the development of the T_2 relaxation as a function of time [15].

The T_2 relaxation time is always less than or equal to the T_1 relaxation time. This means that T_2 relaxation is always faster than T_1 relaxation. The recovery of magnetization along the z-axis is independent from the decay of magnetization along the x-y plane. The difference between the T_1 and the T_2 relaxation times is caused by a phenomenon called dephasing. Dephasing can be explained by interaction between nuclei and or by the external magnetic field inhomogeneities. Before the 90° radio frequency pulse is applied there is no phase coherence between the protons. When exposed to the magnetic field B_0 the nuclei will align in the z-direction. The nuclei might precess at the same speed, but they are not synchronized i.e. they are not in phase. When the 90° pulse is applied, flipping the magnetization into the X-Y plane, the protons are spinning synchronized with each other i.e. the protons will be in phase[17].

When the protons re-emit their excess energy, they start to de-phase i.e. fall out of the synchronized spinning. The process from total in-phase to totally out-of-phase, and the reduction to 37% of the transverse magnetization, is called T_2 relaxation. The magnetic field of one proton is influenced by the magnetic fields of other protons, meaning that one vector might slow down while another speed up. The influence continues, and the de-phasing increases. The result is a strong initial signal, as the RF pulse is applied, before a rapidly decreasing signal, as the nuclei fall out of phase. This specific kind of signal is called free induction decay, or FID for short[17].

1.2.4 MRI instrument, Fourier transformation and K-space

The MRI instrument is build up by five main components: a magnet, gradient coils, RF-coils, scanner control electronics, and animal/sample handling accessories [18], see figure 1.16 for an illustration [19]. The magnet provides a static magnetic field, completely time invariant. The gradient coils produce a gradient field, a time-dependent magnetic field. The radio frequency coils, driven by the RF power amplifiers, produce pulsed high frequency electromagnetic fields [18].

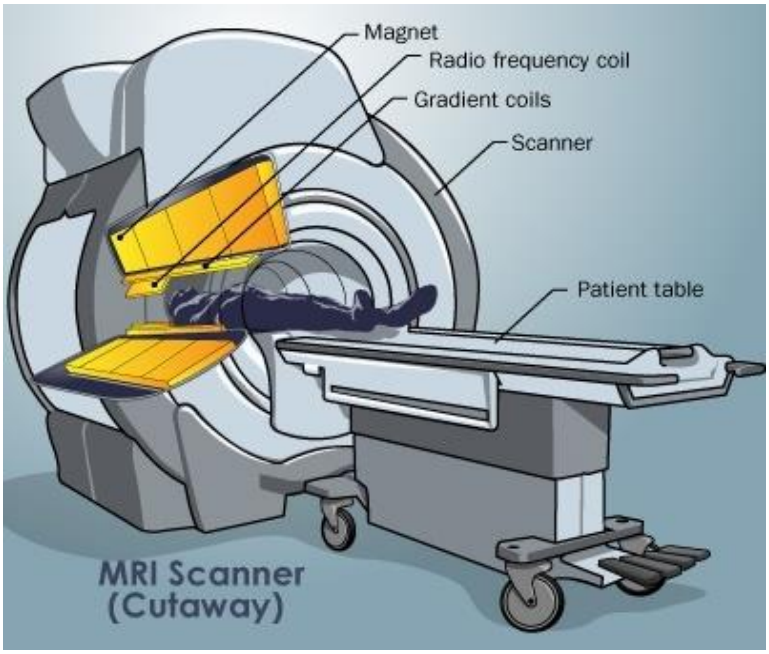

Figure 1.16 The main components of the MRI Instrument: magnet, radio frequency coils, gradient coils, scanner, and patient handling accessories [19]

There are several types of MRI instruments. Among these are the closed bore of cylindrical design, superconducting MRI instrument, which is used for this master thesis. The coils in this instrument are immersed in liquid helium to achieve superconducting conditions and allowing for a stable homogenous field to occur [20].

An MR image is a frequency and phase map of the protons in the object or patient being imaged. The map is generated by unique magnetic fields at each point, through the whole image. To obtain an image, spatial localization of the MR signal needs to be performed. This is achieved by the use of gradient coils. Three orthogonal gradient coils are required, G_x and G_y, referred to as transverse gradients, and G_z, referred to as the longitudinal gradient. These gradients are produced by passing of a current, through wire coils arranged on a cylindrical surface. By establishing a gradient in the three direction, x, y, and z, it becomes possible to locate and examine a specific part of a sample, even if the object is homogenous. The gradient allows the item that is being imaged to be divided into numerous slices of various thicknesses. Gradient coils are required to have a high current efficiency, short switching time, gradient linearity over a large volume, low power consumption, and minimal interaction with other equipment [21].

The radio frequency coil can function as a transmitter and a receiver, at the same time. When the RF-coil is used as a transmitter it generates a magnetic field, B_1, perpendicular to B_0. B_1 is turned on for brief moments to produce radiofrequency pulses. When the RF-coil is used as a receiver it is responsible for detecting the MRI signal. The net magnetic flux from the excited protons are captured by the coil and an induced electric current is generated. This signal is amplified and digitalized through an analog to digital converter and the Fourier transformation. Most MRI instruments have a separate receiver coil, that will perform the same job as the RF-coil [20].

Signals measured in MRI are a combination of signals from all over the object that is being imaged. The signal is composed of a series of sine waves, that each will have an individual frequency and amplitude. To convert the signal from time domain into frequency domain Fourier transformation is used. The signal is encoded with magnetic field gradients, making frequency and phase related to position. The signal needs to be transformed to a digital representation, through an analog-to-digital converter. The resonant frequencies of protons are often greater than many ADCs can process. A phase-coherent difference signal is therefore generated based on the frequency and phase of the radiofrequency pulse. The Nyquist frequency, ω_{NQ}, specifies the maximum frequency that can be accurately processed by the ADC:

$$\omega_{NQ} = \frac{Total\ number\ of\ datapoint}{2} * Sampling\ time \tag{1.7}$$

For MRI data, ω_{NQ} can be from 500-500 000Hz. To exclude the frequencies above the ω_{NQ}, a low-pass-filter is used prior digitization. The frequencies that are excluded are mostly signals that are considered as noise [15].

To reconstruct an image, Fourier transformation needs to be performed. A Fourier transformation is a mathematical procedure that converts the information from a signal in the time domain to a complex number in the frequency domain. Any periodic signal can be written as a sum of sine waves with various amplitudes, frequencies, and phases [22].

$$s(t) = a_0 + a_1 \sin(\omega t + \phi_1) + a_2 \sin(2\omega t + \phi_2) + a_3 \sin(3\omega t + \phi_3) + \cdots \tag{1.8}$$

Where a_i represents the amplitude
ϕ_i are the phase shifts
ω is the fundamental frequency, where the higher order 2ω and 3ω are called harmonics.

The Fourier transformed signal is often referred to as the temporary image space. The temporary image space is a matrix in which data from the digitalized signals are stored during data acquisition. This temporary space is called k-space. K-space is displayed as a quadratic box, like figure 1.17 [17]. The positioning of the signals being filled into k-space is dependent on the signal intensity. Low intensity signals are placed in the center of k-space, while high frequency signals are spaced around the center. The low intensity signals contain information about contrast, while the high frequency signals contain information about spatial resolution and sharpness. The K-space is symmetrical from left to right, as well as from top to bottom[17].

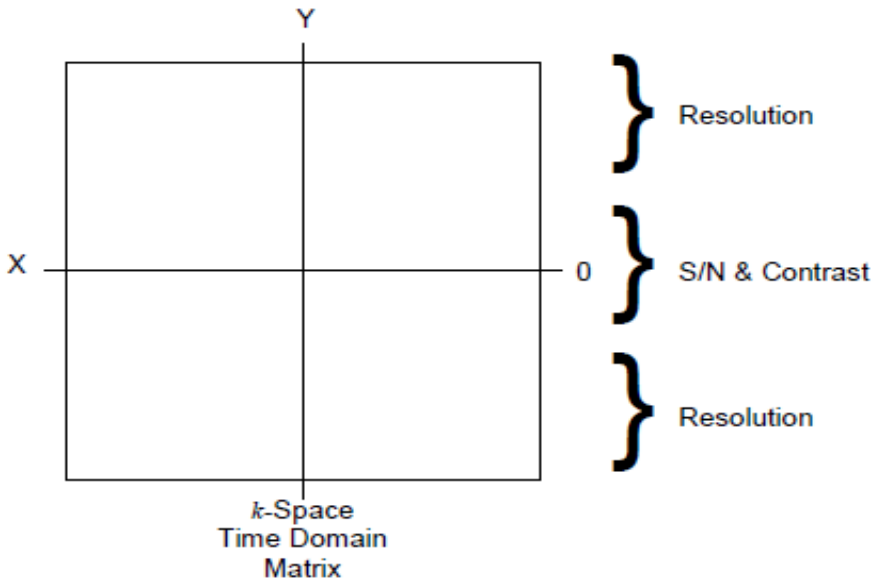

Figure 1.17 Illustration of the filling of K-space. Low intensity signals are placed in the center of k-space and gives information about the contrast and signal to noise ratio. The higher intensity signals are spaced around the center and contain information about the spatial resolution and sharpness [17].

The scan matrix is built up of the phase encoding direction, MXPE, and the frequency encoding i.e. the read-out direction, MXRO. To illustrate the meaning of the scan matrix MXPE x MRO, 256x512 is used as an example. MXPE specifies the number of lines in K-space, e.g. 256 lines. As the phase encoding of the signals is done one line at a time, the whole process of excitation needs to be repeated as many times as specified by MXPE, e.g. 512 [17].

1.2.5 Pulse sequence timing diagram

The radio frequency settings used in the production of an MR image constitutes a pulse sequence. This contains the hardware instructions, directly selected by the operator. Different equipment manufacturers use different pulse sequences and operates with different names for them. Comparison of techniques and protocols are therefore complicated. Timing diagrams represent a schematic representation of the basic steps that are performed by the different hardware components during sequence execution. The timing diagram makes comparison of pulse sequences easier, see figure 1.18 for a simple illustration. The general features for timing diagrams are the same although there may be several differences depending on the manufacturer. The time elapsed during a sequence execution is indicated from left to right along the horizontal axis. To describe any pulse sequence with a timing diagram, at least four lines are required; one representing the radio frequency transmitter and one representing each gradient, labeled as G_{SLICE}, G_{READ}, and G_{PHASE}, G_X, G_Y, and G_Z. Each of these lines corresponds to a different hardware component. Supplementary lines may be added for indication of other activity such as analog-to-digital converter. [15]

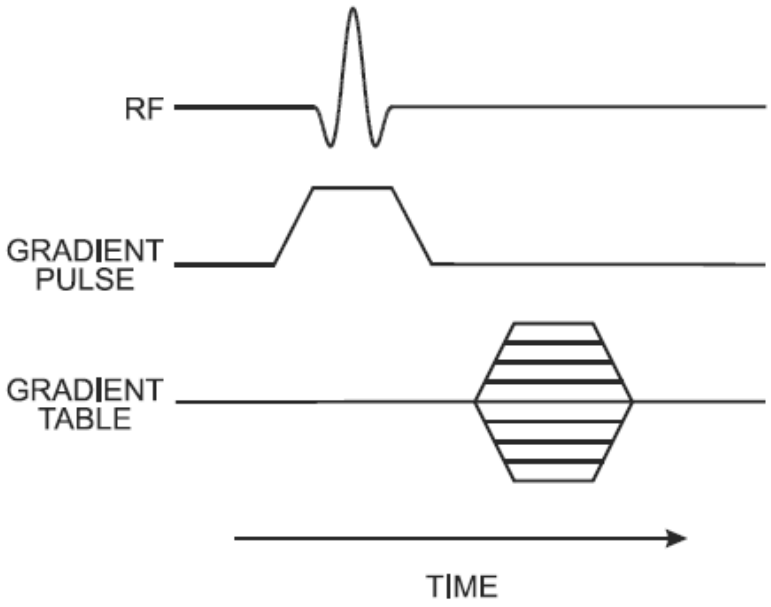

Figure 1.18 Simple timing diagram. Each line represents different hardware components. Gradient activity that are constant are shown as a constant deviation from baseline, while activity that varies are shown as a dashed region to illustrate multiple values [15].

The spin echo sequence is a commonly used pulse sequence. The spin echo sequence has at least two radio frequency pulses, an excitation pulse, 90°, and numerous refocusing pulses, 180°, that generates the spin echoes. The repetition time, TR, for a spin echo sequence is the time between successive excitation pulses for a given slice. The echo time, TE, defines the time from the excitation pulse to the echo maximum. A timing diagram for the spin echo pulse sequence is illustrated in figure 1.19 [23].

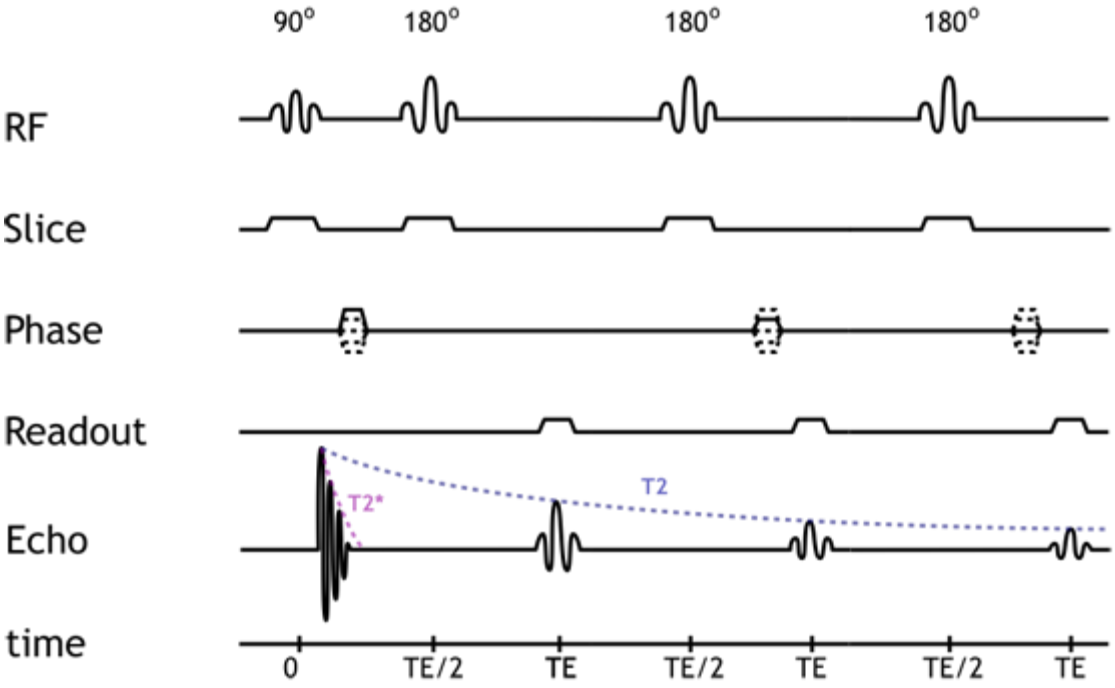

Figure 1.19 - Timing diagram for the spin echo sequence. Gradient activity that are constant are shown as a constant deviation from baseline, while activity that varies are shown as a dashed region to illustrate multiple values [23].

1.2.6 T_2 relaxation within a Porous medium

The molecular mobility of a nucleus will influence its relaxation process, especially the transverse relaxation, T_2 [24]. A fluid situated within the pores of a porous medium, will be given an enhanced relaxation, due to collisions with the pore walls. This means that hydrogen atoms in free fluid water will give a slower T_2 relaxation time than hydrogen atoms in water within a tight pore. The tighter the pore is the faster the relaxation process will happen. The T_2 relaxation time for a porous medium is given the following formula [25]:

$$\frac{1}{T_{2measured}} = \frac{1}{T_{2bulk}} + \gamma \frac{\Delta B_0}{\Delta r} + \rho \frac{S}{V} + \frac{1}{12}\gamma^2 TE^2 {G_0}^2 D \qquad (1.9)$$

Where
ρ is surface relaxation
$\frac{S}{V}$ is surface to volume ratio
γ is the gyromagnetic ratio of the hydrogen atom
$\frac{\Delta B_0}{\Delta r}$ variation within the magnetic field
TE is the echo time
G_0 is the internal gradients susceptibility differences
D is the diffusion coefficient

$\gamma \frac{\Delta B_0}{\Delta r}$ is eliminated by the spin echo sequence, and can therefore be neglected when this sequence is applied

$\frac{1}{T_{2bulk}} \ll \rho \frac{S}{V} + \frac{1}{12}\gamma^2 TE^2 {G_0}^2 D$ and can therefore be neglected

Formula (1.9) can then be simplified to the following:

$$\frac{1}{T_{2measured}} = \rho \frac{S}{V} + \frac{1}{12}\gamma^2 TE^2 {G_0}^2 D \quad (1.10)$$

If the applied echo time is kept low, it is the surface to volume ratio that will influence the measured T_2 relaxation process the most. Larger pores will have a lower surface to volume ratio, and smaller pores will have a larger surface to volume ratio [26]. To illustrate this, assume that the pore is spherical and use the following formulas.

Area of a sphere:

$$A = 4\pi r^2 \quad (1.11)$$

Volume of a sphere:

$$V = \frac{4\pi r^3}{3} \quad (1.12)$$

Surface to volume ratio:

$$\frac{A}{V} = \frac{4\pi r^2}{\frac{4\pi r^3}{3}} = \frac{3}{r} \quad (1.13)$$

Where r is the radius of the pore.

From these formulas, it become clear that as r increases, the surface to volume ratio will decrease. This will result in a faster, i.e. shorter, T_2 relaxation time for the smaller pores.

The MRI signal from T_2 relaxation decays as an exponential curve given by formula (1.14). This curve is illustrated by figure 1.20a. Further analysis, with the inverse Laplace transformation, will give a T_2 relaxation time distribution based on the decay curve, see figure 1.20b.

$$M(t) = A_0 e^{-\frac{t}{T_2}} \quad (1.14)$$

Where A_0 is the amplitude of the initial signal

T_2 is the transverse relaxation time

t: time

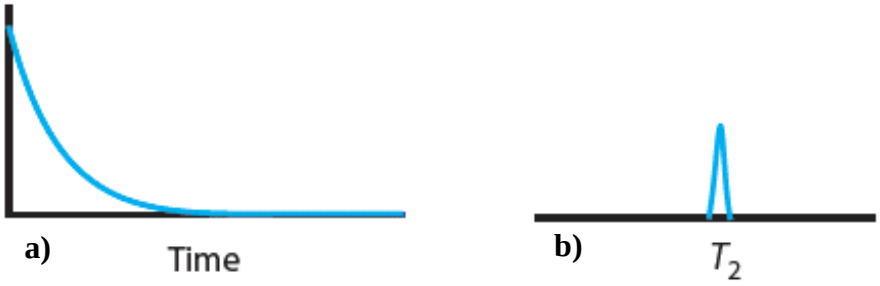

Figure 1.20 – a) The decay curve for T_2 relaxation time [26].

b) T_2 relaxation time distribution from analysis with the inverse Laplace transformation [26].

A complex porous media will contain pores with several different sizes. The T_2 relaxation time will hence give several different values, and give different solutions to formula (1.14). Each pore will then create its own decay curve, expanding formula (1.14) to formula (1.15):

$$M(t) = A_a e^{-\frac{t}{T_{2a}}} + A_b e^{-\frac{t}{T_{2b}}} + \cdots + A_N e^{-\frac{t}{T_{2N}}} \quad (1.15)$$

Where a, b, … N, represents a set of different T_2 values from a, to N.

The decay curve from formula (1.15) will be the sum of all the separate decay curves. The curve will be estimated at the mean value of the T_2 relaxation process. When analyzing these signals with the inverse Laplace transformation, the result will be a distribution of several T_2 relaxation times. This will give a more complex distribution as illustrated in figure 1.21b [26]. The lower T_2 values correspond to the smaller pores. The amplitude corresponds to the amount of pores with that exact T_2 value [26]. The distribution gives an indication of how the relative pore size distribution within a porous medium looks like. Relaxation times between 2-5ms will indicate a micro pore, 5-50ms indicates a meso pore, and 100-400ms indicates macro pores [26]. Micro pores are usually defined as pores with a diameter less than 2.0 nm, meso pores as pores between 2.0 nm and 50 nm, and macro pores as pores with a diameter greater than 50nm [27].

The resulting T_2 relaxation time will also be dependent on field strength of the magnetic field, and the molecular bonding of the responding nuclei. The higher the field strength, the lower the measured T_2 relaxation time will be. The tighter a hydrogen nucleus is bound, corresponding to the molecular mobility, the faster the T_2 relaxation will occur. If the echo time is increased, the measured T_2 relaxation process will no longer be highest influenced by the pore size relation. The internal gradients susceptibility differences and the diffusion coefficient will have a greater influence on the measured T_2 relaxation process. To achieve a direct link between the T_2 relaxation time and the pore size demands more knowledge about the porous media and the fluids situated within its pores.

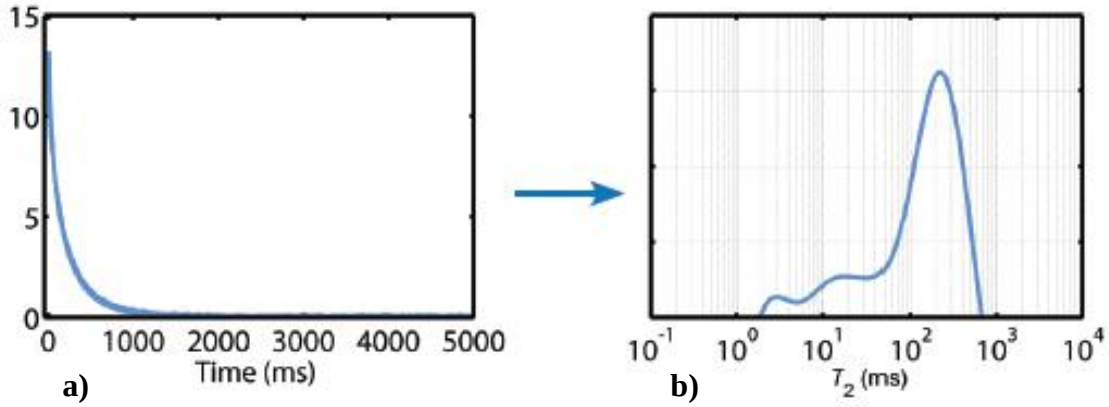

Figure 1.21 - a) The decay curve for T_2 relaxation time [26].

b) T_2 relaxation time distribution from analysis with the inverse Laplace transformation [26].

1.3 Wettability

1.3.1 Definition

The wettability of a solid surface gives information about how a fluid will spread on the surface. When a liquid, a gas and a solid surface is present, the wettability of the surface can be defined by Young's equation, formula (1.16) [28].

$$\cos\theta = \frac{\sigma_{SG}-\sigma_{SL}}{\sigma_{LG}} \qquad (1.16)$$

Where σ_{SG} defines the "effective" boundary tension between the solid- and gas phase

σ_{SL} defines the "effective" boundary tension between liquid- and solid phase

σ_{LG} defines the "effective" boundary tension between liquid- and gas phase

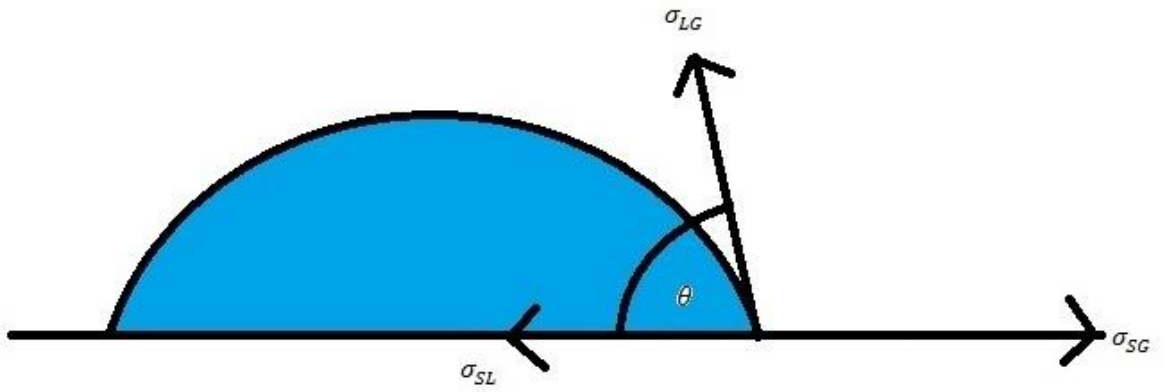

Figure 1.22 Illustration of the force balance at the solid-liquid-gas interface.

Young's equation describes the force balance between a liquid, gas, and solid surface, see figure 1.22 for an illustration of the situation. The angle that can be calculated through Young's equation is called contact angle, and will define the wettability of a solid surface, see table 1.4 [28]. The contact angle describes the shape of the droplet that is formed once a drop of fluid is added to a solid surface.

Table 1.4 Classification of wetting behavior in terms of contact angle [28].

Contact angle	Degree of wetting
$\theta=0°$	Wetting
$0°<\theta<90°$	Partially wetting
$90°<\theta<180°$	Partially non-wetting
$\theta=180°$	Non-wetting

In petroleum engineering literature, a somewhat different classification is used to be able to differentiate between different surfaces. Table 1.5 categorizes different kinds of surfaces depending on the contact angle that will form between a droplet of water and a solid surface [29]. This characteristic of the surface is important because it gives information about how the fluids in a porous medium will behave. On a water-wet surface, it will be mainly water that spreads directly on the surface, as longs as water is present, and the pressure conditions allows for it.

Table 1.5 Contact angles as defined in Petroleum engineering [29].

Contact angle θ	Wettability of surface
0°-30°	Strongly water wet
$30° - 75°$	Moderately water-wet
$75° - 105°$	Neutrally wet
105°-150°	Moderately oil-wet
$150° - 180°$	Strongly oil wet

1.3.2 Alteration of Wettability

Wettability is a character that can be alternated, either slowly by natural causes or more controlled by addition of other molecules to the solid surface. A liquid will spread onto a solid-gas interface if the spreading coefficient, $S_{L/S}$, is positive:

$$S_{L/S} = W_S = \sigma_{SG} - \sigma_{LG} - \sigma_{SL} \geq 0 \quad (1.17)$$

The spreading coefficient is equal to the work of spreading, W_S. Given water as an example, a positive spreading coefficient means that water will spread on the surface, and the surface is categorized as water wet. If the spreading coefficient is negative, the water will not spread, and the surface is oil-wet. Given the same liquid, gas and solid surface, formula (1.17) states that in order to alter from water wet to oil-wet, one has to alternate the interaction between the solid surface and the liquid, and create a negative spreading coefficient [28]. There are several different methods to alter the wettability of a surface, depending on the surface one starts with, and what degree of wetting one would like to achieve.

An effective way to alternate the wettability, from water wet to oil wet, is to use trimethylchlorosilane, TMCS. Silane, in general, adheres to a surface that possesses hydroxyl groups, by covalent bonds. Examples of surfaces with hydroxyl groups includes various minerals, including quartz, and other oxides [28]. The process of alteration of the wettability with TMCS is called silylation and is illustrated in figure 1.23.

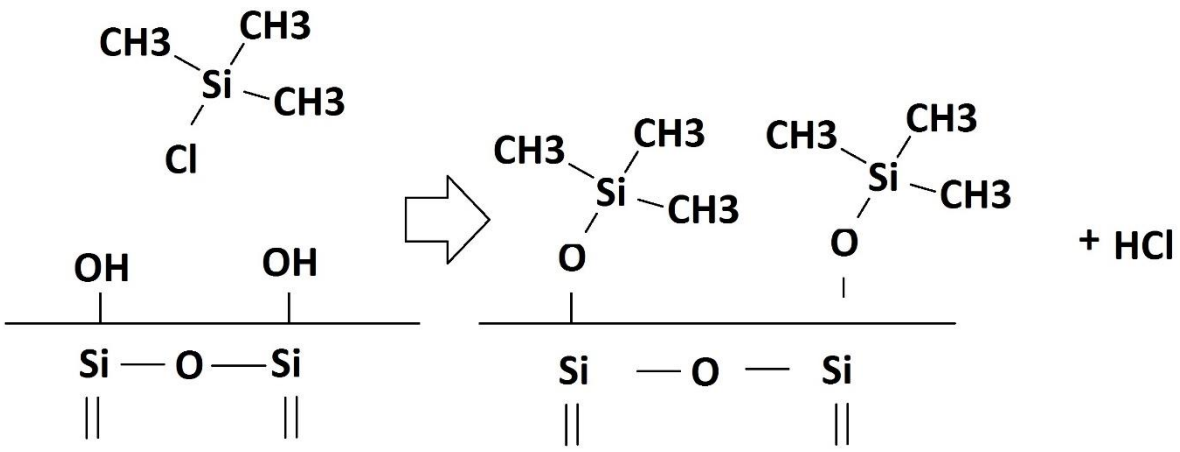

Figure 1.23 Silylation of a quartz surface

A quartz surface is illustrated in figure 1.23. Hydroxyl groups are connected to the quartz surface resulting in water being the wetting phase. When TMCS is present it will adhere to the oxygen, and the hydrogen will bind to the chloride, so HCl will be precipitated. The trimethylsilane groups that is now bound to the surface will cause it to prefer oil as its wetting phase, instead of water [30].

1.3.3 MRI Characterization of Wettability

As illustrated in figure 1.24, a water-wet system will have water closest to its pore walls while an oil-wet system will have oil closest to its pore walls, when both phases are present. This means that for an oil-wet system, when both water and oil present, the water will not be in direct contact with the pore walls of the porous media. For the water-wet system water will be in direct contact with the pore walls, when the two fluids are present. The relaxation time for hydrogen will be different for water in bulk and for water situated within pores. Water molecules that are in contact with a solid surface will relax faster than water molecules in a bulk. When measuring the relaxation time for a system of two different phases it is thought that one can, in theory, separate the surface according to wettability, if the saturation of fluids and the corresponding relaxation times are known. Wettability can hence be characterization through MRI [16].

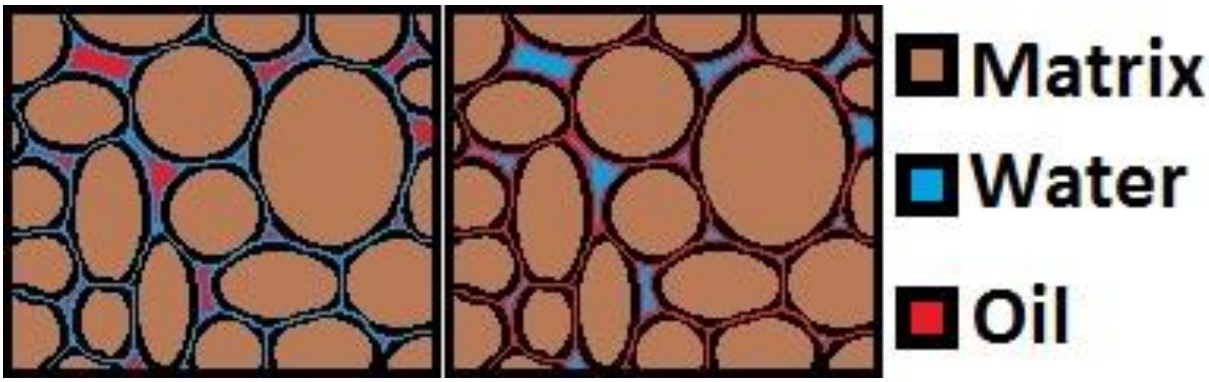

Figure 1.24 Illustration of a porous medium filled with two different immiscible fluids. The first picture shows a water-wet system, while the second picture displays an oil-wet system.

1.4 Objective

The main objective for this thesis has been to study the formation and the dissociation of THF hydrates within a porous medium by using magnetic resonance imaging. By monitoring the signal intensity in the response from hydrogen nuclei when exposed to radio frequency waves, a relative hydrate saturation within a sample can be estimated. The hydrate saturation can be estimated on a local scale and for the total sample simultaneously. The hydrate saturation is significant for improved comprehension of the permeability and how fluids will flow within a porous medium containing fluids and hydrates.

The following approaches will be investigated:

- Adjustments of MRI protocols suitable for investigation of hydrates in porous media.
- Using signal intensity to observe how fluids and porous media interact.
- Using signal intensity to monitor hydrate formation and dissociation, and to estimate the hydrate saturation.
- Using T_2 relaxation time mapping to investigate potential differences in interaction between fluids and porous media caused by wettability preferences of porous media.
- Using T_2 relaxation time mapping to investigate potential differences in formation and dissociation of hydrates caused by wettability preferences of porous media.

2 Method and Experimental set up

2.1 Bruker MRI instrument, ParaVision, and MRI techniques

The MRI instrument used for experimental work for this thesis is the BRUKER BioSpec 47/40 USR with a superconducting magnet. Figure 2.1 displays an image of the instrument. USR is short for ultra-shielded and refrigerated magnet. This type of magnet uses liquid helium to achieve the superconducting condition. The USR magnet does not need any refilling of helium, the refrigeration technology continuously recycles any helium that might boiled off [18]. The MRI instrument provides a field strength of 4,7 Tesla. As hydrogen is used for the NMR sequel, the magnet will operate with a frequency at approximately 200MHz. This can be estimated with the Larmor Frequency, formula (1.1). A field strength of 4,7 Tesla is considered a medium field strength. In general, the T_1 relaxation time will increase with increasing field strengths, while the T_2 relaxation time will decrease [31].

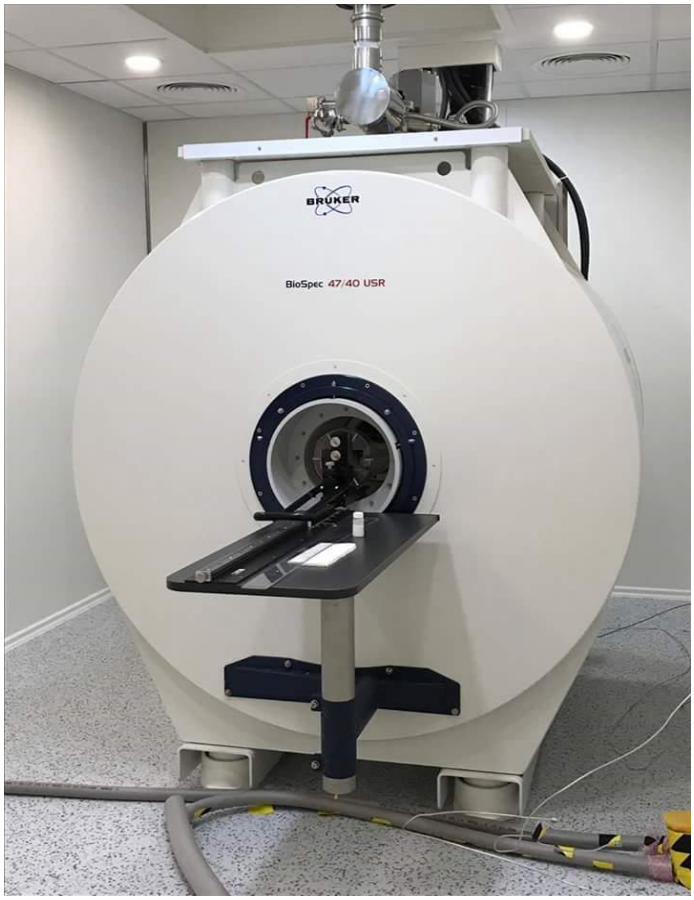

Figure 2.1 - Image of the MRI instrument at Statoil ASA.

The MRI instrument is placed within a Faraday cage, to avoid interference with external RF signals, and to protect external devices from the RF fields emitted by the instrument. When working with such a powerful and expensive instrument it is very important to maintain the safety measures and guidelines that are established. It is of uttermost importance that any items that are magnetic must be kept out of the magnet room, to withhold the safety for both the instrument and the operator. This will also limit the tools that can be used within this room. The instrument is provided with a quench tube, in case of emergencies. The quench tube will allow for de-energizing of the magnet within seconds, as the liquid helium cooling the instrument is released. However, this will destroy the magnet.

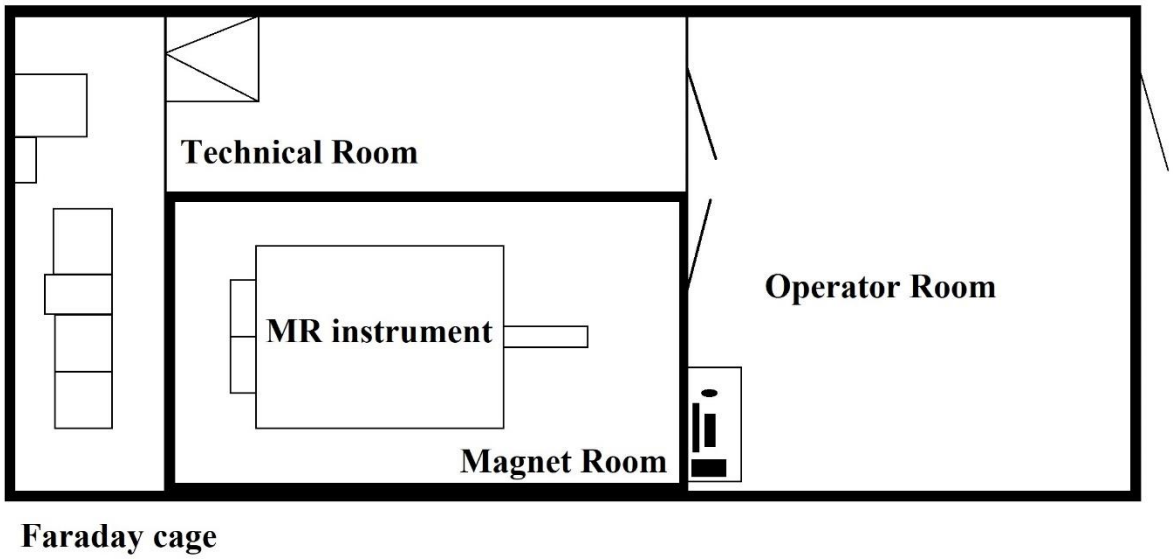

Figure 2.2 - Schematic illustration of the MRI laboratory at Statoil ASA. The MRI instrument is placed within a faraday cage. The Operator Room is where the operator controls the instrument. The technical room is where the electrical power distributor is placed, while the Magnet room is where the MR instrument is placed.

The Bruker MRI instrument uses the software ParaVision version 6.0.1. This software is the user-interface for operating the MRI instrument, as well as for analyzing and archiving the recorded data [18]. ParaVision sorts the acquired data into a subject and a study. The subject is the main "folder", and can contain several studies. The study is placed below the subject, and contains numerous scans, performed on a sample. Scan is a collective name for all the different MRI techniques that can be applied, and it will contain the acquired data. Each scan is given a name starting with the letter E, then followed by a number according to when the scan was added. The study starts counting at 1, E1, and will not replace any scan number if first created. The software ParaVision can create well-presented reports containing the acquired data [18]. The protocols used for this thesis are mainly the CPMG, RAREst and MSME scans. The next subchapters will describe the different protocols used for this thesis.

2.1.1 Wobble Procedure

A procedure to tune and match the radio frequency coil is mainly required when the load of the sample has changed between consecutive imaging and spectroscopy studies, but as a precaution it should be performed for each new study. Tuning and matching reduces the reflection of radio frequency power during transmission and hence the signal to noise ratio [18]. The tuning and matching procedure within ParaVision is called wobble.

2.1.2 Localizer Proceedure

When acquiring images with an MRI instrument, the objects being imaged must first be localized within the instrument. With the software ParaVision, this is done by a procedure called Localizer_RARE_Multislice, with default settings installed by Bruker. The localizer starts by performing the following, before recording the data:

- Setting reference frequency
- Iterative shimming
- Setting TX reference power
- Calculating shims
- Setting receiver gain

To perform the scan the protocol starts by setting a reference frequency. For this version of ParaVision this frequency is based on hydrogen molecules. So, for every scan, hydrogen is used as the frequency base. After determining the reference frequency, iterative shimming is performed. By shimming, the MRI instrument optimizes its field strength and creates a homogenous field. Magnetic properties can vary within the same sample, creating local changes of the magnetic field strength, called susceptibility field effects. The signals detected from a homogenous field will give more accurate results. Shimming coils are used to compensate for the local changes [18].

The reference power is set for an entire study by the Localizer, unless alternated manually. When the signal intensity is low, the reference power can be difficult to determine. If it is too low, it cannot be determined at all. For samples that are frozen this is a frequent issue. The hydrogen present in these samples are too tightly bound to each other to give off any detectable signal when exposed to the RF waves. To proceed scanning, the reference power can be set manually. This manual determination of the reference power means that it is not optimized for each individual sample. The alternative is to wait until a significant amount of the solid phase has decomposed before one can continue with the scans. This will lead to a significant loss of data from the melting process. One therefore must choose between an approximate reference power, or no recorded data. A good option is to find the reference power on a sample in the liquid state, and use this on the solid samples.

The receiver gain controls the detected MRI signals and ensures that the signals will fit to the analog-to-digital converter [20]. By calibrating this parameter it is ensured that the signal exceeds the background noise signal to noise ratio is correct, making sure that the, but not excessively [15].

The Localizer procedure allows for localization of a sample within the MRI instrument, and is used to further position the other protocols that acquires images. Each time the sample is moved, a new Localizer procedure must be performed to reposition the other protocols.

2.1.3 CPMG Protocol

CPMG is a protocol developed by Carr, Purcell, Meiboom, and Gill, hence the name CPMG. The protocol is based on a cycle of radio frequency pulses, designed to produce pulse echoes and to counteract dephasing as T2 relaxation develops. When a nucleus is placed under the influence of a magnetic field and exposed to a 90° radio frequency pulse, it will flip the net magnetization of the nuclei 90° into the x-y plane, as previously stated in chapter 1.3. This is illustrated in figure 2.3 [17]. The longitudinal magnetization disappears, and transverse magnetization occurs. After the 90° pulse is applied, the transverse magnetization decays, while the longitudinal magnetization reappears. This decay signal is called free induction decay, or FID. This phenomenon happens so quickly that it can be difficult to record. A solution to this is to apply an additional RF pulse. A 180° pulse that will refocus the net magnetization back into phase. When the nuclei are in phase, they send out a signal called an echo, see figure 2.4 [17]. The magnitude of this echo decreases as less and less nuclei are pushed back into phase by the 180° pulses. The series of a 90° pulse, before several refocusing 180° pulses, are called a spin-echo sequence.

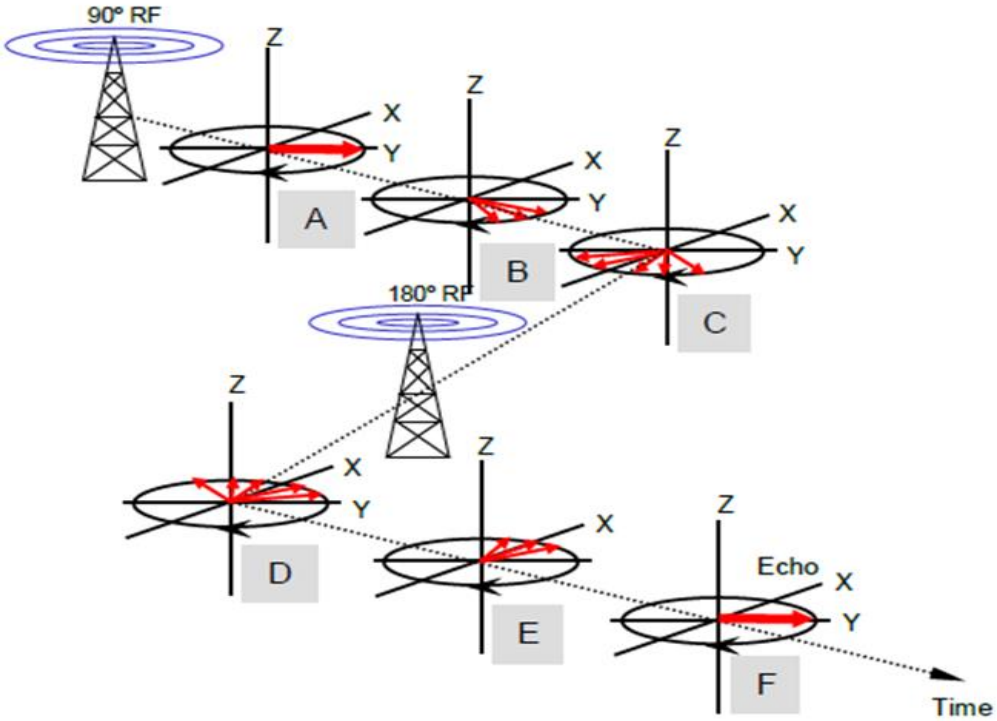

Figure 2.3 - Illustration of a spin echo sequence. First a 90° radio frequency pulse is applied, flipping the net magnetization into the x-y plane. The transverse magnetization will decay while the longitudinal magnetization re-appears. A refocusing 180° pulse is applied to counter act the dephasing in the x-y plane forcing the nuclei back in phase [17].

The spin echo sequence eliminates the enhanced relaxation process that is caused by the magnetic susceptibility differences and the main fields inhomogeneity. With the CPMG protocol the T_2 relaxation time recorded will therefore not be T_2^*. As the T_2 relaxation time will vary mainly dependent on the magnetic field strength and the molecular bonding and mobility of the hydrogen nuclei, the measured T_2 relaxation times in this thesis are given the name T_2^a, the apparent T_2 relaxation time.

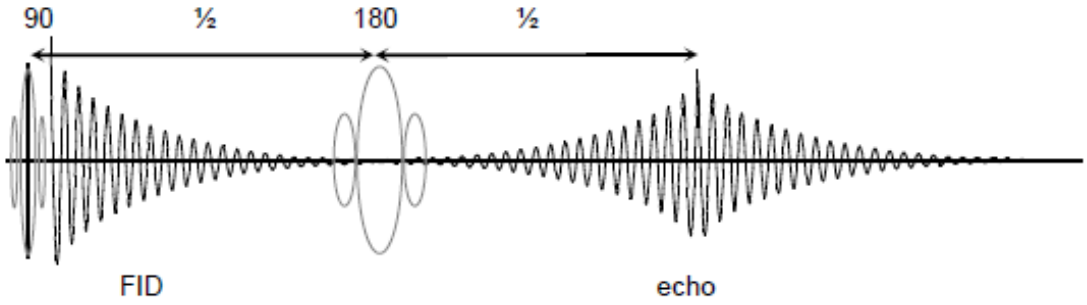

Figure 2.4 - Illustration of the spin echo sequence. A 90° pulse is applied, FID takes place and a refocusing 180° pulse reconstructs the original FID signal. This signal is an echo of from the application of the first 90° pulse [17].

The CPMG scan does not provide an image of the sample, but creates a "map" of the T_2 relaxation times. When performing a CMPG scan the following parameters must be set:

- Echo spacing: determines how much time that passes between each echo.
- Repetition time: determines how much time that passes before the sequence is repeated.
- Averages: determines how many times the measurement is performed. An average value from these measurements is estimated.
- Echoes: determines the number of how many echoes, or how many refocusing pulses that will be applied.

The decay curve from the CPMG scan can be directly displayed in ParaVision, while further analysis of this data is done in MATLAB. Inverse Laplace Transformation is performed on the CMPG scans to find the distribution of the T2 relaxation times.

2.1.4 RAREst Protocol

RAREst is short for Rapid Acquisition with Refocused Echoes for Short echo Time and is also based on the spin echo sequence. This protocol acquire images and demands the following settings to be determined before recording a scan:

- Field of view: defines the area inside the MRI instrument that is to be imaged.
- Number and orientation of slices, and direction of reading: The field of view can be divided into numerous slices of optional thickness. The slices can be oriented either in the axial plane, sagittal plane, or in the coronal plane. These orientations are illustrated in figure 2.5. When the MRI instrument is applied for medical use, the patient normally lies within the instrument, giving a situation illustrated in figure 2.5 a) [32]. The samples investigated in this thesis are positioned directly into the instrument, in a standing position. This results in a definition of the planes as illustrated in figure 2.5 b). When slices are chosen in the axial or the sagittal plane, the slices will be given numbers starting from one side of the sample to the other. When the slices are chosen in the coronal plane the slices are given a number from the bottom to the top of the sample. When choosing the slice orientation, one can also choose in what direction, x-, y-, or z-direction, the MRI signals should be recorded, and further placed into k-space. After choosing the number and thickness of slices to divide the sample into, it is important to correct for the "cross-talk" between the slices [17], by making sure that there is no slice gap between the slices.

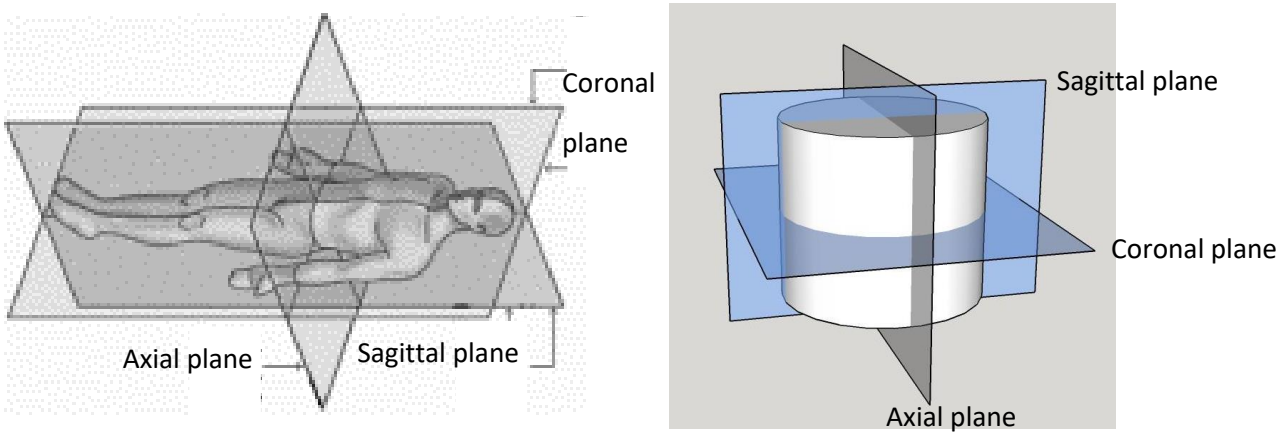

Figure 2.5 - Orientation of the planes for a) a patient laying down [32]. b) a standing sample.

- Image size: sets the resolution for the image. It gives the maximum or minimum value for the number of pixels in the scan. The higher the image size, the higher the resolution.
- Echo time: this is the time between the application of the RF pulse and the peak of the signal induced in the coil is called echo time, TE [20], see figure 2.6 [20]. This parameter decides which relaxation times that are recorded. If the goal is to record the fastest relaxation times i.e. the relaxation that happens within a few milliseconds, this parameter must be kept as low as possible. However, the consequence of a short TE can be not recording the slower relaxation times i.e. the nuclei that needs several seconds to relax back into the original state.

- Repetition time: TR is the time between one 90° pulse to the next 90° pulse i.e. how long time the spin will have to regain the longitudinal magnetization before exposure to a new pulse [15], see figure 2.6 for illustration.

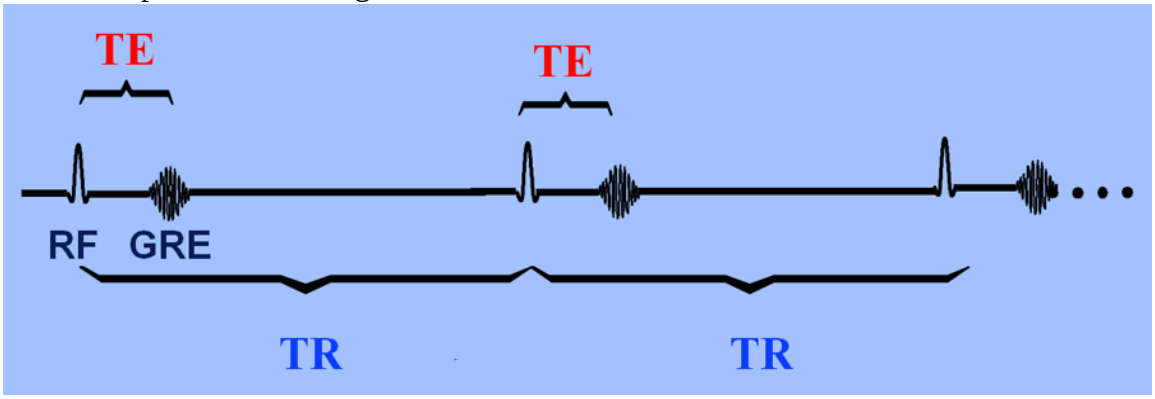

Figure 2.6 - Illustration of TE vs. TR. Figure from MRI Questions and answers: TE from RF pulse to middle of echo. TR time from one pulse to another pulse [20].

- Averages: how many times these measurements are performed before calculating an average value for the scan.
- Repetitions: number of repetitions decides how many times the whole scan is repeated which will give several separate data series, as opposed to an estimated average of the scans.
- Echo spacing: The echo spacing equivalent to the echo time in the RAREst protocol.
- Rare Factor: determines how many 180° pulses that are applied after the 90° pulse.

The images acquired with this protocol are displayed directly in ParaVision. The brightness scale of the image is set by the pixel with the highest recorded intensity, which corresponds to the brightest item in the image. The brightness scale is relative to the image and should not be directly compared to another image. Two images with the same brightness did not necessarily record the same intensity. RAREst images are hence exported from ParaVision to DICOM files and analyzed with MATLAB.

2.1.5 MSME Protocol

The MSME protocol, short for Multi Slice and Multi Echo, is also based on the spin echo sequence. This protocol provides both images and a T_2 analysis of a specific chosen area. The settings for the MSME protocol are almost identical to the settings for the RAREst protocol. Instead of setting the Rare Factor, a number of echo images, are chosen. The number of echo images will correspond to the number of points on the decay curve that can be produced with this scan. The number of echo images will determine how many of the echoes that should be imaged. The MSME scan can, like RAREst, divide the sample into numerous slices of optional thicknesses.

The analysis of the data acquired from MSME can be performed directly in ParaVision through the option View in Image Display. From there choose the Image Sequence Analysis

and a region of interest. A decay curve can hereby be estimated for a specific region of a slice, within a specific area of the sample. An estimated average T_2 relaxation time can also be acquired from this data. The decay curve acquired from the Image Sequence Analysis can be further analyzed with inverse Laplace transformation, just like the CPMG scan.

2.1.6 General settings for the scans

One of the approaches investigated for this thesis was adjustments of MRI protocols for investigation of hydrates in porous media. A general guide line for determination of the most important settings has hence been established.

As a rule of thumb, the echo time and echo spacing should be as low as possible to record the shorter relaxation times. A short echo time or echo spacing can however leave out the slower T_2 relaxation times. As the samples used in this thesis contains sand, only relative fast T_2 relaxation will occur. For the CPMG scan, the echo spacing has been set at 1ms, while for MSME and RAREst the lowest possible value has been used, corresponding to approximately 5,5ms.

Generally, the repetition time should be set to at least 2000ms to allow for full relaxation before the next sequence is started. The repetition time will strongly influence the amount of time each scan will last. The MRI protocols will in this thesis be used to study change over time. As significant change can occur in a relative short amount of time, it will be important to limit the scan time. The repetition time used for the experiments presented in this thesis is 2500ms and 3000ms.

The image size will also largely affect the amount of time it will take to perform a scan. An image with a higher resolution will take longer time to create. When imaging something that changes over time, this is an important factor to evaluate. To record the changes the scan time needs to be limited. If the resolution is too low the resulting images becomes blurry. The image sizes for the scans presented in this thesis has been from 80x80 to 100x100.

By increasing the rare factor, the whole protocol can acquire data much more rapidly, in fact in half the time. The quality of the images however will not be as good as if the image was attained without an additional rare factor. For the experiments included in this thesis the rare factor was set to one.

2.2 Experimental equipment and chemicals

All equipment and chemicals used in this thesis was provided by either Statoil ASA, or by the University of Bergen, Department of Chemistry. The chemicals can be found in table 2.1. The sand used in this thesis is called NC4X, a high purity quartz sand from deposits in Spruce Pine, USA. See Appendix A5 for detailed composition. Quartz is a mineral consisting primarily of silicon dioxide, SiO_2[33].

Table 2.1 - Materials used in this thesis

Material	Purity	Provider
Water	Deionized	Statoil
THF	≥99,8%	Merck, Statoil
Heptane	≥99%	Merck, Statoil
Trimethylchlorosilane	(Puriss) ≥99,0%	Sigma-Aldrich, UIB
Cyclopentane	≥98%	Merck, Statoil
Toluene	≥99,9%	Merck, Statoil
Fluorinert	3M™ Fluorinert™ Electronic Liquid FC-40	3M™, Statoil

The weighing of sand and chemicals was performed with two different scales. The Mettler Toledo scale was used for the smaller amount of liquid and sand, as the scale provides measurements with 4 decimals. The readability for this scale is 0,1 mg. The maximum capacity for this scale is limited to 220grams. For the amounts above 220 grams, the Mettler PK 2000 scale was applied. This scale provides weights with two decimals and has a readability of 0,01g and has a capacity of 2000g.

For drying of sand an incubator and a vacuum pump was applied. After alteration of the sands wettability towards oil-wet, the sand grains were dried within a nitrogen saturated environment, to minimize reaction with oxygen.

For the melting experiments a glass beaker was isolated with bubble wrap to delay the melting procedure. For the cooling experiments a home-made setup was created. A plastic beaker was filled with liquid fluorinert before a tube was coiled around it. This beaker and tube was placed inside yet another plastic beaker, but this one was isolated with a foam-isolating material. The sample glass was placed directly into the fluorinert. An air cooling system was connected to the tube, creating a flow of cooled air in the fluorinert. This will cool the fluorinert and eventually cool the sample glass as well. The air cooler used for this setup was the AiR Jet XR402, with a temperature range from -40°C to 100°C. A flow adjuster and an air

dryer was connected to the air cooler. An illustration of the set-up for these experiments is shown in figure 2.7. A connection between the temperature set on the air cooling instrument, and the temperature measured in the fluorinert is given in table 2.2.

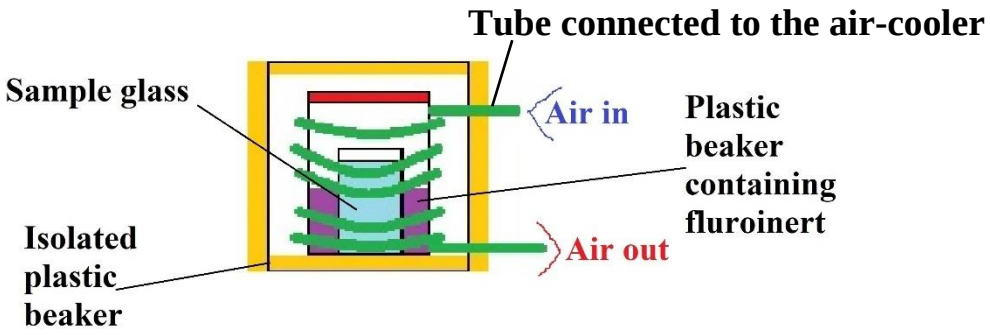

Figure 2.7 - Illustration for the setup of the cooling system. The tube connected to the air cooler is displayed as the green lines surrounding the plastic beaker. Fluorinert is color-less but is here illustrated with purple. The foam isolation is illustrated as the yellow thick lines around the biggest plastic beaker.

Table 2.2 - Temperature log for the cooling system.

Temperature set on the Air Cooling system [°C]	Temperature measure in the fluorinert [°C]
-20	-4
-15	-0,9
-10	1,9
-7,5	3,2
-5	5

When creating any setup intended for MRI use it is very important to continuously test the materials that are being used, to make sure that they do not emit any signal when exposed to a MRI scan. It is also very important to remember that all tools that are to be brought inside the magnet room must be special made.

2.3 Preparation of samples

All samples were prepared at Statoil ASA.

2.3.1 Alteration of wettability and drying procedure

The procedure used to alter the wettability of the quartz sand is a method developed by cooperation between Statoil ASA and the University of Bergen. The calculations made for this procedure as well as the original process for this wettability alteration can be found in Appendix A1. 200 grams of sand was prepared in each glass, and a total of six glasses were prepared.

The following procedure is used to ensure that the sand is water-wet:

1. The sand used in this master thesis is of very high purity and quality, so prewashing of this sand is not necessary. Add strong NaOH, 1 mole, to the sand and let it work for 30 minutes.
2. Pour out as much as possible of the NaOH before adding 1 molar HCl. Let this work for 10 minutes to neutralize the NaOH.
3. Pour out as much as possible of the HCl before washing the sand with deionized water. Use pH paper to make sure that all NaOH and HCl is washed away. The sand needed to be washed with at least 10 liters of deionized water before the pH value showed no traces of NaOH or HCl.
4. Keep the sand wet in distilled water until use. If the sand dries, the wettability may change.
5. The sand was dried in an incubator under vacuum conditions, to minimize reactions with oxygen, before it was ready for use.

The following procedure is used to create the oil-wet sand:

1. Perform the same procedure as when ensuring for water-wet sand, and dry the sand under vacuum.
2. Coat the surface with silane to make it oil-wet. In this thesis, 2 mass % trimethylchlorosilane in heptane, was used to coat the sand grains. If exposed to heat the procedure will go faster [30], hence the sand was left at 50℃ for about 2 hours.
3. The sand grains were rinsed twice with heptane. After alteration, the sand was dried in a nitrogen saturated atmosphere, to minimize reaction with oxygen.

2.3.2 Sample preparations

A complete list of all the samples that are presented in this thesis is given in table 2.3. More details about these samples can be found in Appendix A2-A4. When preparing the samples, the sand was added to the sample glasses first. The liquids were then ensured to submerge the sand and left to completely distribute in the sand. The surplus liquids were removed before the samples were examined further with the application of MRI, and before the samples were placed in the freezer. For samples 13 and 14, the lighter fluid was added to sand first and scans were recorded. The denser fluid was added after this and a new set of measurements performed. The denser fluid will then be forced by gravity to displace the lighter fluid.

Table 2.3 - List of samples referred to in this master thesis.

Sample	Description	Used for
1	C5H10 and H2O 1:6	Visual inspection
2	C5H10 and H2O 1:17	Visual inspection
3	THF and H2O 1:17	Visual inspection
4	THF oil-wet sand	Sand experiment
5	THF water-wet sand	Sand experiment
6	H2O oil-wet sand	Sand experiment
7	H2O water-wet sand	Sand experiment
8	Heptane oil-wet sand	Sand experiment
9	Heptane water-wet sand	Sand experiment
10	Heptane and H2O oil-wet sand	Sand experiment
11	Fluorinert and H2O oil-wet sand	Sand experiment
12	Fluorinert oil-wet sand	Sand experiment
13	Fluorinert water-wet sand	Sand experiment
14	THF and H2O 1:15 water-wet sand	Melting experiment and cooling experiment
15	THF and H2O 1:15 oil-wet sand	Melting experiment and cooling experiment
16	THF and H2O 1:20 water-wet sand	Melting experiment
17	THF and H2O 1:20 oil-wet sand	Melting experiment

2.4 Experimental Work

Samples 4 to 17 have all been examined with the MRI protocols RAREst, CPMG and MSME. The settings for the protocols can be found in Appendix A2-A4. Samples 14 to 17 were all stored at -10°C before allowed to continuously melt within the MRI instrument as scans were performed for the melting experiments. Samples 14 and 15 were also used for the cooling experiments. Samples 1-3 were all used for visual inspection. Sample 3 was placed in the freezer for rapid hydrate growth, but stored within a cooler set at 2°C.

2.5 Data Analysis

MATLAB and/or Excel has been used for data analysis that was not possible to perform with ParaVision. MATLAB is a software mostly used to solve mathematical operations. For this thesis the version R2016b – academic use, is used.

2.5.1 Intensity development

The images acquired from the RAREst protocol can be viewed directly in ParaVision. These images are scaled according to the strength of signal that is detected. White parts in the image gave off high intensity signal while grey areas gave lower intensity signal. Two different images can therefore look very similar to one another, even though there could be a significant difference in the signal intensity between them. To avoid this issue, these images are written to a DICOM-file, which can be read by MATLAB. The file now contains the intensity information, not the image portrayed in ParaVision. MATLAB has been used to graphically display the intensity development from the RAREst images. The signal from the sample will vary as a function of time as the hydrate is melting. As no detectable signal is recorded when the sample is solid, the intensity from the sample will increase as the hydrate melts.

The intensity development can be directly linked to the hydrate saturation, by assuming that the relative MRI intensity is proportional to the amount of liquid present in the sample [34]. As the hydrate melts, more of the THF and water solution will turn liquid, and hence increase as the hydrate melts. Estimation of hydrate saturation, by the "bulk method" is done by using formula (2.1) to calculate the saturation of hydrate as they nucleate [35].

$$S_i = \frac{I_0 - I_i}{I_0} \times 100\% \tag{2.1}$$

Where S_i is the saturation of hydrates at a given time

I_0 is the intensity from the sample when all is in liquid form

I_i is the intensity at a given time

2.5.2 Inverse Laplace Transformation

The Laplace Transformation is a mathematical procedure that connects a function of a real variable, e.g. t, to a function of more complex variables, like frequency, s. The inverse Laplace transformation will then see the problem the other way around. When you already have the complex variables and you need to find the more "real" variables, the Inverse Laplace Transformation can be used.

The decay curve for the T_2 relaxation time consist of several different equations compressed into one average equation to give one average curve as a result. The curve is a result of many different T_2 relaxation times, each with their own decay curve, put together to make one average curve. To find these T_2 relaxation times the inverse Laplace Transformation is used. The inverse Laplace transformation will decompose the MRI response and give a distribution of the different T_2 relaxation time values, creating a T_2 relaxation time distribution map [36]. As the relaxation time will correspond to a relative pore size, the T_2 map will correspond to a map of the relative pore size distribution in a measured sample.

The CPMG and the MSME scan will both give exponential decay curves as the resulting data. The CPMG scan provides a measurement performed on the total sample. The MSME scan provides measurements within specific regions of the sample and provides the value with a standard deviation. The inverse Laplace transformation can be applied for both scans, to find the T_2 relaxation time distribution.

3 Results

Chapter 3 features the results from the experimental work used for this thesis. Pilot studies are presented first, with comments regarding the initial approach for this thesis; to use cyclopentane as the hydrate former. The rest of this chapter consist of the results from MRI investigations of the samples 4 to 17. A complete list of all samples that are presented in this chapter can be found in table 2.3. For the sand experiments samples 4 to 13 were examined. The melting experiments are presented next, where samples 14 to 17 were examined. The last subchapter presents the results from the cooling experiments, using samples 14 and 15.

Studies with MRI result in large amounts of data. The data that were analyzed for this thesis, but not presented in this chapter, can be found in Appendix A2-A4.

3.1 Pilot studies – Cyclopentane

The initial approach for this thesis was to use cyclopentane as the hydrate former. Cyclopentane is a hydrophobic compound and would provide an analog to the formation of methane hydrates, but without high pressure conditions. Sample 1 and 2 were prepared on the 13th of February and 23rd of February 2017. The samples were stored at -10°C, for rapid hydrate growth to occur. Hydrate growth with cyclopentane as the hydrate former proved to be difficult. Cyclopentane has a freezing point of -93,3°C [37], but can form hydrates, together with water, at 7,7°C [38, 39]. Visual inspection of samples 1 and 2 found that hydrates were only formed at the cyclopentane-water interface, the remains in the samples were left in liquid form. As THF is completely miscible with water it was chosen as the hydrate former instead of cyclopentane. Later, more than half a year after samples 1 and 2 were prepared, it was established through visual inspection that cyclopentane-hydrates had however been formed. No measurements were performed on these samples.

3.2 Sand Experiments

Samples 4 to 13 were prepared for the sand experiments to look for potential differences in the T_2 relaxation process and signal intensity caused by the wettability preference of the porous media. Sample 12 and 13, oil-wet and water-wet sand containing fluorinert, were prepared for the single purpose of illustrating that no signal can be detected from the sand grains alone. Fluorinert is a fluorocarbon oil [40] that does not contain any hydrogen molecules and will therefore not give any signals to the MRI instrument. Fluorinert is hence not detectable with the MRI instrument. As no signal was detected there are no further results to present for sample 12 and 13. Samples 4 to 13 have only been examined at room temperature.

3.2.1 RAREst Images

Figures 3.1 to 3.8 display images of samples 4 to 11. The images were acquired with the protocol RAREst and were collected directly from ParaVision. The samples that only contain one fluid, samples 4 to 9, are presented first, before the samples containing two fluids, samples 10 and 11. Only one slice from each sample is presented in this subchapter, the remaining slices from the samples can be found in Appendix A2, figures A2.0.2 to A2.0.13, A2.0.15, A2.0.16, and A2.0.18.

No further analysis was performed on these RAREst images as none of the samples are expected to have any significant change in intensity response. The images are mainly included to portray the samples that are further studied with the CPMG and MSME protocols.

Samples 4 to 9, sand with one fluid

Figures 3.1 to 3.6 display a significant difference in brightness between the images, even though they are assembled directly from ParaVision. The brightness scale in a RAREst image, when viewed in ParaVision, is adjusted according to the part of the image that gives off the highest signal intensity and is therefore relative to each image. Two images that seem to have the same brightness scale might not necessarily have the same intensity scale. The differences in brightness between the images in figures 3.1 to 3.6 are still significant. Samples 6 and 7, sand containing water, gave the brightest images and therefore the highest intensity, see figures 3.5 and 3.6. The darkest images with the lowest intensity signal were recorded for samples 4 and 5, sand containing THF, see figures 3.1 and 3.2. The figures 3.1 and 3.2 display a lower signal to noise ratio as a direct consequence from the lower signal intensity.

Figure 3.1. display two RAREst images of sample 4, oil-wet sand with THF.

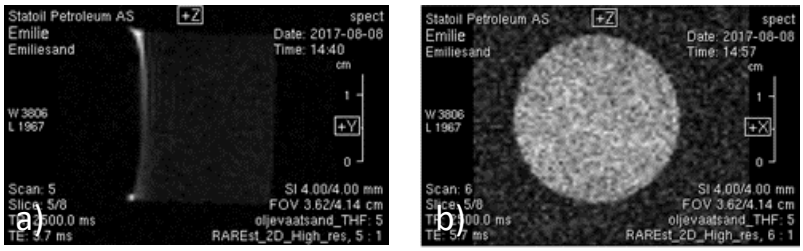

Figure 3.1 - a) Oil-wet sand with THF from sagittal orientation. The RAREst image displays slice 5 of 8. b) Oil-wet sand with THF from the coronal orientation. The RAREst image displays slice 5 of 8.

Figure 3.2. display two RAREst images of sample 5, water-wet sand with THF.

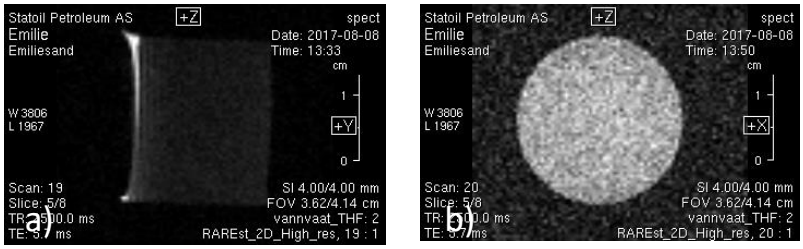

Figure 3.2 - a) Water-wet sand with THF from sagittal orientation. The RAREst image displays slice 5 of 8. b) Water-wet sand with THF from the coronal orientation. The RAREst image displays slice 5 of 8.

Figure 3.3. display two RAREst images of sample 6, oil-wet sand with H_2O.

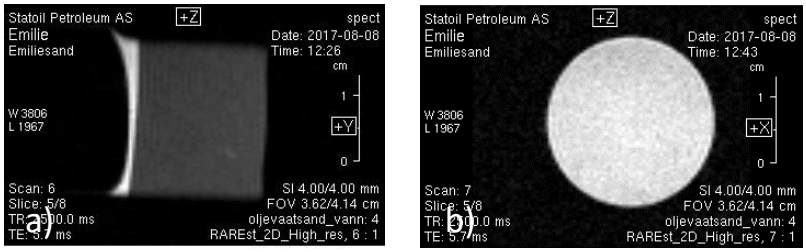

Figure 3.3 - a) Oil-wet sand with H_2O from sagittal orientation. The RAREst image displays slice 5 of 8. b) Oil-wet sand with H_2O from the coronal orientation. The RAREst image displays slice 5 of 8.

Figure 3.4. display two RAREst images of sample 7, water-wet sand with H_2O.

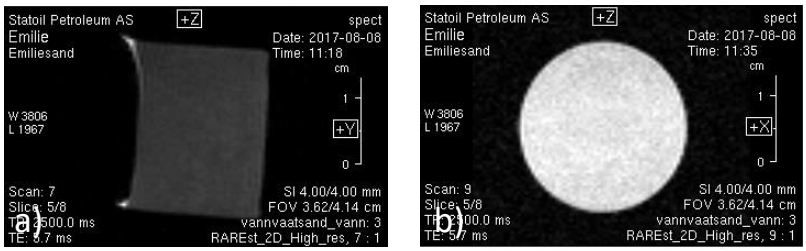

Figure 3.4 - a) Water-wet sand with H_2O from sagittal orientation. The RAREst image displays slice 5 of 8. b) Water-wet sand with H_2O from the coronal orientation. The RAREst image displays slice 5 of 8.

Figure 3.5. display two RAREst images of sample 8, oil-wet sand with heptane.

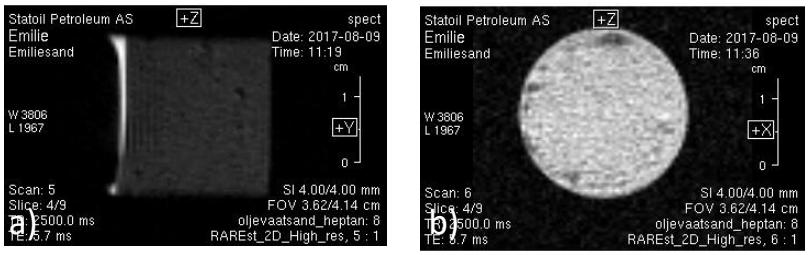

Figure 3.5 - a) Oil-wet sand with heptane from sagittal orientation. The RAREst image displays slice 4 of 9. b) Oil-wet sand with heptane from the coronal orientation. The RAREst image displays slice 4 of 9.

Figure 3.6. display two RAREst images of sample 9, water-wet sand with heptane.

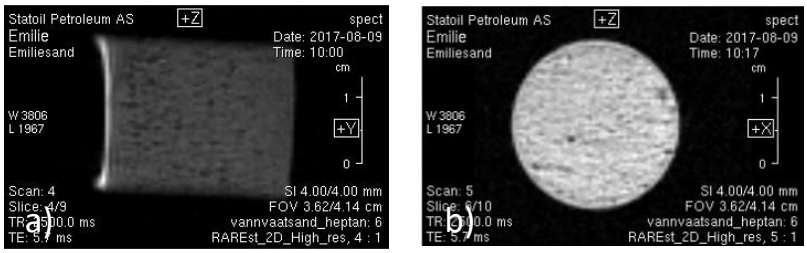

Figure 3.6 – a) Water-wet sand with heptane from sagittal orientation. The RAREst image displays slice 4 of 9. b) Water-wet sand with heptane from the coronal orientation. The RAREst image displays slice 6 of 10.

The effect that the orientation of the images has on the brightness scale is significant in these figures. As some free fluid water was present on the top of the samples, the hydrogen nuclei present here will give off a higher signal intensity than the hydrogen nuclei present between the sand grains. This phenomenon is caused by a freer motion for the hydrogen nuclei in the free fluid water. The higher signal intensity will result in a brighter image. A direct result of this is that the fluid situated between the sand grains is given a darker color when recorded from the sagittal orientation, than what is recorded from the coronal orientation.

Figures 3.5.b) and 3.6.b) display darker areas within their structure. These darker spots represent areas within the samples where a lower or no signal was recorded. This can be caused by two situations; either there is sand present without any liquid between the sand grains, or it could be “air bubbles” within the structures, not allowing liquid, or sand to be present. For these samples is it most likely sand without any liquid present between the pores, as no holes were visible from visual inspection.

Samples 10 and 11, sand with two fluids

Figure 3.7 displays a RAREst image of sample 10, oil-wet sand with water and heptane. The figure displays the same tendencies found in figures 3.5b) and 3.6b). Darker areas are present within the structure of the sample, though not observable through visual inspection. These areas are most likely sand without any liquid present between the grains.

Sample 10 was prepared in a larger sample glass and contains more sand, heptane, and water than the rest of the samples that were prepared for this thesis. As a direct result of the increased amount of liquid present for this sample, the signal to noise ratio improved. There are several reasons to why this sample glass was not used for further experiments. First, to fill this glass, a larger amount of both sand and fluids are needed. Second, if the glass is to be placed within some sort of isolation, adding to its original size, it would not fit inside the MRI instrument. The sample glass was however suitable for the imaging techniques as no artifacts were detected.

Figure 3.7 - Oil-wet sand containing heptane and water. The RAREst image is from the coronal orientation and displays slice 28 of 32.

Figure 3.8 displays two RAREst images of sample 11, first oil-wet sand with water and second oil-wet sand with water and fluorinert. As the sample was removed from the MRI instrument to add fluorinert, it cannot be guaranteed that the second image is situated in the exact same position within the sample, but it is relatively close. After addition of fluorinert the image portrays darker areas in the middle of the sample, most likely to be the fluorinert as it will not be visible on MRI images. The fluorinert will displace water, due to its higher density, pushing its way down in the sample.

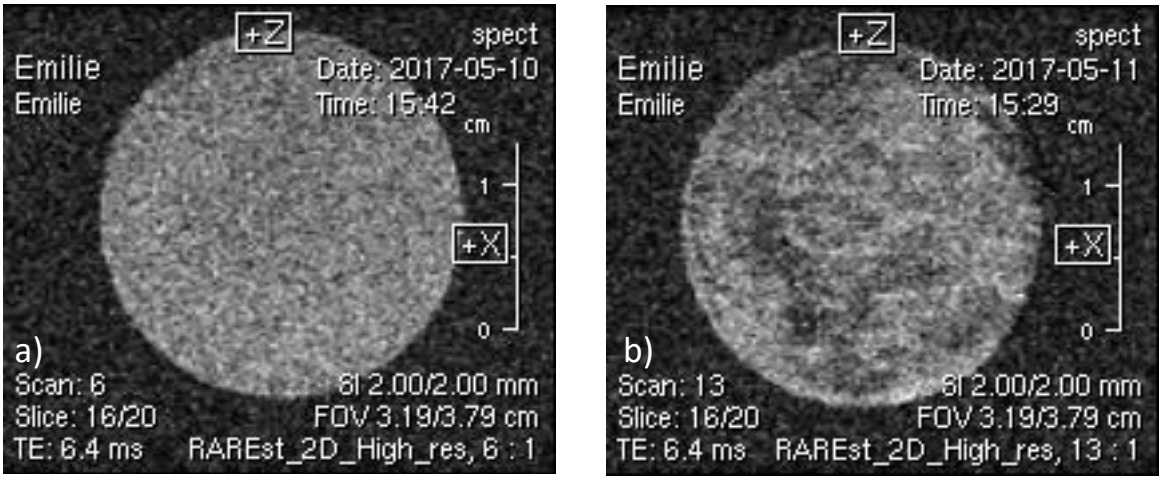

Figure 3.8 - a) Oil-wet sand with water from coronal orientation. The RAREst image displays slice 16 of 20.
b) Oil-wet and with water and fluorinert from the coronal orientation. The RAREst image displays slice 16 of 20.

3.2.2 CPMG Results

The CPMG protocol measures the T_2 relaxation process and provides an average value from the total sample that is being investigated. By further analysis through the inverse Laplace transformation the result is decomposed into a "map" of estimated apparent T_2 relaxation time, T_2^a, given from the hydrogen nuclei present within the sample. As explained in chapter 1.2.6, T_2 Relaxation within a Porous Medium, the relaxation time distribution for a porous medium can be related to a relative pore size distribution. The settings used for the smoothing parameter within the inverse Laplace transformation can be found in Appendix A2.

Samples 4 to 9, sand with one fluid

Figure 3.9 displays the decay curves from the T_2 relaxation process, for the samples 4 to 9. As the decay curves from samples 4 and 5, sand containing THF, approaches 0 intensity after only a few milliseconds these curves cannot be used for further analysis of T_2^a relaxation time distribution.

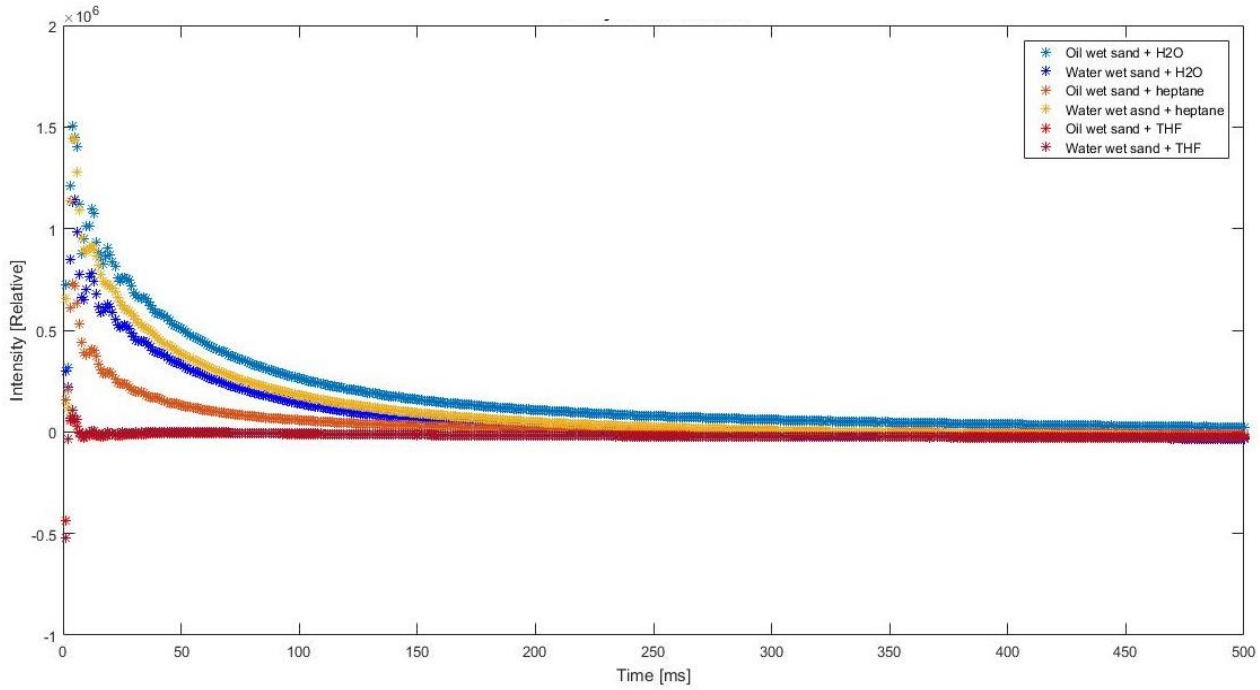

Figure 3.9 – Decay curves from T_2 relaxation from samples 4 to 9. The curves for the samples 4 and 5, sand containing THF, cannot be used for further analysis.

Figure 3.10 shows the T_2^a relaxation time distribution from the decay curves displayed in figure 3.9. The distribution is estimated through the inverse Laplace transformation.

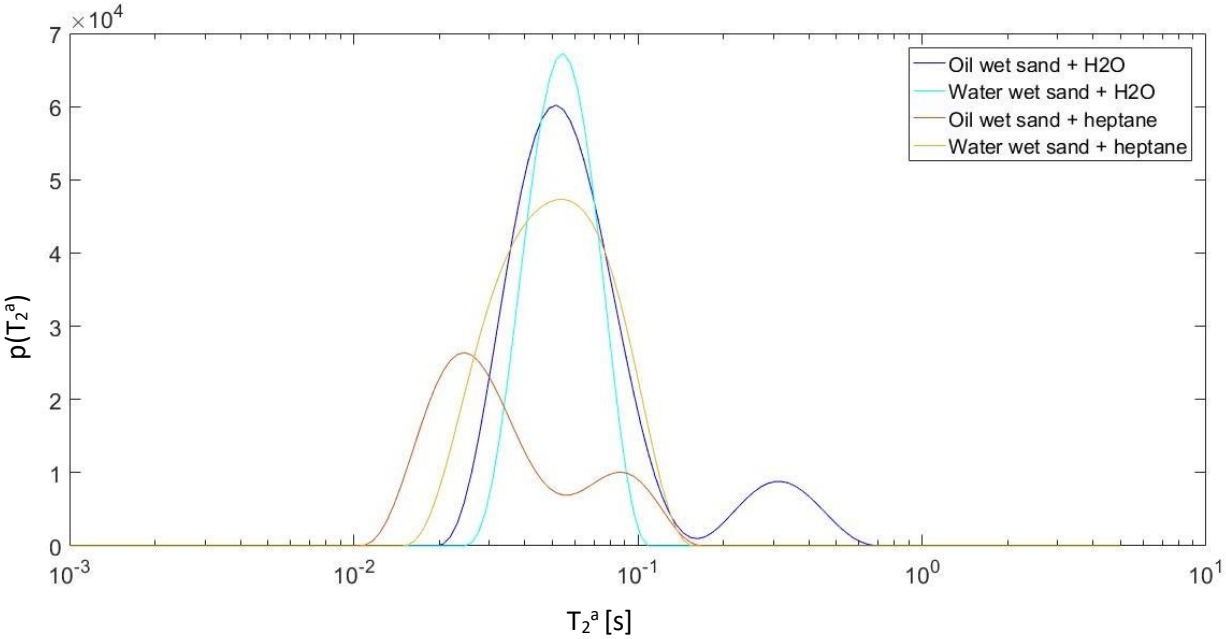

Figure 3.10 – T_2^a relaxation time distribution from CPMG scans from figure 3.9. The oil-wet sand displays a tendency of having two peak-values for the T_2^a relaxation time.

The peak values from the T_2^a relaxation time distribution are included in table 3.1. The peak-value for samples 6, 7, and 9, are approximately equal, but sample 6 has an additional peak with a higher T_2^a relaxation time than the other peaks. The T_2^a relaxation time distribution for sample 8 is significantly different. Like sample 6, sample 8 displays two peaks, but neither of these can be found at the same T_2^a relaxation time as for the other samples. The density of the T_2^a relaxation time is not as high for sample 8, as it is for sample 6, 7, and 9. The samples containing water, sample 6 and 7, display the highest density of the T_2^a relaxation time. Though it might appear as if sample 8 is spread wider than sample 7 and 9, which could explain the lower density, it is important to note that the scale on the x-axis on this plot is logarithmic. Though the peaks appear to be evenly distributed, the further to the right the peak is positioned the wider it spreads.

Samples 6 and 8, the oil-wet sand, had two peak values from the T_2^a relaxation time distribution. This can illustrate that these samples consist of two different pore sizes. Through the RAREst images there are no clear indications to why specifically these two samples would consist of two pore sizes. Figures 3.3a), 3.5a) and 3.6a) display a larger amount of free fluid on top of the sand grains, than what figure 3.4a) illustrates. If samples 6, 8, and 9, corresponding to the figures 3.3a), 3.5a) and 3.6a), all displayed two pore sizes this free fluid present on the top of the sand grains could explained the two peak values. However, since the CPMG results for sample 9 does not display the tendency of two relative pore sizes, an explanation is not clear from the results.

Table 3.1 – Peak values from T_2^a relaxation time distribution in figure 3.10.

T2 relaxation time for:	largest peak [ms]	smaller peak [ms]
Oil wet sand w/H2O	51,0	329,8
Water wet sand w/H2O	54,2	
Oil wet sand w/heptane	24,5	85,8
Water wet sand w/heptane	52,6	

Samples 10 and 11, sand with two fluids

Figure 3.11 shows the decay curves from the T_2 relaxation process for sample 10, oil-wet sand containing heptane and later heptane and water. After the addition of water to the sample, the signal intensity increases. As more hydrogen nuclei are added to the sample, this result was expected.

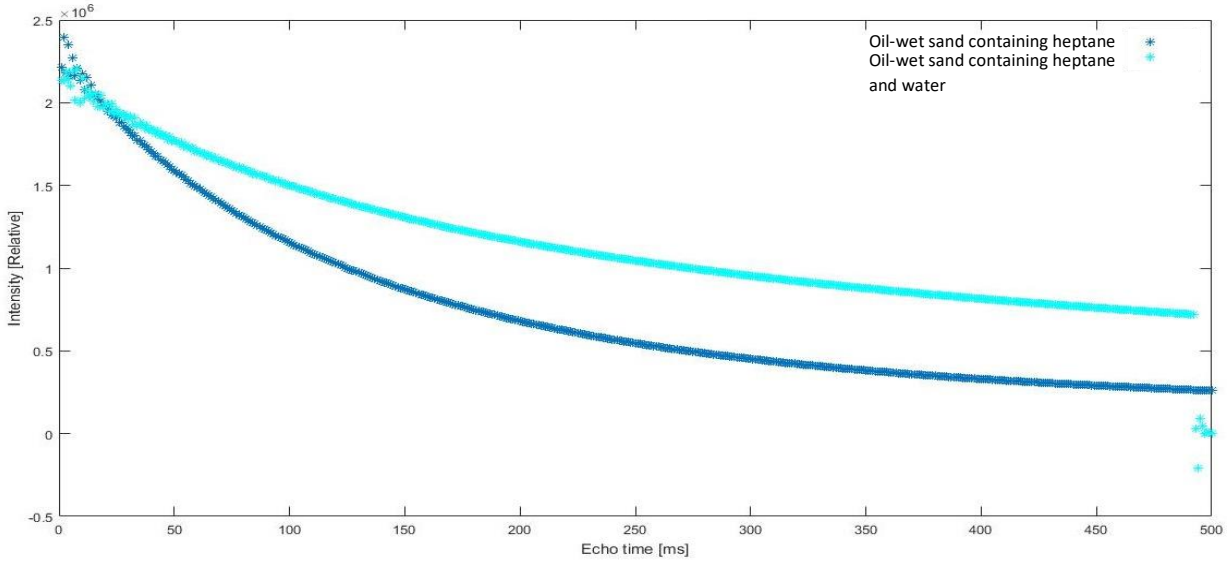

Figure 3.11 - Decay curves from T_2^a relaxation for sample 10, oil-wet sand containing heptane, and oil-wet sand containing heptane and water.

Figure 3.12 display the T_2^a relaxation time distribution from the decay curves in figure 3.11. The distribution is estimated through the inverse Laplace transformation. The two scans display a different distribution of the T_2^a relaxation time. When the sample only contains heptane, one peak value is obtained. When water is added to the sample there are two peak values obtained through the inverse Laplace transformation.

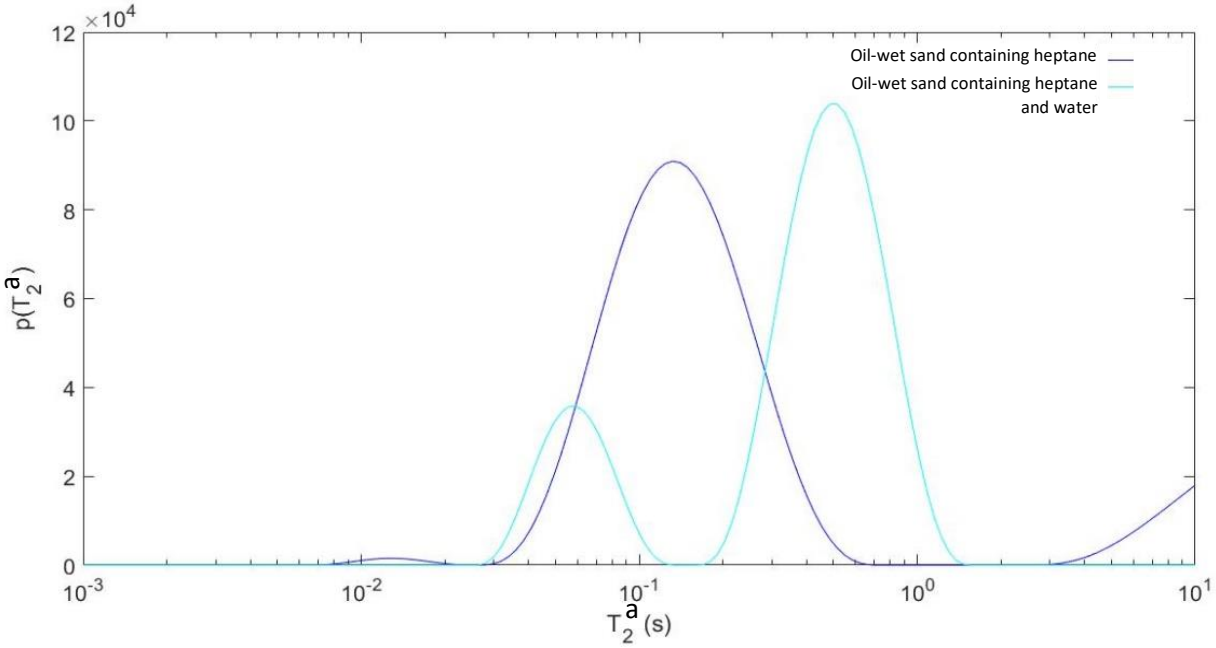

Figure 3.12 – T_2^a relaxation time distribution from CPMG scans in figure 3.11. Oil-wet sand with heptane is represented by the dark blue line, and oil-wet sand with water and heptane is represented by the light blue line.

The peak values from the T_2^a relaxation time distribution in figure 3.12 are given in table 3.2. Heptane and water are immiscible and should give two different peak values as their hydrogen nuclei are bound to different molecules. The interaction between water and heptane resulted in a shift in the T_2^a relaxation time distribution. The largest peak from the second CPMG scan is shifted to the right for the peak from the previous scan, giving a significantly higher peak value. The second smaller peak that appears in this distribution has a lower value than the original peak. Changes in the T_2^a relaxation time distribution was expected as the water was added to the sample. Water has a higher density than heptane and should be forced by gravity to displace heptane and move downwards in the sand. As the sand in this sample was oil-wet it was expected that heptane would remain closest to pore walls and that water would be present in the middle of the pore. The expected result from the T_2^a relaxation time distribution would have been the original peak as well as an additional peak for the water. The interaction between the heptane and the pore-walls should be unchanged. As both fluids add to the resulting signal it is not clear which relaxation times that corresponds to which molecules.

Table 3.2 - Peak values from T_2^a relaxation time distribution in figure 3.12.

T_2 relaxation time for:	Peak one [ms]	Peak two [ms]
Oil-wet sand containing heptane	131,7	-
Oil-wet sand containing heptane and water	57,6	490,9

Figure 3.13 show the decay curves from sample 11, first oil-wet sand containing water and then oil-wet sand containing water and fluorinert. The signal intensity slightly decreased as the fluorinert was added. The two decay curves are not as different from each other as the two curves in figure 3.11 were for sample 10. As fluorinert does not respond to the radio frequency waves it will not give any additional signal when added to the sand and water. So, a potential increase in intensity would not be from additional hydrogen atoms.

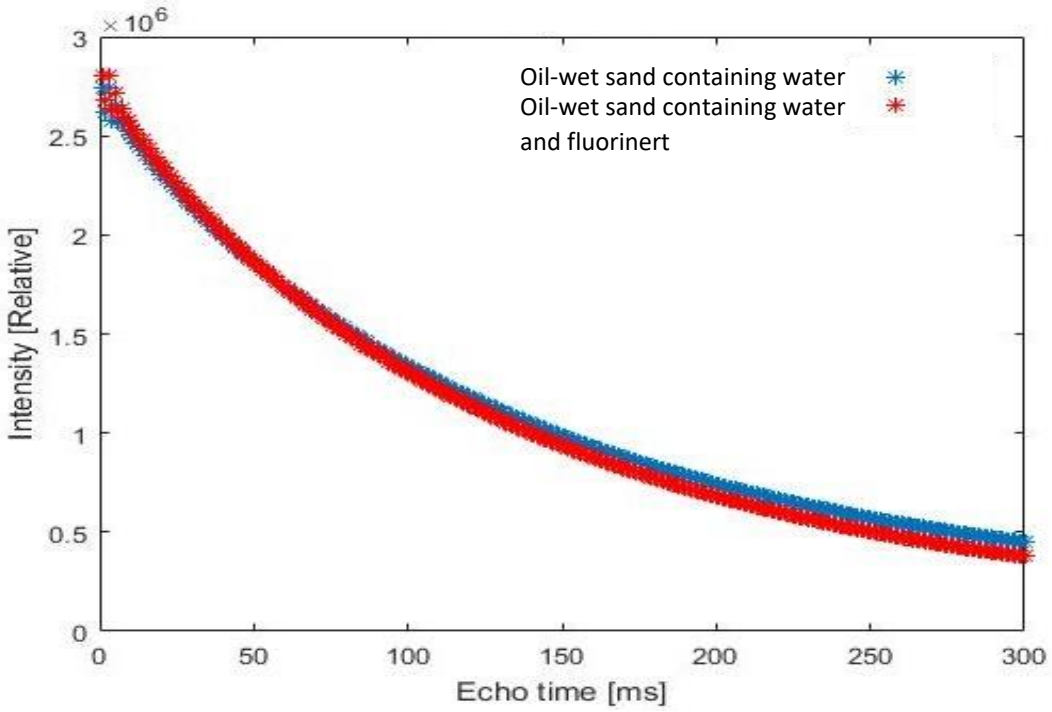

Figure 3.13 - Decay curves from T_2 relaxation for sample 10, oil-wet sand with water, and oil-wet sand with water and fluorinert.

Figure 3.14 display the T_2^a relaxation time distribution from the decay curves in figure 3.13. The distribution is estimated through the inverse Laplace transformation. The density of the T_2^a relaxation time increases as the fluorinert is added, and the distribution of the T_2^a relaxation time is slightly narrower. As fluorinert is denser than water it is expected to displace the water and adhere to the surface of the oil-wet sand. The water will then be placed in the middle of the pores, and this was expected to result in a slower T_2^a relaxation time. No significant amount of change was found for this experiment, so this assumption is not supported by the results.

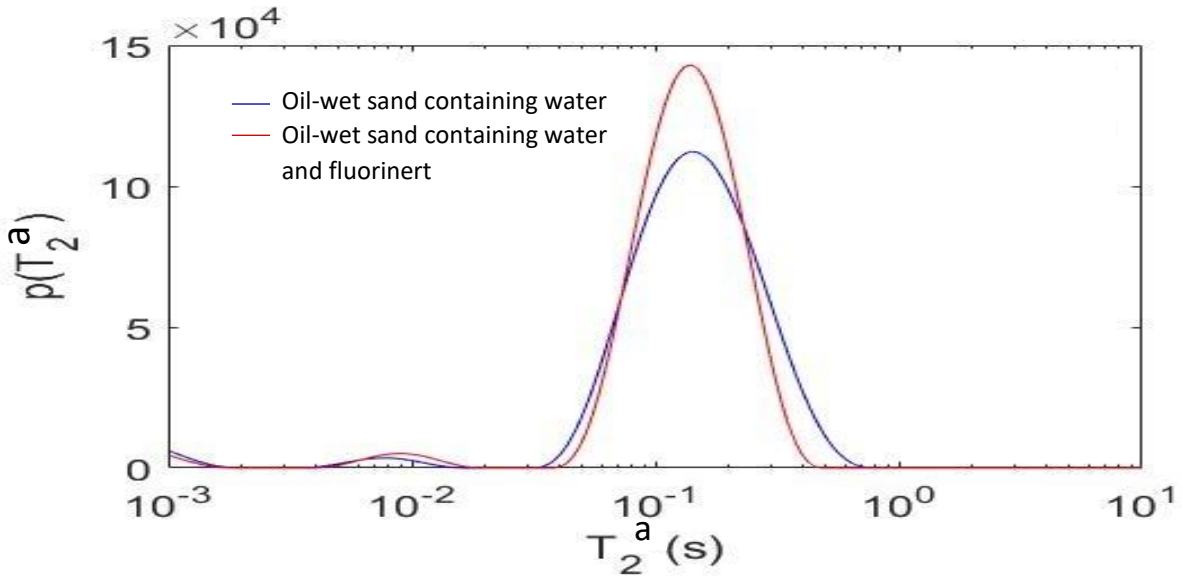

Figure 3.14 – $T_2{}^a$ relaxation time distribution from CPMG scans in figure 3.13. Oil-wet sand with water is represented by the blue line, and oil-wet sand with water and fluorinert is represented by the red line.

Table 3.3 displays the peak values from figure 3.14. The peak value does not change as the fluorinert is added to the sample.

Table 3.3 – Peak values from $T_2{}^a$ relaxation time distribution in figure 3.14.

T2 peak	[s]	[ms]
Oil-wet sand containing water	0,1405	140,5
Oil-wet sand containing water and fluorinert	0,1450	140,5

3.2.3 MSME Results

Like the RAREst protocol, the MSME protocol allows for division of the sample into slices. A specific region of interest, ROI, within these slices can be chosen for further analysis of the T_2 relaxation process. An estimated peak-value for the T_2^a relaxation time can be achieved directly from ParaVision. The data from the ROI can also be exported from ParaVision and analyzed by the same inverse Laplace transformation program as used for the CPMG scans in MATLAB. The settings for the MSME scan differs from the CPMG scan and the analysis by the inverse Laplace transformation will give a different distribution of the T_2^a relaxation time.

Samples 4 to 9, sand with one fluid

The MSME scans of the samples 4 to 9 were performed in both the coronal orientation and the sagittal orientation. These samples were divided into 4 slices, for both orientation, where slice 3 was chosen for further analysis. The ROI for these samples are displayed in figures A2.0.25 and A2.0.26 in Appendix A2. Table 3.4 displays the peak-value for T_2^a relaxation times for samples 4 to 9 from ParaVision as well as from the inverse Laplace transformation. The result from the inverse Laplace transformation is, at the most, 5 standard deviation away from the result assembled directly from ParaVision. Samples 4 and 5, sand containing THF, display approximately the same T_2^a relaxation time within both types of wettability of the porous media. Samples 6 and 7, sand with H_2O, display a faster T_2^a relaxation time for the water-wet sand than for the oil-wet sand from the coronal orientation. For the sagittal orientation this tendency is the opposite. Samples 8 and 9, with heptane, show a faster relaxation for the oil-wet sand from both orientations.

Table 3.4 – Peak values for T_2^a relaxation time distribution from MSME scans of samples 4 to 9.

Sample	T2 CORONAL PARAVISION [ms] ± 1std	T2 SAGITAL PARAVISION [ms] ± 1std	T2 CORONAL ILT [ms]	T2 SAGITTAL ILT [ms]	ROI [cm2]
Oil-wet sand w/H2O	17,2 ± 0,4	15,8 ± 0,4	17,1	13,7	0,26
Water-wet sand w/H2O	15,8 ± 0,4	17,3 ± 0,4	13,7	17,1	0,26
Oil-wet sand w/heptane	11,5 ± 0,3	10,0 ± 0,4	11,0	8,9	0,26
Water-wet sand w/heptane	19,7 ± 0,5	19,0 ± 0,4	19,2	17,1	0,26
Oil-wet sand w/THF	10,0 ± 0,4	10,4 ± 0,7	8,9	8,9	0,26
Water-wet sand w/THF	10,0 ± 0,4	9,9 ± 0,5	8,9	8,9	0,26

Figure 3.15 shows the T_2^a relaxation time distribution for the samples 4 to 9. The data is collected from a specific region of interest, chosen within slice 3, from the coronal orientation. The result from samples 8 and 9, sand with heptane, shows the greatest difference between the oil-wet and water-wet sand. The oil-wet sand has a significantly lower T_2^a relaxation time and both for the peak value and for the density of the T_2^a relaxation times.

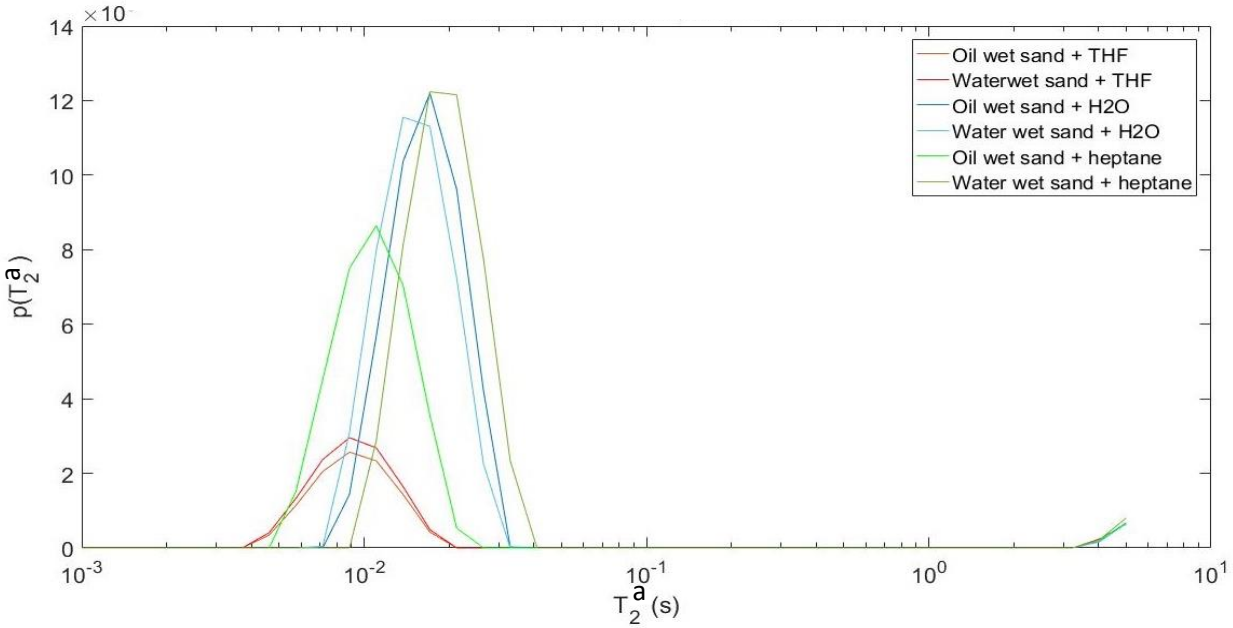

Figure 3.15 - The T_2^a relaxation time distribution from the MSME scans of samples 4 to 9 from the coronal orientation.

Figure 3.16 shows the T_2^a relaxation time distribution for the samples 4 to 9. The data is collected from a specific region of interest, chosen within slice 3, from the sagittal orientation. Also here, the greatest difference between the two sands is recorded for heptane. The result for water in the two different sands are the opposite from the coronal orientation.

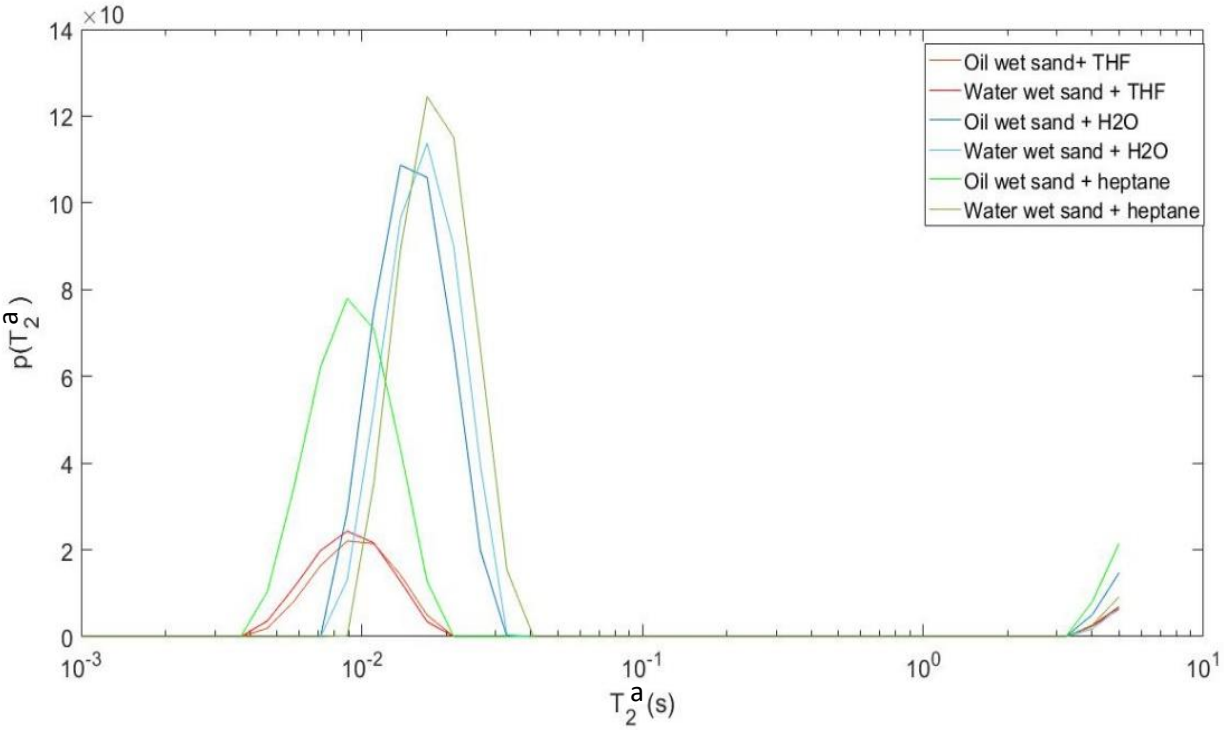

Figure 3.16 - The T_2^a relaxation time distribution from the MSME scans of samples 4 to 9 from the sagittal orientation.

Sample 11, sand with two fluids

The MSME scans of sample 11, oil-wet sand with water and later fluorinert, were performed in the coronal orientation. This sample was divided into 5 slices, where slice 3 and slice 5 were chosen for further analysis. The ROI for these samples are displayed in figure A2.0.28 in Appendix A2. Table 3.5 displays the peak-value for T_2^a relaxation times for the sample from ParaVision as well as from the inverse Laplace transformation. The peak values are almost identical for both slices, before and after the addition of fluorinert.

Table 3.5 – Peak values from T_2^a relaxation time distribution for sample 11.

Sample description and slice number	T_2 relaxation time from ParaVision [ms]	± 1Std	ROI [cm^2]	T_2 relaxation time from ILT [ms]
Oil-wet sand containing water S3	16,3	0,2	0,16	16,4
Oil-wet sand containing water S5	15,0	0,1	0,16	14,1
Oil-wet sand containing water and fluorinert S3	16,4	0,2	0,16	16,4
Oil-wet sand containing water and fluorinert S5	15,2	0,2	0,16	14,1

Figure 3.17 displays the T_2^a relaxation time distribution acquired with the MSME scan, for sample 11 when the oil-wet sand contained just water, and when it contained water and fluorinert. The peak for slice 3 shows no change after the addition of fluorinert. The peak for slice 5 shows a small decrease in density of the T_2^a relaxation time value, but is still found at the same position. The addition of fluorinert did not increase the T_2^a relaxation time for water.

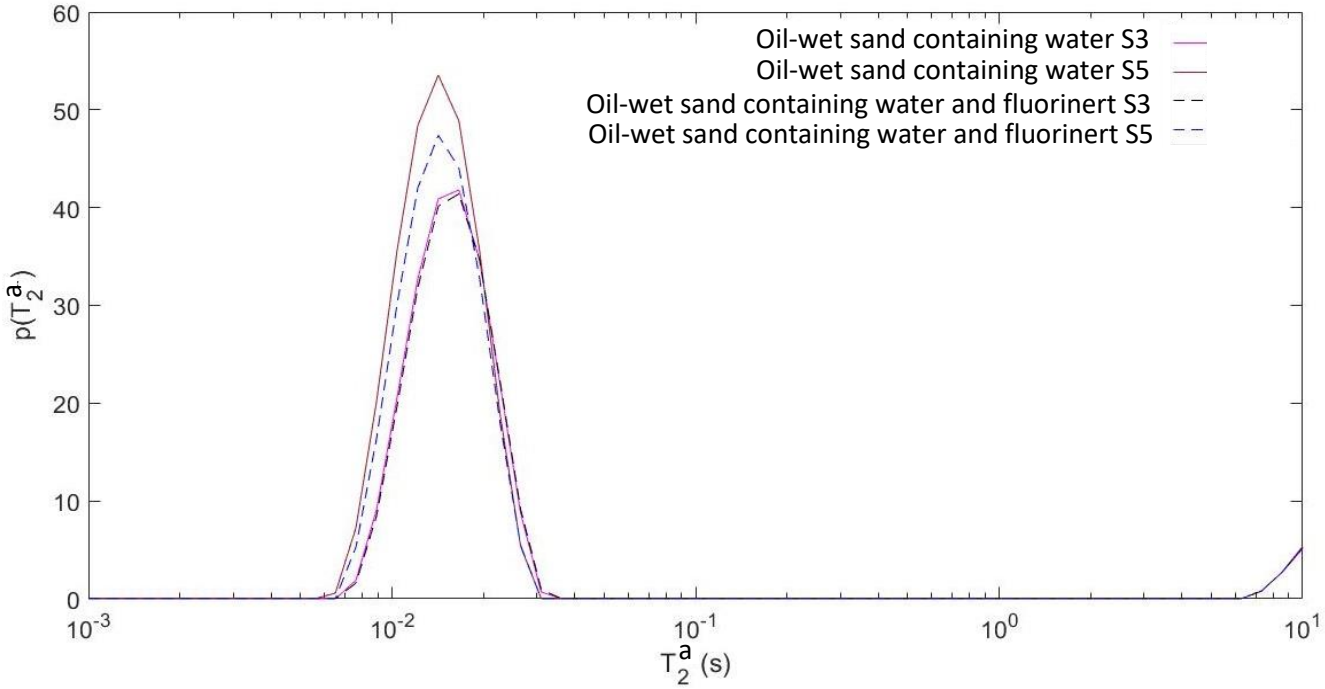

Figure 3.17 – The T_2^a relaxation time distribution for oil-wet sand containing water and oil-wet sand containing water and fluorinert.

MSME scans were not performed on sample 10, oil-wet sand with heptane and water.

3.3 Melting Experiments

Samples 14 to 17 were used for melting experiments. To ensure that hydrates would be formed rapidly in these samples, the samples were cooled to -10°C. After a sample was frozen, it was placed within an isolated plastic beaker, before placed in the MRI instrument, were it melted continuously as scans were performed.

To ensure that hydrates had been formed, sample 3, a mixture of THF and water with the relation 1 mole to 17 moles, was cooled in the same way. After this sample was completely frozen it was placed at 2°C to ensure that no dissociation occurred. After several days the THF hydrates were just as solid as they were at -10°C. The samples 14 to 17 were also placed in this same cooler several times, to ensure for the same, though when the melting experiments were performed they were collected directly from the freezer.

3.3.1 RAREst Images

The RAREst images used for analysis in this subchapter are exported from ParaVision as DICOM-files. These DICOM-files can be read and analyzed by MATLAB. To illustrate how the hydrate saturation data is analyzed sample 15 is used as an example. Sample 15 contains oil-wet sand and a hydrate mixture with the relation 1 mole THF to 15 moles H_2O. The corresponding RAREst images and graphs for samples 14, 16 and 17, can be found in Appendix A3. All images recorded for the melting experiments are from the sagittal orientation.

Figure 3.18 illustrates how sample 15 was divided into 11 slices, each with a thickness of 4mm. The images are from the last RAREst scan, 3,26hours after the first RAREst. Slices 1, 2, 9, 10, and 11, are included to illustrate that there is “noise” present, giving a constant background signal intensity.

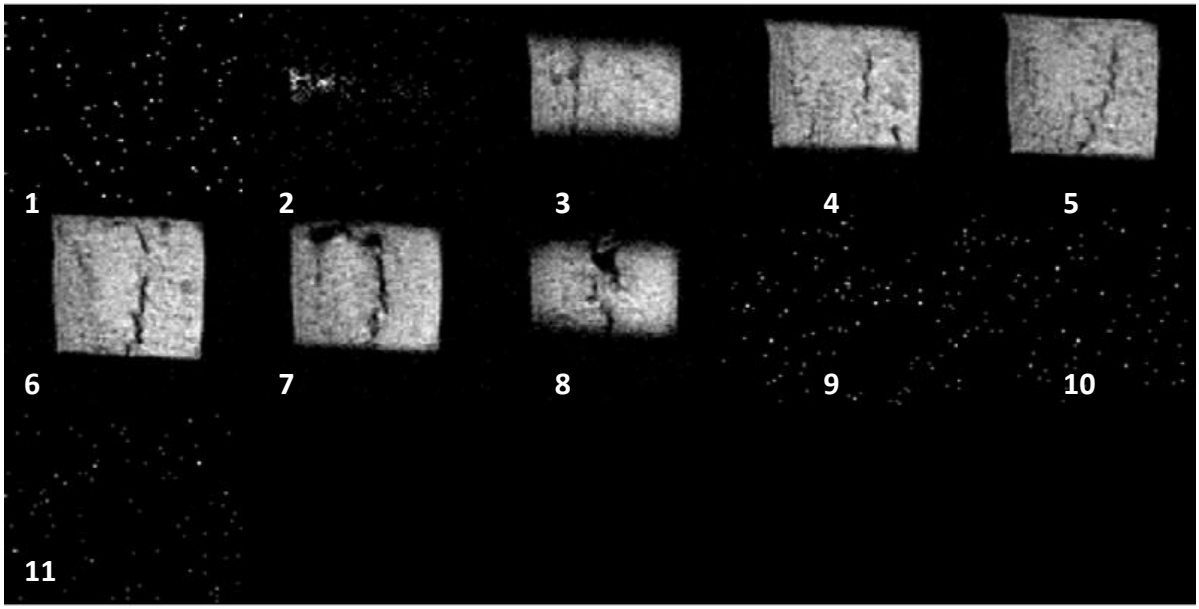

Figure 3.18 - Illustration of how sample 15, oil-wet sand with the mixture of THF to H_2O 1:15, is divided into slices. These images are from the last scan, as 3,26hours have passed from the first RAREst scan.

On the images in figure 3.18 there are black lines cutting through the sample. These lines represent areas within the sample where no signal is recorded. This can be a result of either sand without any contact with fluid, or a crack in the sample where no sand or fluid is present. By visual inspection it was concluded that the areas were cracks, where no sand nor fluid was present. The cracks rather consisted of air. Whether these cracks were present before the hydrates were formed in the sand, or not, was not established by these MRI studies, but visual inspection upon preparing the samples did not register any signs of these cracks.

Figure 3.19 displays the development of intensity as the hydrates are dissociating. The intensity is given as a function of slice number and each line represents a point in time. The intensity will increase as the hydrates are dissociating, giving a time development that follows the arrow in the figure. When the THF hydrates are completely dissociated the intensity will decrease and the intensity development moves in the opposite direction as the sample is heated.

As the first slice containing any significant signal is slice 3, there is no increase of intensity for slice 1 and 2, as the hydrate melts. The same holds for slices 9, 10, and 11, as the last slice with signal is slice 8. As one moves to the middle of the sample, more signal is obtained due to the curvature of the sample glass. This explains the convex shape of figure 3.19. Slice 5 will record a larger amount of the sample than e.g. slice 8.

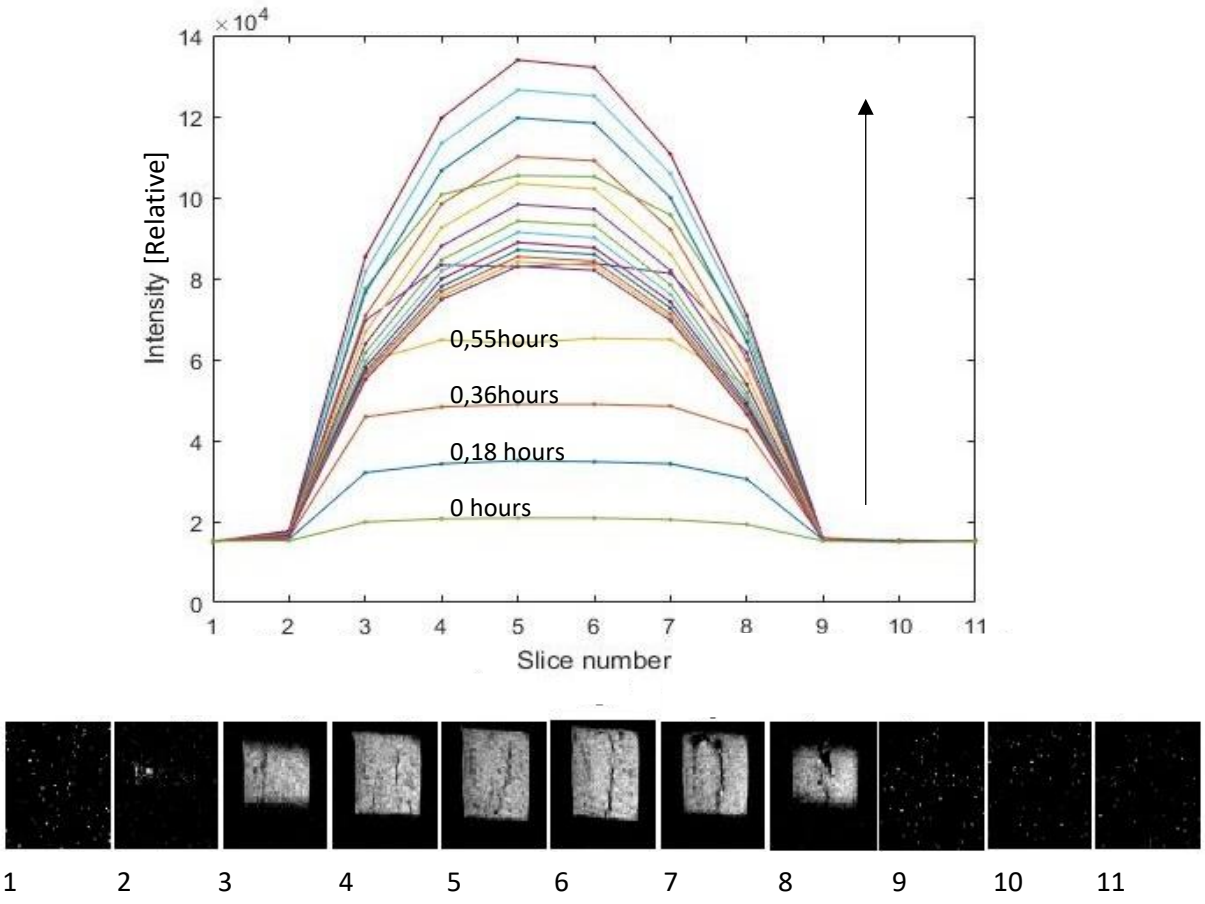

Figure 3.19 – Intensity development for sample 15, oil-wet sand and a mixture of H_2O to THF of 15mol:1mol. The slice number is given on the x-axis and each line represents a point in time.

Figure 3.20 displays the RAREst images of slice 5 from sample 15 as it melts over time. The images show a clear increase in brightness as time passes. When hydrogen nuclei in water are in a solid state they will relax so rapidly that the signal they emit will not be recordable above the background noise. The signal intensity given from the sample will increase as an increasing amount of hydrogen nuclei transfer to a liquid state. The RAREst images will therefore become brighter as the sample is melting.

From these images it is also clear that the THF hydrates start dissociating in the outer edges of the sample. As this sample is removed from -10°C and placed within an isolated beaker at room temperature, this is expected. The heat is transferred from the surroundings to the sample, so the heat must travel through the edges. MRI provides a way to trace the melting structure of solids.

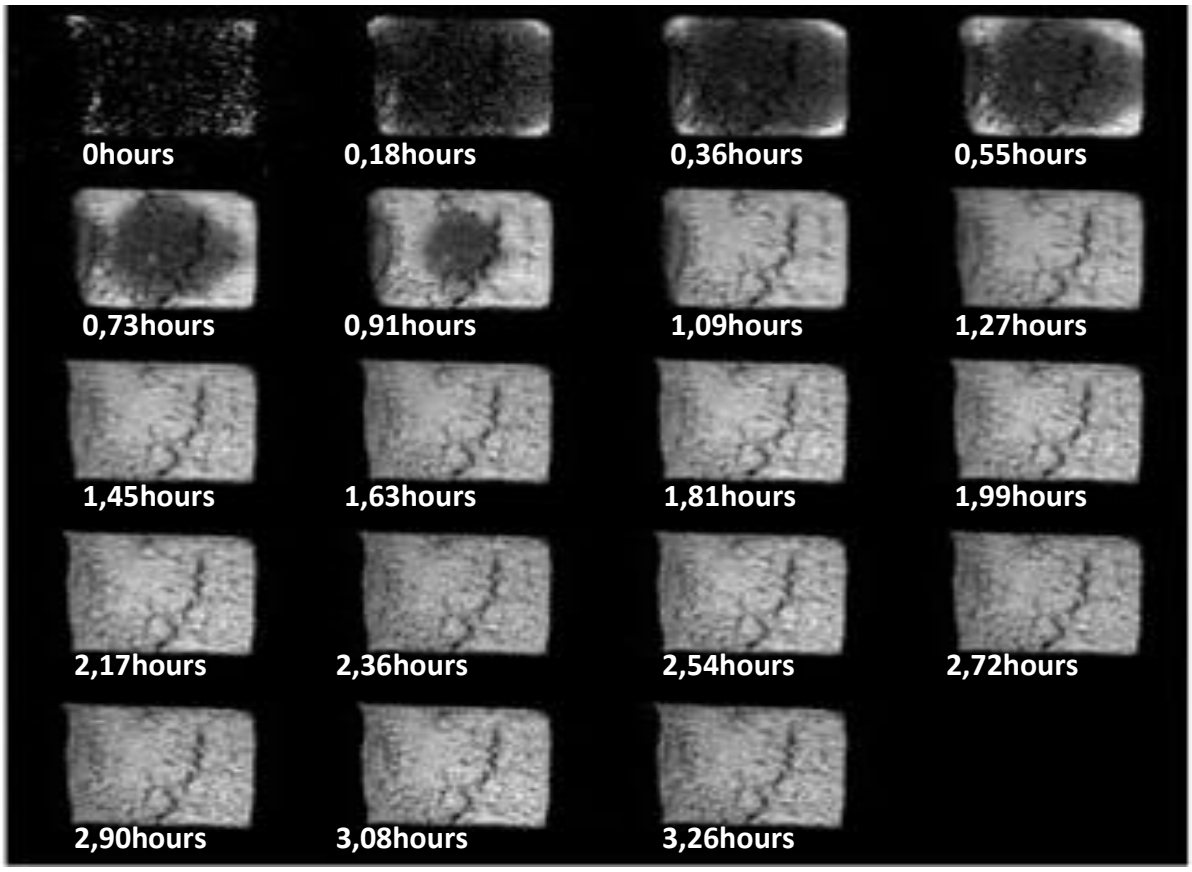

Figure 3.20 - RAREst images of slice 5 from sample 15, as the hydrates are dissociating.

Figure 3.21 illustrates the intensity development from sample 15 as a function of time. Each line represents a slice from the sample. The lines at the bottom of this figure has captured the noise from the surroundings, through slices 1, 2, 9, 10, and 11. The intensity of the signal will increase continuously as the hydrates are dissociating. The curves all have a maximum point, before a decrease in signal intensity is registered. This maximum point is thought to represent the time of complete dissociation. After this point the sample is heated to room temperature. As the temperature of the sample is rising, the settings for the RAREst scan are most likely no longer suitable. The same development, of the decreasing curve, was also recorded in the results from measurements on the dissociation process of THF hydrates in bulk, performed by previous master student Celine Eriksen [41].

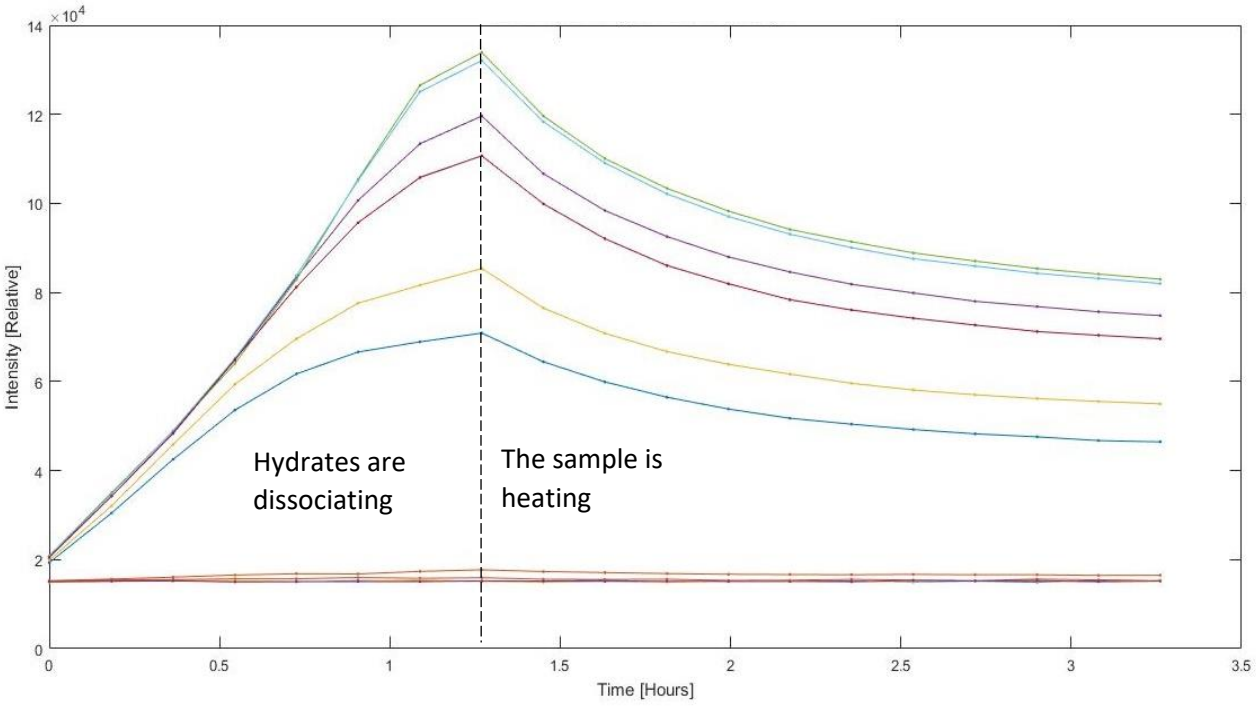

Figure 3.21 - Intensity development as a function of time for sample 15. Each line represents a slice of the sample. The lines towards the bottom of the figure, displays the slices included to record the noise during the RAREst scans, slices 1, 2, 9, 10, and 11. As the hydrates are dissociating the signal intensity increases. When the dissociation process is complete a decrease in signal intensity is recorded, as the sample is heated to room temperature.

Figure 3.22 displays the total intensity development over time, as all the slices are summarized and displayed as one total development. As the slices containing noise display no development, the addition of these slices will not affect the trend of the curve. The maximum point of the graph indicates the point in time where the dissociation of the THF hydrates is complete, the rest of the graph is not used for further analysis. Notice that the maximum point in figures 3.21 and 3.22 does not correspond to the apparent completion of melting in figure 3.20. Figure 3.20 only portray the dissociation happening in slice 5. Each slice is 4 mm thick and is only displayed in two dimensions. Though it can appear on the RAREst images that the dissociation process is complete, the development of the signal intensity shows that more dissociation occurs, as the signal intensity is still rising.

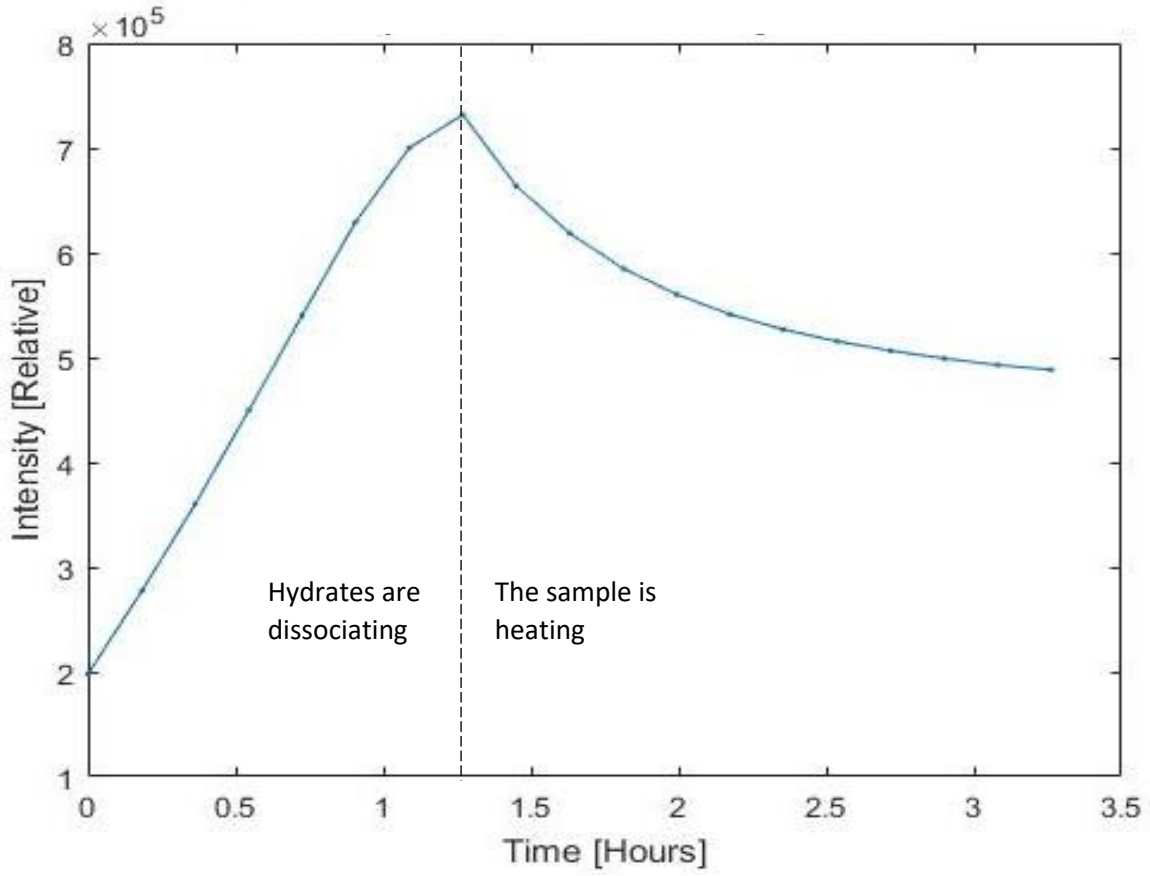

Figure 3.22 – Total intensity development as a function of time for sample 15. THF hydrates are dissociating until the maximum point of signal intensity is reached. After this point the signal intensity will decrease as a result of the sample being heated.

Figure 3.23 shows the intensity development per slice after corrections for the signal intensity are made. The noise captured in each scan is removed by calculating an average value for the noise from slices 1, 10, and 11. The average value is calculated for each scan time and removed from each slice presented in the figure. As slice 1, 2, 9, 10 and 11, mainly consists of noise these are not included in this figure. The decreasing signal that was recorded after the dissociation of hydrates was complete is also removed from the signal intensity portrayed in this figure.

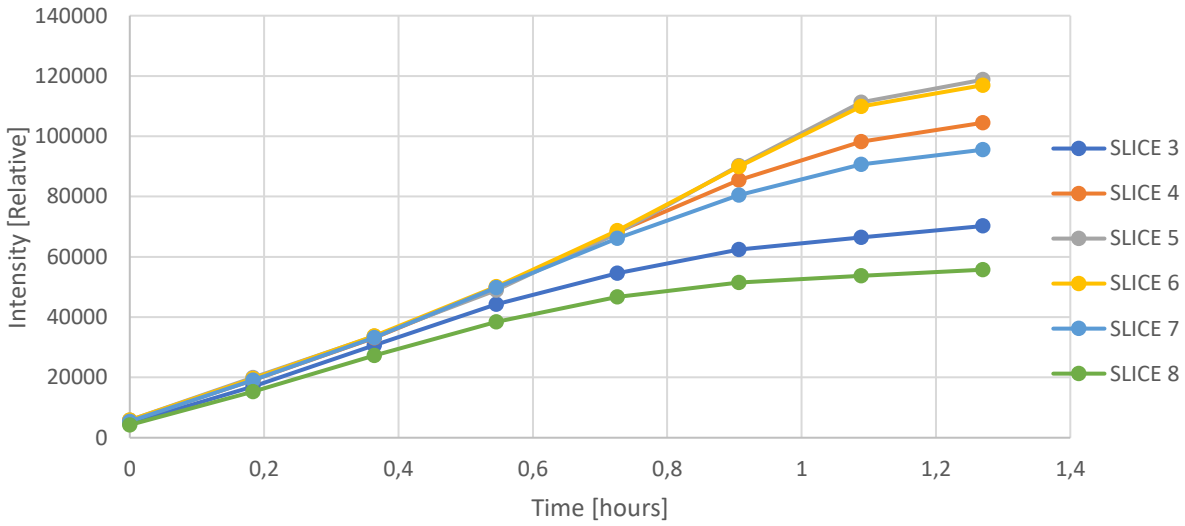

Figure 3.23 - Intensity development for each slice containing hydrates in sample 15, oil-wet sand containing a mixture of 1 mole THF per 15 moles of H2O. The figure is corrected for noise and the completion of dissociation of the hydrates.

The intensity development for the slices are close to linear and the THF hydrates are dissociating through a steady development. The data from this figure is further used for estimation of hydrate saturation, by formula (2.1). The peak signal intensity as the dissociation of the hydrates is completed is used as the intensity when the sample is completely in liquid form, I_0. The estimation of THF hydrate saturation is performed for each slice and the result is displayed as a function of time in figure 3.24.

Figure 3.24 shows the decline in relative hydrate saturation, for each individual slice, as a function of time. As the THF hydrates are dissociating, the relative hydrate saturation is decreasing.

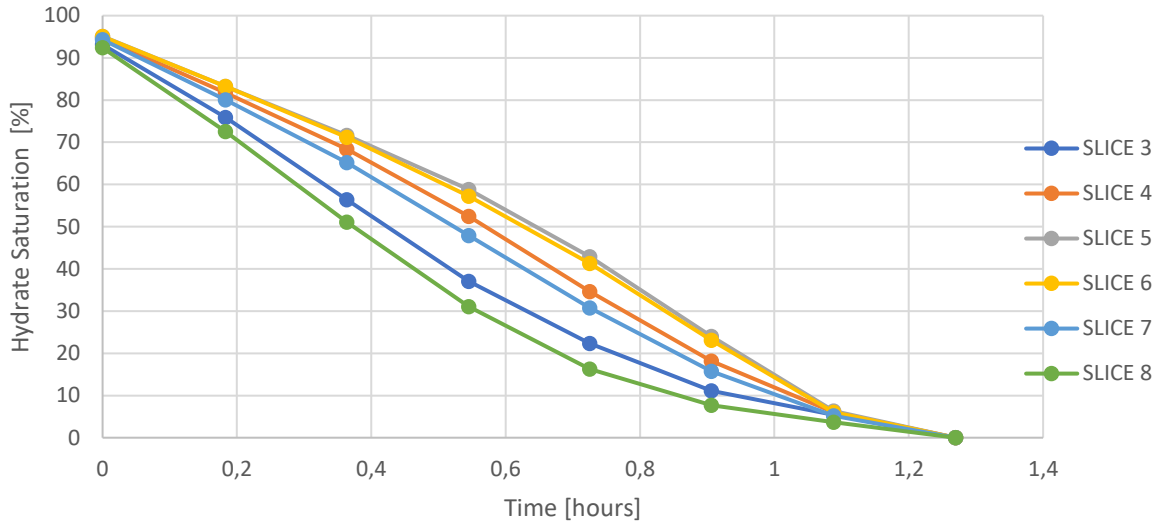

Figure 3.24 - Hydrate saturation per slice as a function of time. As the sample is heated, the hydrates dissociate.

Figure 3.25 displays the total intensity development, from sample 15, as a function of time when all the slices from figure 3.23 are summarized. The development of the curve shows a steady increase in signal intensity as the hydrates dissociate.

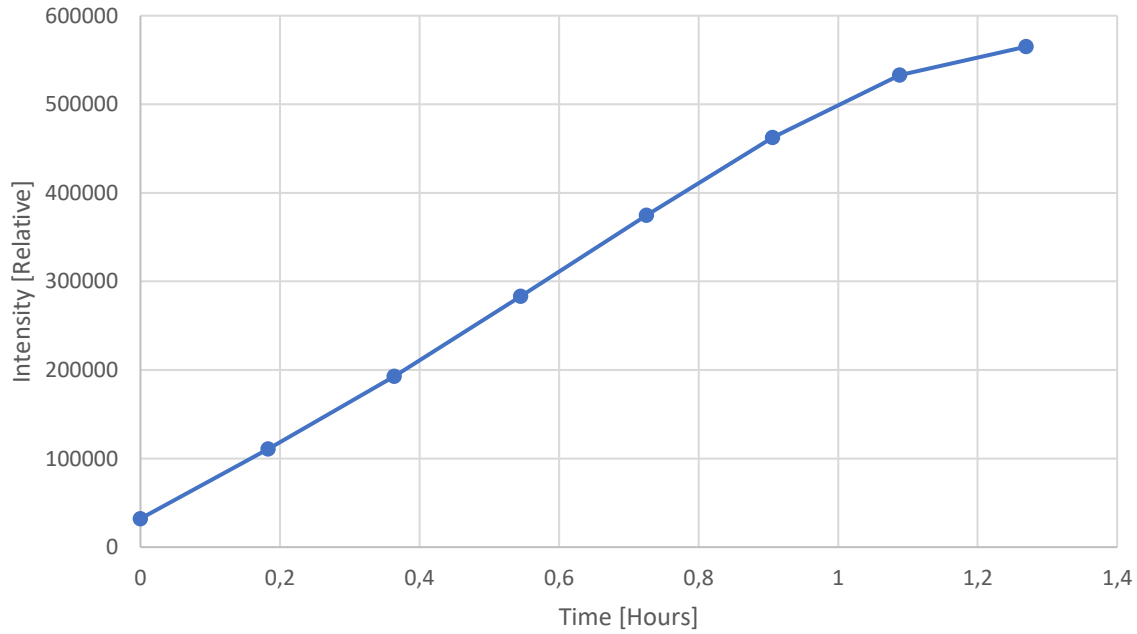

Figure 3.25 - Intensity development for sample 15 as a function of time, when all slices are summarized to one.

Figure 3.26 shows the relative hydrate saturation from the whole sample as a function of time. The relative THF hydrate saturation shows a steady decrease as the sample is melting.

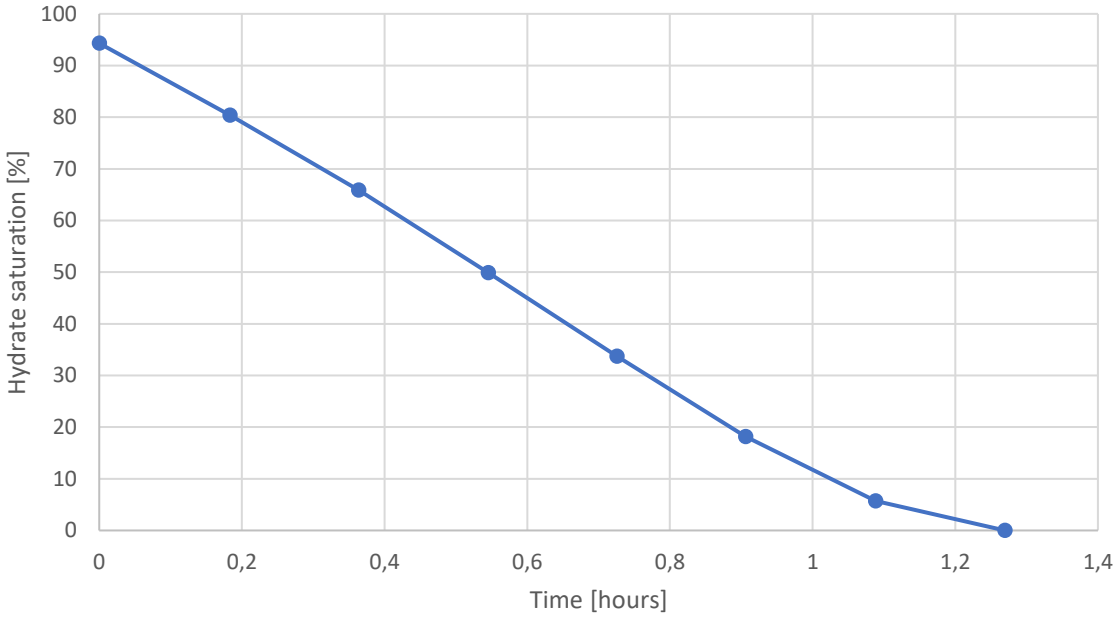

Figure 3.26 – Relative hydrate saturation for sample 15 as a function of time, as all slices from figure 3.24 are summarized.

The same analysis was performed on the RAREst images recorded of samples 14, 16, and 17. Corresponding figures to figure 3.18 to 3.26 can be found in appendix A3, figures A3.0.2 to A3.0.22. The total signal intensity development as a function of time for all four samples are given in figure 3.27. The total signal intensities displayed in the figure are all corrected for noise and for the completion of hydrate dissociation. Figure 3.27 portrays a close to linear development for all the four samples. The difference in intensity reflects on the amount of liquid that was added to each sample. No significant differences between melting processes, caused by the wettability preference of the porous media, were recorded.

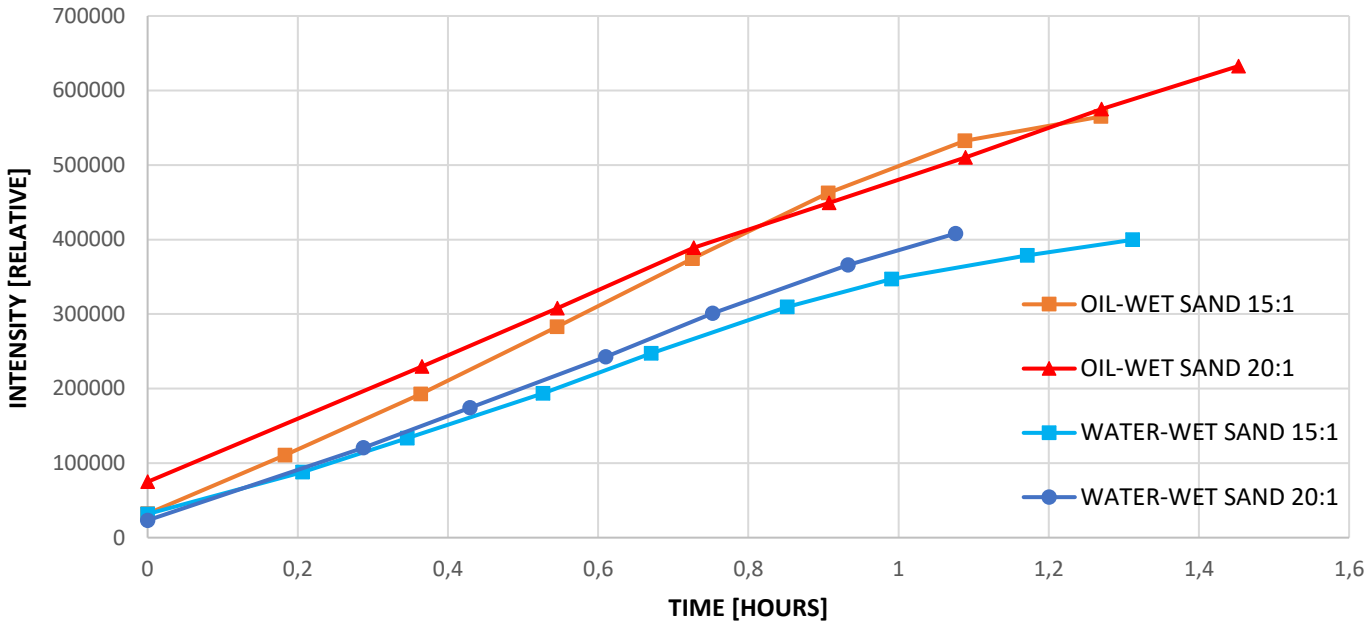

Figure 3.28 - Intensity development as a function of time, as hydrates are dissociating in samples 14-17.

Figure 3.28 displays the relative THF hydrate saturation as a function of time, from the four different THF hydrate samples. The decrease in saturation is close to linear and starts at around 90% saturation for all samples. The amount of THF and water molecules within the sample will influence the dissociation time. The decrease in THF hydrate saturation is caused by steady heat transfer from the surroundings. No significant differences caused by the wettability preferences of the porous media are visible from these results.

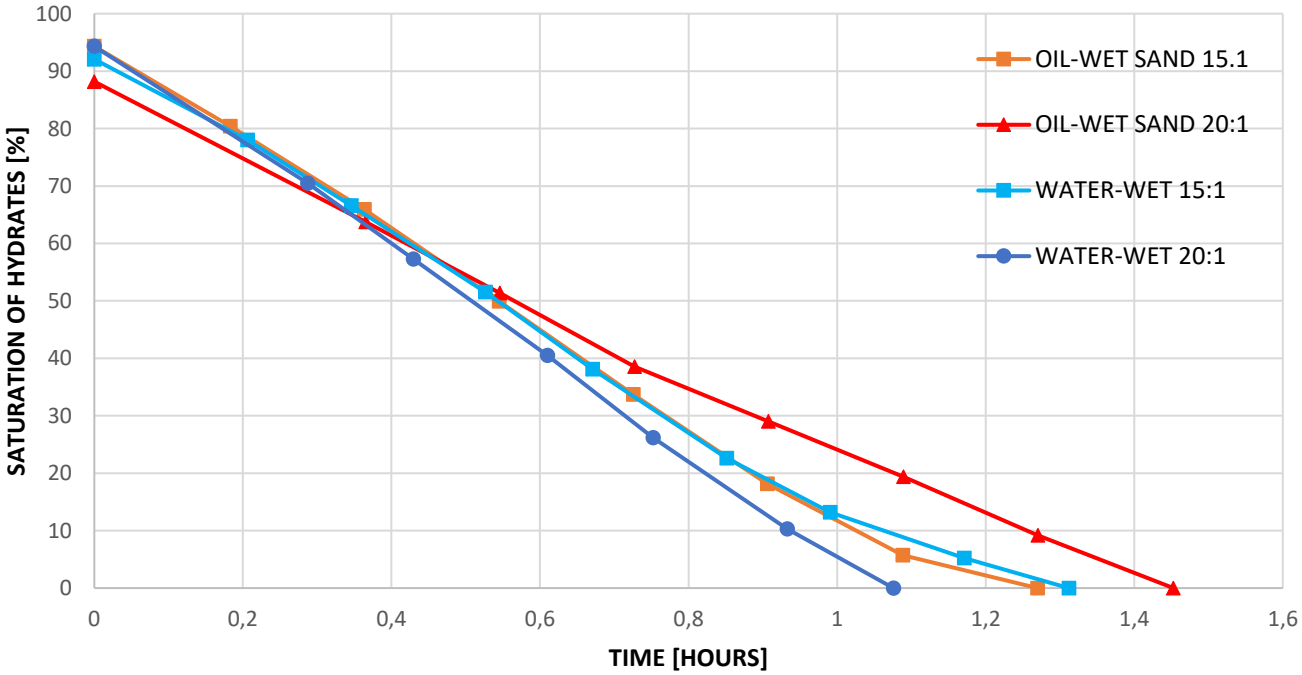

Figure 3.27 - Hydrate saturation as a function of time, as the hydrates dissociates in samples 14 to 17.

3.3.2 CPMG Results

The data presented in this subchapter are estimated through the inverse Laplace Transformation. The decay curves with the original CPMG data can be found in Appendix A3, together with the settings used for the inverse Laplace transformation. Additional portraying of the T_2^a relaxation time distribution can also be found in Appendix A3.

Figure 3.29 display the T_2^a relaxation time distribution from inverse Laplace transformation of decay curves for samples 14 and 15. Figure 3.30 display the T_2^a relaxation time distribution from inverse Laplace transformation of decay curves for samples 16 and 17. All peak values can be found in tables 3.6 and 3.7.

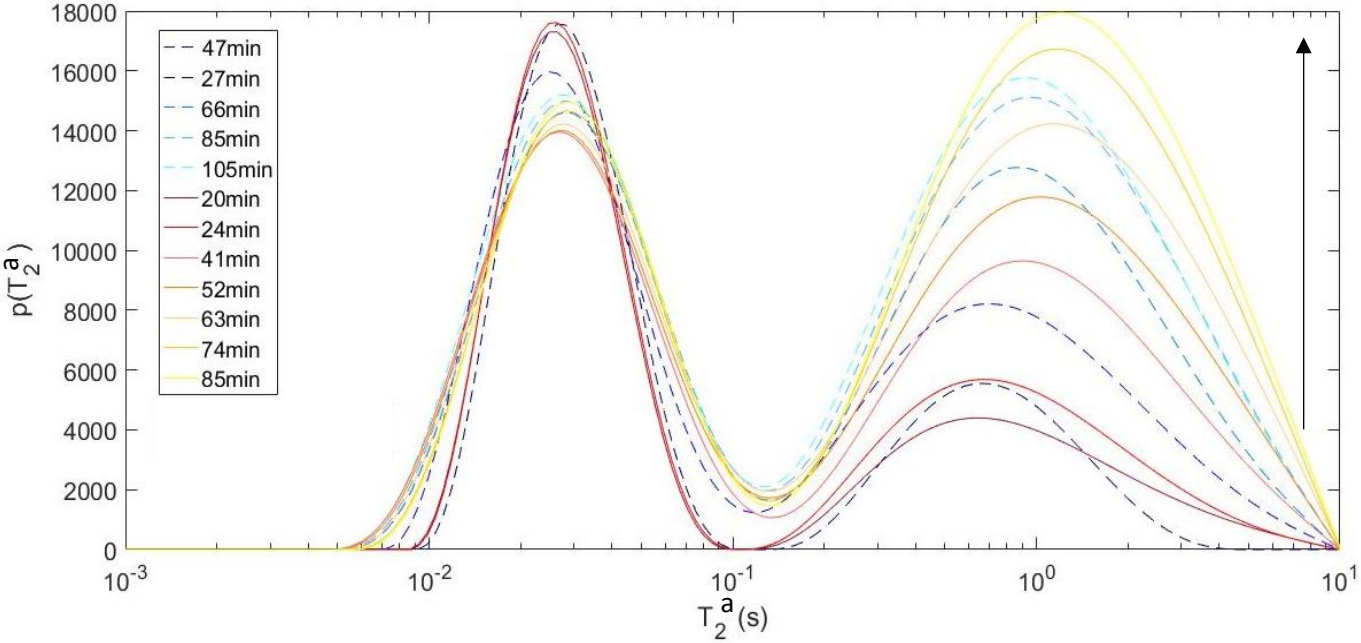

Figure 3.29 - T_2^a relaxation time distribution development as dissociation takes place for samples 14 and 15. Blue dashed lines are for the water-wet sand. Purple to yellow solid lines are for the oil-wet sand. The development over time follows the direction of the arrow.

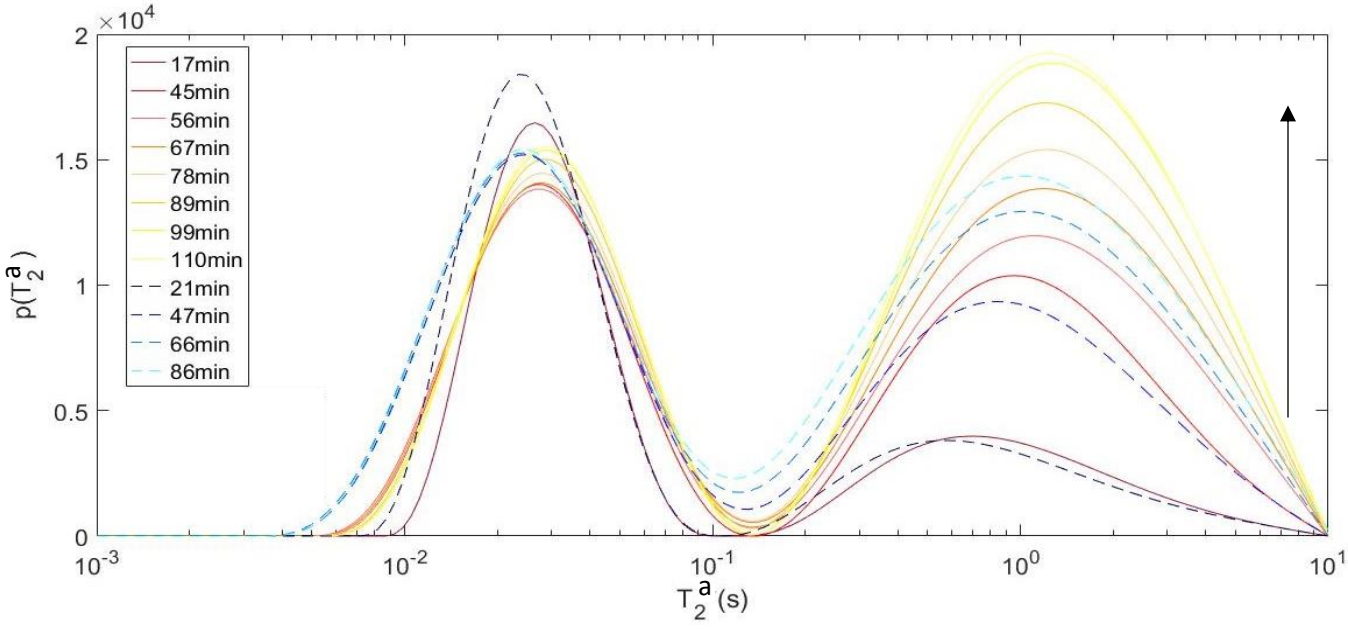

Figure 3.30 - T_2^a relaxation time distribution development as dissociation takes place for samples 16 and 17. Blue dashed lines are for the water-wet sand. Purple to yellow solid lines are for the oil-wet sand. The development over time follows the direction of the arrow.

Figures 3.29 and 3.30 display a similar development as the THF hydrates are dissociating. The figures show the T_2^a relaxation time distribution from all the scans recorded as the hydrates within the samples dissociate. Both figures display two peak values for the T_2^a relaxation time distribution for both water-wet and oil-wet sand. As time passes, the two peaks develop differently. The first peak in figure 3.29, with the lower T_2^a relaxation time values, increases its peak T_2^a relaxation time value by 4,3ms for the oil-wet sand, and by 0,9ms for the water-wet sand, see table 3.6. The density of these values decreases from the first scan, before displaying a tendency of growth.

The second peak in figure 3.29, with higher T_2^a relaxation time values, increases its peak T_2^a relaxation time value by 563,1ms for the oil-wet sand, and by 295,8ms for the water-wet sand. The density of the second peak increases significantly. The T_2^a relaxation time distribution from a porous medium can correlate to a relative pore size distribution. The significant growth for the second peak as the THF hydrates are dissociating can illustrate that these are the relative pore size that the hydrates mainly form within, or at least represent the pore size that the THF hydrates dissociate slower within.

The first peaks in figure 3.30, with the lower T_2^a relaxation time values, increases its peak T_2^a relaxation time value by 3,5ms for the oil-wet sand, and by 1,5ms for the water-wet sand, see table 3.6. Like in figure 3.29, the density of these values decreases significantly from the first scan, before displaying a tendency of growth. The second peak in figure 3.30, with higher T_2^a relaxation time values, increases its peak T_2^a relaxation time value by 476,4ms for the oil-wet sand, and by 440,2ms for the water-wet sand. The density of the second peak increases significantly also here.

The development from the dissociation appears to be similar within sand with two different preferences of wettability. However, the T_2^a relaxation time distribution plots show lower peak T_2^a relaxation time values for the water-wet sand than for the oil-wet sand. The hydrogen nuclei between the oil-wet sand grains use longer time on the T_2 relaxation process, and relax slower than between the water-wet sand grains.

The higher peak T_2^a relaxation time values for the oil-wet sand could either be caused by a greater pore size of the oil-wet sand, or by the wettability effect. As TMS is added to the surface of the oil-wet sand grains this could give the sand a greater grain size which would result in a greater pore size. The wettability effect of the oil-wet sand results in the water and THF trying to avoid contact with the oil-wet surface. This could result in the hydrogen nuclei not being positioned as close to the pore walls as water and THF would be in the water-wet sand. Comparing these results to the results from the sand experiment, could indicate that this phenomenon is mainly caused by the wettability of the sand grains.

The peak values from T_2^a relaxation time distribution portrayed in figure 3.29 are specified in table 3.6.

Table 3.6 - Peak values for T_2^a relaxation time distribution from figure 3.29, sand with the mixture H_2O:THF 15:1.

Oil-wet sand 15:1 time	peak one [ms]	peak two [ms]	Water-wet sand 15:1 time	peak one [ms]	peak two [ms]
20min	25,7	658,9	-	-	-
24 min	25,7	658,9	27 min	27,3	658,9
41 min	27,3	897,5	-	-	-
52 min	26,5	1016,0	47 min	24,9	700,9
63 min	26,5	1149,0	66 min	28,2	843,7
74 min	30,0	1149,0	-	-	-
85 min	30,0	1222,0	85 min	28,2	954,7
-	-	-	105 min	28,2	954,7

The peak values from T_2^a relaxation time distribution portrayed in figure 3.30 are specified in table 3.7.

Table 3.7 - Peak values for T_2^a relaxation time distribution from figure 3.30, sand with the mixture H_2O:THF 20:1.

Oil-wet sand 20:1 time	peak one [ms]	peak two [ms]	Water-wet sand 20:1 time	peak one [ms]	peak two [ms]
17 min	26,5	745,6	21 min	23,4	514,5
45 min	26,5	954,7	47 min	24,9	843,7
56 min	28,2	1149,0	-	-	-
67 min	28,2	1222,0	66 min	24,9	954,7
78 min	28,2	1222,0	-	-	-
89 min	29,1	1222,0	86 min	24,9	954,7
99 min	30,0	1222,0	-	-	-
110 min	30,0	1222,0	-	-	-

3.3.3 MSME Results

The MSME scans of the samples 14 to 17 were performed in the sagittal orientation. These samples were divided into 7 slices and slice 3 was chosen for further analysis. From slice 3 a specific region of interest, ROI, with the size of 0,26 cm^2, was selected. The ROI for each sample was selected as the default ROI chosen by ParaVision, to ensure that the same specific area is analyzed for each scan. The ROI for these samples are displayed in figures A3.0.35 to A3.0.38 in Appendix A3. Additional portraying of the $T_2{}^a$ relaxation time distribution and the settings for the inverse Laplace transformation can also be found in Appendix A3.

The $T_2{}^a$ relaxation time distribution from the ROI was estimated through the inverse Laplace transformation. Figure 3.31 display the $T_2{}^a$ relaxation time distribution for samples 14 and 15 achieved from the MSME scans. Each peak represents a point in time. The peak-values for the $T_2{}^a$ relaxation time can be found in table 3.8.

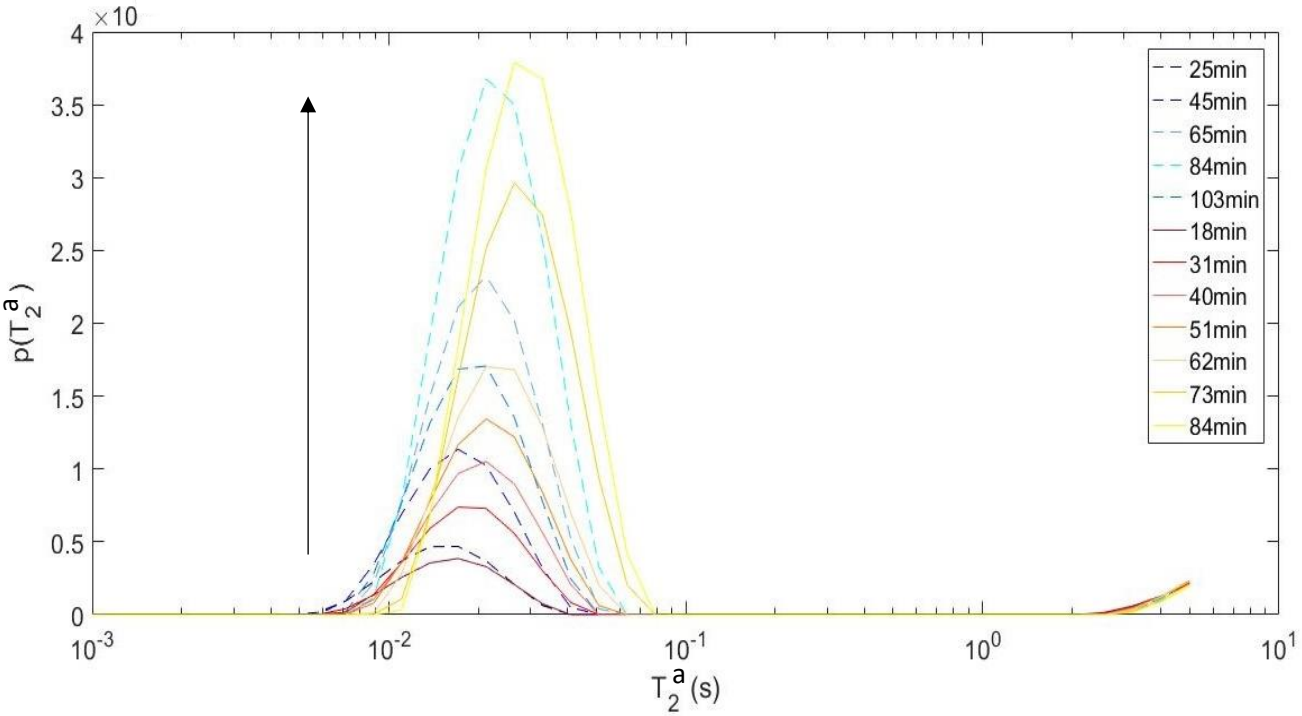

Figure 3.31 - $T_2{}^a$ relaxation time distribution for samples 14 and 15 acquired in the sagittal orientation. The samples are divided into 7 slices, and a specific region of interest within slice 3 was used for further analysis. Blue dashed lines are for the water-wet sand. Purple to yellow solid lines are for the oil-wet sand. The development over time follows the direction of the arrow.

Figure 3.32 displays the MSME results after inverse Laplace transformation for sample 16 and 17. The peak-values for the T_2^a relaxation time can be found in table 3.8.

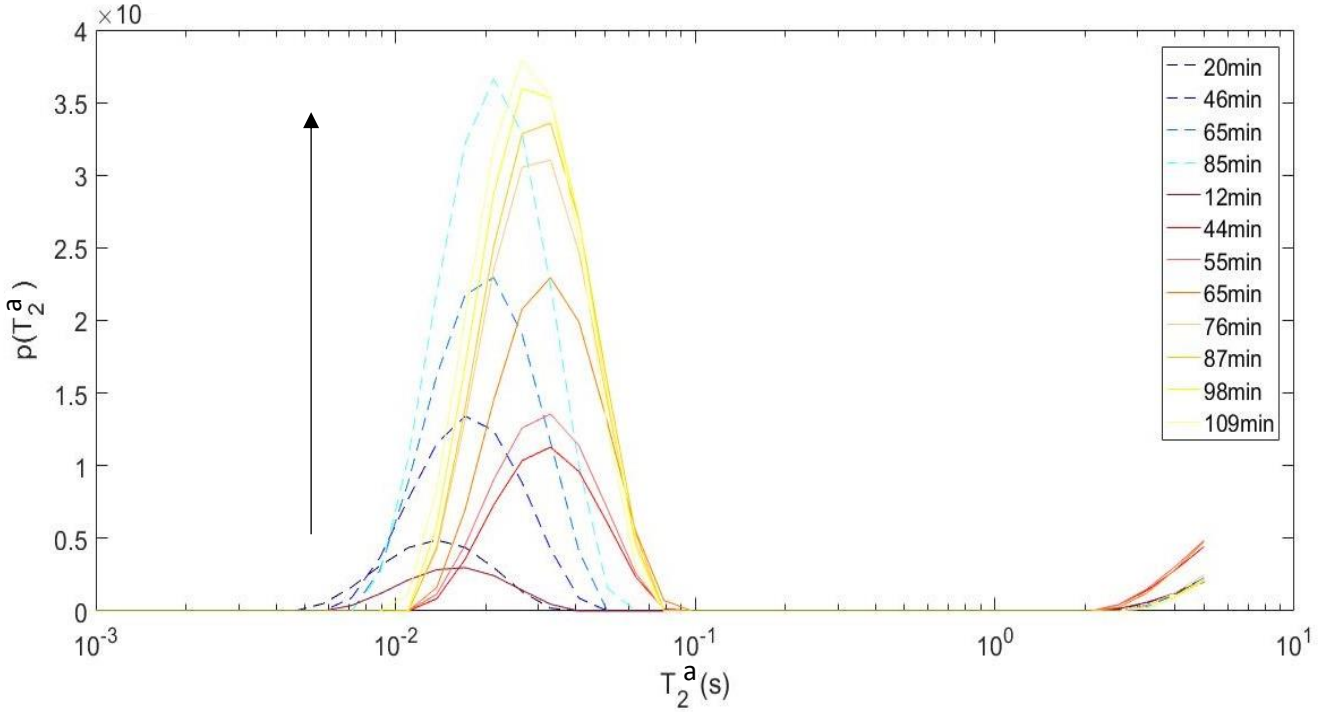

Figure 3.32 - T_2^a relaxation time distribution for samples 16 and 17 acquired in the sagittal orientation. The samples are divided into 7 slices, and a specific region of interest within slice 3 was used for further analysis. Blue dashed lines are for the water-wet sand. Purple to yellow solid lines are for the oil-wet sand. The development over time follows the direction of the

Figures 3.31 and 3.32 display equal tendencies as time passes, an increasing peak value for the T_2^a relaxation time and increasing density of the measured T_2^a relaxation times. The observed increase of the peak T_2^a relaxation time value is not as significant as for the CPMG scan. The T_2^a relaxation time distribution in figure 3.31 and 3.32 are different from the distribution in figures 3.29 and 3.30, obtained with the CPMG scan. The MSME scan only portrays one peak, and a significantly lower peak T_2^a relaxation time. As the distinctive development is similar to the second peak of the CPMG scan, it is assumed that the peaks from the MSME scan represents the second peak of the CPMG scan. The echo spacing, or echo time, is increased with the MSME scan, hence the same T_2^a relaxation time distribution as in the CPMG scan will not be recorded. As TE increases, the influence of the gradient on the T_2^a relaxation time will increase, see formula (1.10). This explains the lower T_2^a relaxation time recorded with the MSME scan. The fastest relaxing nuclei that were recordable with the CPMG scan are not recordable by the MSME scan. The trend with a higher peak T_2^a relaxation time value for the oil-wet sand is however also observable from the MSME scan.

Table 3.8 - Peaks from T_2 relaxation time distribution from MSME scans

Time elapsed [min] (water-wet 15:1)	T2 relaxation time ILT [ms] (water-wet 15:1)	Time elapsed [min] (water-wet 20:1)	T2 relaxation time ILT [ms] (water-wet 20:1)	Time elapsed [min] (oil-wet 15:1)	T2 relaxation time ILT [ms] (oil-wet 15:1)	Time elapsed [min] (oil-wet 20:1)	T2 relaxation time ILT [ms] (oil-wet 20:1)
25 min	15,4	20 min	13,7	18 min	17,1	12 min	17,1
-	-	-	-	31 min	19,2	-	-
45min	17,1	46 min	17,1	40 min	21,3	44 min	32,9
-	-	-	-	51 min	21,3	55 min	32,9
65min	21,3	65 min	21,3	62 min	23,9	65 min	32,9
-	-	-	-	73 min	26,5	76 min	32,9
84min	21,3	85 min	21,3	84 min	26,5	87 min	32,9
-	-	-	-	-	-	98 min	26,5
103min	21,3	-	-	-	-	109 min	26,5

3.4 Cooling Experiments

Sample 14 and 15 were used for the cooling experiments that are presented in this subchapter. For these experiments, the procedure started with freezing the samples at -10°C. Several unsuccessful attempts to re-form THF hydrates within the MRI instrument in order to record the hydrate formation were performed. A frequent issue was that the sample was submerged into the fluorinert too soon, before it was cooled below 5°C, which resulted in too much dissociation for regrowth to occur.

Sample 14 was placed in the fluorinert while it was cooling. This allowed part dissociation to occur. As the fluorinert was cooling the air cooling system was set to -20°C, which corresponded to approximately -4°C in the fluorinert, when completely cooled. When the sample was no longer visible on the RAREst images, the air-cooler was set to -5°C, corresponding to a temperature of around 5°C in the fluorinert, slightly above the melting point for THF hydrates. This increase in temperature resulted in dissociation of the hydrates. The sample was then left within the fluorinert at approximately 5°C for more than 10 hours. As the temperature was kept constant, the previously recorded decrease in intensity, as the sample was heated, was not recorded for this sample.

Sample 15 was placed in the fluorinert when it was already cooled, and the air cooler was then turned off. This allowed for partially melting of the hydrate, before the air cooler was turned back on, at -20°C, allowing for hydrates to grow back. As the fluorinert was re-cooling, now simultaneously as the sample, the growth took place at a slower pace than for sample 14. When the hydrates had formed the air-cooler was turned completely off allowing for dissociation of the hydrates. As the temperature was not constant here, the previously observed decrease of signal intensity was recorded for this sample, as the sample and the fluorinert were simultaneously heated to room temperature.

3.4.1 RAREst Images

Sample 14, water-wet sand with the mixture H_2O:THF 15:1

This sample was examined in both the coronal and the sagittal direction. Figure 3.33 illustrates how the sample was divided into 16 slices in the coronal orientation, from bottom to top. Slice 1 is included to illustrate that there is "noise" present, giving a constant "background" signal intensity.

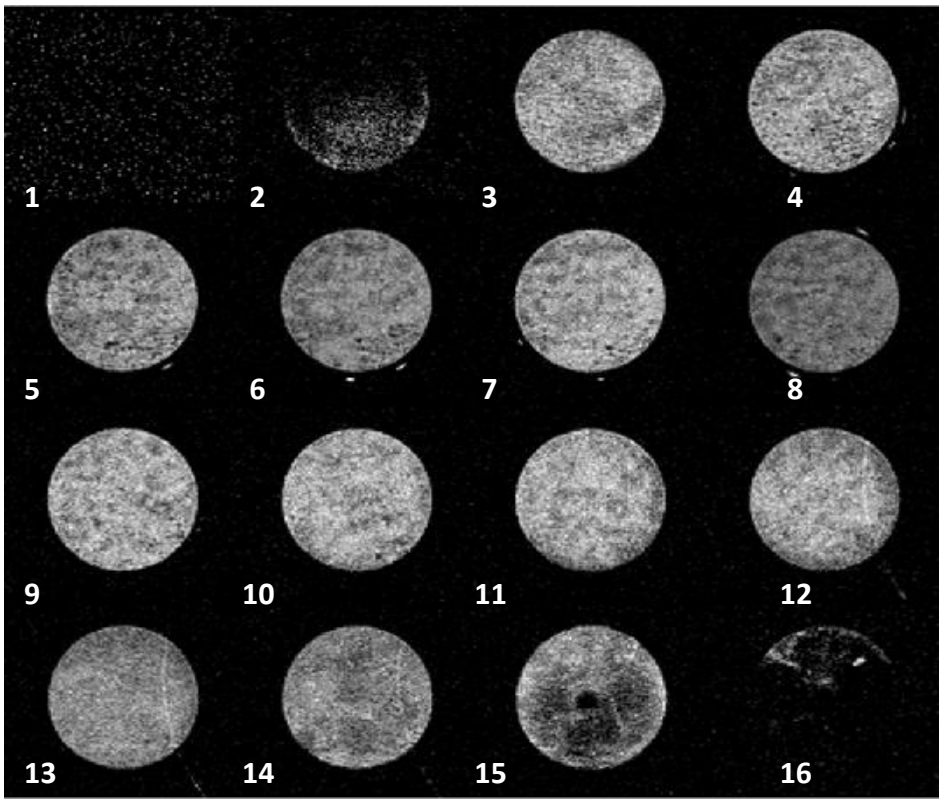

Figure 3.33 – Illustration of how sample 14, water-wet sand with the mixture of THF to H_2O 1:15, is divided into 16 slices. These images are from the last scan, as 18,89hours have passed from the first RAREst scan.

These images are taken from the last RAREst scan in the coronal orientation, 18.89hours after the first RAREst scan in the coronal orientation. Notice how the tube from the air cooling set-up is visible in slices 12 to 14. After hours of cooling the fluorinert, water molecules will condense at the surface on the tube, causing the tube to become visible on the RAREst images. The water molecules condensing on the tube surface will add to the signal intensity recorded in the images.

Figure 3.34 displays the RAREst images of slice 13 from sample 14 as it melts over time. The images are acquired in the coronal orientation. The tube surrounding the beaker with fluorinert becomes visible on the RAREst images, after 5,17hours of cooling the fluorinert. As the air that flows through the tube is cooler than the surrounding air, water molecules will condense on its surface. The hydrogen nuclei in these water molecules will respond to the radio frequency waves from the MRI instrument and give an additional intensity response. The signal recorded with the RAREst scan is no longer only from the sample, but also from hydrogen molecules situated on the surface of the tube.

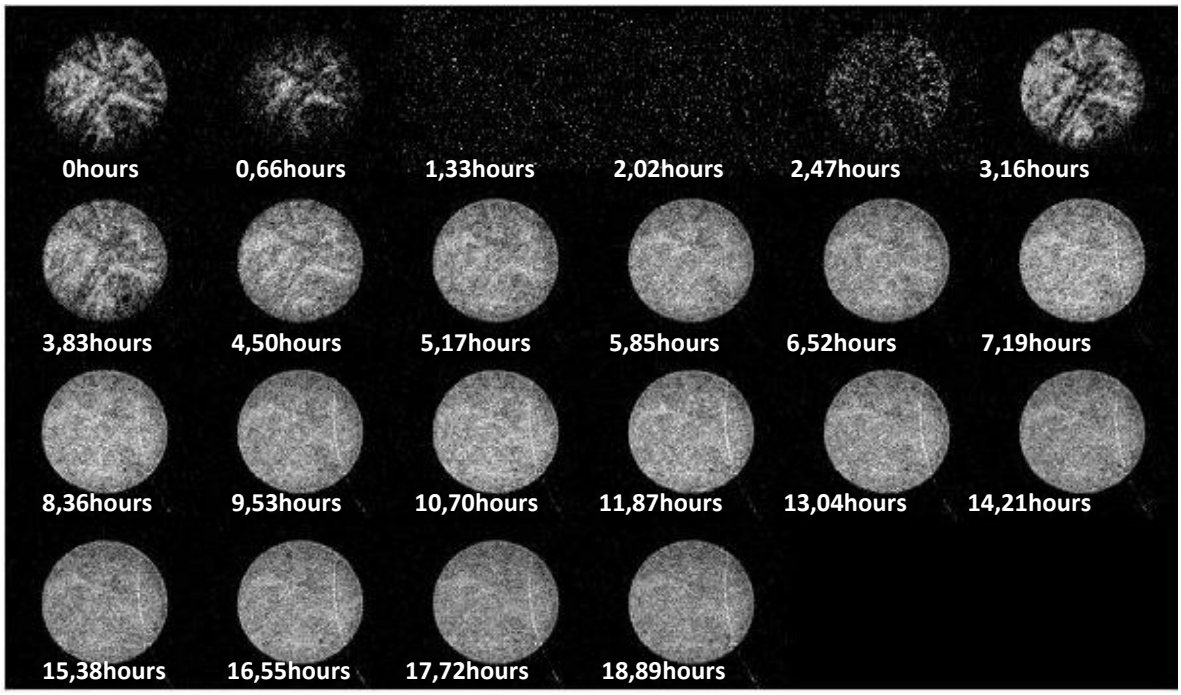

Figure 3.34 – RAREst images of the intensity development over time for slice 13 from sample 14. For this slice the importance of orientation becomes very clear as the tube cooling the fluorinert around the sample becomes visible as water condense on its surface.

The first images in figure 3.34 are recorded as the hydrates are re-forming, causing the sample to disappear from the RAREst images. The signals from the hydrogen nuclei within the THF hydrates are no longer recordable above the noise. After the air-coolers temperature is increased, the hydrates will start to dissociate. The crystal structure within the THF hydrates are visible from the coronal orientation. Crystal structures within the THF hydrate samples were not visible in the RAREst images from the melting experiments.

Figure 3.35 display the intensity development for each slice from sample 14 from the coronal orientation, after corrections for noise and the point in time where hydrate dissociation is completed are performed. Slices 1, 2, 14, 15 and 16 are not included here as they mainly consist of noise. As the THF hydrates are forming, the signal intensity is decreasing. When the THF hydrates dissociate the signal intensity increases again.

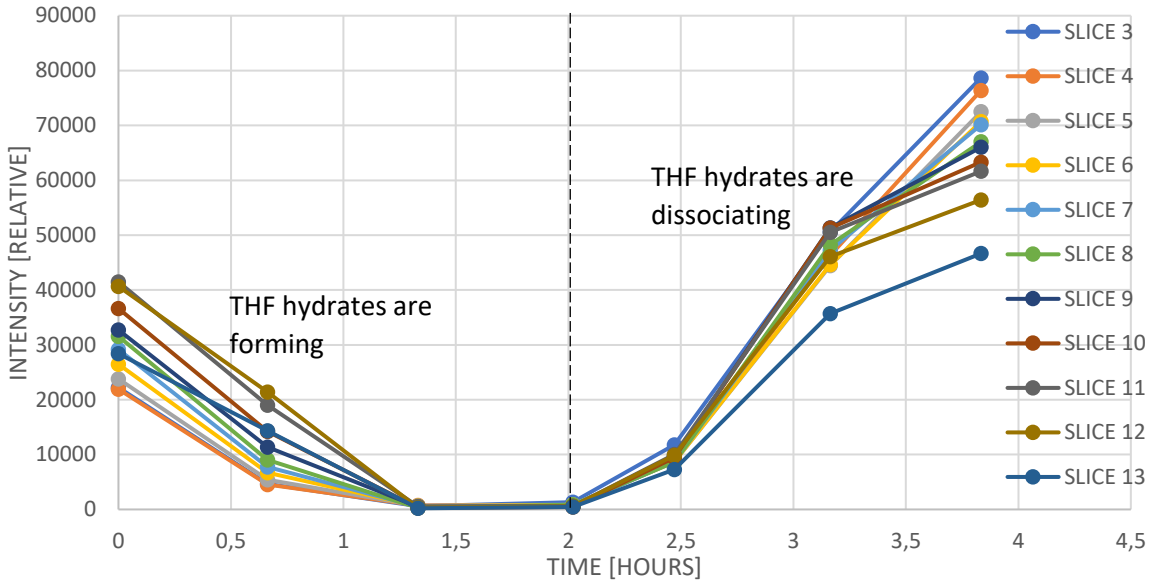

Figure 3.35 - Intensity development for each slice from the coronal orientation as a function of time, sample 14.

Figure 3.36 display the relative hydrate saturation as a function of time for each slice within sample 14. The saturation increases as the signal intensity is decreasing and hydrates are reforming. When the air-cooler is then set at a temperature above the melting point, the hydrates are dissociating, causing an increase in signal intensity and decrease in THF hydrate saturation within the slices.

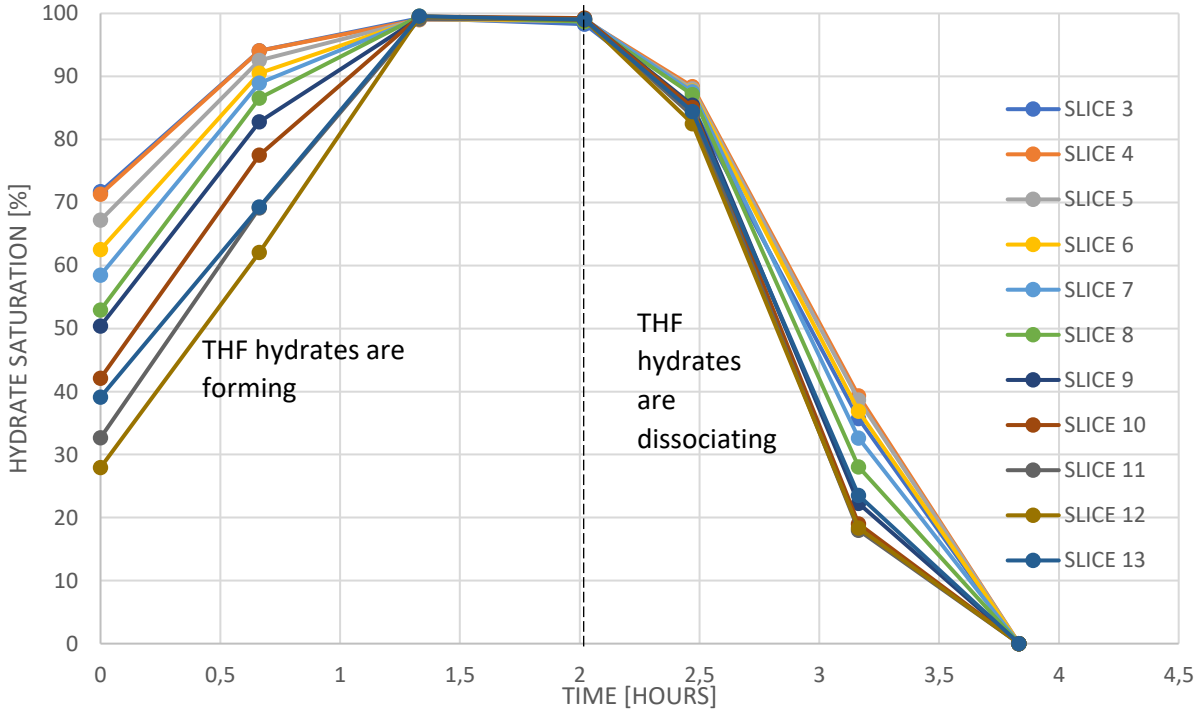

Figure 3.36 – Relative hydrate saturation for each slice from the coronal orientation as a function of time, sample 14.

Figure 3.37 display the signal intensity from figure 3.35, when all the slices are summarized to give one total signal intensity as a function of time. The signal intensity decreases as hydrates are forming, and increases as hydrates dissociate.

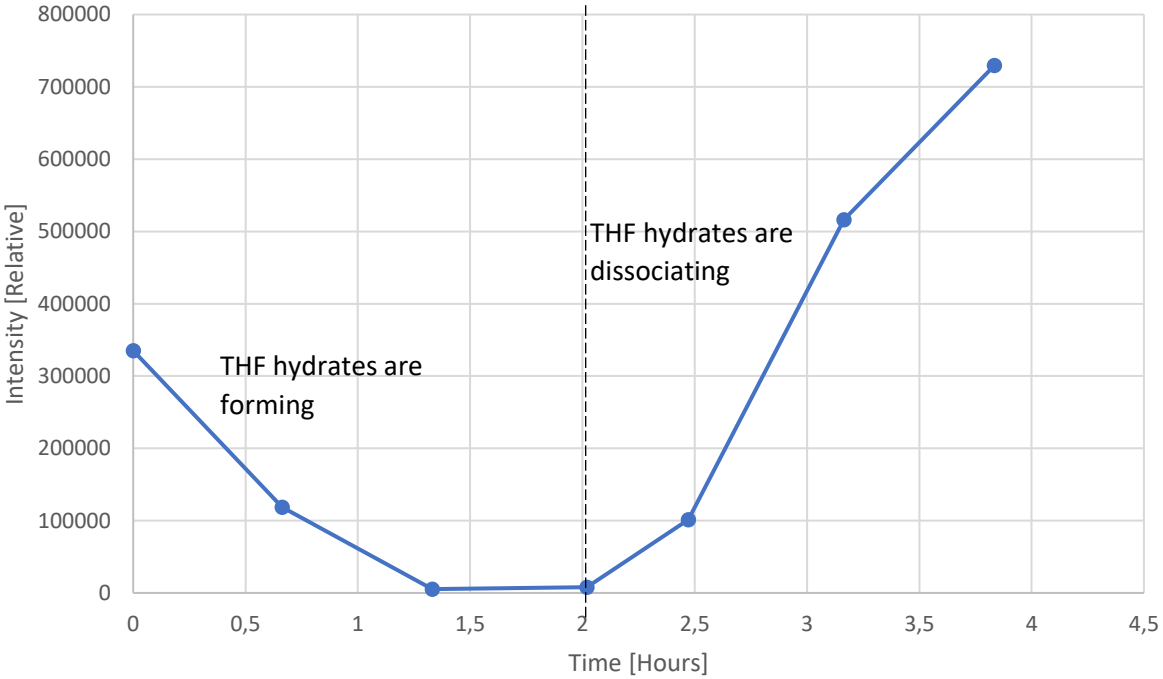

Figure 3.37 - Intensity development as a function of time for sample 14, from the coronal orientation. All slices summarized.

Figure 3.38 display the relative saturation of hydrates as a function of time. As the hydrates are forming there is an increase in relative hydrate saturation. As the hydrates are dissociating the relative hydrate saturation decreases.

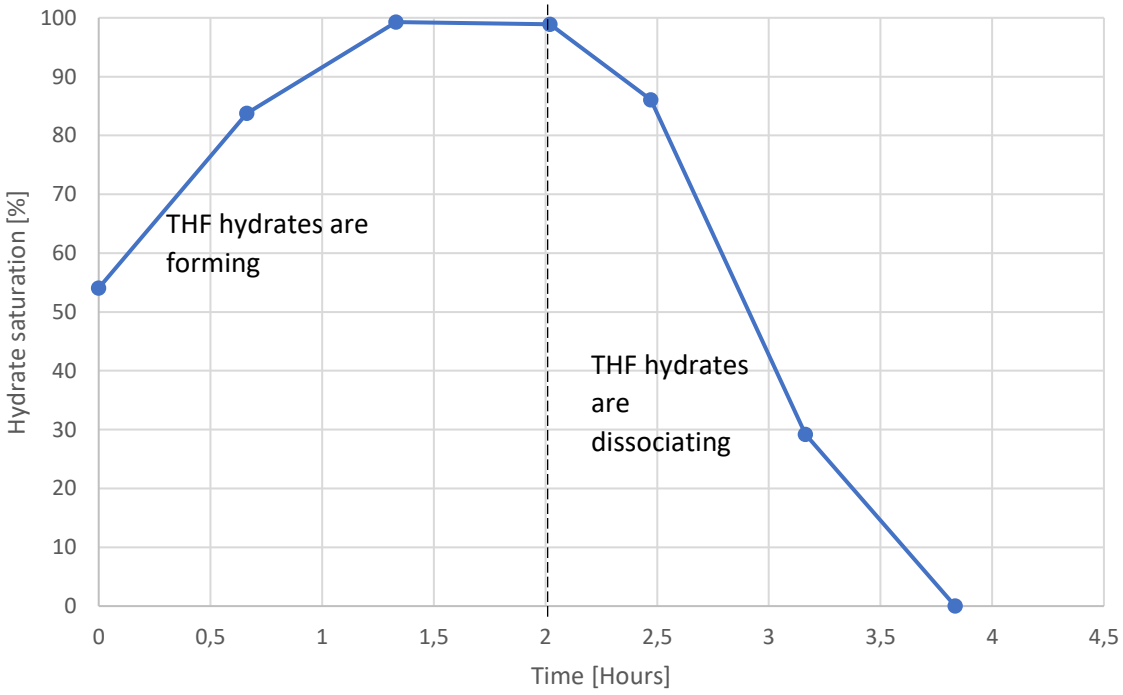

Figure 3.38 – Relative hydrate saturation as a function of time for sample 14 from the Coronal orientation. All slices summarized.

Figures 3.39 to 3.44 display corresponding data to that displayed in the figures 3.33 to 3.38, but now from the sagittal orientation. The major differences to notice is that the tube from the cooling setup is not as visible in this direction as it was in the coronal direction. In figures 3.39 and 3.40, the tube is only visible as a white dot above the sample, to the left in the RAREst images. The sagittal orientation is therefore preferable when it comes to considerations regarding the tube.

Figure 3.39 illustrates how sample 14, water-wet sand with the mixture 15:1 of H_2O and THF, is divided into 16 slices in the sagittal direction. Slices 1, 2 and 16 are included to illustrate that there is noise present, giving a constant background signal intensity.

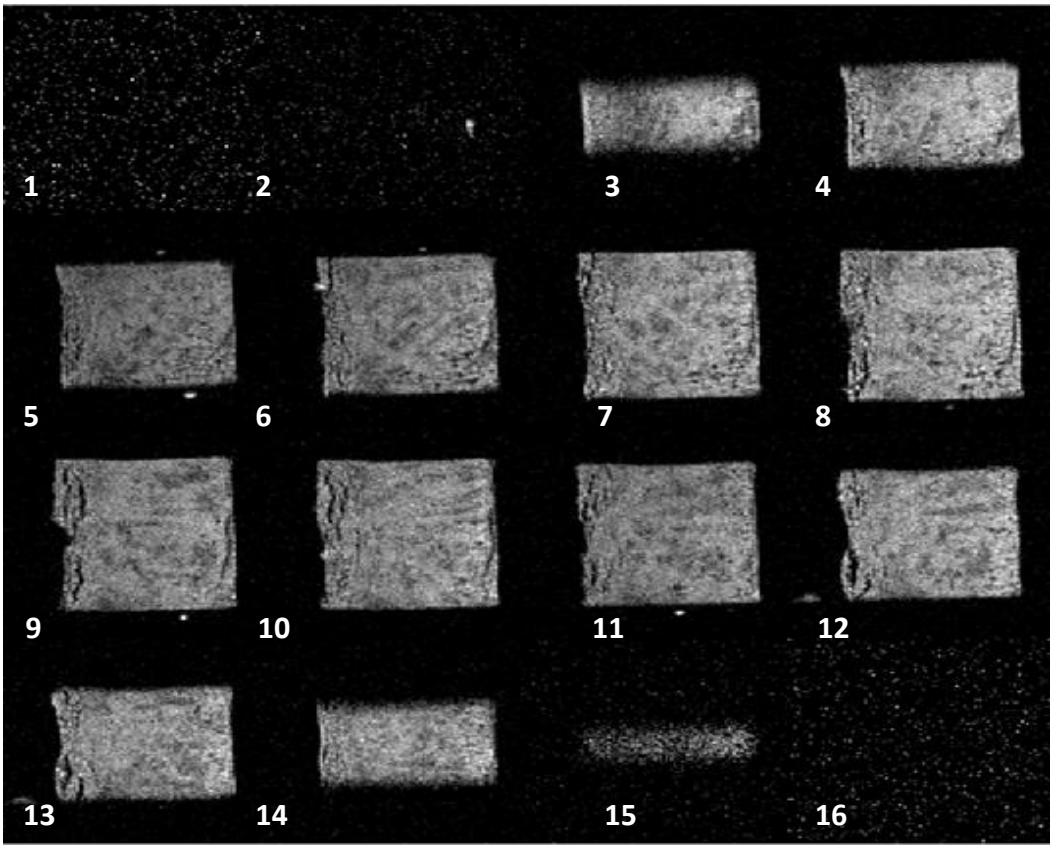

Figure 3.39 - Illustration of how sample 14, water-wet sand with the mixture of THF to H_2O 1:15, is divided into 16 slices of the sagittal orientation. These images are from the last scan, as 18,89hours have passed from the first RAREst scan.

Figure 3.40 displays the RAREst images of slice 13 from sample 14 as it melts over time. The tube surrounding the beaker with fluorinert is visible on the RAREst images, as a white dot above the top of the sample. As the air that flows through the tube is cooler than the surrounding air, water molecules will condense on its surface. The hydrogen nuclei in these water molecules will respond to the radio frequency waves from the MRI instrument.

The figure 3.40 display that the crystal structure is not as visible within the sample from this orientation as it was for the coronal orientation, but a pattern is present. The pattern seems to be more permanent from this orientation as it is present even after the THF hydrates have dissociated. The RAREst images of sample 14 recorded for the cooling experiments are the only images that display a crystal structure within the sand.

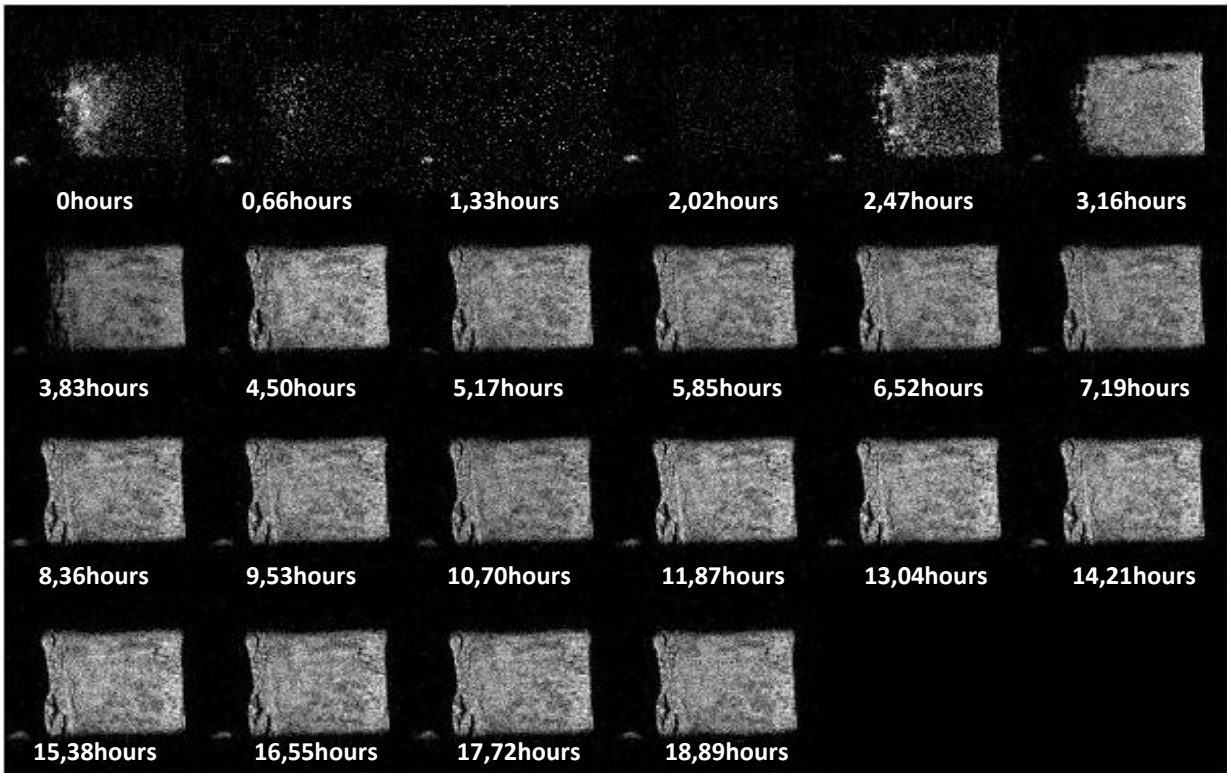

Figure 3.40 - RAREst images of the intensity development over time for slice 13 from sample 14 of the sagittal orientation. For this slice the importance of orientation becomes very clear as the tube cooling the fluorinert around the sample becomes visible as water condense on its surface.

Figure 3.41 display the intensity development in each slice as a function of time for sample 14 from the sagittal orientation, after correction for noise and point of complete hydrate dissociation. The signal intensity recorded from each slice is more distributed from the sagittal orientation. This is caused by the curvature of the sample glass, leaving a different amount of signal giving hydrogen nuclei within each slice. The signal intensity decreases as hydrates are forming and increases as hydrates are dissociating.

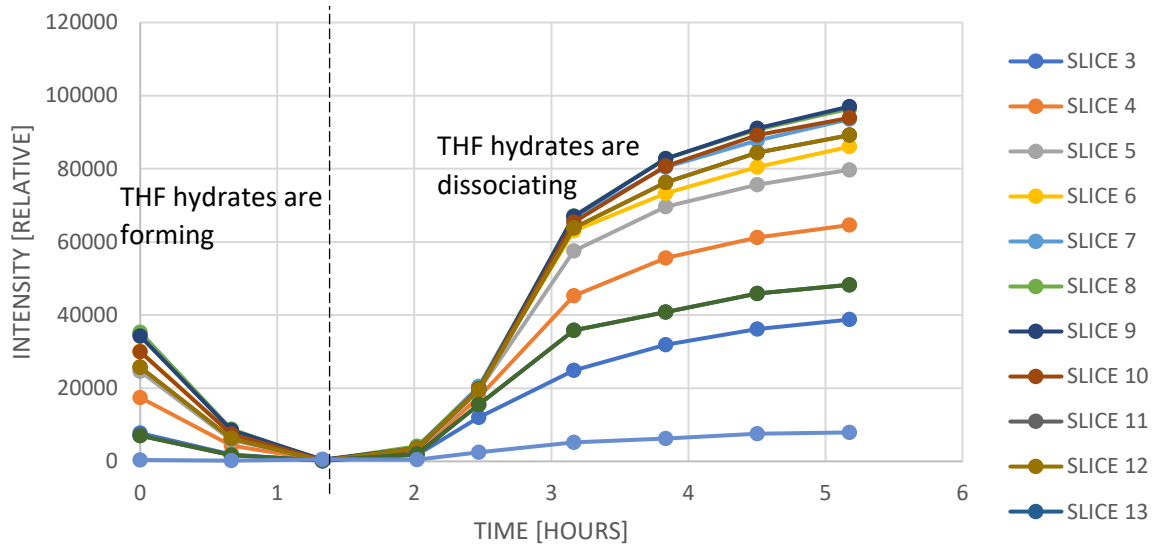

Figure 3.41 - Intensity development in each slice as a function of time, after noise is removed, from sagittal orientation for sample 14.

Figure 3.42 display the relative saturation of hydrates in each slice as a function of time for sample 14 from the sagittal orientation. The relative saturation of hydrates increases as hydrates are forming and decreases as hydrates are dissociating.

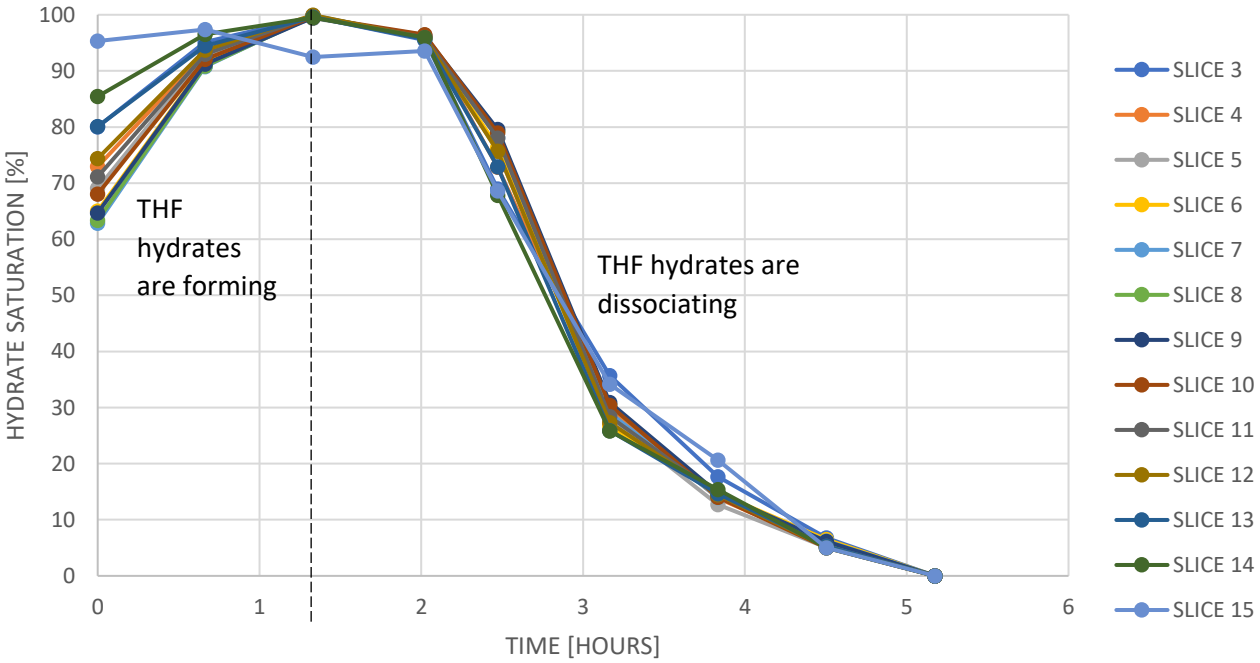

Figure 3.42 – Relative saturation of hydrates in each slice as a function of time for sample 14, from sagittal orientation.

Figure 3.43 displays the intensity development as a function of time for sample 14, from the sagittal orientation, as all slices are summarized, and after correction for noise and the point of complete dissociation are performed. As the RAREst scan cannot be performed in the two directions simultaneously the figures 3.37 and 3.43, portraying the same kind of data, will not be identical. The two different orientations will capture different points in time of the melting process. The relative saturation plots will hence not be equal either.

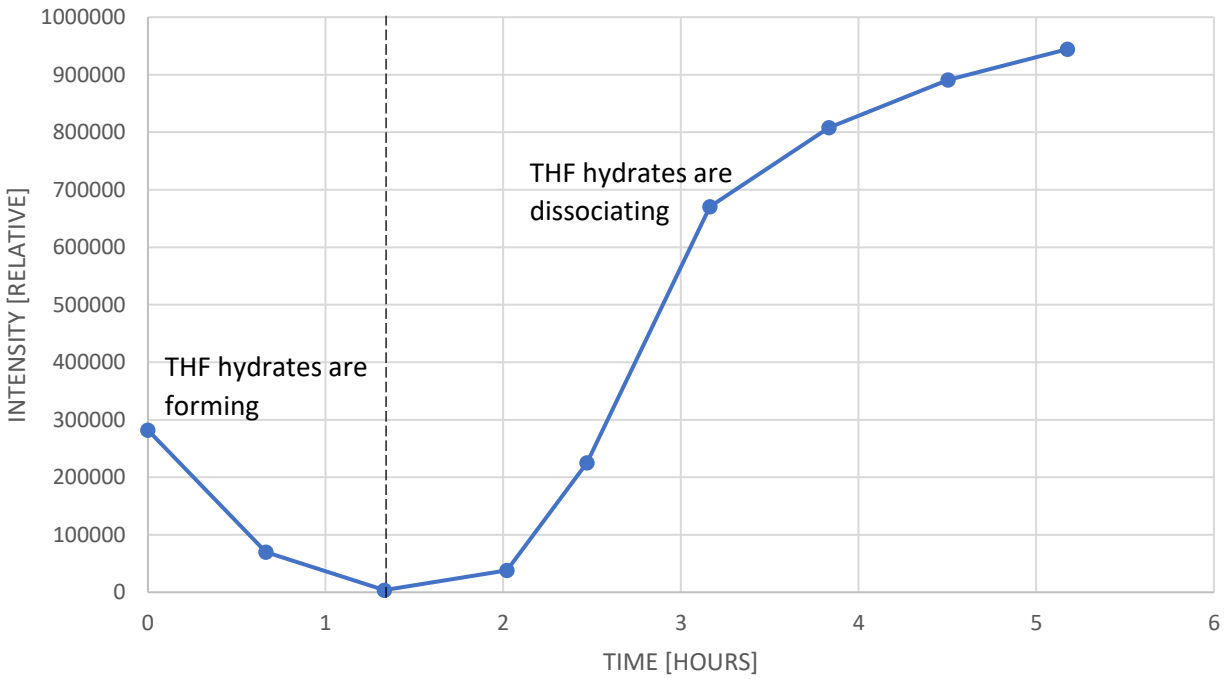

Figure 3.43 - Intensity development as a function of time for sample 14 from the sagittal orientation as all slices are summarized.

Figure 3.44 display the relative saturation of hydrates as a function of time for sample 14 as all the slices from the sagittal orientation are summarized. The relative saturation of hydrates increases as the hydrates are forming and the signal intensity decreases. As the hydrates are dissociating, and the signal intensity increases, the relative hydrate saturation will decrease.

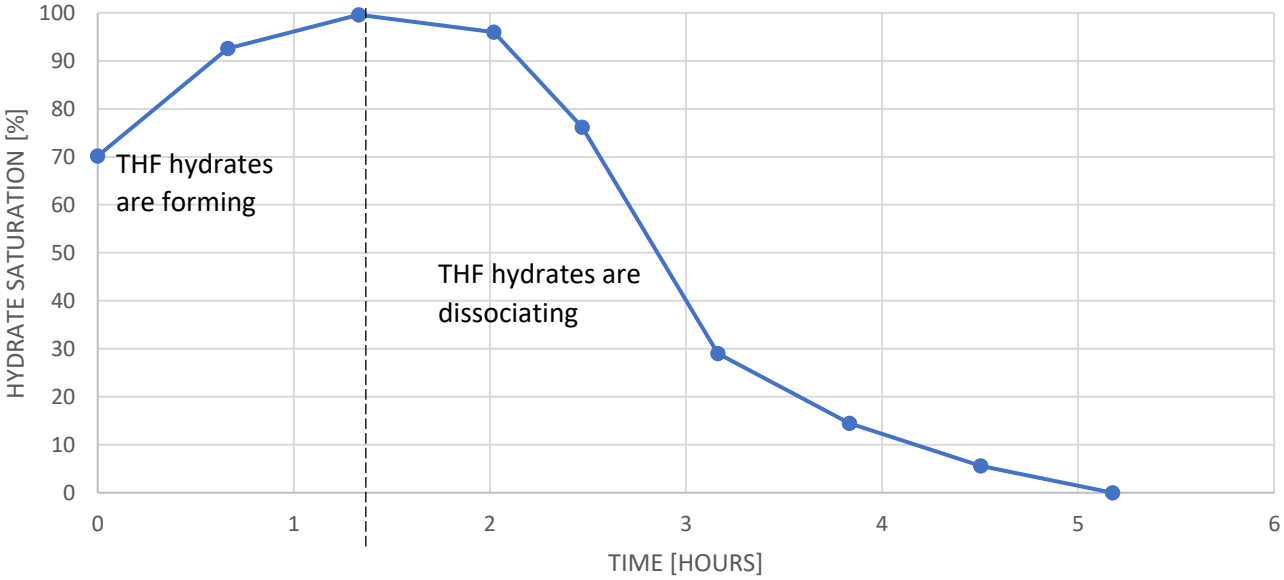

Figure 3.44 – Relative hydrate saturation development as a function of time for sample 14 from the sagittal orientation as all slices are summarized.

Figure 3.45 displays the intensity development for the formation and dissociation process of THF hydrates in sample 14, water-wet sand with the mixture 1:15 from the sagittal orientation. All the slices from sample 14 are summarized to represent the sample with a total value. The signal intensity decreases in the beginning of the experiment as hydrates are reforming. When no signal is detected above the background noise the temperature of the air cooler was increased to correspond to a temperature within the fluorinert of approximately 5°C. As the air-cooler was heating the fluorinert, the sample was heated simultaneously. The hydrates within the sample dissociated, resulting in an increasing signal intensity. The temperature of the system was set at a specific temperature and the previously recorded decrease of signal intensity, recorded for the other samples, was not recorded in this experiment.

The sample was left at a determined temperature for several hours after the dissociation of hydrates were complete. The result in figure 3.45 shows that the previously recorded decrease of signal intensity is caused by heating of the samples. This means that after all hydrogen nuclei that were present in solid form are transferred to a liquid state no further heating occurs. The melting temperature of sample 14 must be approximately 5°C.

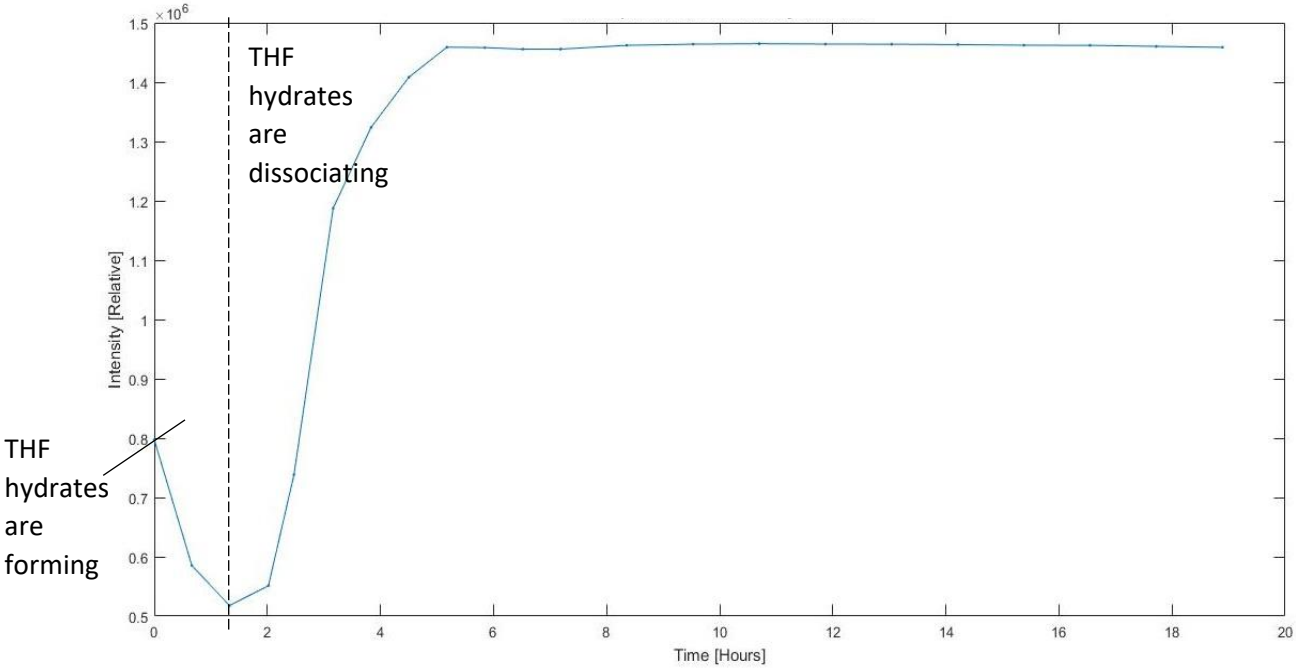

Figure 3.45 - Intensity development as a function of time for sample 14, water-wet sand with the mixture THF:H_2O 1:15, from the sagittal orientation. All slices are summarized to one total value of intensity development. The intensity decreases at first as the hydrates are re-forming, before dissociation occurs as the temperature in the fluorinert is quickly altered to approximately 5°C. After dissociation is complete the previously recorded decrease in intensity is not recorded here. The temperature is set at 5° and the sample is not heated further.

Sample 15, oil-wet sand with the mixture H_2O:THF 15:1

Figures 3.46 and 3.47 displays the RAREst images of slice 6 from sample 15 as it melts over time. The images are acquired in the sagittal orientation. For this experiment an additional layer of isolation was added around the tube of the cooling setup, to prevent water from condensing on its surface. This prevented the tube from being visible on the RAREst images, but upon visual inspection of the setup it was confirmed that water was still condensing on the tube.

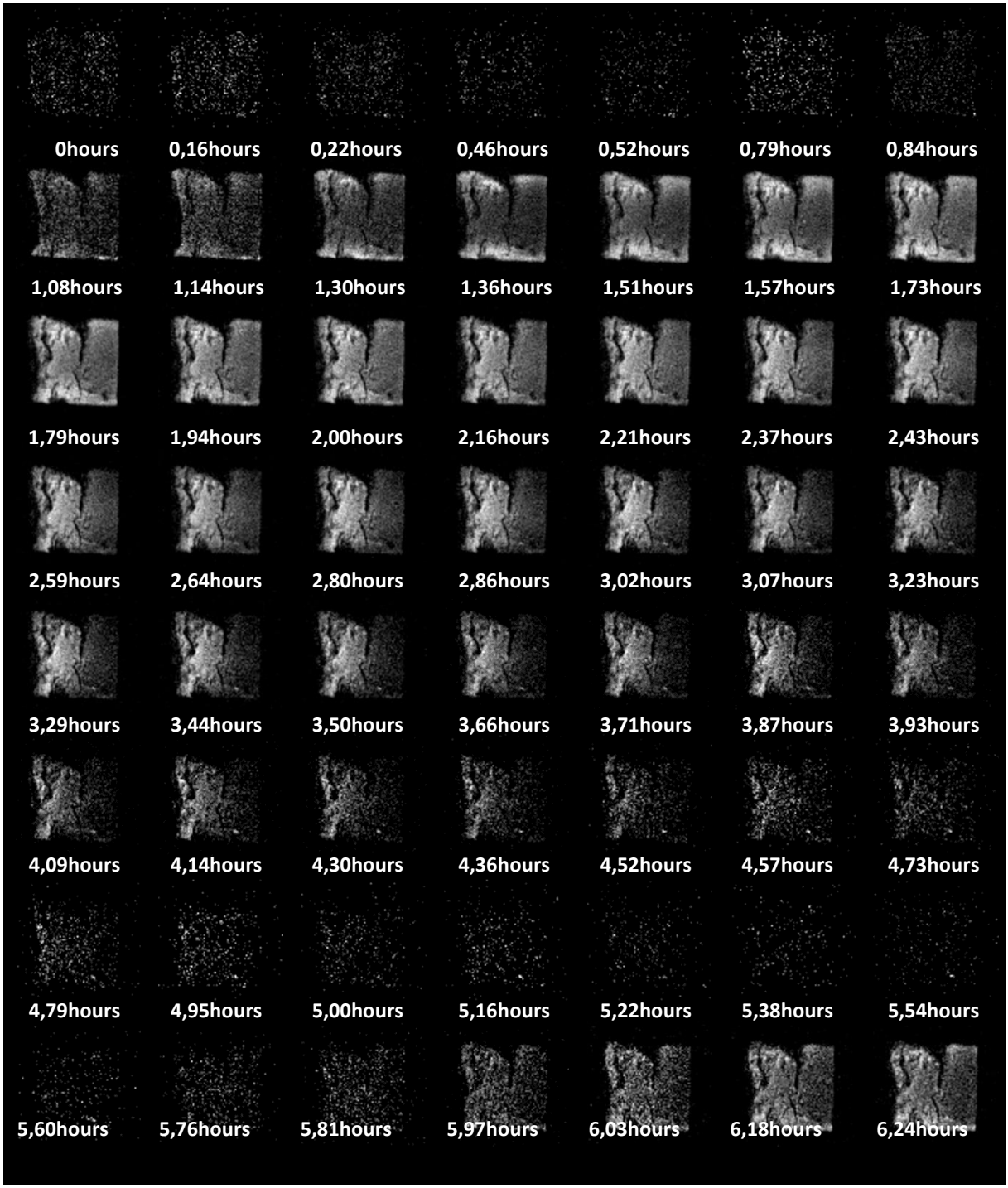

Figure 3.46 - Part one of RAREst images of sample 15, oil-wet sand with the mixture THF:H2O 1:15. The images display the signal intensity development over time for slice 6 from the sagittal orientation.

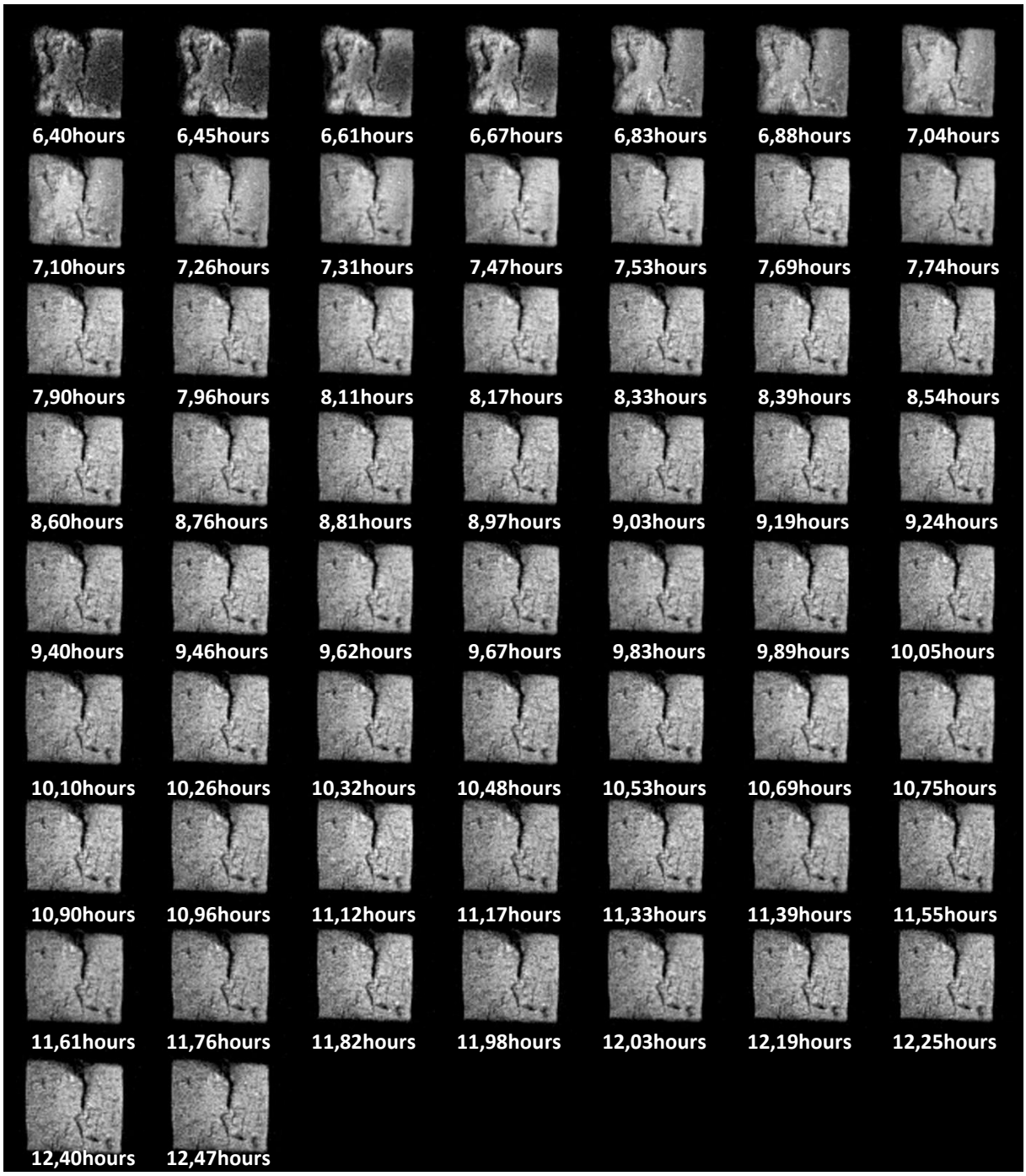

Figure 3.47 - Part two of RAREst images of sample 15, oil-wet sand with the mixture THF:H2O 1:15. The images display the signal intensity development over time for slice 6 from the sagittal orientation.

From the images in figures 3.46 and 3.47 the dissociation and formation of THF hydrates are clearly visible. The darker and grainy images, where the sample is not visible, illustrates when the THF hydrates have formed. As the hydrates dissociate the sample becomes visible, and the signal to noise ratio improves for the RAREst images.

Figure 3.48 illustrates how sample 15, oil-wet sand with the mixture 15:1 of H_2O and THF, is divided into 9 slices in the sagittal direction. Slices 1, and 9 are included to illustrate that there is noise present, giving a constant background signal intensity.

This sample contains several of visible cracks. The collapse of one these is even visualized in figure 3.47. The first image displays a larger black crack in the top of the sample. As time pass and the hydrates are dissociating the size of this crack decreases.

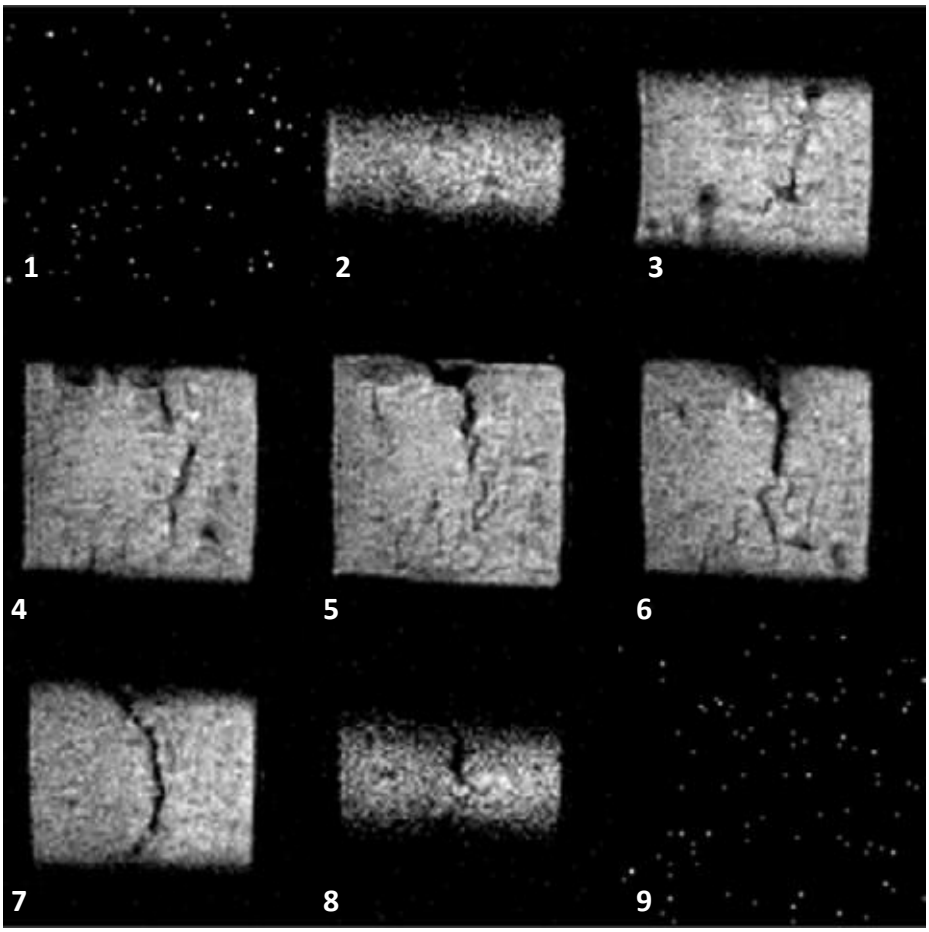

Figure 3.48 - Illustration of how sample 15, oil-wet sand with the mixture of THF to H_2O 1:15, is divided into 9 slices of the sagittal orientation. These images are from the last scan, as 12,47hours have passed from the first RAREst scan.

Figure 4.49 display the signal intensity in each slice as a function of time for sample 15. The corrections for noise and the point in time where the hydrate dissociation is completed have been performed on the data presented in this figure. Signal intensity increases as the hydrates are dissolving and decreases as they are re-forming. Sample 15 was placed within the fluorinert as the fluorinert was cooling. The air cooling setup was then completely turned off leaving the sample and fluorinert to be heated by the surrounding air. When the sample reappeared on the RAREst images the air cooler was turned back on, forcing the THF hydrates to reform. When the sample disappeared from the RAREst images the second time the air cooler was turned off again, leaving the fluorinert and sample to be heated by the surroundings once more.

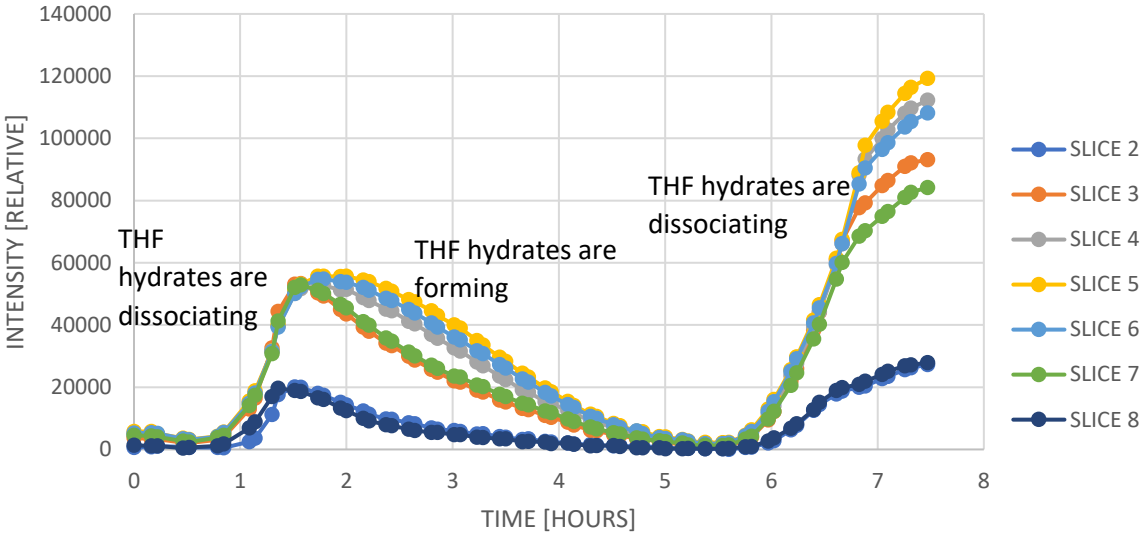

Figure 3.49 - Intensity development in each slice as a function of time for sample 15.

Figure 3.50 displays the relative saturation of hydrates in each slice as a function of time. The data were recorded from the sagittal orientation. The relative hydrate saturation is estimated from the data in figure 3.49 by formula (2.1). The saturation decreases as the fluorinert and the sample were heated by the surroundings. The air cooler is started again forcing the hydrates to reform and the saturation increases. When the signal completely disappears from the RAREst images the air cooler is completely shut off once more. The hydrates are dissociating as the fluorinert is heated by the surroundings, decreasing the hydrate saturation.

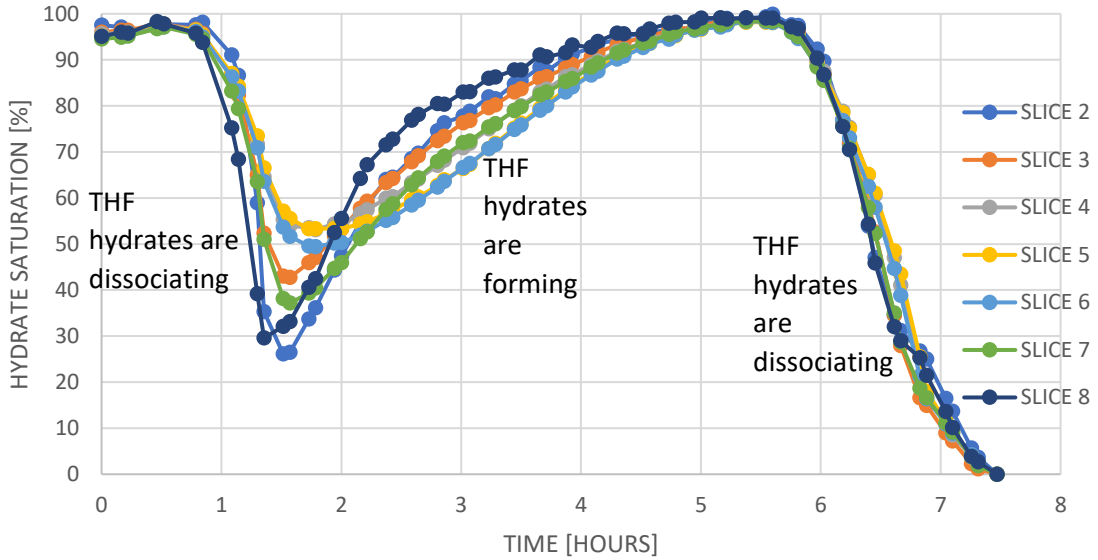

Figure 3.50 – Relative saturation of hydrates in each slice as a function of time for sample 15.

Figure 3.51 displays the intensity development as a function of time for sample 15 for all the slices summarized from the sagittal orientation. The intensity is corrected for noise and for the completion of the dissociation process of hydrates. The signal intensity increases as the hydrates dissociate, and decreases as hydrates form.

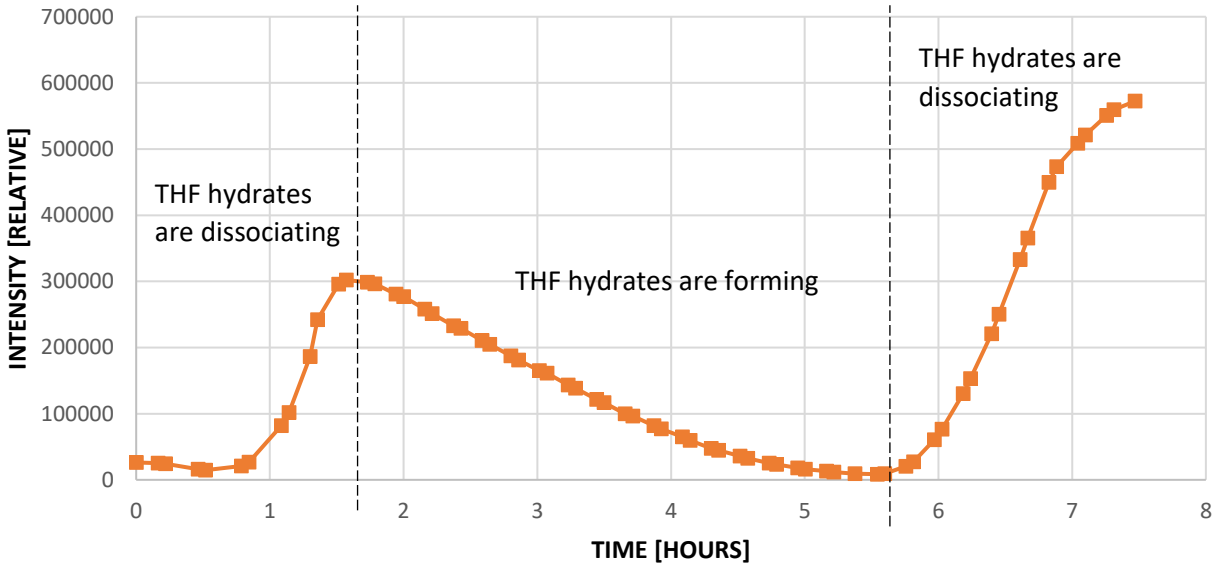

Figure 3.51 - Intensity development as a function of time for sample 15 as all slices are summarized and corrected for.

Figure 3.52 displays the development for relative saturation of hydrates from sample 15 as a function of time. The relative hydrate saturation decreases as hydrates are dissociating and increases as hydrates are forming.

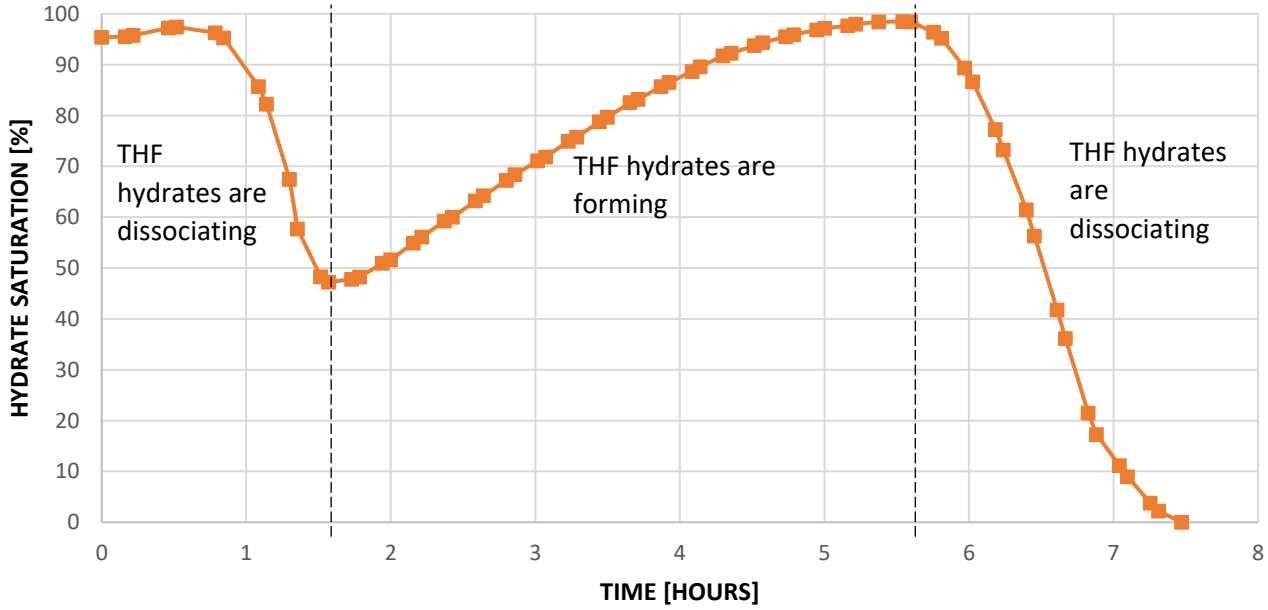

Figure 3.52 – Relative saturation of hydrates as a function of time for sample 15, when all slices are summarized and after correction for noise and the completion of the dissociation process of hydrates were performed.

3.4.2 CPMG Results

Sample 14, water-wet sand with the mixture H_2O:THF 15:1

The CPMG protocol was only applied on sample 14. Due to water condensing on the surface of the tube, an additional intensity occurred. It is not possible to choose a region of interest for the CPMG scan, so this additional intensity cannot be avoided. The decay curves for sample 14 are available in appendix A4, figures A4.0.17 and A4.0.18. Figure 3.53 shows the development as hydrates are forming in sample 14, while figure 3.54 displays the development as the hydrates are dissociating.

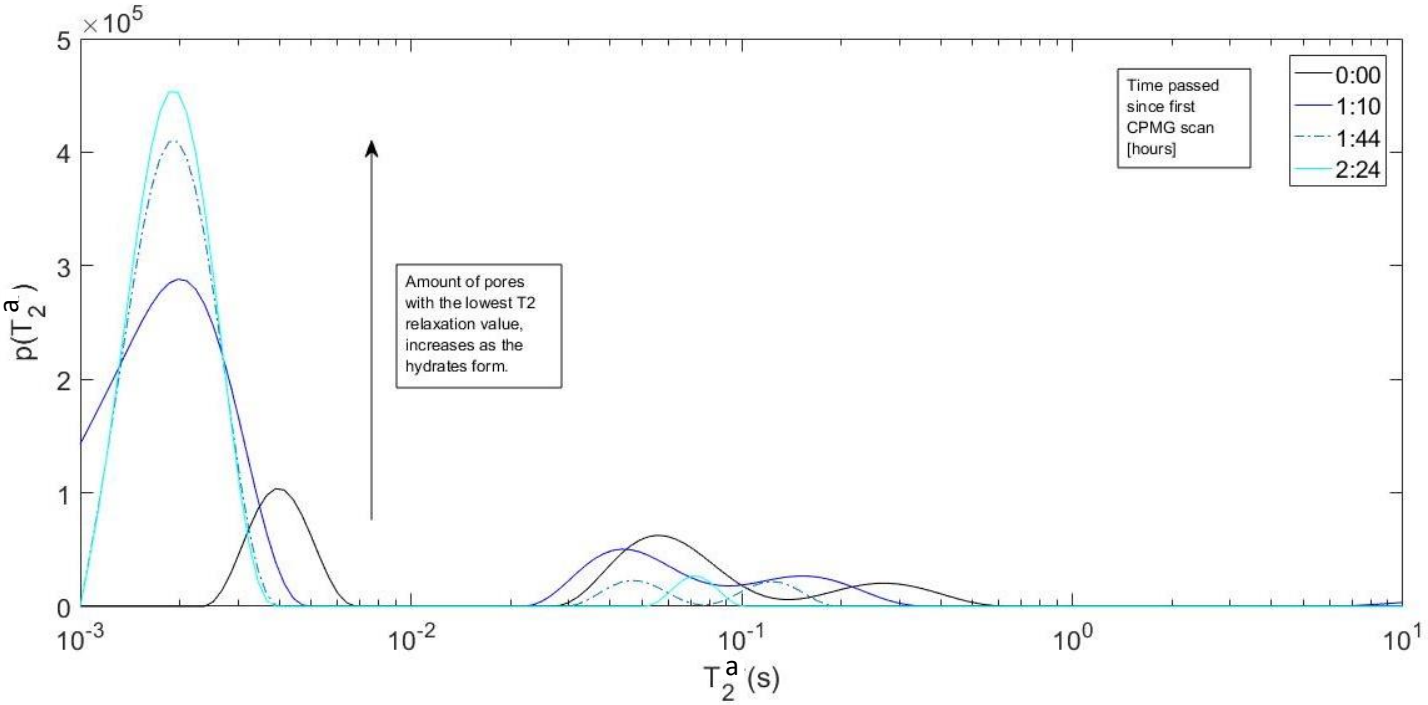

Figure 3.53 - T_2^a relaxation time distribution as hydrates are forming in sample 14.

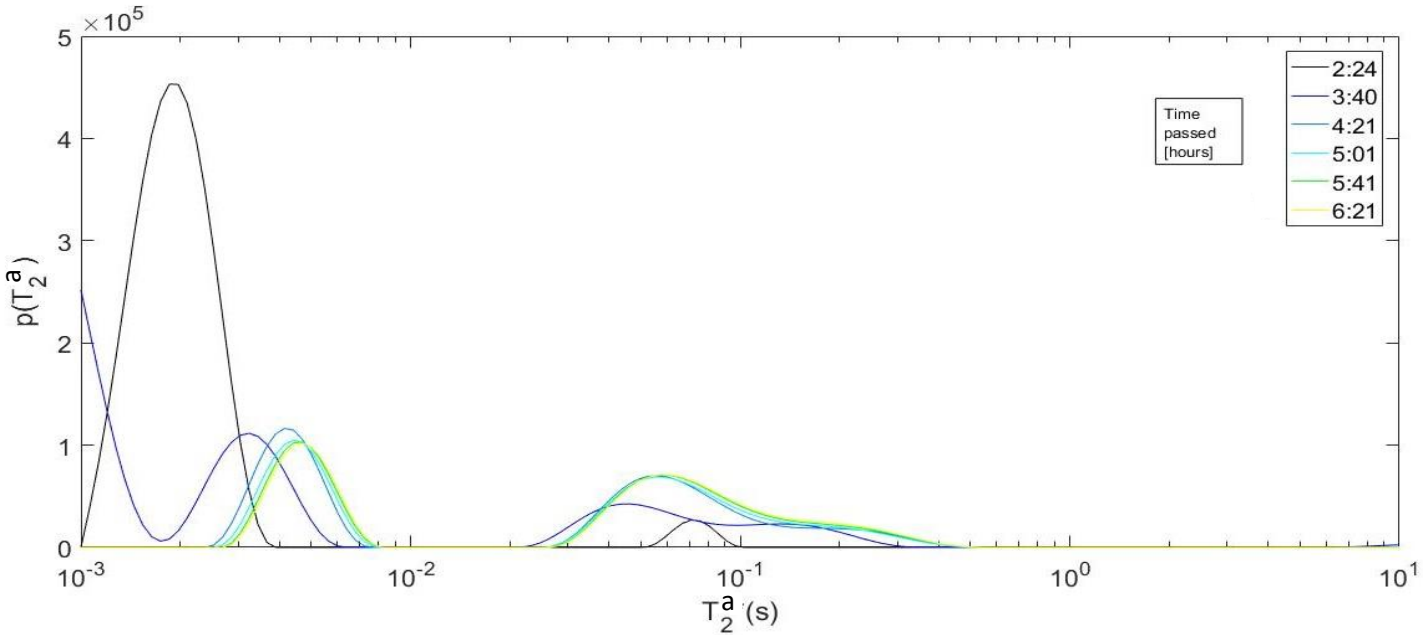

Figure 3.54 – T_2^a relaxation time distribution as the hydrates are dissociating in sample 14.

Peak values for the T_2^a relaxation time distribution from figure 3.53, the CPMG scans performed as the THF hydrates are forming, are displayed in table 3.9.

Table 3.9 - Peak values for the T_2^a relaxation time distribution from CPMG scan of sample 14 as the hydrates are reforming.

Time passed since first CPMG scan [hours:min]	Peak-value peak 1 [ms]	Peak-value peak 2 [ms]	Peak-value peak 3 [ms]
0:00	4,02	55,59	277,3
1:10	1,97	43,41	149,5
1:44	1,91	46,18	124,2
2:24	1,91	-	73,45

Peak values for the T_2^a relaxation time distribution from figure 3.54, the CPMG scans performed as the THF hydrates are dissociating, are displayed in table 3.10.

Table 3.10 - Peak values for the T_2^a relaxation time distribution from CPMG scan of sample 14 as the hydrates are dissociating.

Time passed since first CPMG scan [hours:min]	Peak-value peak 1 [ms]	Peak-value peak 2 [ms]	Peak-value peak 3 [ms]
2:24	1,91	-	73,45
3:40	3,24	44,80	149,5
4:21	4,14	55,59	216,6
5:01	4,41	59,13	216,6
5:41	4,69	59,13	216,6
6:21	4,69	59,13	216,6

Figure 3.53 shows that as the THF hydrates are forming, the T_2^a relaxation times are decreasing. Figure 3.54 displays that as the THF hydrates are dissociating the values are increasing. The distribution is however not similar to the distribution recorded in the melting experiments. No trends are visible. The tube from the cooling setup clearly affects the recorded signal. The resulting figures from these scans, are most likely not representative for the sample as there are additional water molecules present on the surface of the tube used for the cooling setup.

3.4.3 MSME Results

Sample 14, water-wet sand with the mixture H_2O:THF 15:1

Figure 3.55 displays the development of T_2^a relaxation time distribution as the hydrates are forming in sample 14, water-wet sand with the mixture THF:H_2O of 1:15, from the coronal orientation. Figure 3.56 displays the development of T_2^a relaxation time distribution as the hydrates are dissociating from the coronal orientation. The region of interest within this slice is displayed in figure A4.0.21 in appendix A4. The peak values for figure 3.55 are displayed in table 3.14, while peak values for figure 3.56 are displayed in table 3.15.

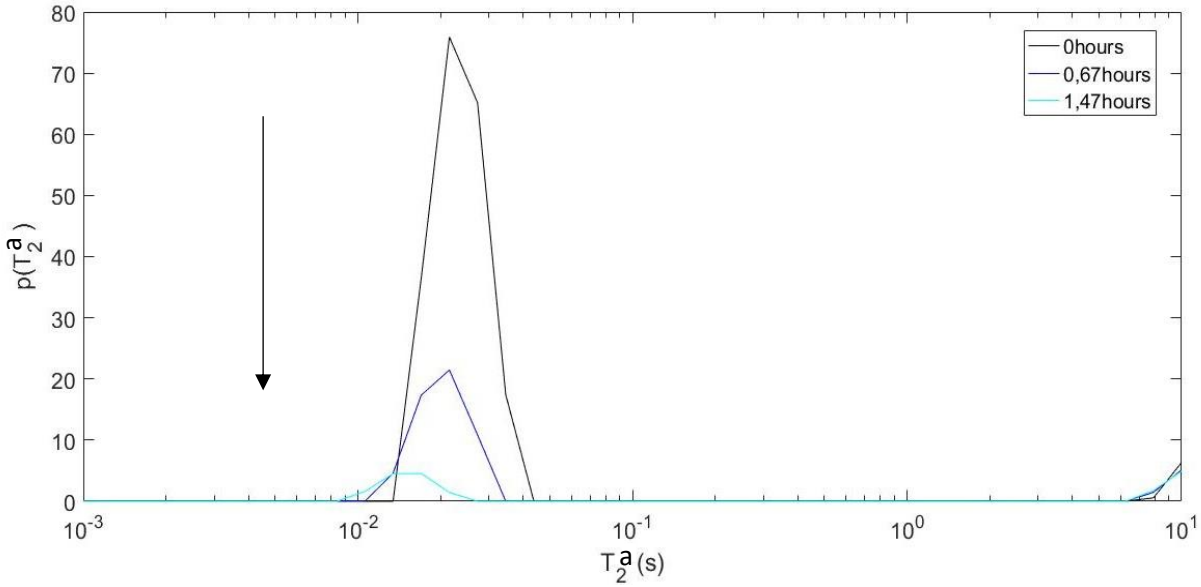

Figure 3.55 - T_2^a relaxation time distribution as hydrate forms, from the coronal orientation of sample 14. The development of the peak follows the direction of the arrow.

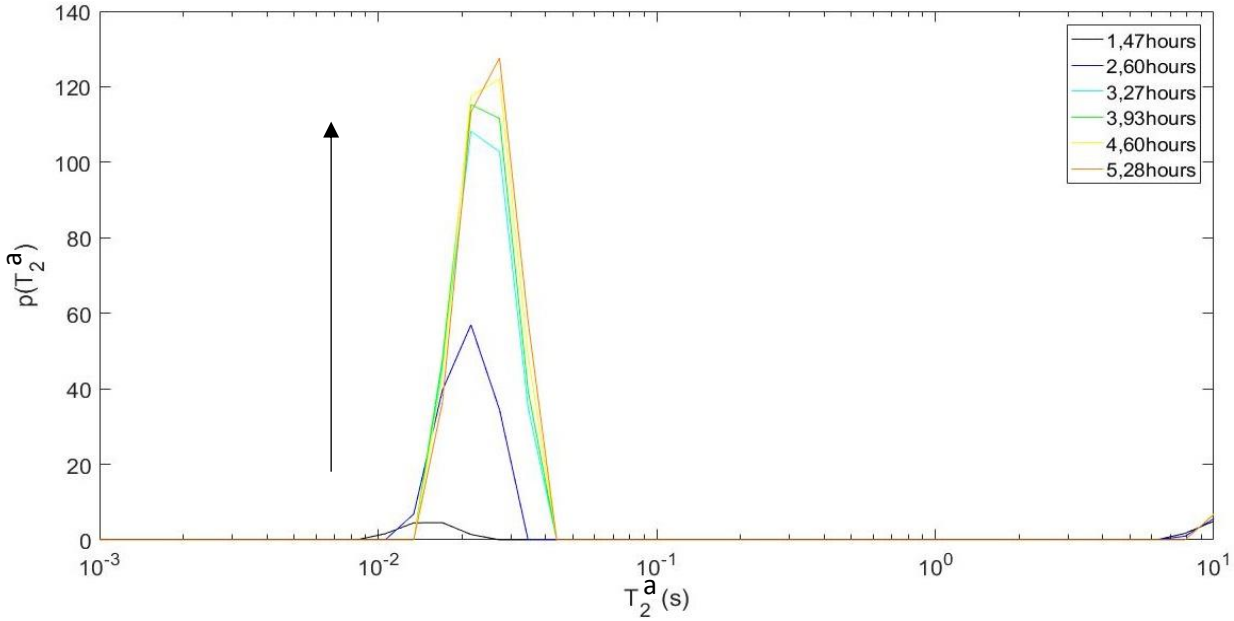

Figure 3.56 - T_2^a relaxation time distribution as hydrate melts, from the coronal orientation of sample 14. The development of the peak follows the direction of the arrow.

Figure 3.57 displays the development of T_2^a relaxation time distribution as the hydrates are forming in sample 14, from the sagittal orientation. Figure 3.58 displays the development of T_2^a relaxation time distribution as the hydrates are dissociating from the coronal orientation. The region of interest within this slice is displayed in figure A4.0.20 in appendix A4. The peak values for figure 3.57 are displayed in table 3.14, while peak values for figure 3.58 are displayed in table 3.15.

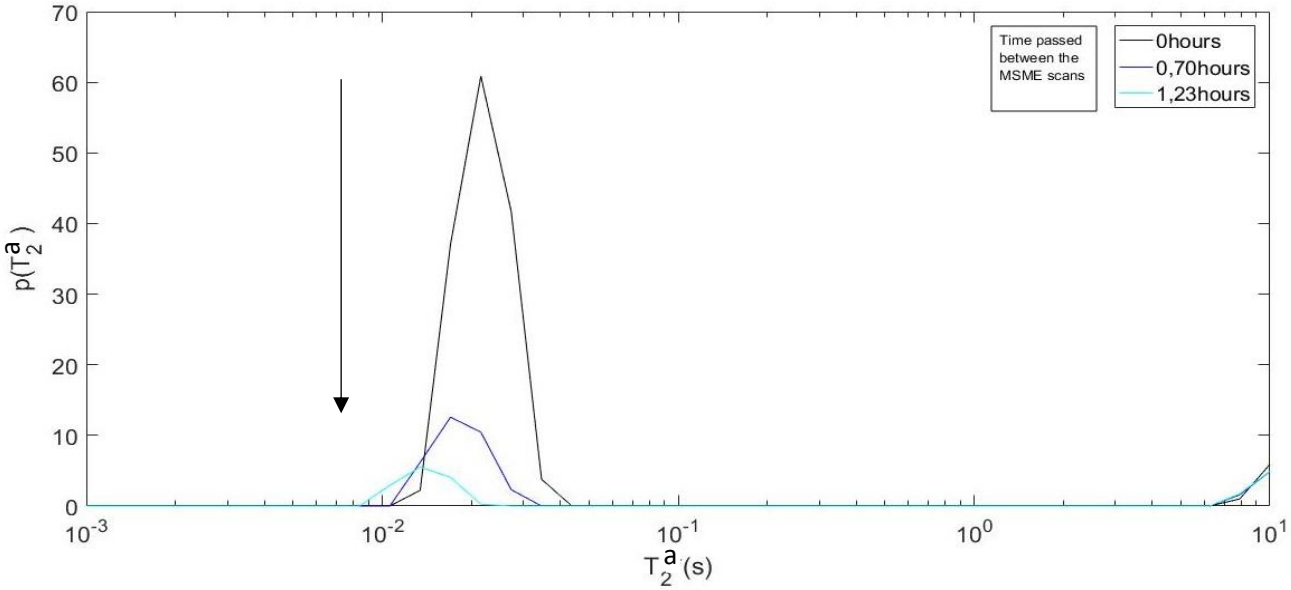

Figure 3.57 – T_2^a relaxation time distribution as hydrates are forming, from the sagittal orientation of sample 14. The development of the peak follows the direction of the arrow.

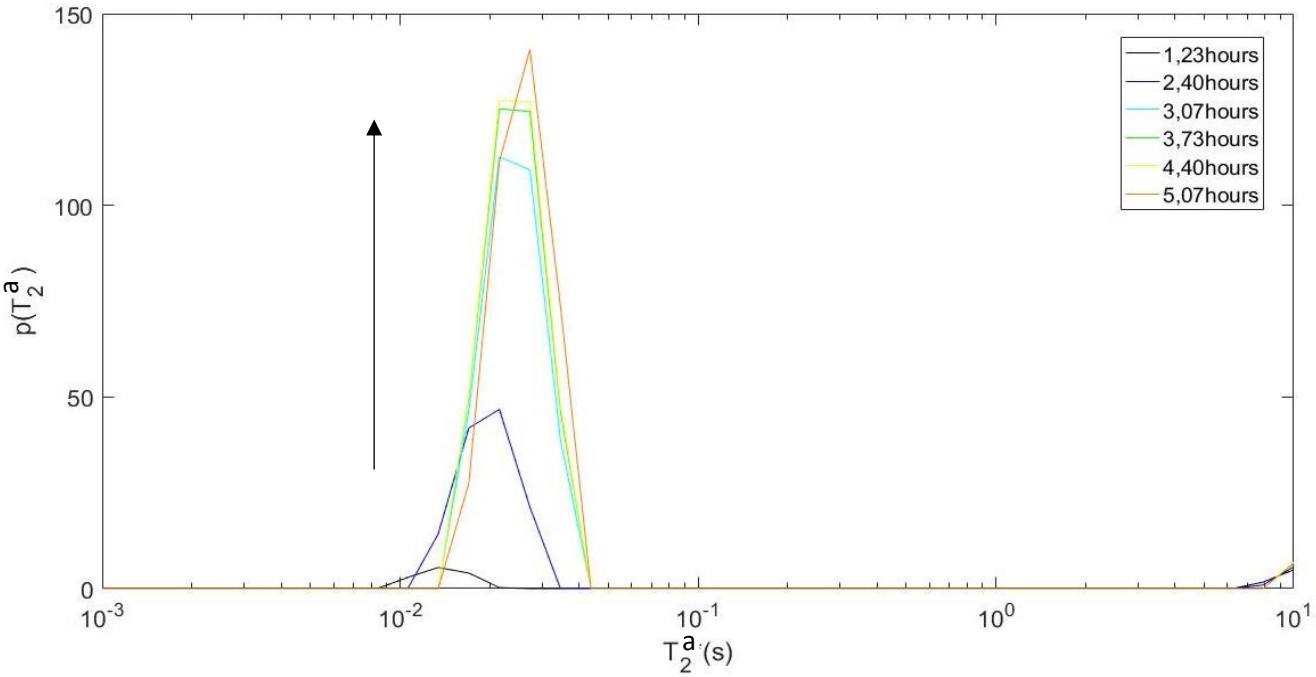

Figure 3.58 - T_2^a relaxation time distribution as hydrates are melting, from the sagittal orientation of sample 14. The development of the peak follows the direction of the arrow.

Peak values from the T_2^a relaxation time distribution in figures 3.55 and 3.57, as the hydrates are forming are given in table 3.11.

Table 3.11 - Peak T_2^a relaxation time values as the hydrate forms, water-wet sand with the mixture THF:H_2O 1:15.

Time passed since first MSME scan [hours]	ROI	T2 ParaVision Coronal [ms]	1 std	ILT Coronal [ms]	Time passed since first MSME scan [hours]	ROI	T2 ParaVision Sagittal [ms]	1 std	ILT Sagittal [ms]
0	0,26	23,7	0,5	21,0	0	0,26	22,3	0,5	21,7
0,67	0,26	20,7	1,0	21,0	0,70	0,26	18,8	1,2	17,0
1,47	0,26	15,9	2,3	17,0	1,23	0,26	14,6	2,3	13,7

Peak values from the T_2^a relaxation time distribution in figures 3.56 and 3.58, as the hydrates are dissociating are given in table 3.12.

Table 3.12 - Peak T_2^a relaxation time values as the hydrate melts, water-wet sand with the mixture THF:H_2O 1:15.

Time passed since first MSME scan [hours]	ROI	T2 ParaVision Coronal	1 std	ILT Coronal	Time passed since first MSME scan [hours]	ROI	T2 ParaVision Sagittal	1 std	ILT Sagittal
1,47	0,26	15,9	2,3	17,0	1,23	0,26	14,6	2,3	13,7
2,60	0,26	21,3	0,6	21,7	2,40	0,26	20,1	0,7	21,7
3,27	0,26	24,3	0,5	21,7	3,07	0,26	24,5	0,5	21,0
3,93	0,26	24,5	0,4	21,7	3,73	0,26	24,6	0,5	22,3
4,60	0,26	24,9	0,5	26,8	4,40	0,26	24,7	0,5	24,5
5,28	0,26	25,4	0,5	26,8	5,07	0,26	26,1	0,5	26,8

The T_2^a relaxation time distribution from the two orientations show similar developments. As the hydrates are forming, the peak T_2^a relaxation time is decreasing in value and in density. As the hydrates are dissociating, the peak T_2^a relaxation time is increasing in value and in density. As more hydrogen nuclei are present in fluid state, there are more hydrogen nuclei present to perform measurements on, and the density T_2^a relaxation time will increase. There is a difference in the recorded T_2^a relaxation time caused by the orientation of the MSME scan. This could be simply caused by the fact that the region of interests are different, so an equal average value T_2^a relaxation time cannot be estimated, as it is not the same region that is investigated.

Sample 15, oil-wet sand with the mixture H_2O:THF 15:1

Figure 3.59 displays the development of T_2^a relaxation time distribution as the THF hydrates are dissociating in sample 15. The region of interest is illustrated in figure A4.0.23 in appendix A4. The peak values are displayed in table 3.13.

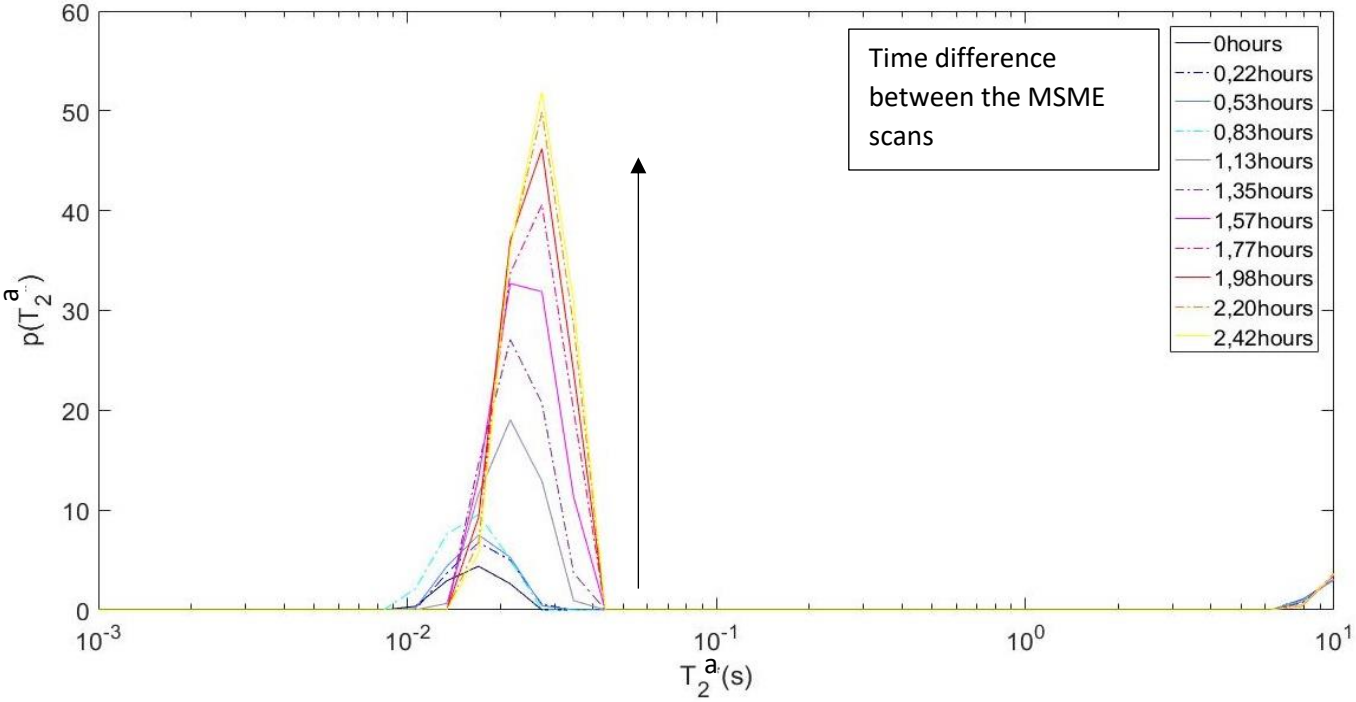

Figure 3.59 – The T_2^a relaxation time distribution as hydrate is melting in sample 15. The development of the peak follows the direction of the arrow.

Table 3.13 – Peak-values for T_2^a relaxation times for the oil-wet sand with a mixture 15:1 as the hydrate partially melts.

Time passed from the first MSME scan [hours]	T_{2a} value from ParaVision [ms]	1 std	ROI	T_2^a from ILT [ms]
0	17,9	1,3	0,26	16,95
0,22	18,2	1,7	0,26	16,95
0,53	17,3	2,4	0,26	16,95
0,83	16,5	1,1	0,26	16,95
1,13	22,2	1,0	0,26	21,65
1,35	23,1	0,8	0,26	21,65
1,57	24,5	0,7	0,26	22,33
1,77	25,8	0,6	0,26	26,83
1,98	26,1	0,6	0,26	27,66
2,20	26,6	0,6	0,26	26,83
2,42	26,9	0,7	0,26	26,83

Figure 3.60 displays the development of T_2^a relaxation time distribution as the hydrates are forming. The peak values are displayed in table 3.14.

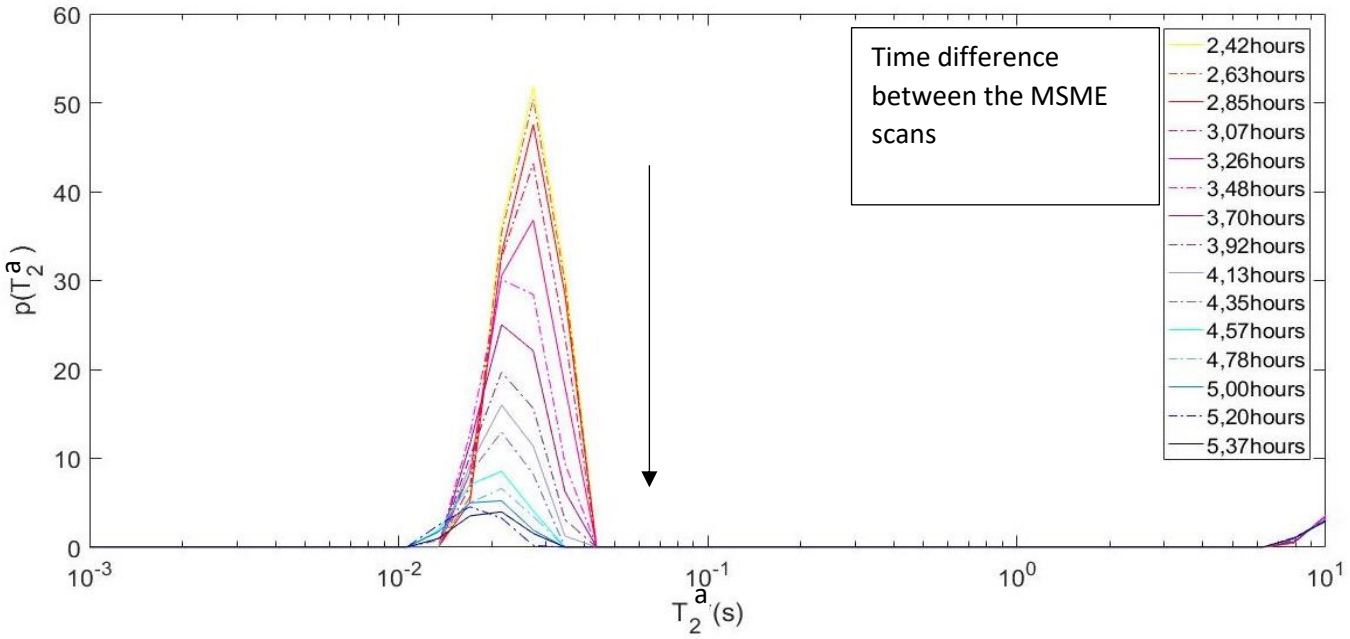

Figure 3.60 - T_2^a relaxation time distribution for oil-wet sand with the mixture THF:H_2O 1:15, as hydrates form within the MRI instrument. The development of the peak follows the direction of the arrow.

Table 3.14 – Peak-values for T_2^a relaxation time values for oil-wet sand with a mixture 15:1 as the hydrates grow back.

Time passed from the first MSME scan [hours]	T_2^a value from ParaVision [ms]	1 std	ROI	T2 from ILT [ms]
2,42	26,9	0,7	0,26	26,83
2,63	26,9	0,7	0,26	26,83
2,85	26,9	0,7	0,26	27,66
3,07	26,4	0,6	0,26	27,66
3,26	25,8	0,7	0,26	27,66
3,48	24,3	0,6	0,26	21,65
3,70	23,9	0,8	0,26	21,65
3,92	23,3	0,8	0,26	21,65
4,13	22,7	0,9	0,26	21,65
4,35	21,8	1,3	0,26	21,65
4,57	20,6	1,4	0,26	21,00
4,78	21,1	1,3	0,26	21,65
5,00	20,0	1,5	0,26	21,65
5,20	18,1	1,9	0,26	17,48
5,37	20,4	2,0	0,26	21,00

Figure 3.61 displays the development of T_2^a relaxation time distribution as the hydrates are dissociating the final time. The peak values are displayed in table 3.15.

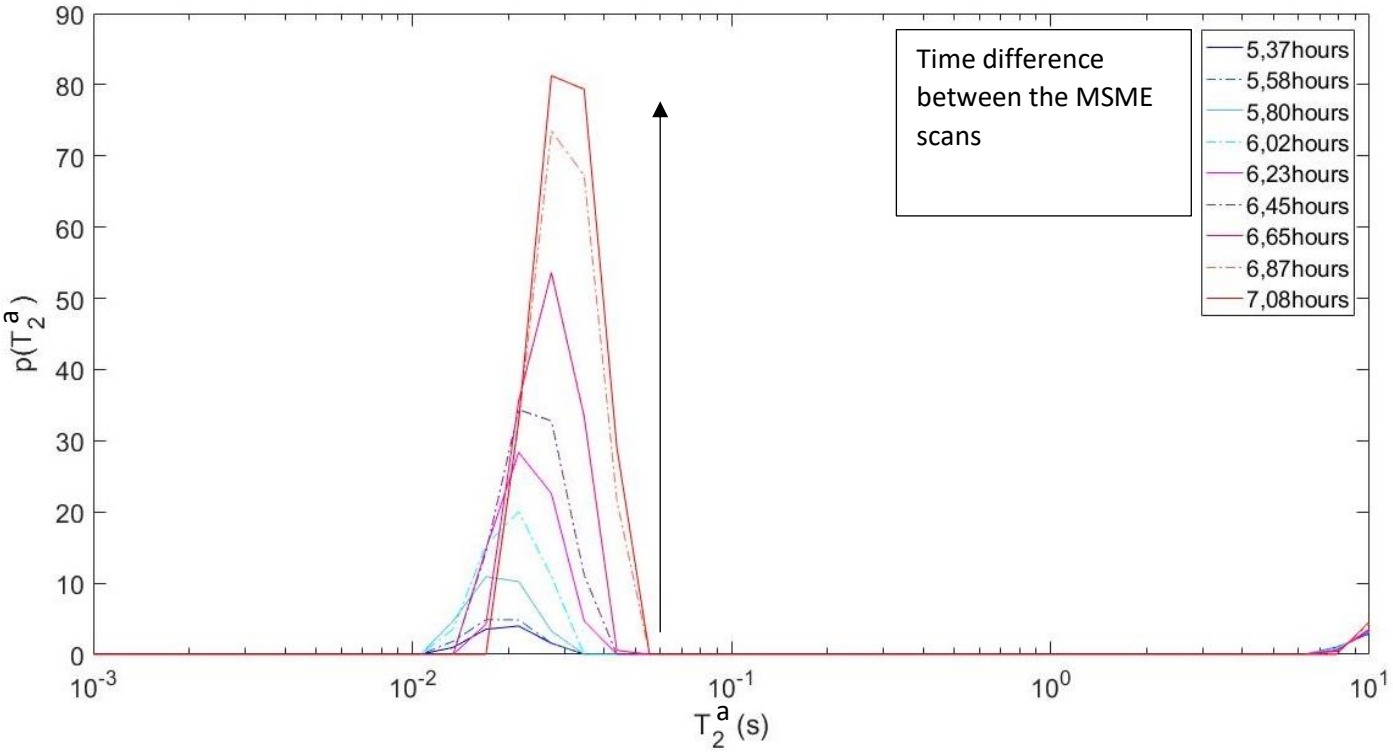

Figure 3.61 - T_2^a relaxation time distribution for oil-wet sand with the mixture THF:H_2O 1:15, as hydrates are melting. The development of the peak follows the direction of the arrow.

Table 3.15 - Peak T_2^a relaxation time values for oil-wet sand with a mixture THF:H_2O 1:15 as the hydrate melts the second time.

Time passed from the first MSME scan [hours]	T_2^a value from ParaVision [ms]	1 std	ROI	T2 from ILT [ms]
5,37	20,4	2,0	0,26	21,00
5,58	19,7	1,7	0,26	17,48
5,80	19,3	1,1	0,26	17,48
6,02	20,9	0,8	0,26	21,00
6,23	23,3	0,7	0,26	21,65
6,45	24,4	0,7	0,26	22,33
6,65	27,2	0,6	0,26	27,66
6,87	30,4	0,9	0,26	27,66
7,08	30,9	0,8	0,26	27,66

From figures 3.59 to 3.61 and tables 3.13 to 3.15, it is rather clear that as hydrates are forming within a porous medium, the recorded T_2^a relaxation time distribution will decrease. The density and the peak value for the T_2^a relaxation times that are recorded as hydrates are forming decreases. As the hydrates dissociate this trend is the complete opposite. As hydrates are melting the density of the T_2^a relaxation times will increase, and the peak value of the T_2^a relaxation time will also increase. By monitoring the T_2^a relaxation time distribution one can clearly tell weather hydrates are forming or dissociating within a sample.

4 Discussion

This chapter features a discussion regarding results presented in chapter 3, and the MRI protocols used to obtain them. The discussion is divided into 4 subchapters; one for each MRI protocol and one for the importance of temperature control.

4.1 RAREst Protocol and Relative Hydrate Saturation

The RAREst protocol creates images by recording the signal intensity given from hydrogen nuclei situated within the sample that is being examined. The signal is encoded based on positioning within the sample which results in a direct image showing where hydrogen nuclei are present. The imaging technique gives the opportunity divide the item into several slices of optional orientation. This makes it possible to view how fluids interact with the porous media. Darker images represent lower recorded signal intensities and brighter images represent higher recorded signal intensities.

The significance of the orientation of the images is illustrated by the results in chapter 3. There are clear differences in the brightness scale when images are recorded in the coronal and sagittal orientation as they capture different parts of the sample. Details that are visible in one orientation, might not be visible from the other orientation. For determining the orientation of the images, the system that is being examined must be considered. Though time consuming it might be useful to try several orientations before deciding what orientation that provides the best result. By choosing the sagittal orientation for the cooling experiments the appearance of the tube was avoided. For the sand experiments the interaction between the fluids and the porous media was displayed better from the coronal orientation. The axial orientation was not used for images included in this thesis.

The dependency on signal intensity for the RAREst images is significant. When hydrates are formed the hydrogen nuclei that are present exist in solid state. Hydrogen nuclei situated within water in a solid phase will not give a detectable signal when exposed to radio frequency waves. The samples will therefore not be detectable with RAREst images. As hydrates are dissociating, converting hydrogen nuclei into a liquid state, the recorded signal intensity will increase. When there is a significant development in the signal intensity response, RAREst images are useful to record this change.

As the hydrates were placed under room temperature the cause of the dissociation process was heat transfer from the surroundings. This is visible in the RAREst images of hydrates dissociating, found in subchapter 3.3.1. The samples all started the melting process from the outer edges of the sample and ended in the middle of the sample. When all hydrates had dissociated the samples continued to be heated towards room temperature.

The signal intensity from the RAREst images were plotted in various ways to display the development. When plotted as a function of time it became visually clear that the signal intensity increased over time, reaching a maximum point. After this point the signal intensity decreased. This decrease in signal intensity was also observed by previous master student Celine Eriksen when performing measurements on dissociating hydrates in a bulk situation [41]. The maximum point on the signal intensity curve is assumed to represent the point in time where all hydrates have dissociated. When no further dissociation of hydrates can occur, the samples continues to be heated until room temperature is reached. It is assumed that the cause of the decrease in this period is that the settings for the RAREst scan are no longer suitable for the sample. Experiments performed by Eriksen, on a THF and water mixture cooled to -10°C, but without any hydrate growth, showed that the decrease in signal intensity occurred as the liquid sample was being heated. These data are presented in figure 4.19 and 4.20 in chapter 4.3.1.1 of her master thesis [41].

The RAREst images provide a way to monitor the physical state of hydrogen nuclei within the sample that is examined. By using the maximum point from the curves displaying signal intensity as a function of time as I_0 in formula (2.1), the relative hydrate saturation within a sample can be estimated. As the signal intensity increases the hydrate saturation decreases. For the hydrate samples presented in this thesis, the signal intensity was recorded slice by slice for each sample. This provides the opportunity to estimate the relative hydrate saturation on a local scale. When the signal intensity for each slice is summarized into representing the total sample, the total relative hydrate saturation can be estimated.

4.2 Temperature Control

For experiments involving hydrates temperature control must be emphasized. To eliminate any doubt about the presence of ice, the temperature development of the sample is critical. Temperature control within an MRI instrument is however a significant issue. The thermistor that was used for the correlation between the temperature set on the air cooler and in the fluorinert contains magnetic components. Measuring the temperature of the sample within the MRI instrument was hence not possible. Temperature measurements of melting hydrates outside the MRI instrument was performed by previous master student Celine Eriksen and can be found under the subchapter 4.2 of her master thesis [41].

For the cooling experiments a setup for achieving better temperature control of the system was created. The cooling experiment performed on sample 14 display a significant result. This sample was dissociated at a determined temperature, approximately 5°C. Figure 3.45, displaying the signal intensity from the sagittal orientation as a function of time, show an interesting development. As hydrates are forming the signal intensity decreases. When the air cooler is set at a temperature corresponding to approximately 5°C within the fluorinert surrounding the sample, the signal intensity is increasing. As the THF hydrates dissociate this increase is expected. When the maximum point of the signal intensity curve is reached the previously recorded decrease in signal intensity is not observable for this sample. As temperature is set to approximately 5°C, the sample will not be heated further. The resulting signal intensity remains constant. This supports the interpretation that the decrease of signal intensity discussed above, is an artifact caused by heating of the sample. The intensity development for sample 14 in the cooling experiment will increase as more hydrogen nuclei become present in a liquid state, and increases until all hydrates are dissociated when a constant signal intensity is recorded. This result can be used to prove that the melting temperature of sample 14 is slightly below 5°C and that it must have been hydrates that were present in the sample.

4.3 CPMG Protocol and T_2^a Relaxation Time Distribution

The CPMG protocol examines the T_2 relaxation process from hydrogen nuclei present within a sample. The actual T_2 relaxation time of hydrogen nuclei are difficult to measure. The magnetic susceptibility within a sample and the inhomogeneity of the main field adds to the dephasing process of the T_2 relaxation. As a result, an enhanced relaxation time will be recorded, T_2^*. However, by applying a spin-echo sequence these effects are thought to be eliminated.

Even with the CPMG scan that utilizes a spin-echo sequence for T_2 relaxation process measurements results may vary depending on the applied settings and the magnetic field strength of the MRI instrument. As the magnetic field strength of an instrument increases, the T_2 relaxation time that is measured will decrease, i.e. the relaxation of the nuclei occurs faster. The decay curves presented in this thesis are therefore specified to represent an apparent T_2 relaxation process, T_2^a relaxation time.

The inverse Laplace transformation is used to transform the decay curves from the CPMG scan into representing a T_2^a relaxation time distribution for the sample that is examined. This distribution can be thought to represent a relative pore size distribution of a porous medium. The distribution of the T_2^a relaxation time depends on both the porous media, and the fluids that are situated within the pores.

The results from the sand experiment shows that some of the samples display a tendency of two peak values for the T_2^a relaxation time. Why some samples show two peak values and some only show one is not established in this thesis. Through these experiments it is shown that as the amount of hydrogen nuclei present increases, so will the signal intensity.

From the melting experiments a similar development between the same types of sand was recorded. The oil-wet sand had the same peak values for the T_2^a relaxation times for both hydrate mixtures. The water-wet sand had the same peak value for the T_2^a relaxation time for the peak with the higher T_2^a relaxation times. The peaks with the lower T_2^a relaxation times for the water-wet sand were not equal. The oil-wet sand had a slower relaxation time than the water-wet sand. This can be understood as the result of either larger pore sizes for the oil-wet sand, or as a result of the wettability preference of the porous media. By comparing to the results in the sand experiments it is assumed that the higher T_2^a relaxation times for the oil-wet sand is caused by the wettability preference.

For the cooling experiment, the CPMG scan was only performed on sample 14, due to the water molecules condensing on the surface of the tube. The hydrogen nuclei present here will add to the signal that is recorded and give a false display of the T_2^a relaxation time distribution for the sample. A region of interest cannot be chosen for the CPMG scan. The scan protocol records an average T_2^a relaxation time from all signal giving nuclei positioned within the MRI instrument. The only pattern present for the distributions from the cooling experiments, is that lower T_2^a relaxation times increase significantly as hydrates are forming and higher T_2^a relaxation times increase as hydrates are dissociating. The higher T_2^a relaxation times that develops when hydrates are dissociating are widely distributed and does not seem to represent the sample properly. It is clearly influenced by the condense on the tube.

4.4 MSME Protocol and T_2^a Relaxation Time Distribution

The MSME protocol differs from the CPMG scan as a specific region within the sample is investigated, and images are acquired. The settings for the two scan protocols are also different. With the settings investigated for this thesis, the echo spacing for the MSME scan could not be set under approximately 5.5ms, while the echo spacing for the CPMG scan was set at 1ms. Formula (1.10) states that as TE increases the influence that the internal gradient susceptibility has on the T_2 relaxation process increases. Hence a faster T_2^a relaxation time will be recorded. The fastest relaxation times might not be recordable with the MSME scan. The relaxation times that are recordable with the CPMG scan might therefore not necessarily be recordable with the MSME scan, and the relaxation times that can be recorded will not necessarily be equal.

The MSME scan shows that the T_2^a relaxation time depends on the porous media and on the fluid that are situated within its pores. The layer of trimethyl-silane, added to the surface of the sand grains for the oil-wet sand, might add to the grain size of the sand and thereby add to the pore size of the porous media. A larger pore size would give a slower T_2 relaxation. This could be an explanation for the slower relaxation times recorded with the oil-wet sand, but the as the heptane shows the opposite results this is unlikely. The wettability preference of the porous media seems to influence the T_2^a relaxation time, even when only one fluid is present.

The results in this thesis show a tendency of a faster T_2^a relaxation time for the fluid that is the wetting phase in the situated pore structure. Water will have a slower T_2^a for the oil-wet sand and heptane will have a slower T_2^a for the water-wet sand. The only exception from this result was recorded for water in water-wet and oil-wet sand from the sagittal orientation. This result displayed the opposite. The conclusion that the wetting phase of a porous medium will be given a faster relaxation time hence needs further documentation.

By adding a second phase to a sample it was expected to record slower T_2^a relaxation time values as this would cause one phase to be situated close to pore walls while the other would be trapped between the pores. The fluid trapped between the pores is then thought to experience a slower T_2^a relaxation time since it is not in direct contact with the pore walls. This result was not found. It is thus difficult to support that the addition of a second phase will increase the T_2^a relaxation time of the non-wetting phase.

The melting and the cooling experiments displayed a significant development in the recorded T_2^a relaxation time as hydrates were dissociating and forming. A clear development in the density of the T_2^a relaxation time and in the peak T_2^a relaxation time was recorded. As hydrates were dissociating the peak T_2^a relaxation time increased. The density of the T_2^a relaxation time also increased as more hydrogen nuclei were present in a liquid state. As hydrates were reforming the development was exactly the opposite. The T_2^a relaxation time recorded with the MSME scan differ significantly from the T_2^a relaxation time recorded with the CPMG scan.

The MSME scan allows for the opportunity to monitor the T_2^a relaxation time on a local scale. The development of the T_2^a relaxation time is significant and can define whether hydrates are forming or dissociating. By monitoring the T_2 relaxation process it can be determined whether a hydrate sample is dissociating or forming.

5 Conclusion

The main objective for this thesis was to study the formation and the dissociation of THF hydrates within a porous medium using magnetic resonance imaging. Potential differences caused by the wettability preference of the porous media has also been examined. The conclusions drawn from the experiments performed for this thesis are summarized in this chapter.

RAREst images record a significant development of signal intensity as THF hydrates dissociate and reform within a porous medium. Dissociating THF hydrates will give an increasing signal intensity, as hydrogen nuclei are given freer motion when transferring from a solid to a liquid state. The signal from a solid THF hydrate sample will not be detectable above background noise. The signal intensity will hence decrease as hydrates are forming. The RAREst protocol is an excellent way to monitor the state of the THF hydrates. Through the signal intensity one can estimate the relative THF hydrate saturation on local scale and for the total sample.

The RAREst images can also reveal the dissociation and re-forming patterns for the THF hydrates. Through these images one can see that the hydrate samples are dissociating from the outside and inwards to center of the sample. The dissociation is a clear process of heat transfer. The RAREst images give the opportunity to view the THF hydrates from the inside of the porous media.

Through T_2 mapping performed by the CPMG and the MSME protocol a dependency on wettability has been found. The CPMG scan measures the T_2 relaxation process through the whole sample, while the MSME scan analyzes a specific region of interest. The resulting T_2^a relaxation times are significantly different between the two scans, but the same trends are detectable. As hydrates dissociate, a higher density and peak value of the T_2^a relaxation time will occur. The T_2^a relaxation time distribution illustrated a relative pore size and shows that as the hydrates dissociate the pore size grows bigger. Through the CPMG scan a significant dependency of pore size on the hydrate dissociation was also found. The smallest pore sizes showed very little change in development for the melting experiments, compared to the higher pore sizes that displayed a significant development in both density and peak T_2^a relaxation time value. The T_2^a relaxation time can hence give information about the dissociation and re-forming patterns for THF hydrates.

The wettability of the porous media seems to affect the T_2^a relaxation time recorded from the samples. The oil-wet sand shows a systematically higher T_2^a relaxation time than the water-wet sand, when THF and water are situated between the pores. The oil-wet sand is covered with trimethyl-silane and this could possibly add to the grain size creating a bigger pore size for the sand. But results from the sand experiment showed the opposite trend when the sand contained heptane. The T_2^a relaxation time for the oil-wet sand containing heptane is lower than for water-wet sand containing heptane. This indicates that the wettability preference of

the porous media will give the wetting phase a lower T_2^a relaxation time. The wettability of the porous media does not seem to affect dissociation or reforming of the THF hydrates within porous media.

5.1 Further work

As a direct consequence of the acquired results further measurements of T_2^a relaxation time of different fluids in porous media with alternating wettabilities are required in order to understand why the same porous media will give the same fluid a different T_2^a relaxation time when the wettability preference is altered. In order to conclude that the wettability preference of the porous media will give the wetting phase a lower T_2^a relaxation time more measurements are required.

For further measurements performed on hydrates with the application of MRI protocols, an improved cooling set-up within the MRI is recommended. Further testing of materials for isolation, as well as different layouts with better isolation, will be necessary. The need for temperature control is significant. Being able to compare melting temperatures between different hydrates mixtures and simultaneously recording MRI data would be valuable. By analyzing the loss of signal intensity as samples are heated, one could possibly predict the temperature. A corresponding table between signal intensity and temperature of a sample would then need to be established.

An interesting development for the hydrate samples within the porous media was that the hydrates seemed to move the sand around within the sample. Recording RAREst images of the samples before hydrate growth, to compare with the images of the sample after hydrate growth, would probably display very interesting developments. It would further be recommended to perform MSME measurements from the samples and analyze all slices from the scan, to see if one can detect different dissociation processes between the slices. The THF hydrates starts the dissociation process in the outer edges of the samples. The development of the T_2^a relaxation time distribution might hence appear different according to the position of the region of interest within the sample.

Though harder to create, cyclopentane hydrates would be more representative to methane hydrates as both compounds are immiscible with water. For samples prepared for this thesis cyclopentane hydrates would initially only form in the interface between cyclopentane and water. If cyclopentane is to be used as a hydrate former, the samples should be prepared several months before intended use.

APPENDIX

A1 Procedure for alteration of wettability and calculation for amount of chlorotrimethylsilane.

Fukting av sandprøver

Vann-våt sand
Sandprøven gjøres vann-våt på følgende vis:

1. Tilsett en litt zalo + vann for å vaske prøven. Vask godt.
2. Tilsett litt sterk NaOH, 1 mol, og la det virke i 30 minutter.
3. Tilsett 1 molar HCl i 10 minutter for å nøytralisere.
4. Vask med store mengder destillert vann. Bruk pH papir for å sjekke at all NaOH og HCl er vasket bort.
5. Behold prøven fuktig i destillert vann til den skal brukes. Hvis prøven tørkes vil den forandre seg.

Olje-våt sand
Sandprøven gjøres olje-våt på følgende vis:

1. Samme prosedyre som for å lage vann-våt sand.
2. ”Coate” overflaten med Silan for å gjøre den helt olje-våt.
3. Tilsett olje.

Denne metoden er designet for å måle fuktvinkler (utarbeidet av Kjemisk avdeling UiB)

Alteration of wettability of sand

Water-wet sand
The sand is made water-wet by the following procedure:

6. Add some dishwasher soap + water to wash the sample properly.
7. Add strong NaOH, 1 mole, and let it work for 30
8. Add 1 molar HCl for 10 minutes to neutralize the NaOH.
9. Wash with distilled water. Use pH paper to make sure that all NaOH and HCl is washed away.
10. Keep the sand wet in distilled water until use. If the sand dries, the wettability may change.

Oil-wet sand
The sand is made oil-wet by the following procedure:

4. Perform the same procedure as for water-wet sand.
5. Coat the surface with silane to make it oil-wet.
6. Add oil.

This method is designed to measure wettability angles, by the Institute of Chemistry, the University of Bergen.

Calculating how much CTMS necessary for silylation

After viewing the sand through a microscope, the smallest particle found was a little above 150 μm in diameter [42]. Though some particles may be smaller, and some may be larger, this size was used to be sure that the total surface area will be covered. To make the calculation approachable, assume that the particles are spherical.

r=75μm

$$V = \frac{4}{3}\pi r^3 = \frac{4}{3}\pi(75x10^{-6}m)^3 = 1{,}77x10^{-22}m^3$$

Density of quartz sand: $\rho = 2{,}65g/cm^3$

Weight per particle:

$$1{,}77x10^{-22}m^3 = 1{,}77x10^{-6}cm^3$$

$$1{,}77x10^{-6}cm^3 x 2{,}65g/cm^3 = 4{,}69x10^{-6}g$$

How many particles per 1 gram:

$$\frac{1g}{4{,}69x10^{-6}g} = 213196\ particles$$

Area of a particle:

$$A = 4\pi r^2 = 4\pi(75x10^{-6}m)^2 = 7{,}07x10^{-8}m^2$$

Total area of particles in one gram:

$$A\ x\ number\ of\ particles = 7{,}07x10^{-8}m^2\ x\ 213196 = 0{,}015m^2/g$$

To find total surface area of the amount of sand:

$$\frac{0{,}015m^2}{g}\ x\ amount\ of\ sand$$

Chlorotrimethylsilane:

Length of the elements:

C-H: 109 x 10^{-12}m

C-Si: 185x10^{-12}m

Si: d=111x10^{-12}m

C: d=67x10^{-12}m

H: d=53x10^{-12}m

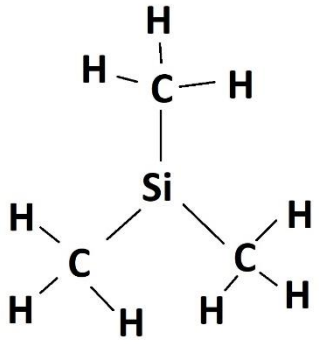

Length of one trimethylsilane particle:

$L = d_{Si} + 2xd_C + 2xd_H + 2xL_{C-H} + 2xL_{Si-C}$

L= 111x10^{-12}m + 2x67x10^{-12}m + 2x53x10^{-12}m + 2x109 x 10^{-12}m + 2x185x10^{-12}m

L=9,39x10^{-10}m

Assume that the shape is a square with each side 9.39x10^{-10}m long.

A=9,39x10^{-10}m x 9,39x10^{-10}m=8,81x$10^{-19}$$m^2$

How many molecules TMS are needed to cover the surface area

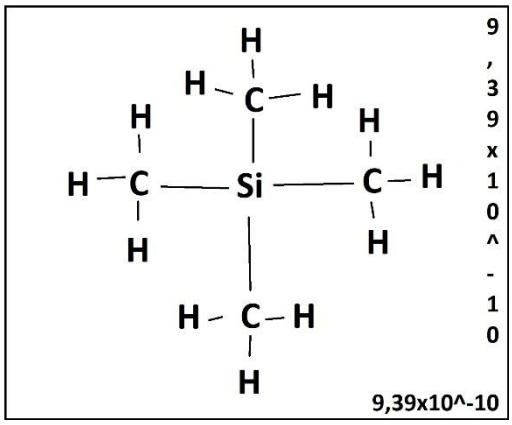

$$\frac{Surface\ area\ of\ sand}{Area\ of\ TMS} = x\ number\ of\ molecules\ on\ the\ surface$$

Molecular weight CTMS: 108,64g/mol

1mol= 6,022x10^{23} molecules

How many molecules needed:

$$\frac{x\ number\ of\ molecules\ on\ the\ surface}{6{,}022x1023\ \text{molecules}} = number\ of\ how\ many\ moles\ of\ CTMS\ needed$$

$$number\ of\ how\ many\ moles\ of\ CTMS\ needed\ x\ Mw\ CTMS = how\ many\ grams\ of\ CTMS\ needed$$

This amount is extremely small, so 2mL will be more than enough for 200 grams of sand. This also corresponds with the description given for other procedures [30].

A2 Additional Information and Results, Sand Experiments

Details about the samples

The following tables show the details about the samples 4 to 13.

Table A2.0.1 - Details about samples 4 to 9, 12, and 13.

Weight of:	Water wet sand/THF	Water wet sand/ Heptane	Water wet sand/ water	Water wet sand/ Fluorinert	Oil wet sand/THF	Oil wet sand/ Heptane	Oil wet sand/ water	Oil wet sand/ Fluorinert
glass [g]	13,55	13,49	13,49	13,63	13,95	13,45	13,57	13,49
sand [g]	15,49	14,65	15,35	15,62	15,57	15,64	15,77	15,31
fluid [g]	5,98	5,93	6,04	19,35	5,56	4,26	6,38	14,03
total with lid [g]	36,83	35,88	36,67	50,35	36,37	35,15	37,51	44,64
removed surplus liquid [g]	1,62	0,21	1,89	2,55	1,65	0,75	1,62	3,46
new total [g]	35,21	35,67	34,78	47,80	34,72	34,40	35,89	41,18

Table A2.0.2 Details about samples 10 and 11.

Weight of:	Oil-wet sand with heptane and water	Oil-wet sand with water and fluorinert
Glass [g]	214,15	15,27 (with lid)
Sand [g]	156,44	18,37
Heptane [g]	31,20	-
Fluorinert [g]	-	1,99
Water [g]	57,18	6,54
Total [g]	458,97	42,18

RAREst Protocol

Samples 4 to 9, sand containing one single fluid

Figure A2.0.1 displays the settings used to acquire the RAREst images of samples 4 to 9. The same settings were used for both coronal orientation and sagittal orientation of the images. The resulting images are shown in figures A2.0.2 to A2.0.13.

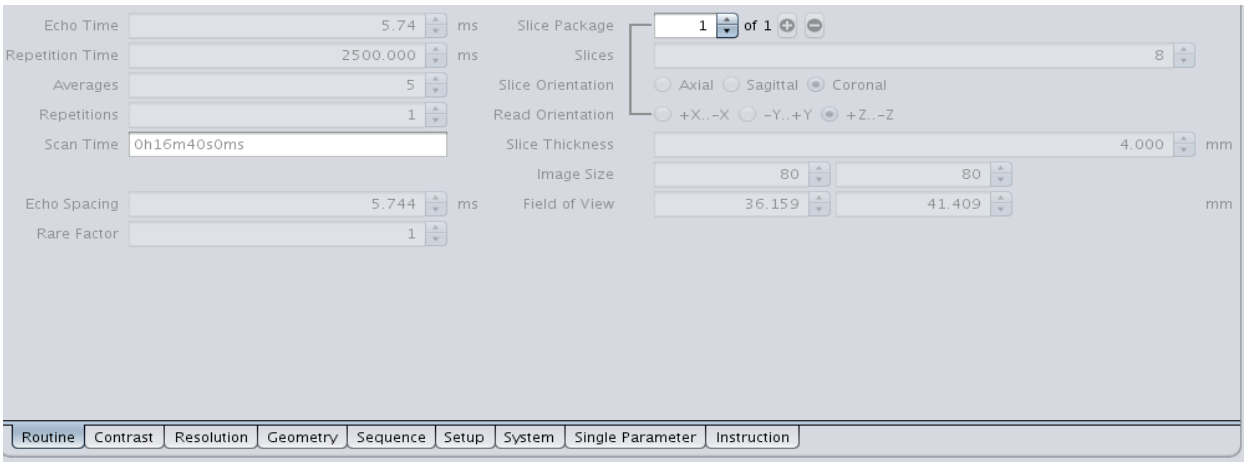

Figure A2.0.1 - Settings for the RAREst scans of samples 4 to 9. The same settings were used for all RAREst scans, both sagittal and coronal orientation. The only parameter that was altered was the field of view and number of slices.

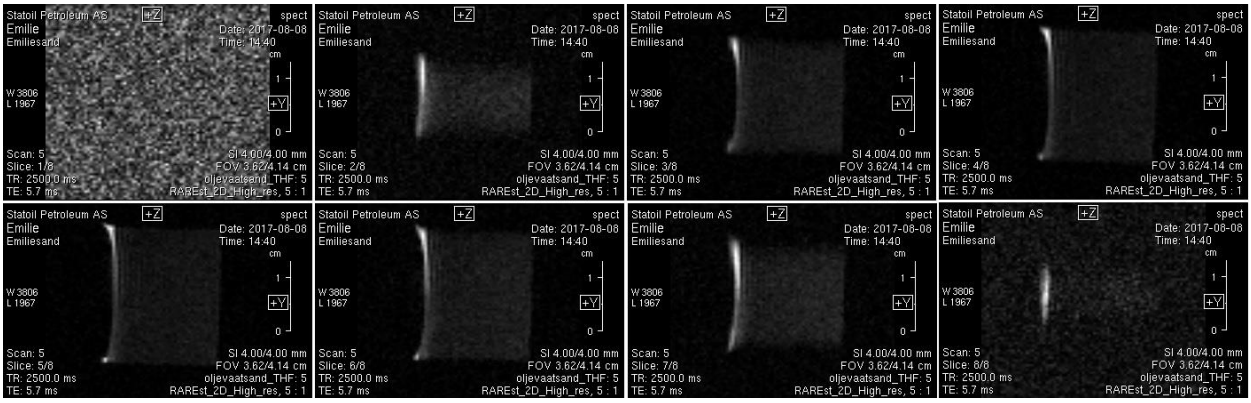

Figure A2.0.2 - Images of sample 4, oil-wet sand with THF, from the sagittal orientation. The first image, from top left corner, is the outer edge of the sample, while the last image, the bottom right image, is in the outer edge on the other side of the sample.

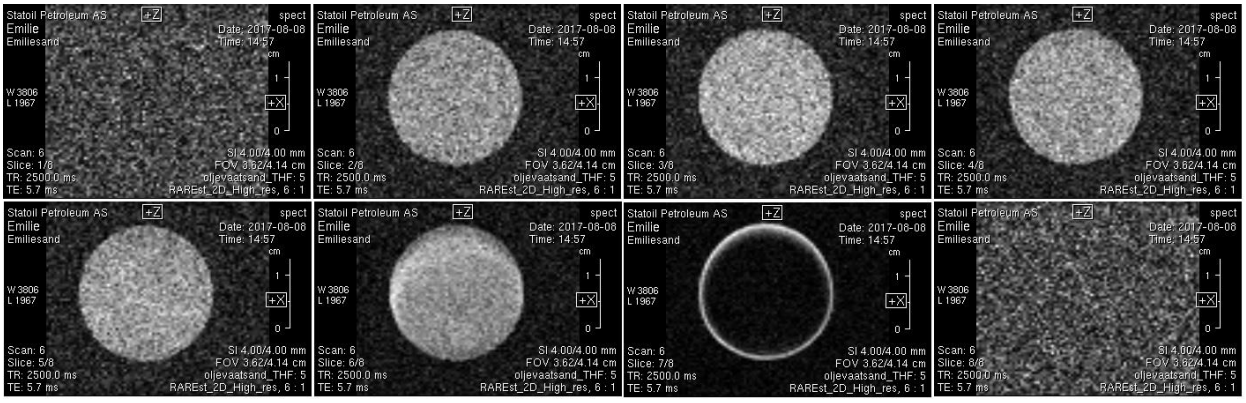

Figure A2.0.3 - Images of sample 4, oil-wet sand with THF, from the coronal orientation. The first image, from top left corner, is the bottom of the sample, while the last image is in the top of the sample.

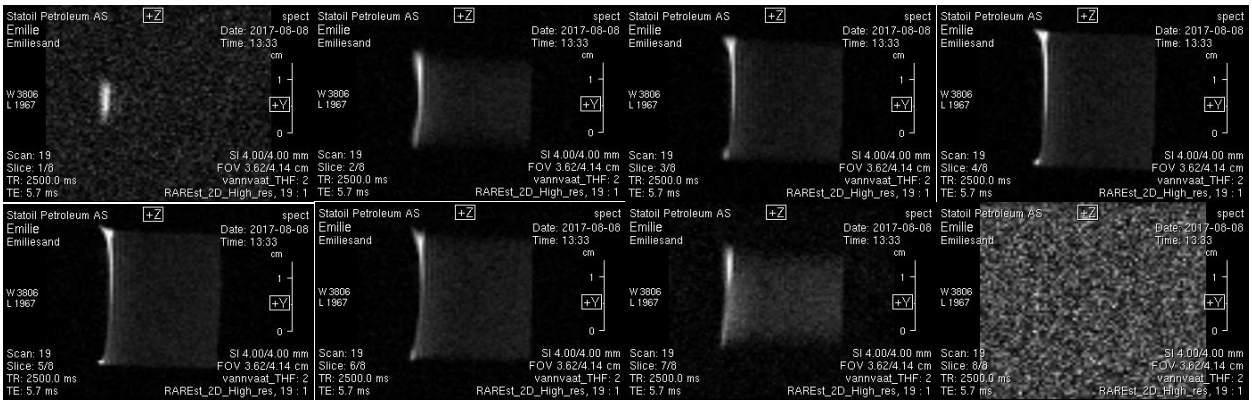

FigureA2. 0.4 - Images of sample 5, water-wet sand with THF, from the sagittal orientation. The first image, from top left corner, is the outer edge of the sample, while the last image, the bottom right image, is in the outer edge on the other side of the sample.

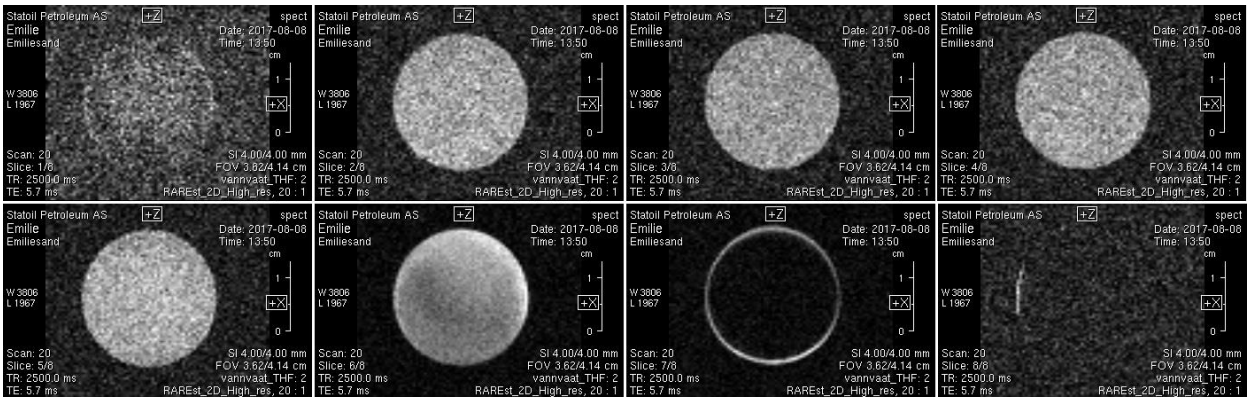

Figure A2.0.5 - Images of sample 5, water-wet sand with THF, from the coronal orientation. The first image, from top left corner, is the bottom of the sample, while the last image is in the top of the sample.

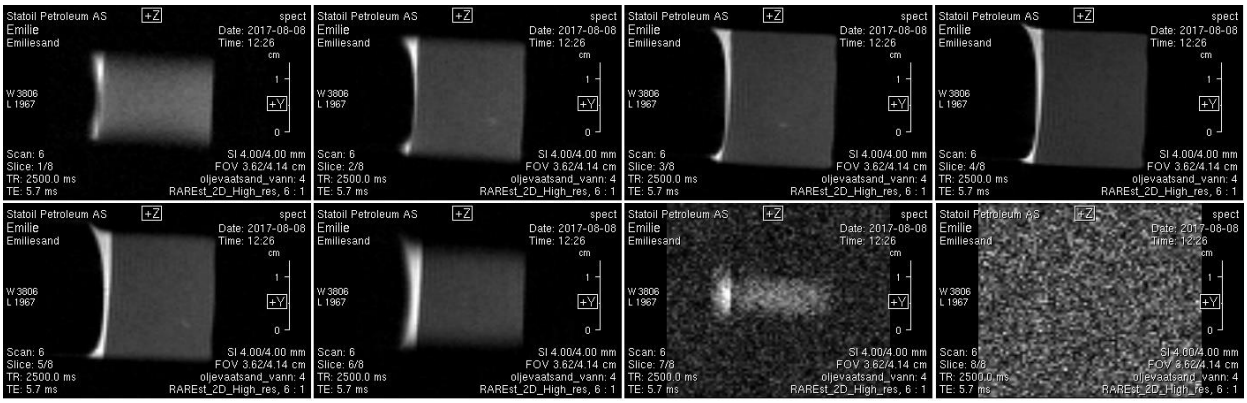

Figure A2.0.6 - Images of sample 6, oil-wet sand with H2O, from the sagittal orientation. The first image, from top left corner, is the outer edge of the sample, while the last image, the bottom right image, is in the outer edge on the other side of the sample.

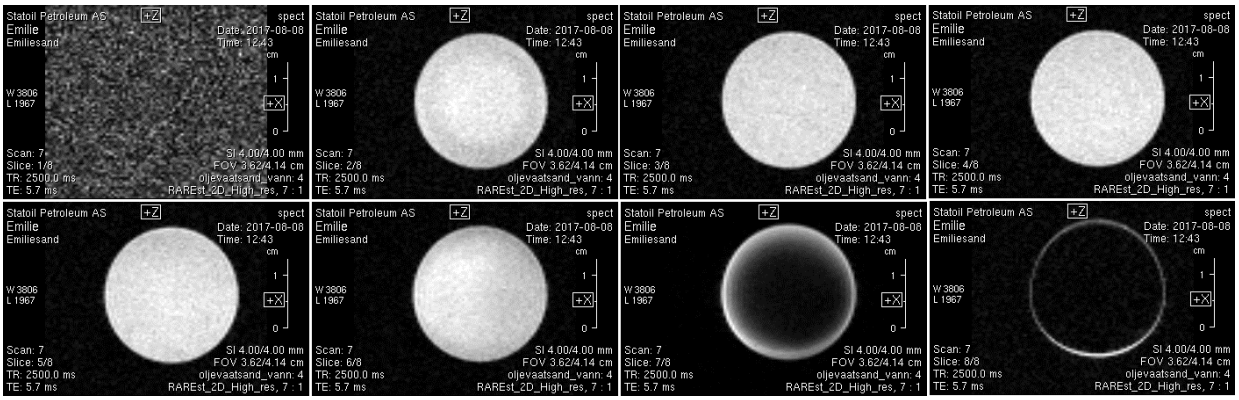

Figure A2.0.7 - Images of sample 6, oil-wet sand with H2O, from the coronal orientation. The first image, from top left corner, is the bottom of the sample, while the last image is in the top of the sample.

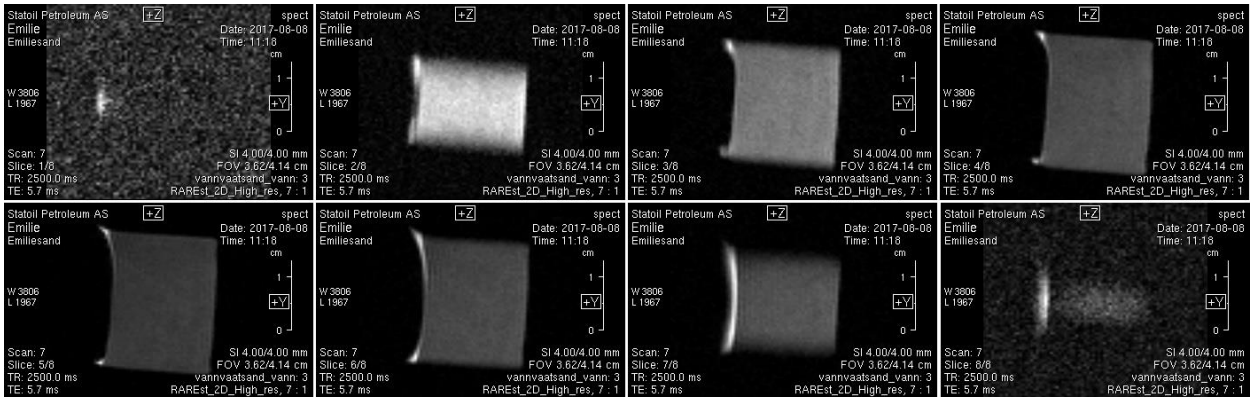

Figure A2.0.8 - Images of sample 7, water-wet sand with H_2O, from the sagittal orientation. The first image, from top left corner, is the outer edge of the sample, while the last image, the bottom right image, is in the outer edge on the other side of the sample.

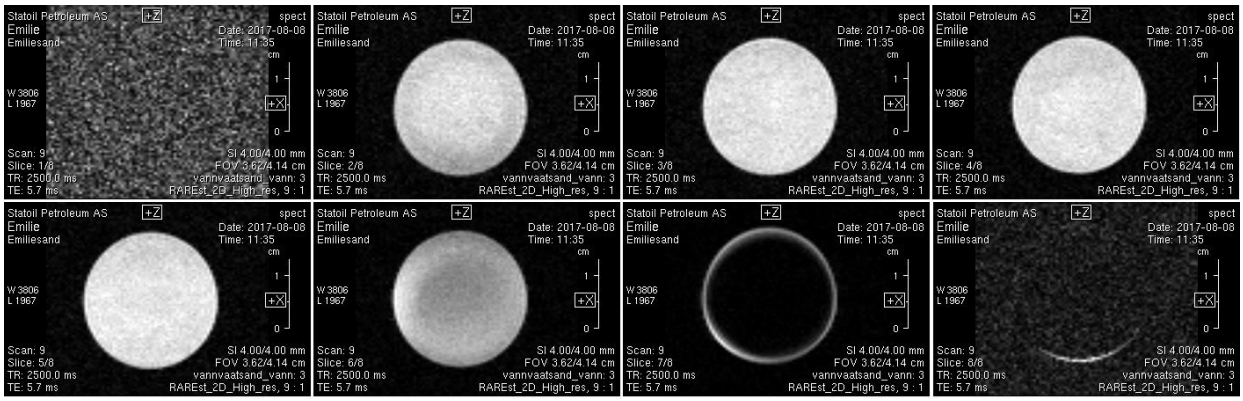

Figure A2.0.9 - Images of sample 7, water-wet sand with H2O, from the coronal orientation. The first image, from top left corner, is the bottom of the sample, while the last image is in the top of the sample.

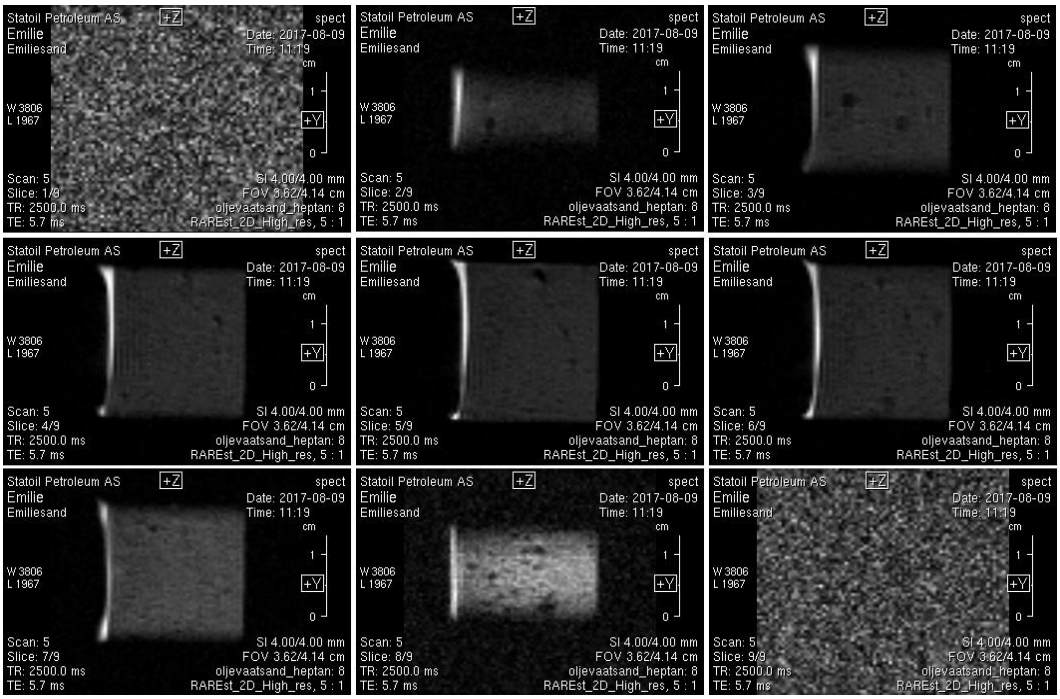

Figure A2.0.10 - Images of sample 8, oil-wet sand with heptane, from the sagittal orientation. The first image, from top left corner, is the outer edge of the sample, while the last image, the bottom right image, is in the outer edge on the other side of the sample.

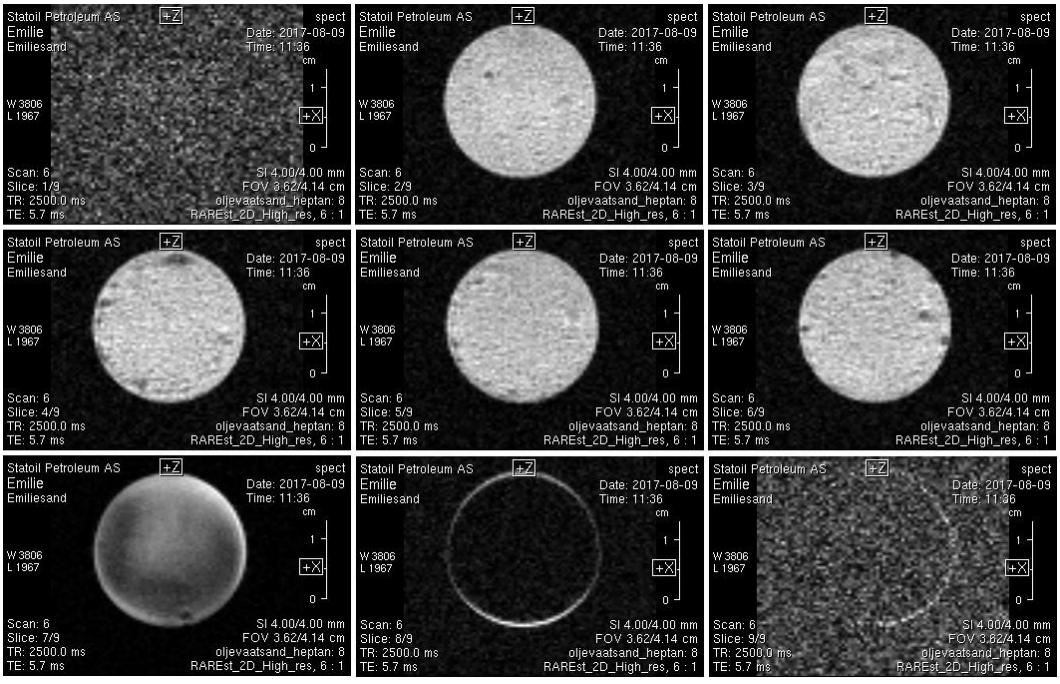

Figure A2.0.11 - Images of sample 8, oil-wet sand with heptane, from the coronal orientation. The first image, from top left corner, is the bottom of the sample, while the last image is in the top of the sample.

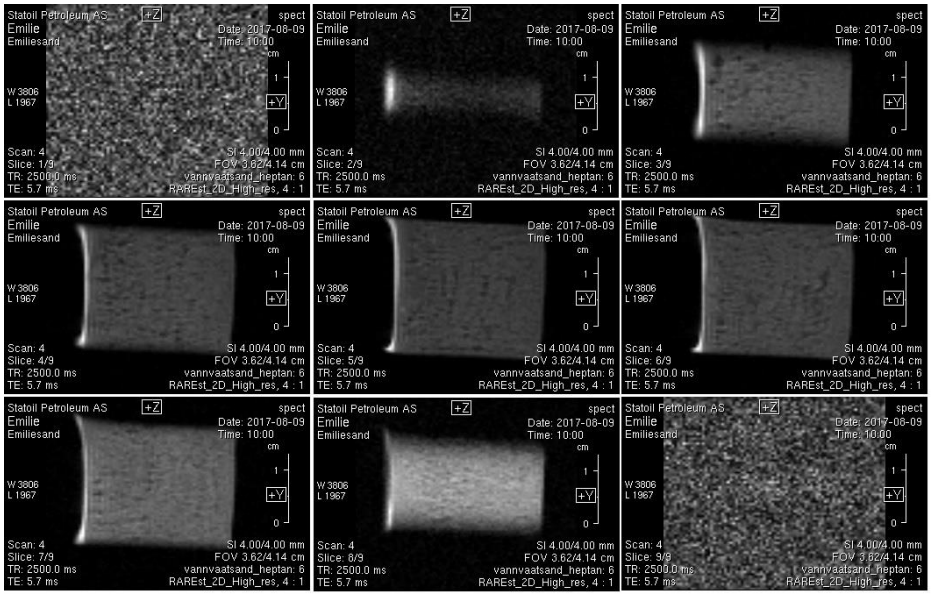

FigureA2. 0.12 - Images of sample 9, water-wet sand with heptane, from the sagittal orientation. The first image, from top left corner, is the outer edge of the sample, while the last image, the bottom right image, is in the outer edge on the other side of the sample.

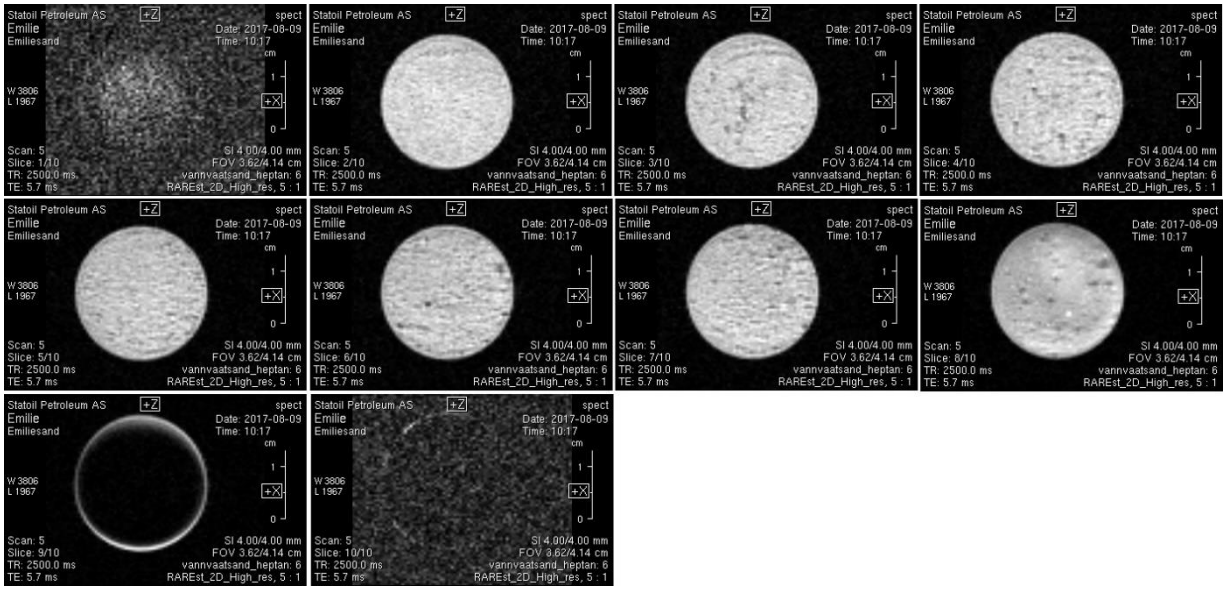

Figure A2.0.13 - Images of sample 9, water-wet sand with heptane, from the coronal orientation. The first image, from top left corner, is the bottom of the sample, while the last image is in the top of the sample.

Samples 10 and 11, sand containing two fluids

Figure A2.0.14 displays the settings used to acquire the RAREst images of sample 11. The resulting images are shown in figures A2.0.15 and A2.0.16.

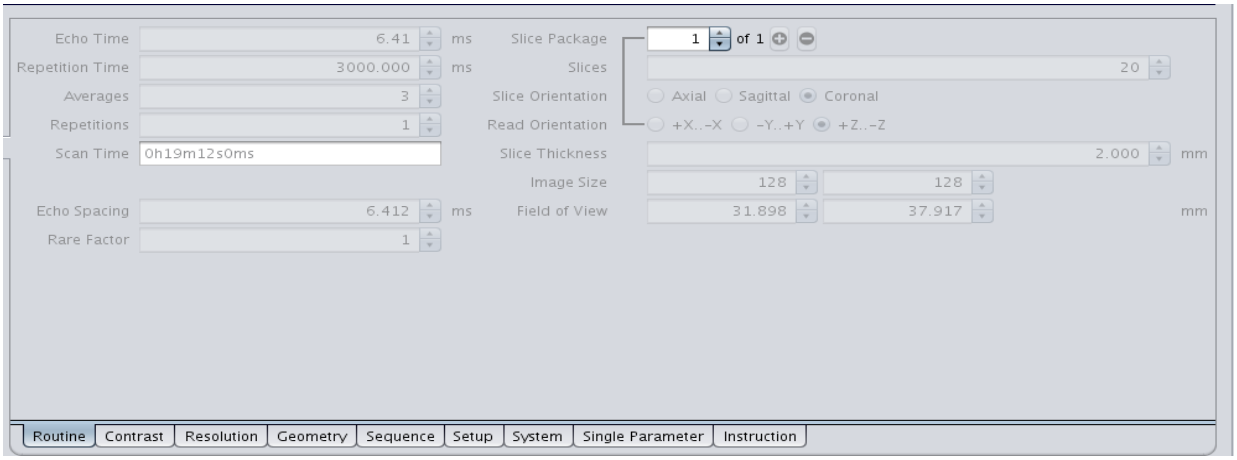

Figure A2.0.14 - Settings for RAREst scans of sample 11.

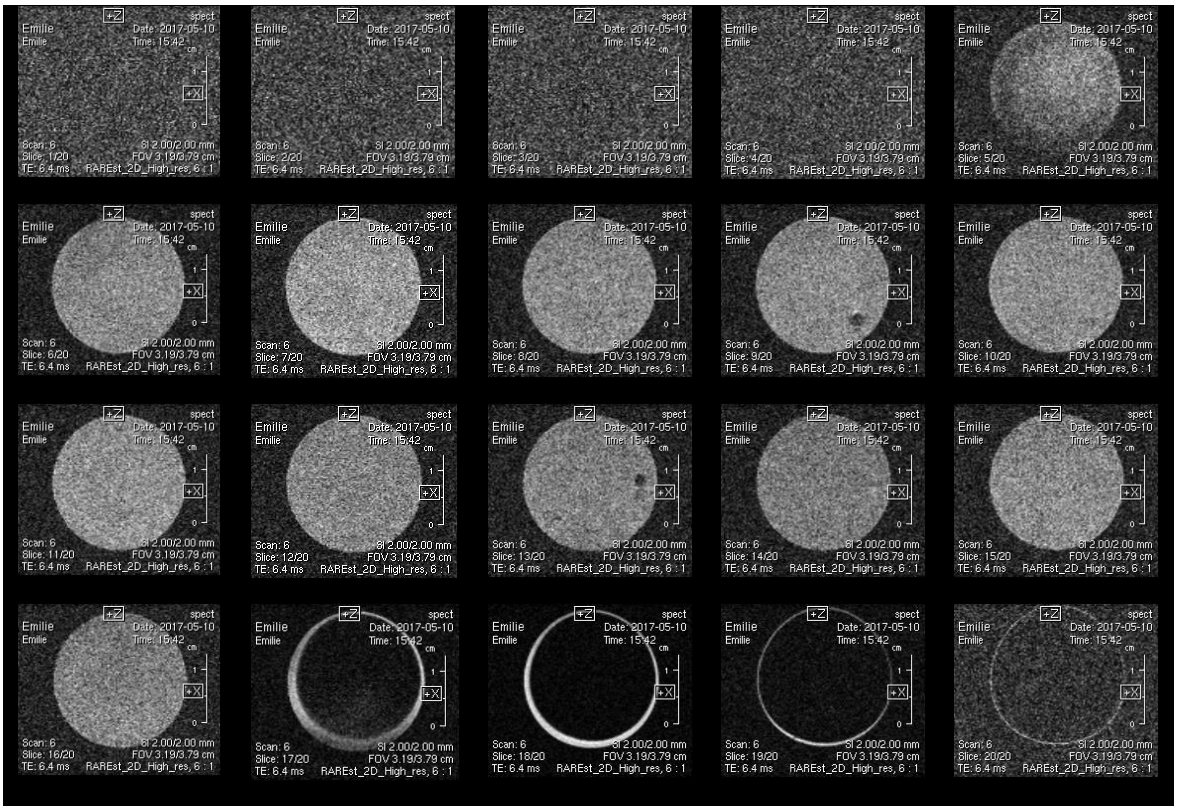

Figure A2.0.15 - Images of sample 11, oil-wet sand with water, from the coronal orientation. The first image, from top left corner, is the bottom of the sample, while the last image is in the top of the sample.

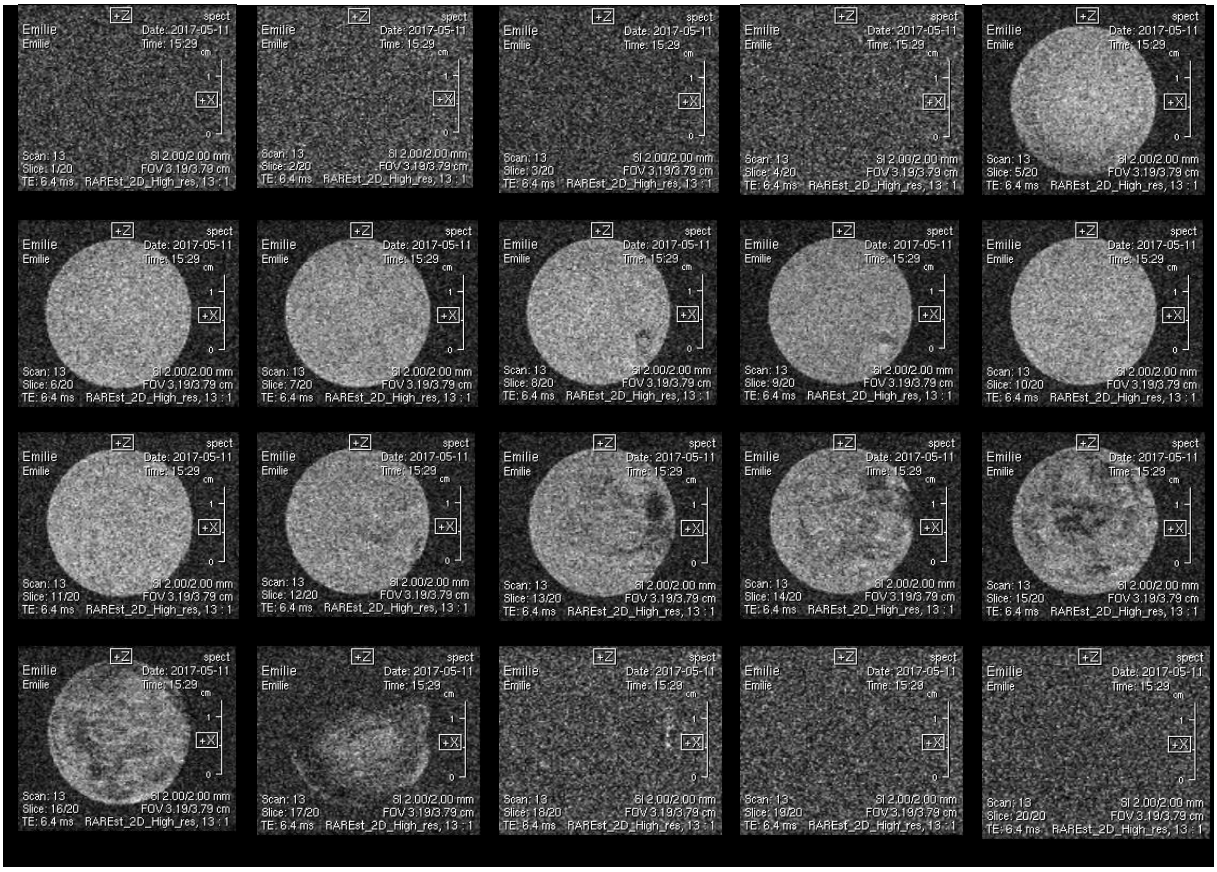

Figure A2.0.16 – Images of sample 11, oil-wet sand with water and fluorinert, from the coronal orientation. The first image, from top left corner, is the bottom of the sample, while the last image is in the top of the sample.

Figure A2.0.17 displays the settings used to acquire the RAREst images of sample 10. The resulting images are shown in figure A2.0.18.

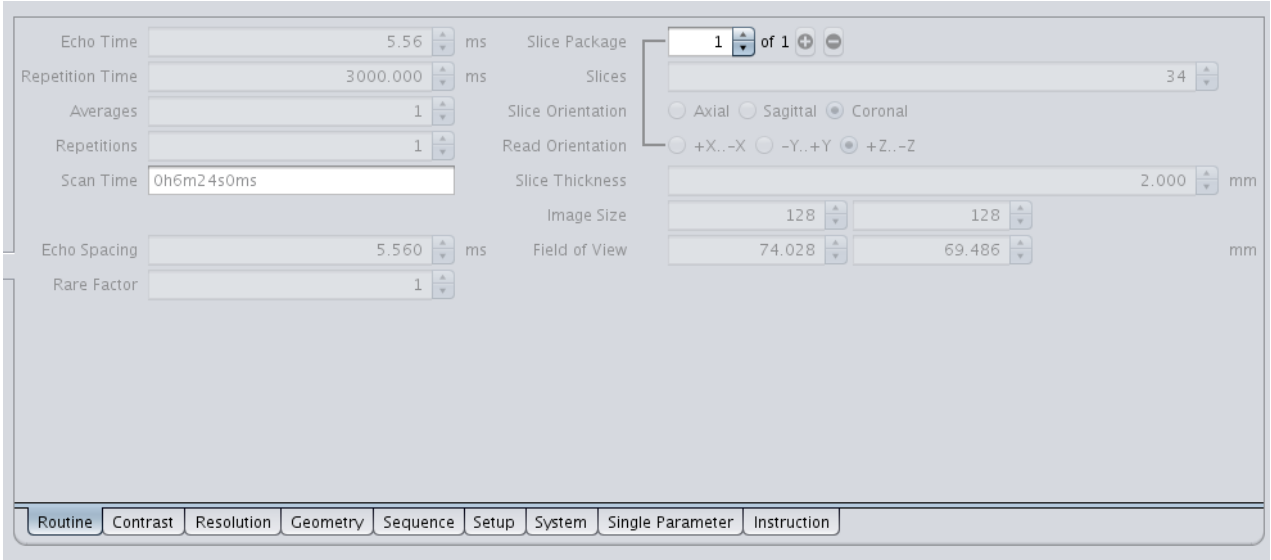

Figure A2.0.17 - Settings for RAREst scans of sample 10.

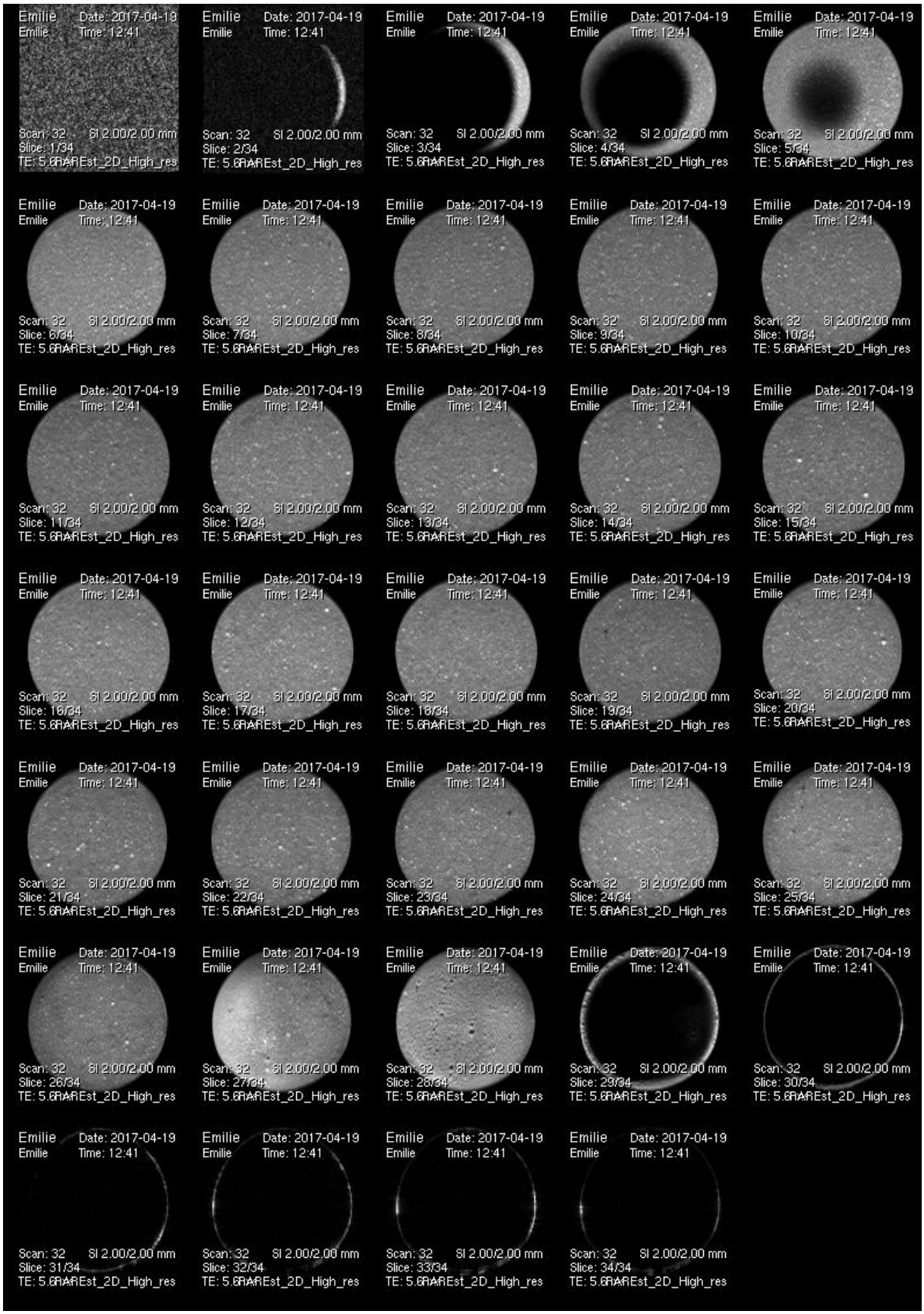

Figure A2.0.18 - Images of sample 10, oil-wet sand with heptane and water, from the coronal orientation. The first image, from top left corner, is the bottom of the sample, while the last image is in the top of the sample. A bigger sample glass was used for sample 12.

CPMG Protocol

Samples 4 to 9, sand containing one single fluid

Figure A2.0.19 displays the settings used to acquire the CPMG measurements of samples 4 to 9.

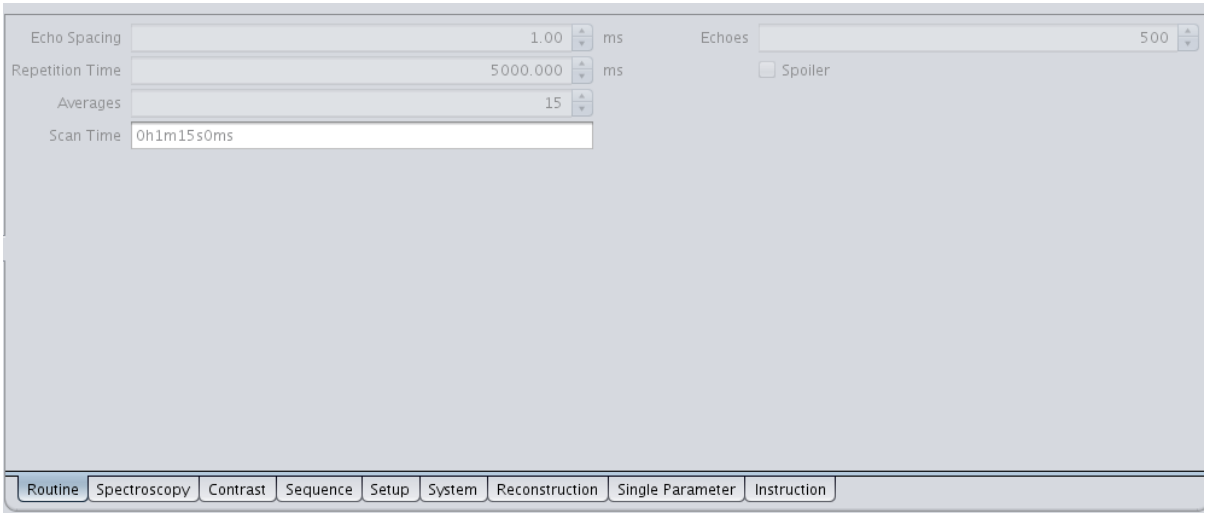

Figure A2.0.19 – Settings used for CPMG scans of samples 5-10.

Samples 10 and 11, sand containing two fluids

Figure A2.0.20 displays the settings used to acquire the CPMG measurements of sample 11.

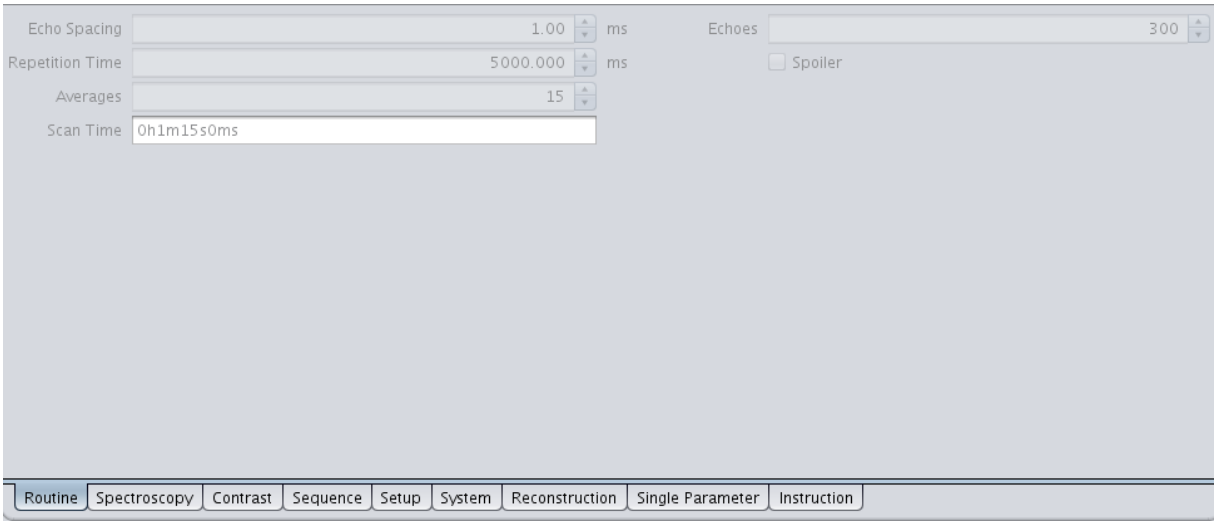

Figure A2.0.20 - Settings used for CPMG scans of sample 11.

Figure A2.0.21 displays the settings used to acquire the CPMG measurements of sample 10.

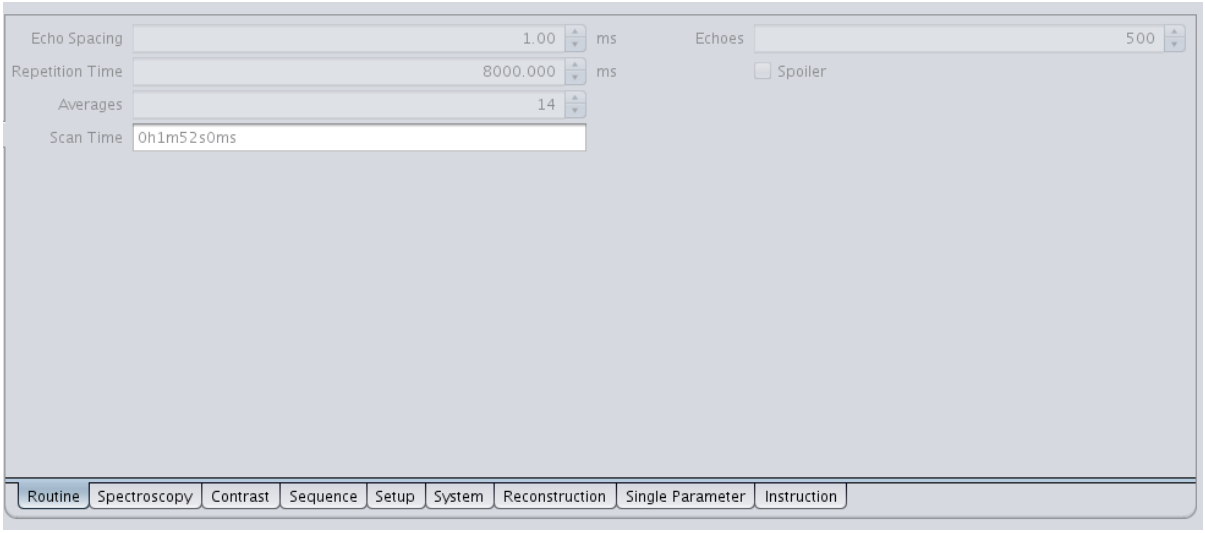

Figure A2.0.21 - Settings used for CPMG scan of sample 10.

Figure A2.0.22 display the decay curve acquired with CPMG scan of sample 10. The echo spacing for these scans was 1,5ms instead of 1ms like the data presented under chapter 3.1.2.

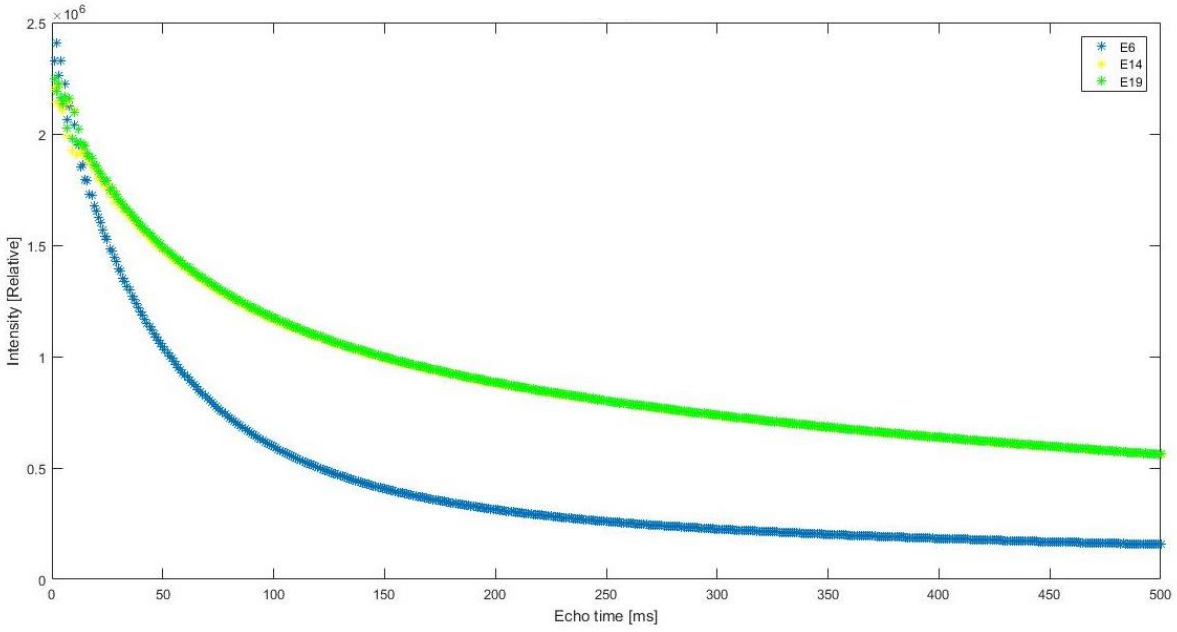

Figure A2.0.22 - Decay curve for CPMG scan for sample 10, oil-wet sand with water and heptane, with echo time 1,5ms. Scan E6 is before addition of water, scan E14 and E19 is after addition of water.

Figure A2.0.23 display the apparent T_2^a relaxation time distribution for sample 10, when echo spacing is 1,5ms. The figure is achieved from inverse Laplace transformation of the data in figure A2.0.22.

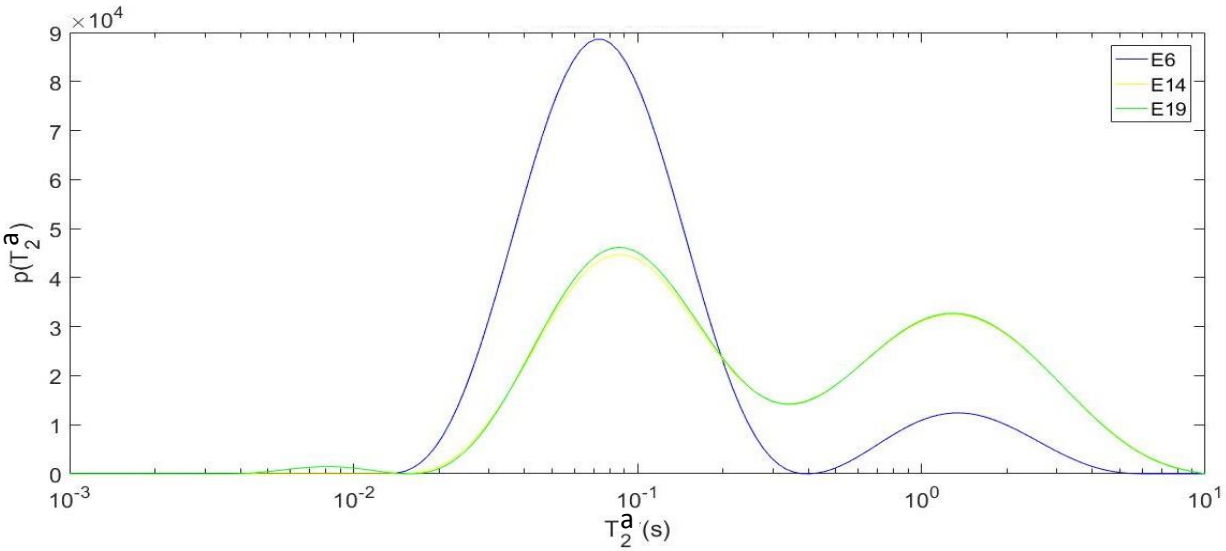

Figure A2.0.23 – T_2^a relaxation time distribution from the data in figure A2.0.22, for sample 10, oil-wet sand with water and heptane, with echo time 1,5ms. Scan E6 is before addition of water, scan E14 and E19 is after addition of water.

For the inverse Laplace transformation of the CPMG data the same nnls-smoothing parameters were applied on all the CPMG scans for samples 4 to 11. The parameters are given in table A2.0.3.

Table A2.0.3 - Smoothing parameters for the inverse Laplace transformation

nnls smoothing parameters for ILT	
Alpha	1e7
T/D min	0,001
Tmax	10
Steps	150

MSME Protocol

Samples 4 to 9, sand containing one single fluid

Figure A2.0.24 shows the settings used for the MSME scans of samples 4 to 9. The settings were the same for both Coronal and Sagittal orientation of slices.

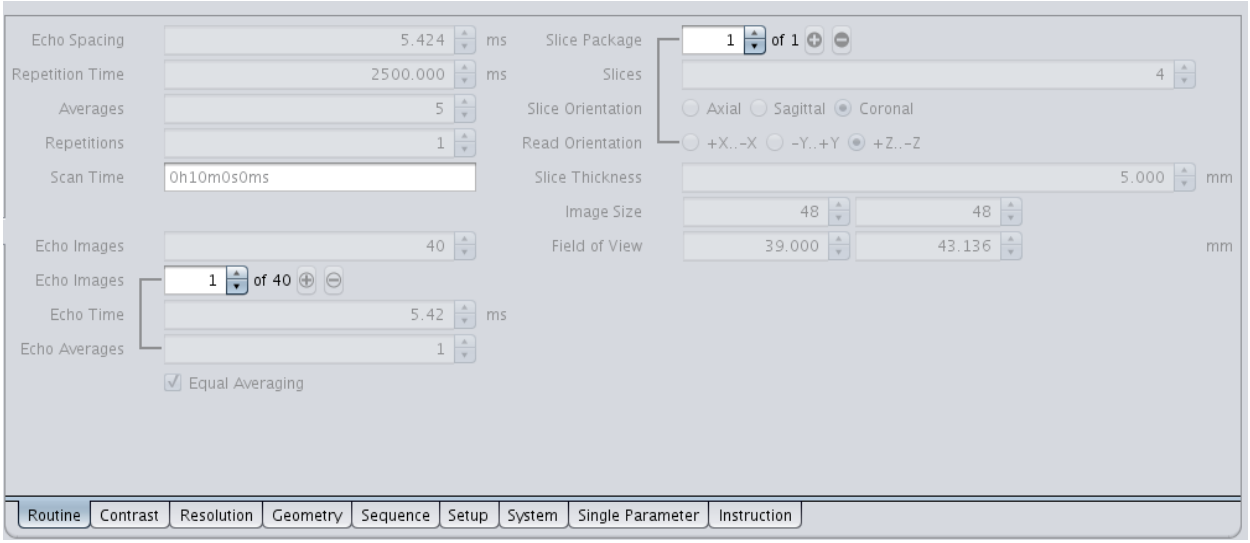

Figure A2.0.24 - Settings used for the MSME scans of samples 4 to 9. The same settings were applied for both sagittal and coronal orientation.

Figure A2.0.25 and A2.0.26 shows the regions of interest for samples 4 to 9, used for the MSME data presented under chapter 3.1.3.

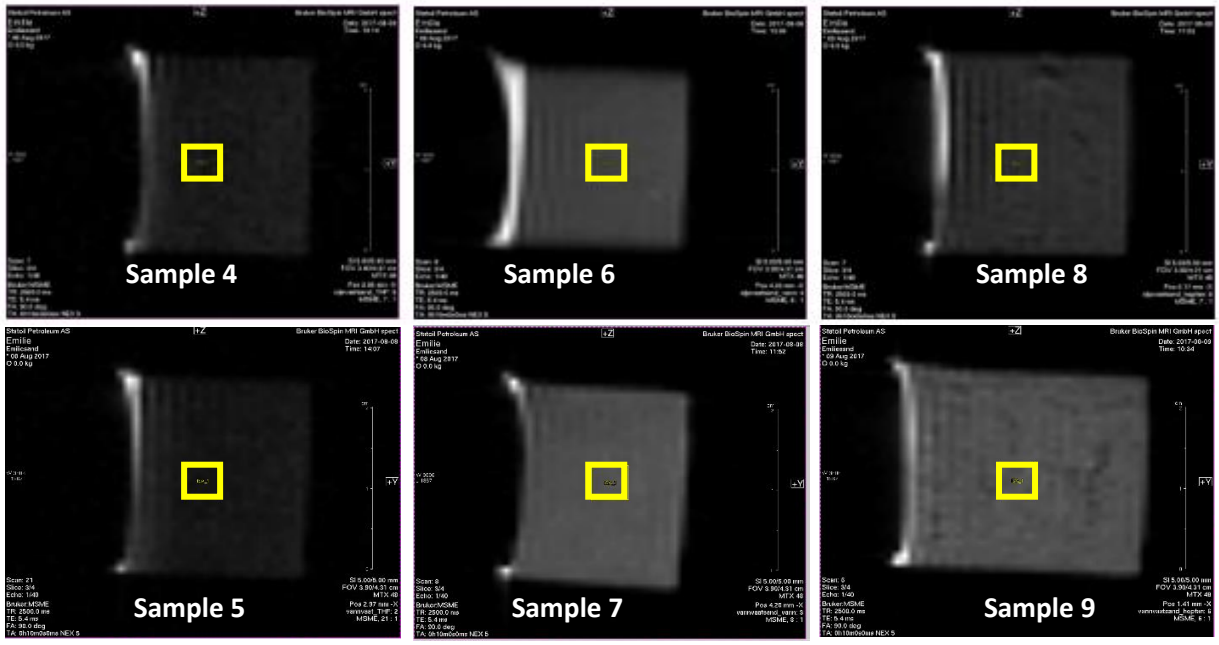

Figure A2.0.25 - Region of interest, displayed by the yellow square, for MSME scans of samples 4 to 9, form the sagittal orientation. Top line from left to wright: oil-wet sand with THF, H2O, C7H16. Lower line from left to wright: water-wet sand with THF, H2O, C7H16.

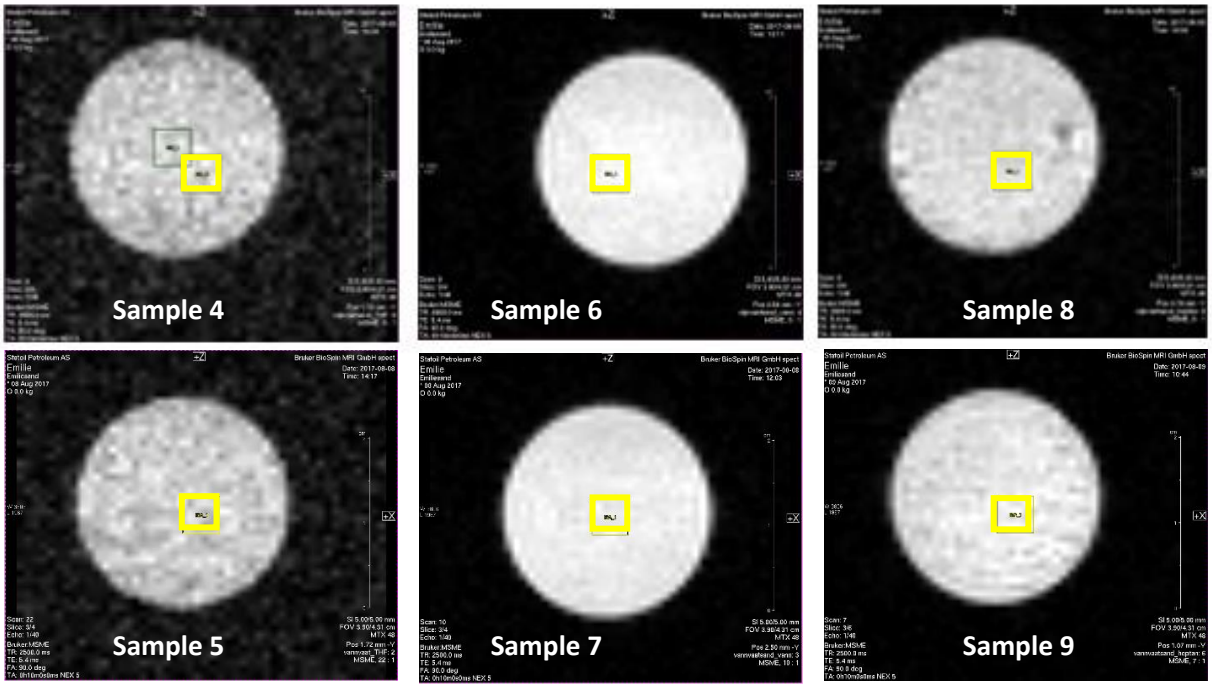

Figure A2.0.26 - Region of interest, displayed by the yellow square, for MSME scans of samples 4 to 9, form the coronal orientation. Top line from left to wright: oil-wet sand with THF, H2O, C7H16. Lower line from left to wright: water-wet sand with THF, H2O, C7H16.

Sample 11, sand containing two fluids

Figure A2.0.27 display the settings for MSME scans on sample 11.

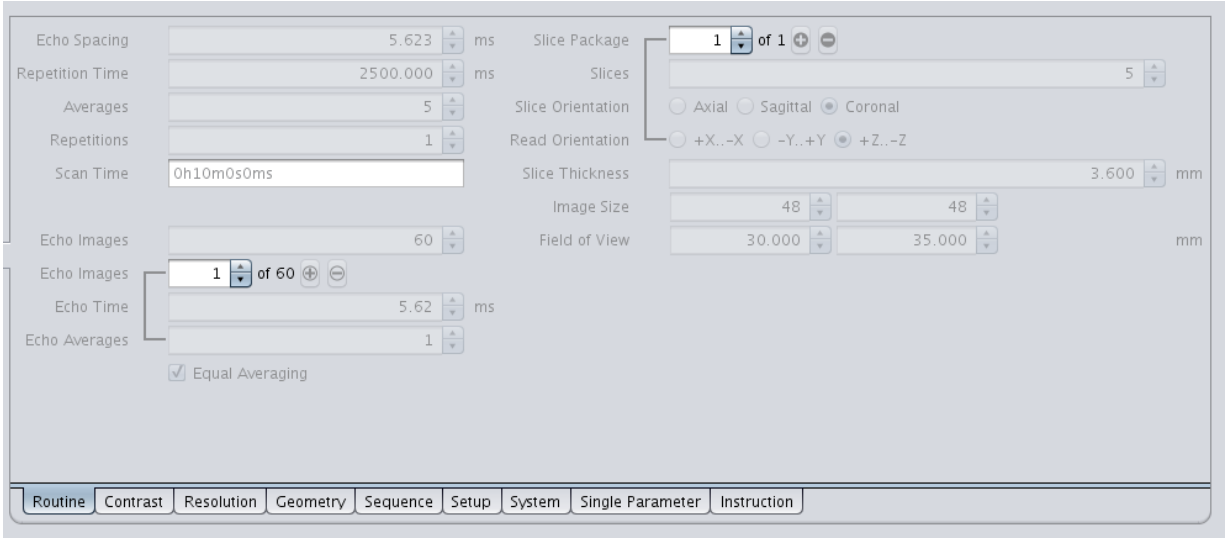

Figure A2.0.27 - Settings for the MSME scans on sample 10.

Figure A2.0.28 displays the region of interest for sample 11 used for the MSME results presented under chapter 3.1.3.

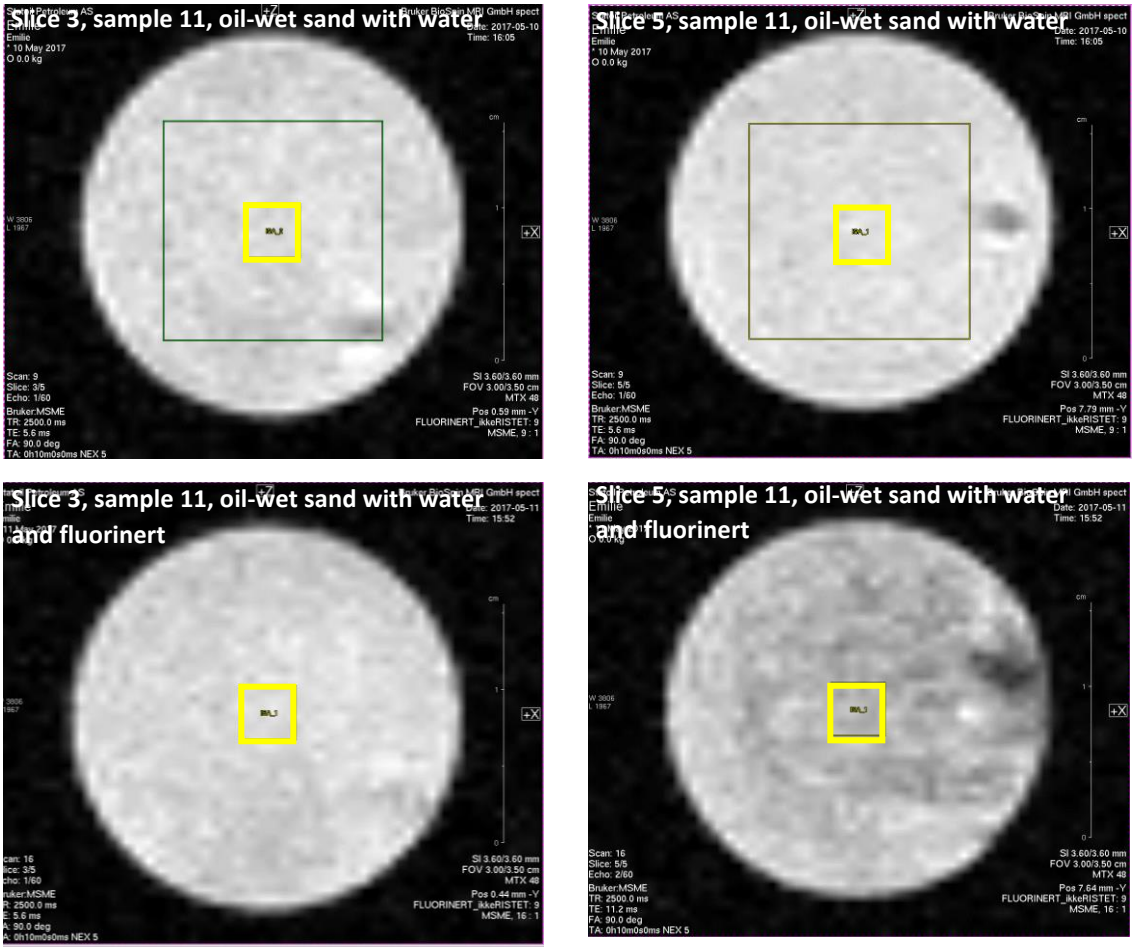

Figure A3.0.28 - Region of interest, displayed by the yellow square, for sample 11.

The smoothing parameters used for the inverse Laplace transformation for samples 4 to 9 and 11 is given in table A2.0.4.

Table A2.0.4 - Smoothing parameters used for the Inverse Laplace Transformation samples 4 to 9, and 11.

nnls smoothing parameters for ILT	Sample 4 to 9	Sample 11
Alpha	1e7	1e8
T/D min	0,001	0,001
Tmax	10	10
Steps	40	60

A3 Additional Information and Results, Melting Experiments

Details about the samples

Samples 14 to 17 were prepared for these experiments. The details about these samples are given in tables A3.0.1 and A3.0.2. Two mixtures were prepared. The first mixture was prepared slightly above the ideal hydration number for THF hydrates, with the relationship of 1 mole THF per 20 moles of H_2O. The second mixture was prepared slightly below the ideal hydration number for THF hydrates, with the mixture of 1 mole THF per 15 moles of H_2O.

Table A3.0.1 - Details about the mixtures used for samples 14 to 17.

Mixture 1		**Mixture 2**	
H_2O:THF	20:1	H_2O:THF	15:1
H_2O [g]	100,37	H_2O [g]	100,96
THF [g]	20,01	THF [g]	26,93
Total [g]	120,38	Total [g]	127,89
Weight % of THF	16,62	Weight % of THF	21,06

Table A3.0.2 - Details about the samples 14 to 17..

	Water-wet 15:1	**Water-wet 20:1**	**Oil-wet 15:1**	**Oil-wet 20:1**
Sand [g]	19,65	19,84	20,01	20,0091
Added liquid [g]	8,01	6,74	8,73	6,95
Removed surplus liquid [g]	1,91	2,75	-	0,46
Total liquid [g]	6,11	3,98	8,73	6,49

RAREst Protocol

Figure A3.0.1 displays the settings used to acquire the RAREst images of samples 14 to 17.

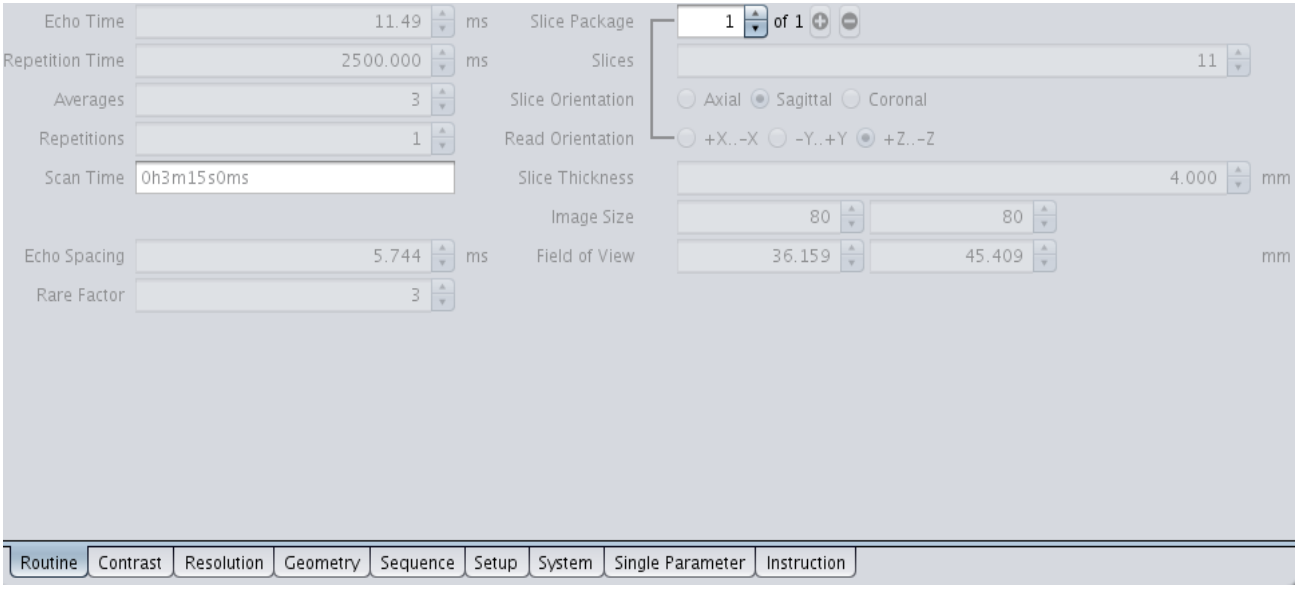

Figure A3.0.1 - Settings for the RAREst scans of samples 14 to 17. The only parameter that was altered was the field of view and number of slices.

Figure A3.0.2 illustrates how sample 14, water-wet sand with the mixture 1:15, was divided into slices.

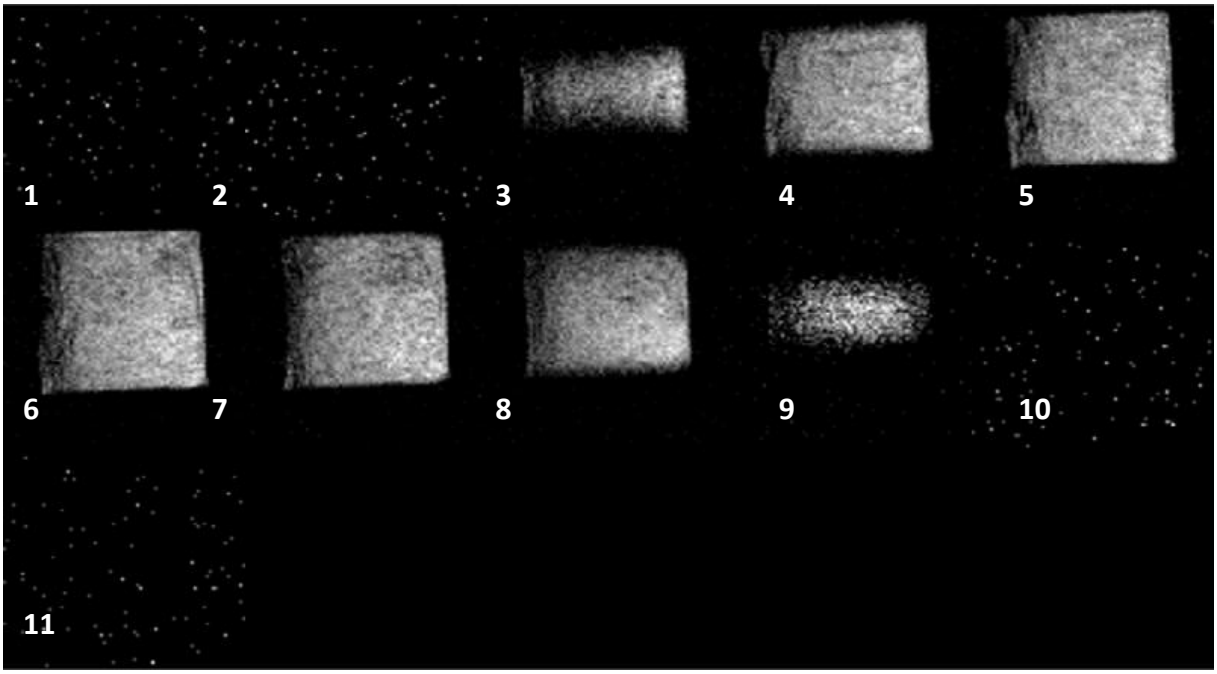

Figure A3.0.2 RAREst images of how sample 14, water-wet sand with the hydration mixture THF:H_2O 1:15, was divided into slices.

Figure A3.0.3 displays the dissociation process of THF hydrates in slice 5 from sample 14, water-wet sand with the mixture THF:H_2O 1:15.

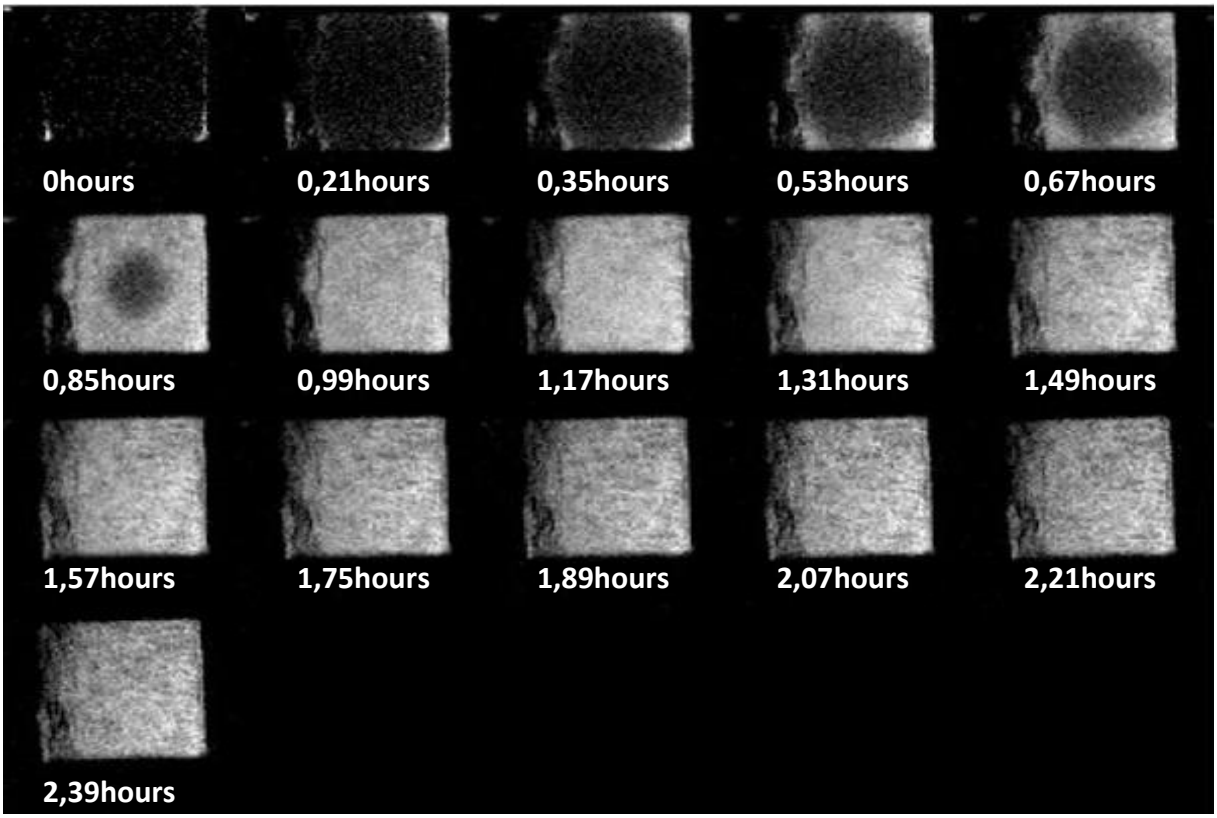

Figure A3.0.3 - RAREst images of slice 5 over time for sample 1.

Figure A3.0.4 displays the development of intensity for the dissociation process of THF hydrates in sample 14, water-wet sand with the mixture THF:H_2O 1:15, where each line represents a point in time. The slice numbers are displayed on the x-axis.

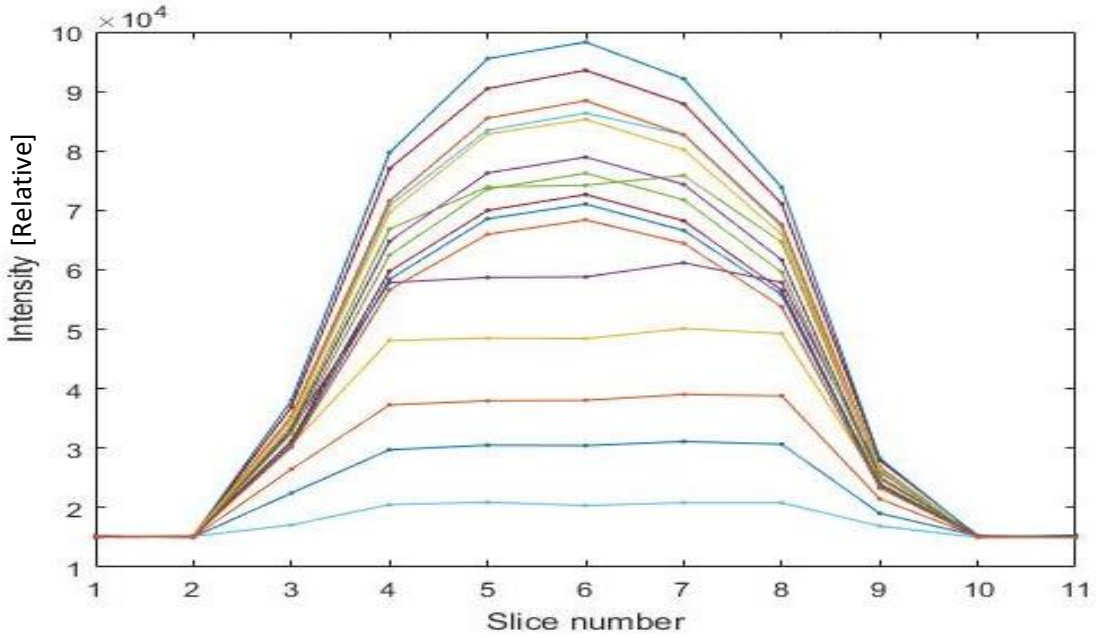

Figure A3.0.4 Intensity development as a function of slice number, for sample 14, water-wet sand with the mixture THF:H2O 1:15. Each line represents a point in time.

Figure A3.0.5 displays the intensity development for the dissociation process of THF hydrates in sample 14, water-wet sand with the mixture THF:H_2O 1:15, where each line represents a slice. The time is displayed on the x-axis.

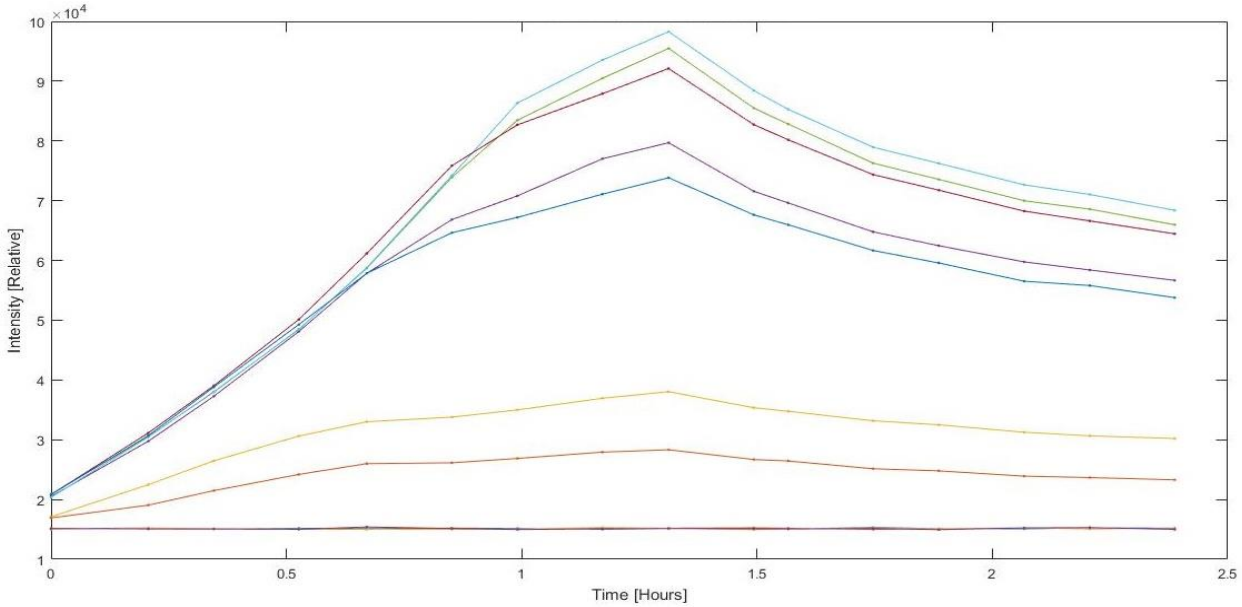

Figure A3.0.5 - Intensity development as a function of time for sample 14, water-wet sand with the mixture THF:H2O 1:15. Each line represents a slice.

Figure A3.0.6 displays the intensity development for the dissociation process of THF hydrates in sample 14, water-wet sand with the mixture THF:H_2O 1:15. All the slices of sample 14 are now summarized to represent the total sample. The time is displayed on the x-axis.

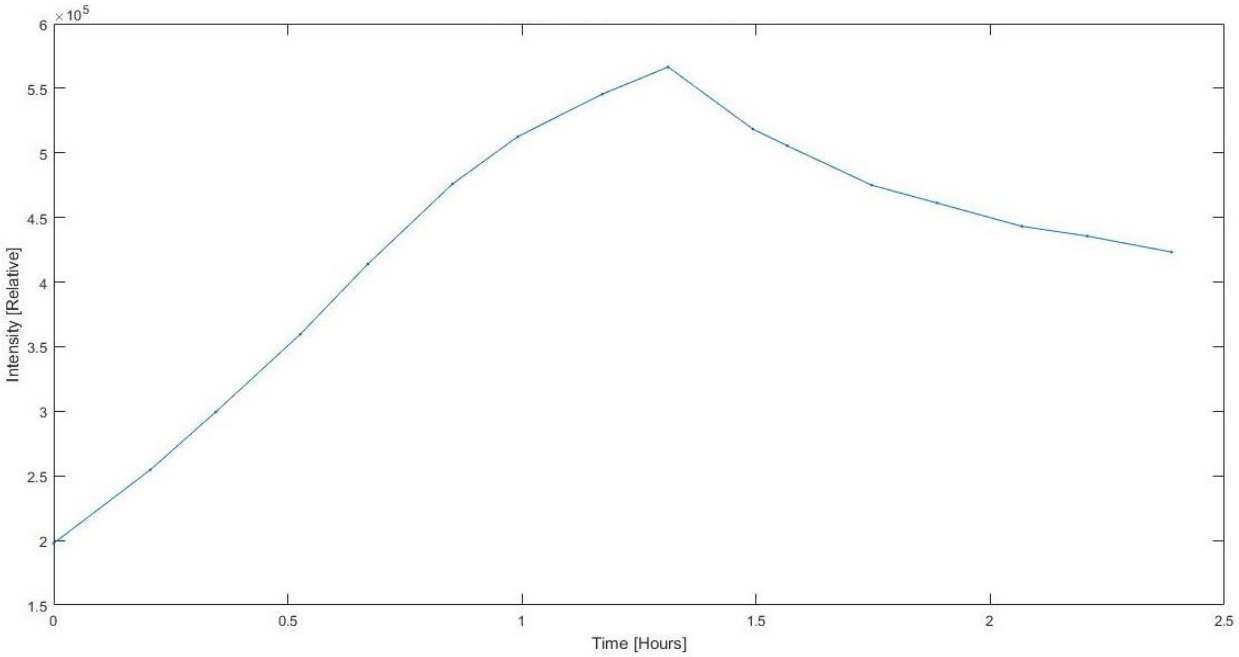

Figure A3. 0.6 - Intensity development as a function of time for sample 14, water-wet sand with the mixture THF:H2O 1:15. All slices are summarized to one total value of intensity development.

Figure A3.0.7 displays the intensity development for the dissociation process of THF hydrates in sample 14, water-wet sand with the mixture THF:H_2O 1:15, as the data has been corrected for noise and stopped at the time of total dissociation of hydrates. Each line represents a slice and the time passed is displayed on the x-axis.

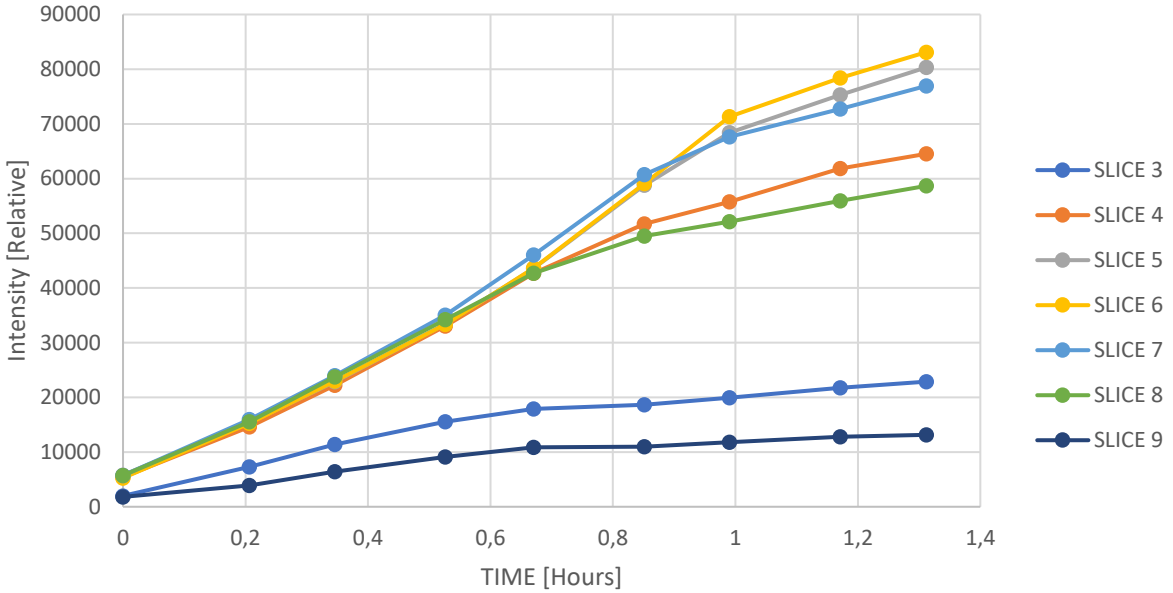

Figure A3.0.7 - Intensity development as a function of time for sample 14, water-wet sand with the mixture THF:H2O 1:15, when the noise is removed, and the total dissociation process of hydrates are corrected for. Each line represents a slice.

Figure A3.0.8 displays the hydrate saturation for the dissociation process of THF hydrates in sample 14, water-wet sand with the mixture THF:H_2O 1:15, as the data has been corrected for noise and stopped at the time of total dissociation of hydrates. Each line represents a slice and the time passed is displayed on the x-axis.

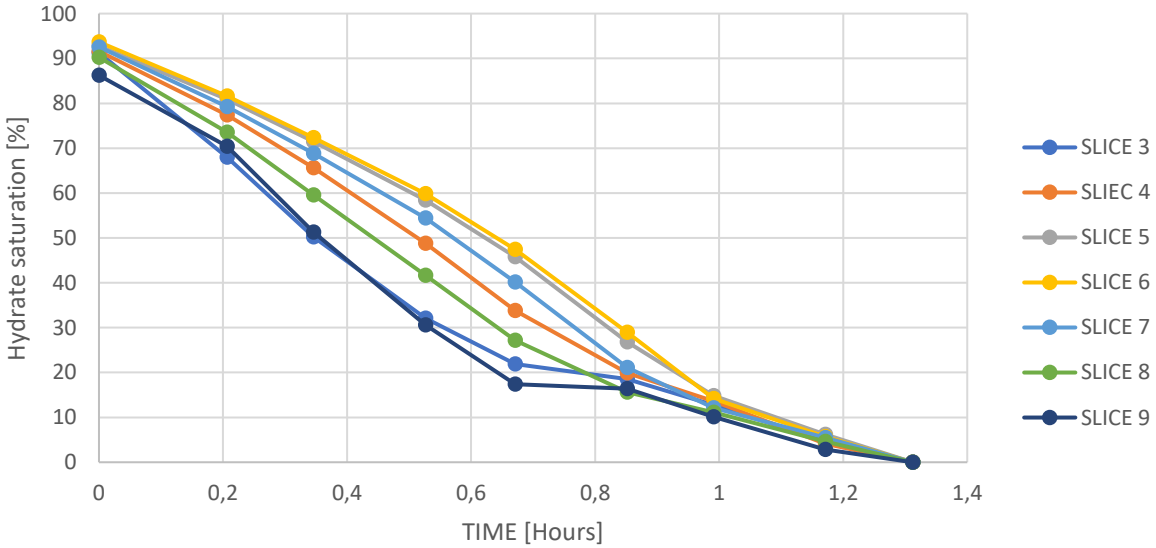

Figure A3.0.8 – Hydrate saturation as a function of time for sample 14, water-wet sand with the mixture THF:H2O 1:15, when the noise is removed, and the total dissociation process of hydrates are corrected for. Each line represents a slice.

Figure A3.0.9 illustrates how sample 3, water-wet sand with the mixture 1:20, was divided into slices.

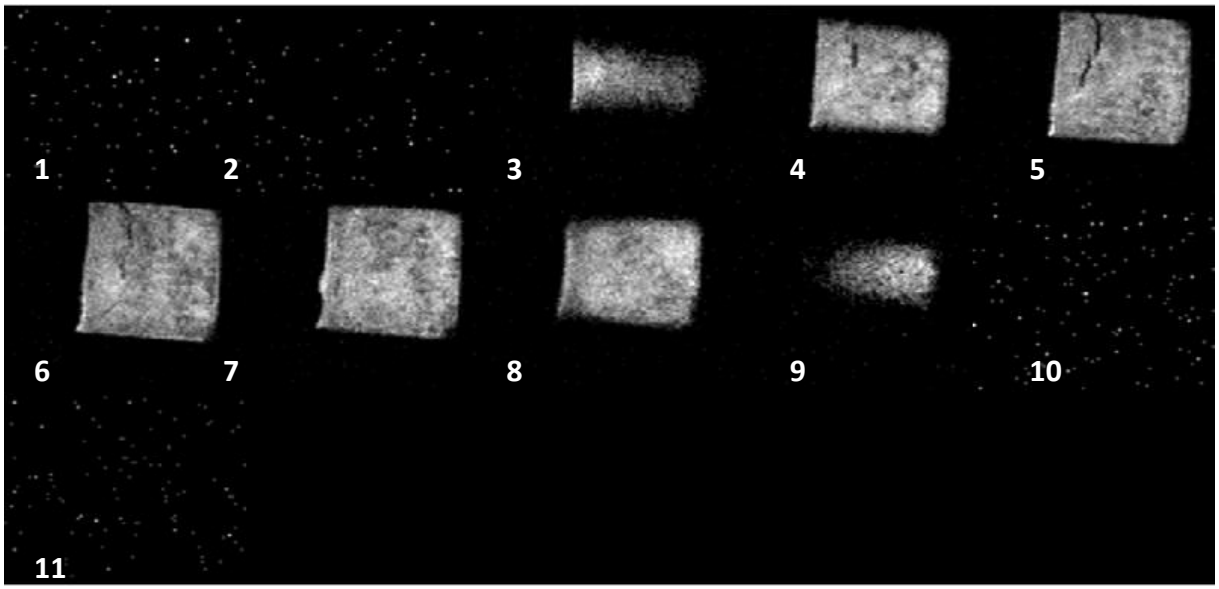

Figure A3.0.9 - RAREst images of how sample 16, water-wet sand with the hydration mixture THF:H2O 1:20, was divided into slices.

Figure A3.0.10 displays the dissociation process of THF hydrates in slice 5 from sample 16, water-wet sand with the mixture THF:H_2O 1:20.

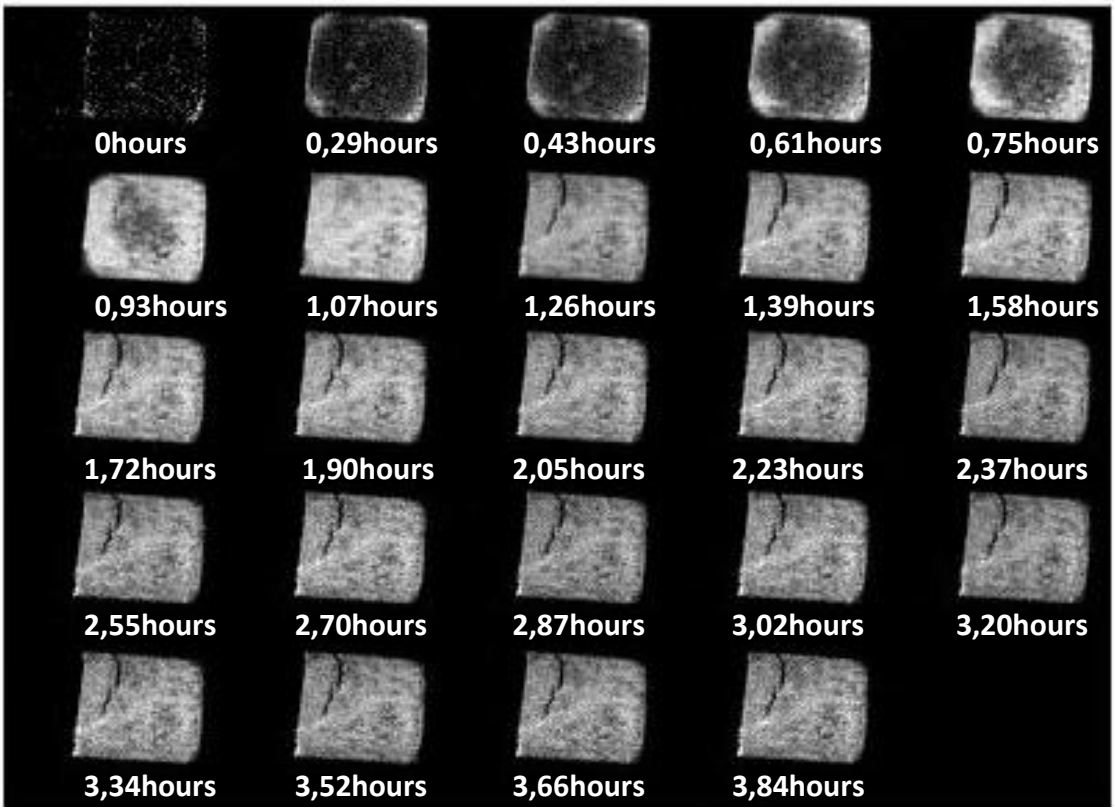

Figure A3.0.10 - RAREst images of slice 5 over time for sample 16.

Figure A3.0.11 displays the development of intensity for the dissociation process of THF hydrates in sample 16, water-wet sand with the mixture THF:H_2O 1:20, where each line represents a point in time. The slice numbers are displayed on the x-axis.

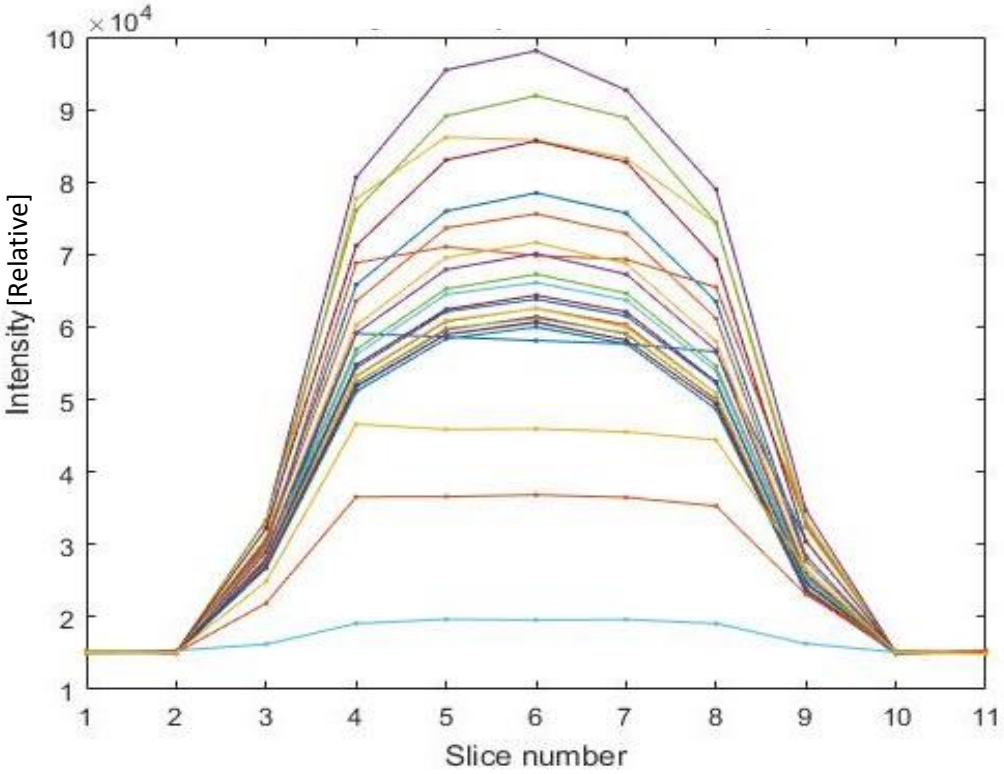

Figure A3.0.11 - Intensity development as a function of slice number, for sample 16, water-wet sand with the mixture THF:H2O 1:20. Each line represents a point in time.

Figure A3.0.12 displays the intensity development for the dissociation process of THF hydrates in sample 16, water-wet sand with the mixture THF:H_2O 1:20, where each line represents a slice. The time is displayed on the x-axis.

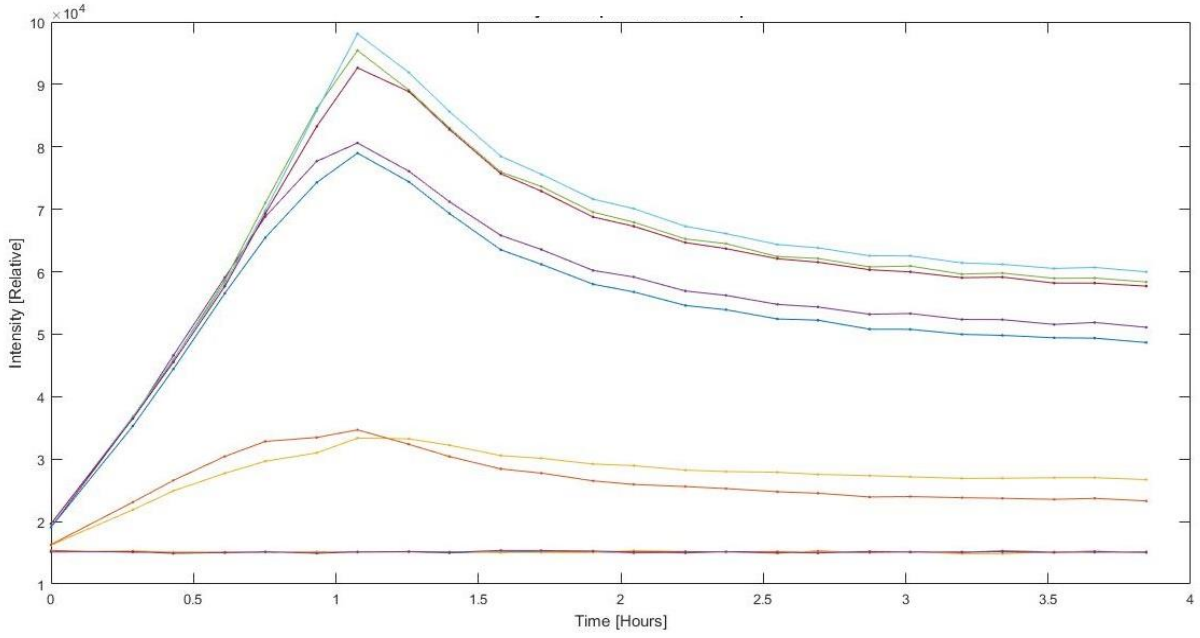

Figure A3.0.12 - Intensity development as a function of time for sample 16, water-wet sand with the mixture THF:H2O 1:20. Each line represents a slice.

Figure A3.0.13 displays the intensity development for the dissociation process of THF hydrates in sample 16, water-wet sand with the mixture THF:H_2O 1:20. All the slices of sample 16 are now summarized to represent the total sample. The time is displayed on the x-axis.

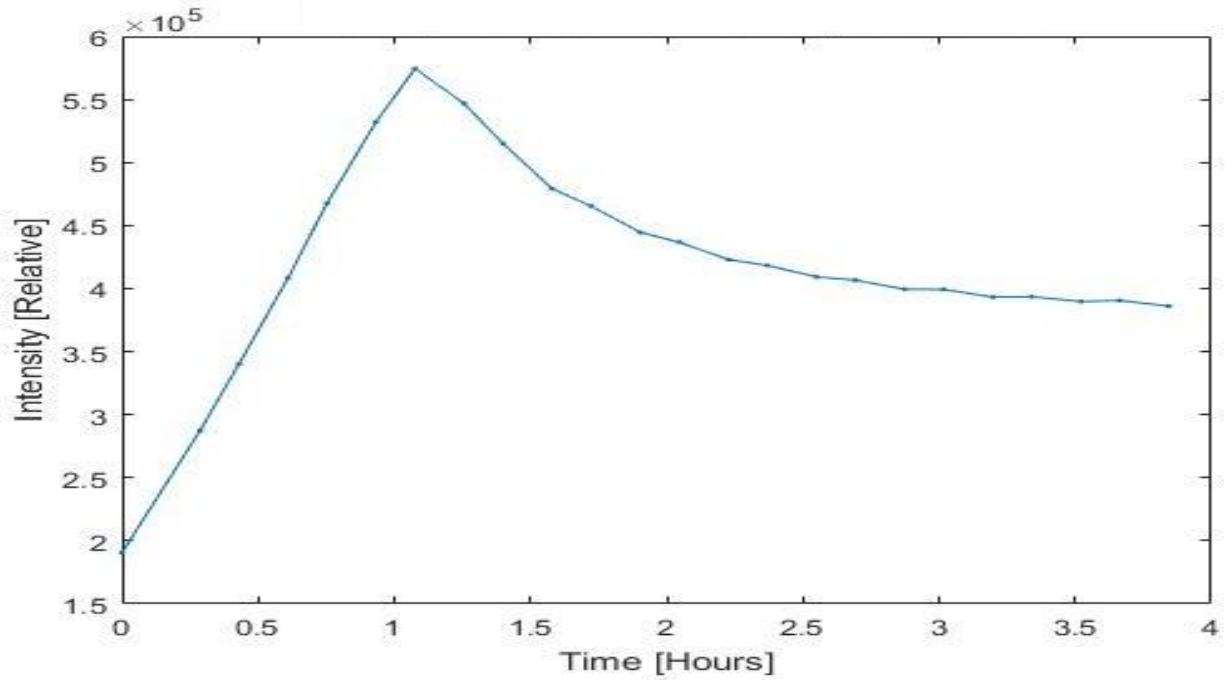

Figure A3.0.13 - Intensity development as a function of time for sample 16, water-wet sand with the mixture THF:H2O 1:20. All slices are summarized to one total value of intensity development.

Figure A3.0.14 displays the intensity development for the dissociation process of THF hydrates in sample 16, water-wet sand with the mixture THF:H_2O 1:20, as the data has been corrected for noise and stopped at the time of total dissociation of hydrates. Each line represents a slice and the time passed is displayed on the x-axis.

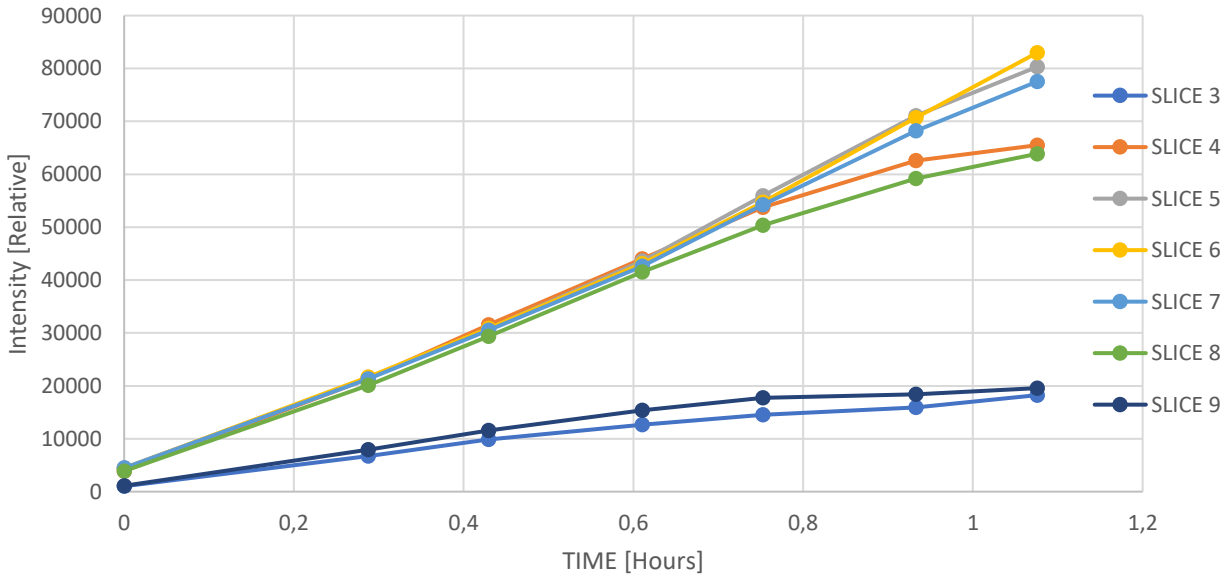

Figure A3.0.14 - Intensity development as a function of time for sample 16, water-wet sand with the mixture THF:H2O 1:20, when the noise is removed, and the total dissociation process of hydrates are corrected for. Each line represents a slice.

Figure A3.0.15 displays the hydrate saturation for the dissociation process of THF hydrates in sample 16, water-wet sand with the mixture THF:H_2O 1:20, as the data has been corrected for noise and stopped at the time of total dissociation of hydrates. Each line represents a slice and the time passed is displayed on the x-axis.

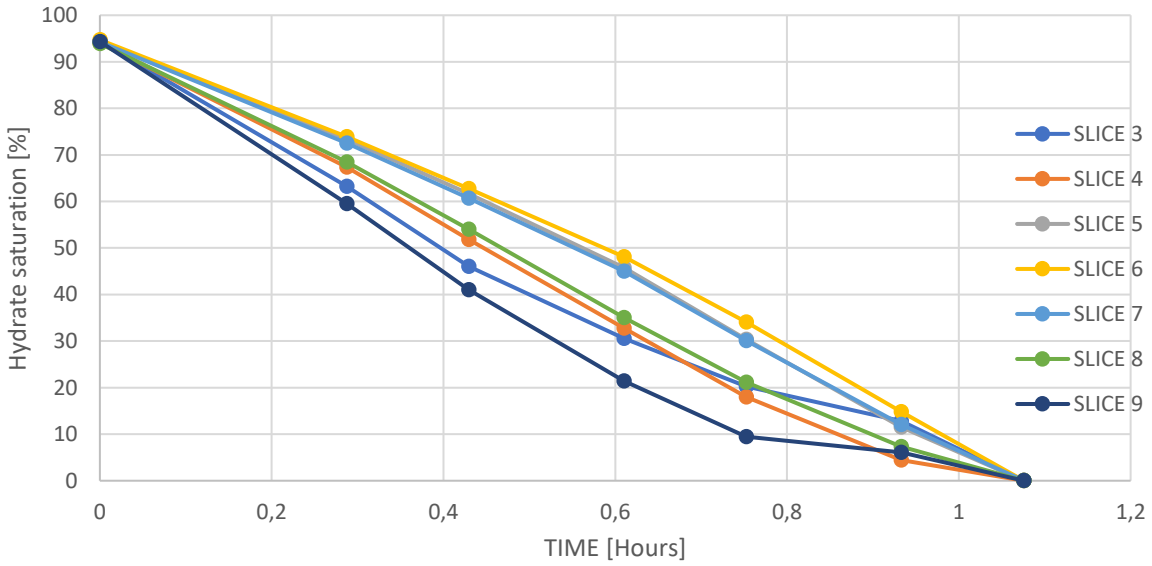

Figure A3.0.15 - Hydrate saturation as a function of time for sample 16, water-wet sand with the mixture THF:H2O 1:20, when the noise is removed, and the total dissociation process of hydrates are corrected for. Each line represents a slice.

Figure A3.0.16 illustrates how sample 17, oil-wet sand with the mixture THF:H_2O 1:20, was divided into slices

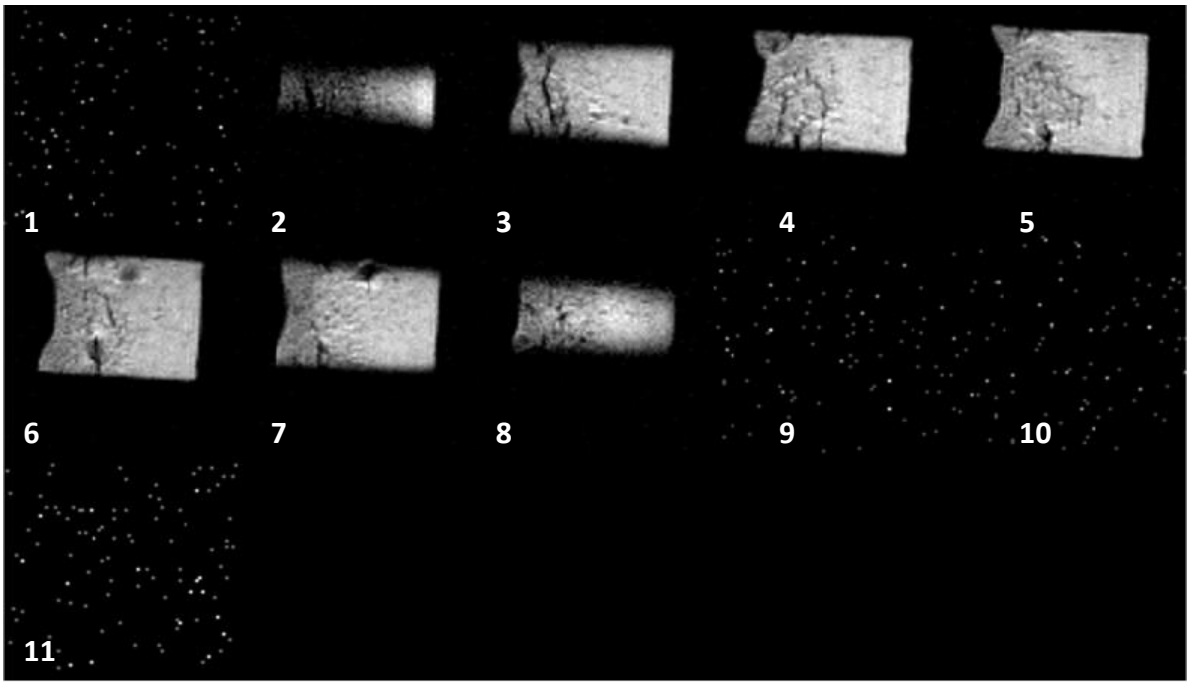

Figure A3.0.16 - RAREst images of how sample 17, oil-wet sand with the hydration mixture THF:H2O 1:20, was divided into slices.

Figure A3.0.17 displays the dissociation process of THF hydrates in slice 5 from sample 17, oil-wet sand with the mixture THF:H_2O 1:20.

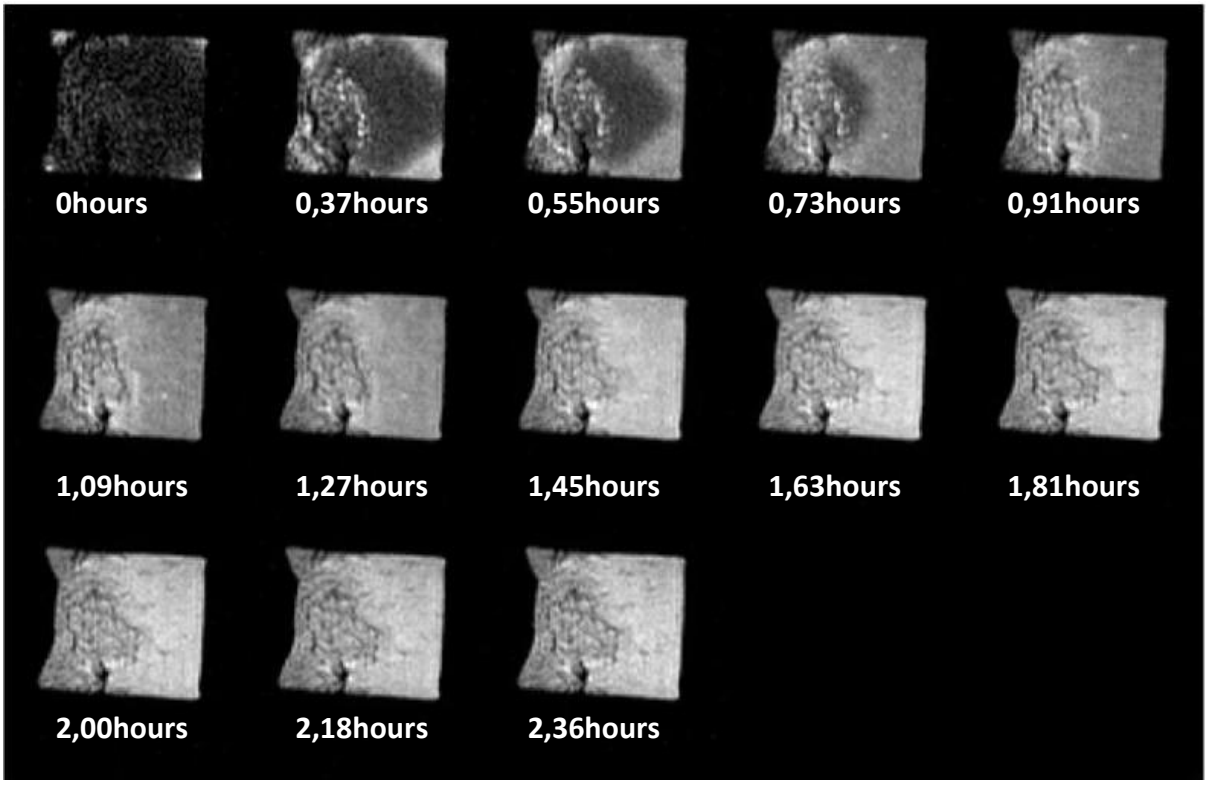

Figure A3.0.17 - RAREst images of slice 5 over time for sample 17.

Figure A3.0.18 displays the development of intensity for the dissociation process of THF hydrates in sample 17, oil-wet sand with the mixture THF:H_2O 1:20, where each line represents a point in time. The slice numbers are displayed on the x-axis.

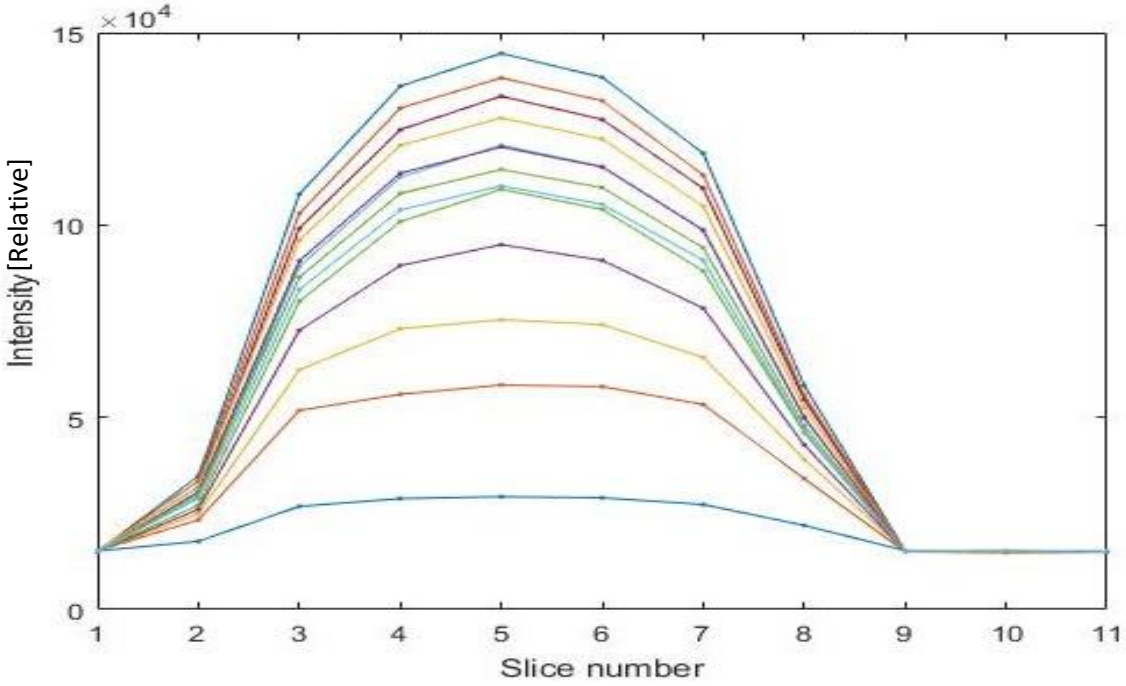

Figure A3.0.18 - Intensity development as a function of time for sample 17, oil-wet sand with the mixture THF:H2O 1:20. Each line represents a point in time.

Figure A3.0.19 displays the intensity development for the dissociation process of THF hydrates in sample 17, oil-wet sand with the mixture THF:H_2O 1:20, where each line represents a slice. The time is displayed on the x-axis.

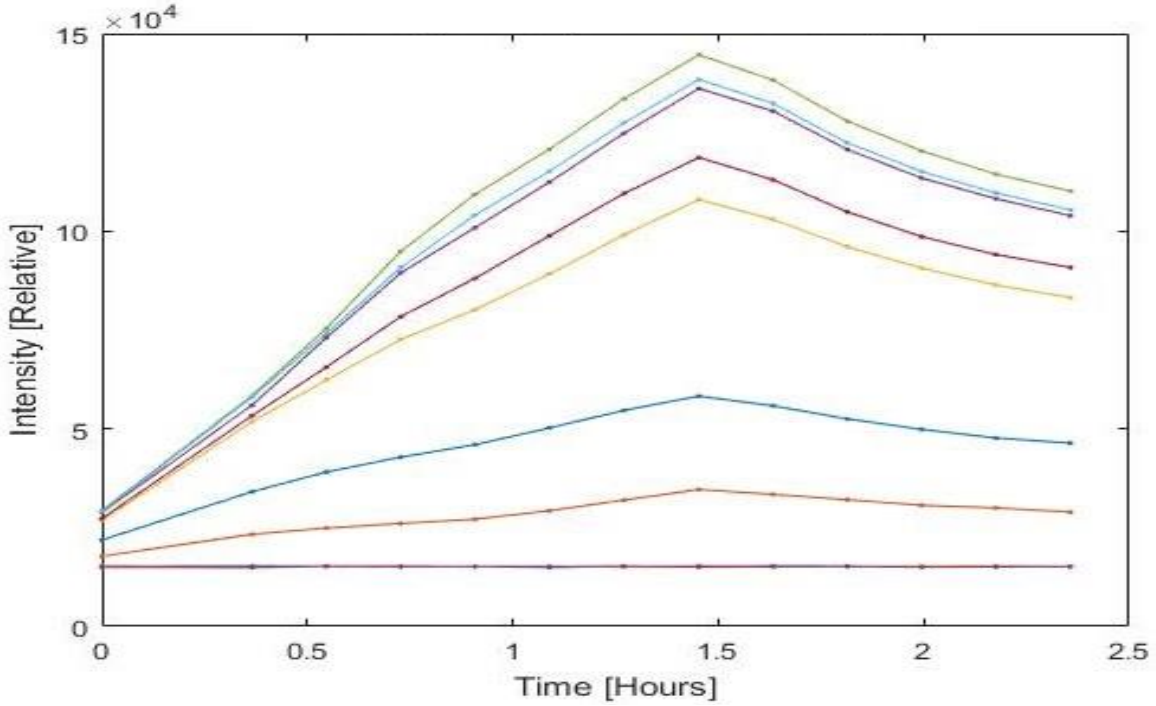

Figure A3.0.19 - Intensity development as a function of time for sample 17, oil-wet sand with the mixture THF:H2O 1:20. Each line represents a slice.

Figure A3.0.20 displays the intensity development for the dissociation process of THF hydrates in sample 17, oil-wet sand with the mixture THF:H_2O 1:20. All the slices of sample 17 are now summarized to represent the total sample. The time is displayed on the x-axis.

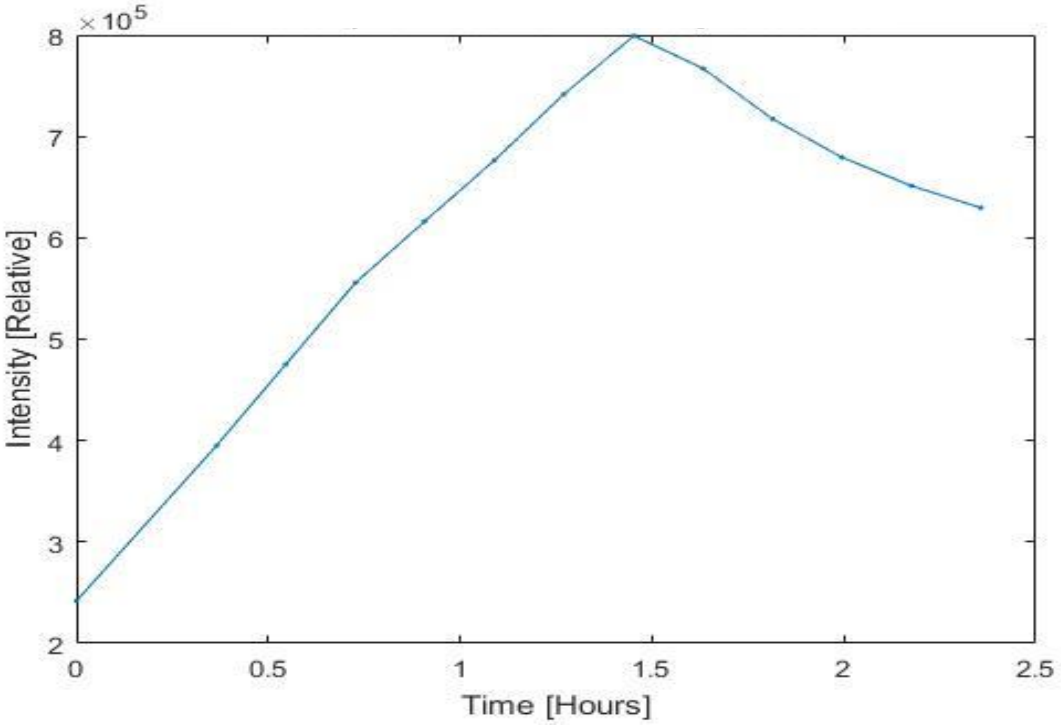

Figure A3.0.20 - Intensity development as a function of time for sample 17, oil-wet sand with the mixture THF:H2O 1:20. All slices are summarized to one total value of intensity development.

Figure A3.0.21 displays the intensity development for the dissociation process of THF hydrates in sample 17, oil-wet sand with the mixture THF:H_2O 1:20, as the data has been corrected for noise and stopped at the time of total dissociation of hydrates. Each line represents a slice and the time passed is displayed on the x-axis.

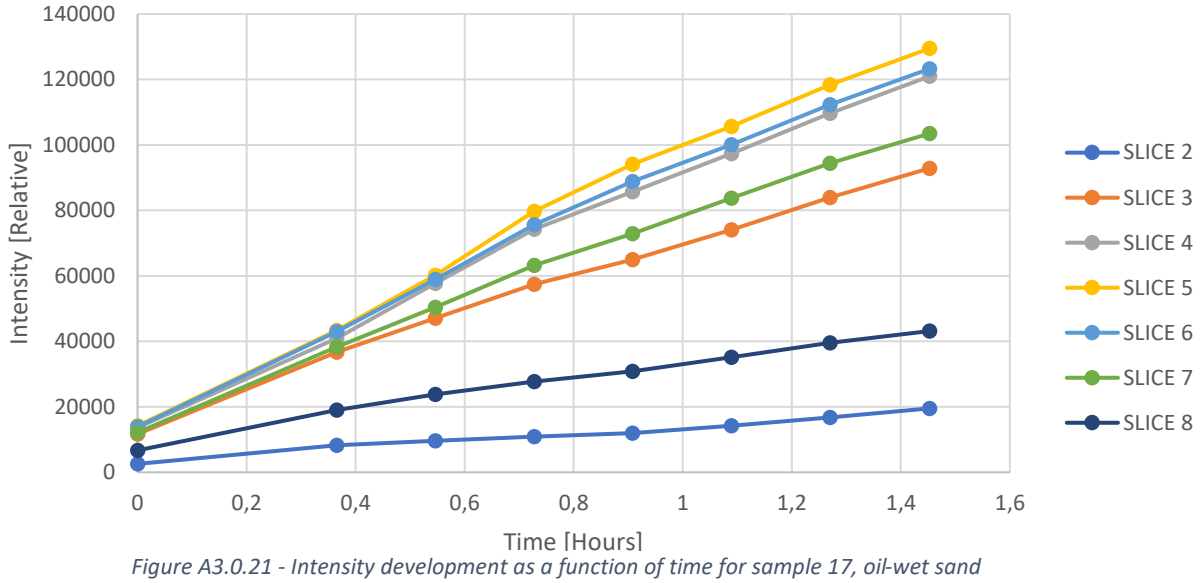

Figure A3.0.21 - Intensity development as a function of time for sample 17, oil-wet sand with the mixture THF:H2O 1:20, when the noise is removed, and the total dissociation process of hydrates are corrected for. Each line represents a slice.

Figure A3.0.22 displays the hydrate saturation for the dissociation process of THF hydrates in sample 17, oil-wet sand with the mixture THF:H_2O 1:20, as the data has been corrected for noise and stopped at the time of total dissociation of hydrates. Each line represents a slice and the time passed is displayed on the x-axis.

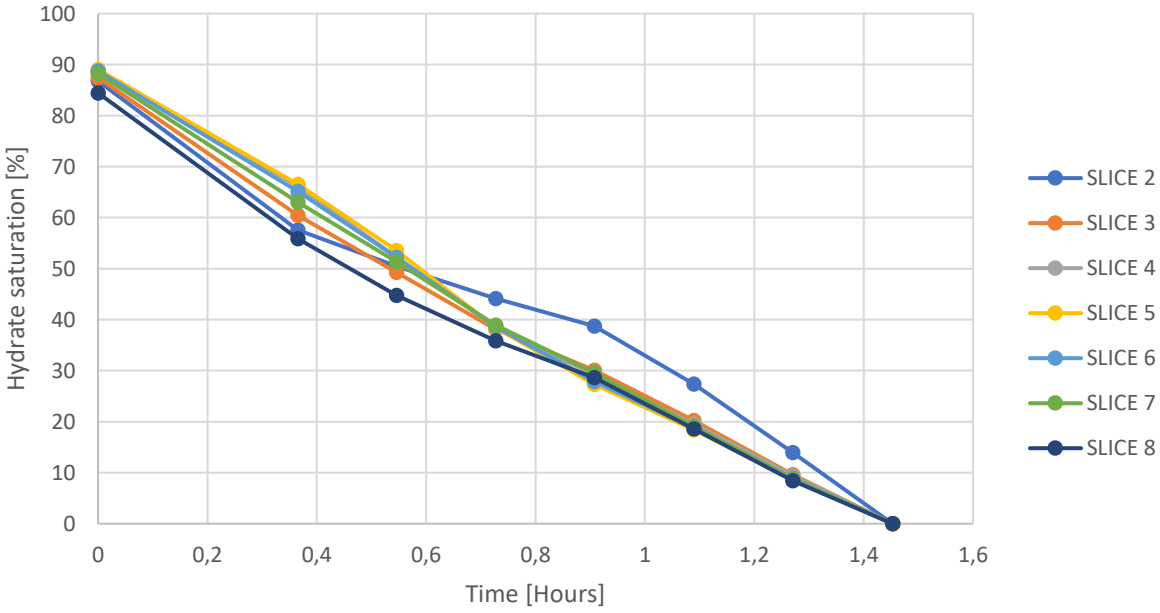

Figure A3.0.22 - Hydrate saturation as a function of time for sample 17, oil-wet sand with the mixture THF:H2O 1:20, when the noise is removed, and the total dissociation process of hydrates are corrected for. Each line represents a slice.

CPMG Protocol

Figure A3.0.23 displays the settings used to acquire the CPMG measurements of samples 4 to 17.

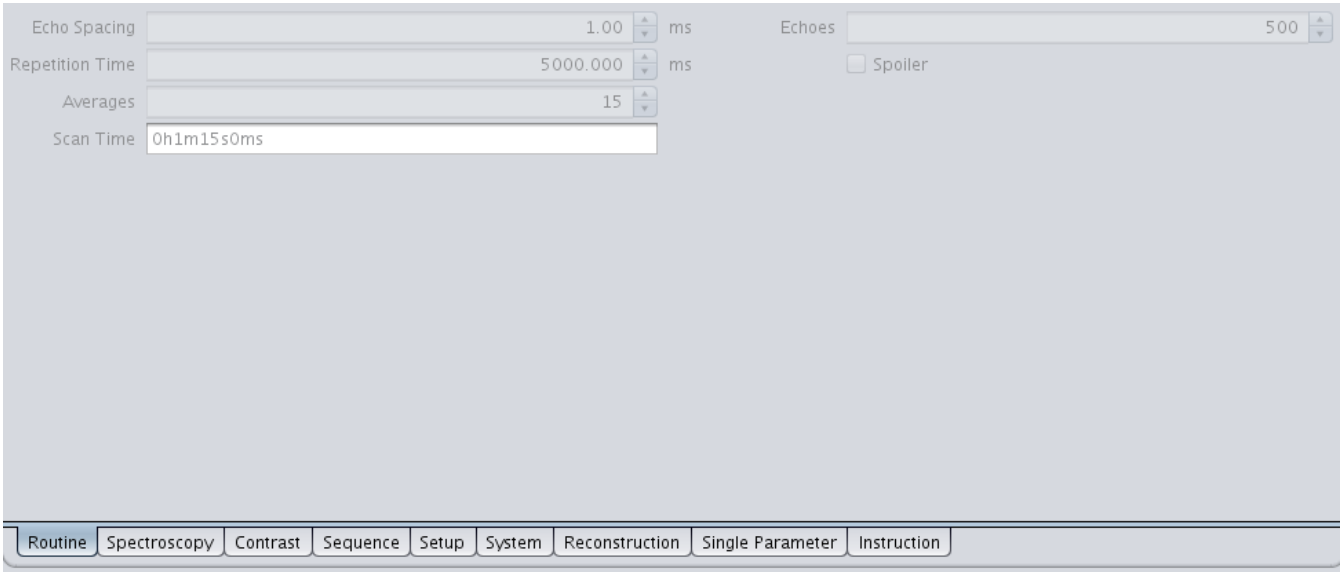

Figure A3.0.23 - Settings for the CPMG scans used for samples 1 to 4.

Figure A3.0.24 displays decay curves for sample 14, water-wet sand with the hydrate mixture THF:H_2O 1:15.

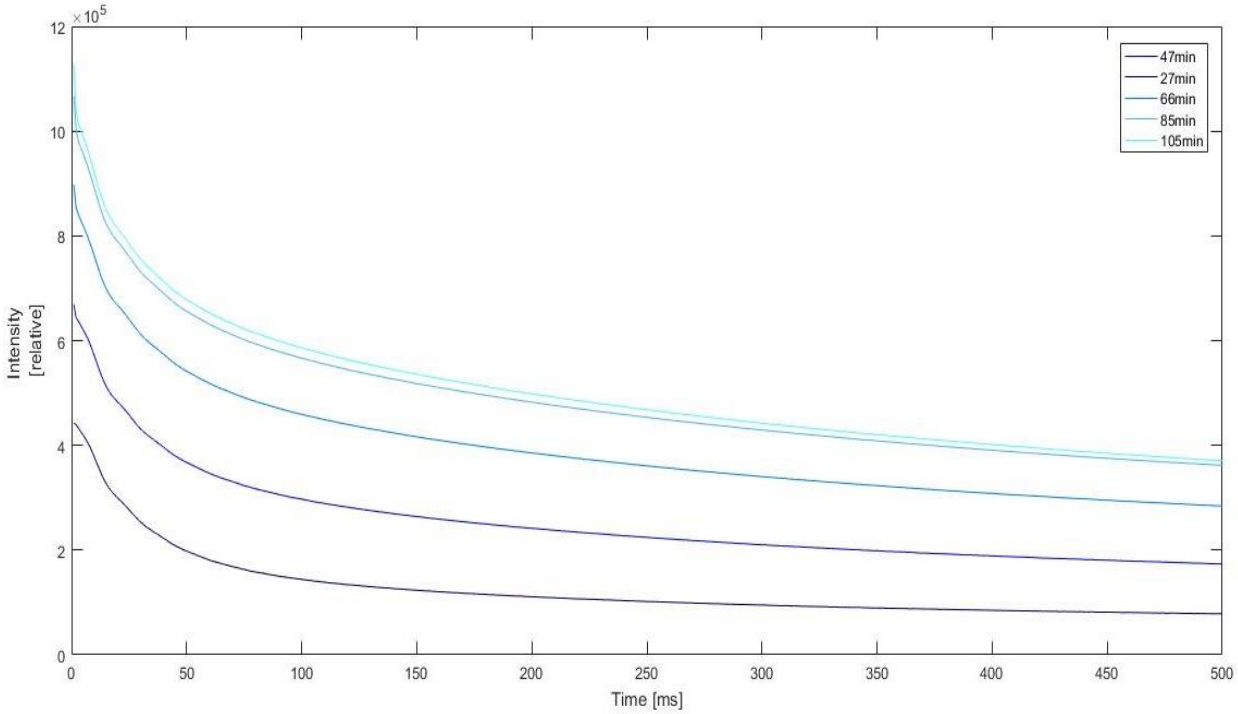

Figure A3.0.24 - Decay curves for sample 14, water-wet sand with mixture THF:H2O 1:15 from CPMG scans.

Figure A3.0.25 displays decay curves for sample 15, oil-wet sand with the hydrate mixture THF:H_2O 1:15.

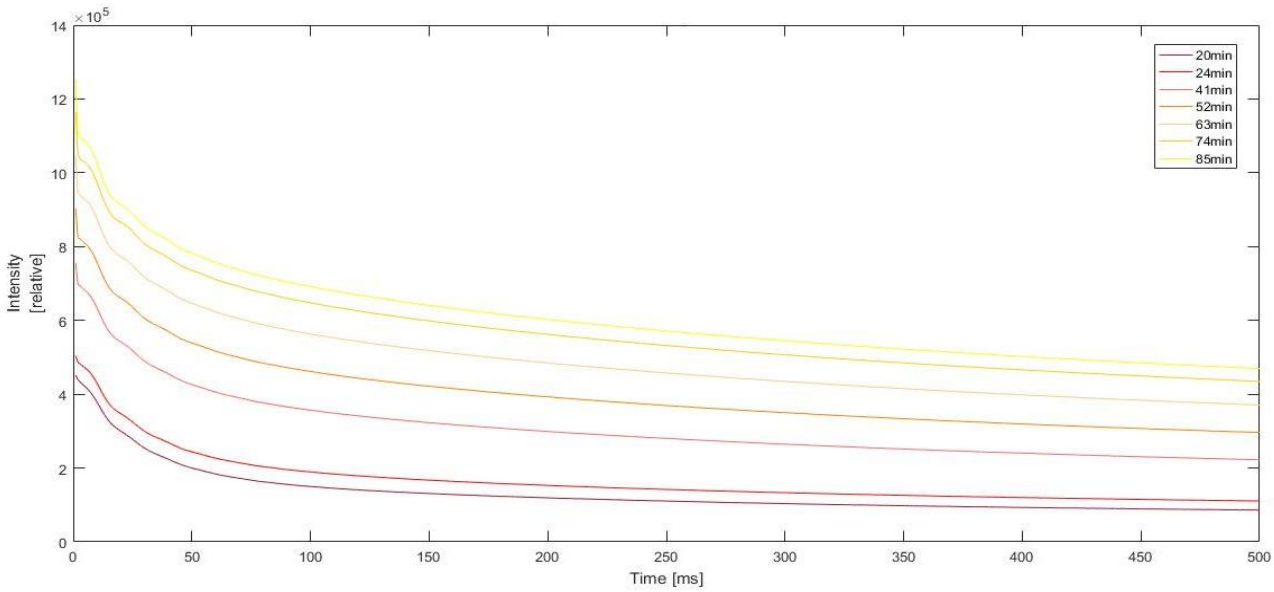

Figure A3.0.25 - Decay curves for sample 15, oil-wet sand with mixture THF:H2O 1:15 from CPMG scans.

Figure A3.0.26 displays decay curves for sample 16, water-wet sand with the hydrate mixture THF:H_2O 1:20.

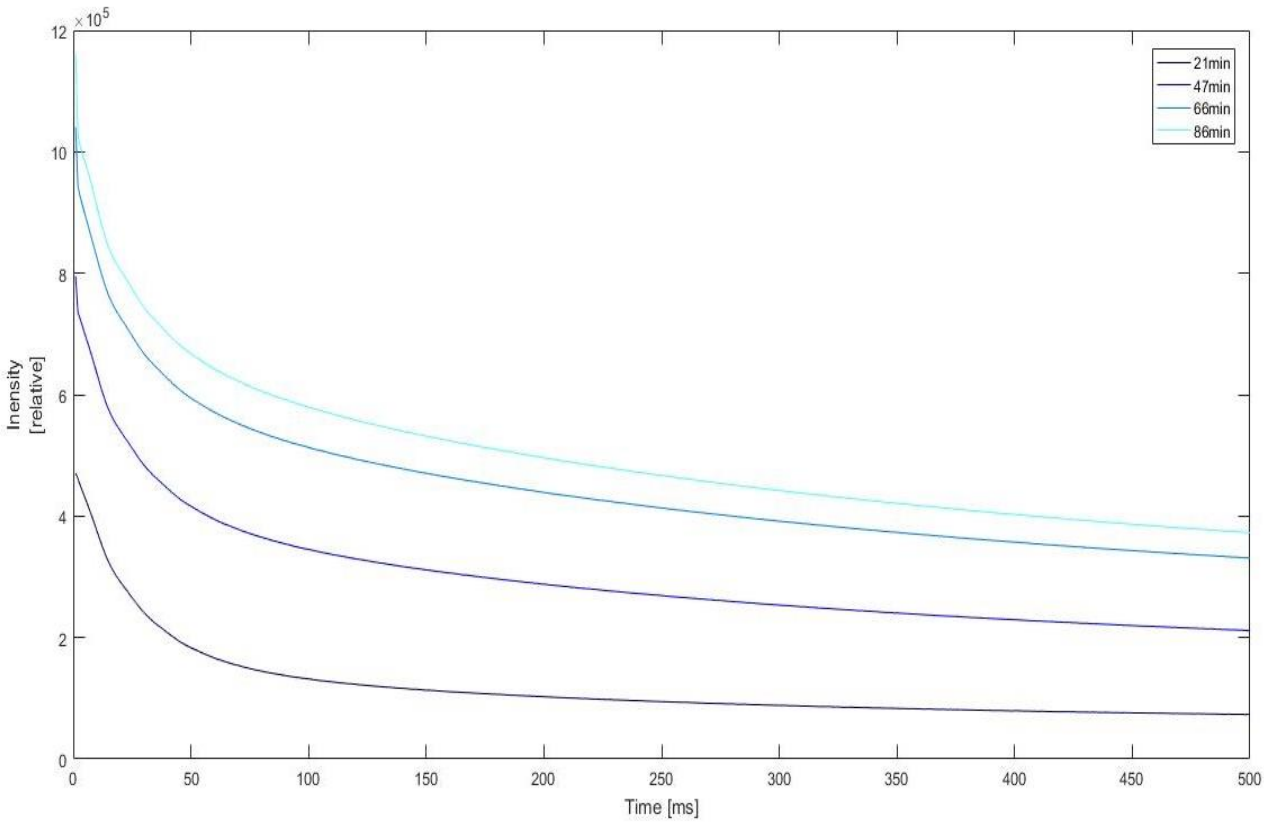

Figure A3.0.26 - Decay curves for sample 16, water-wet sand with mixture THF:H2O 1:20 from CPMG scans.

Figure A3.0.27 displays decay curves for sample 17, oil-wet sand with the hydrate mixture THF:H_2O 1:20.

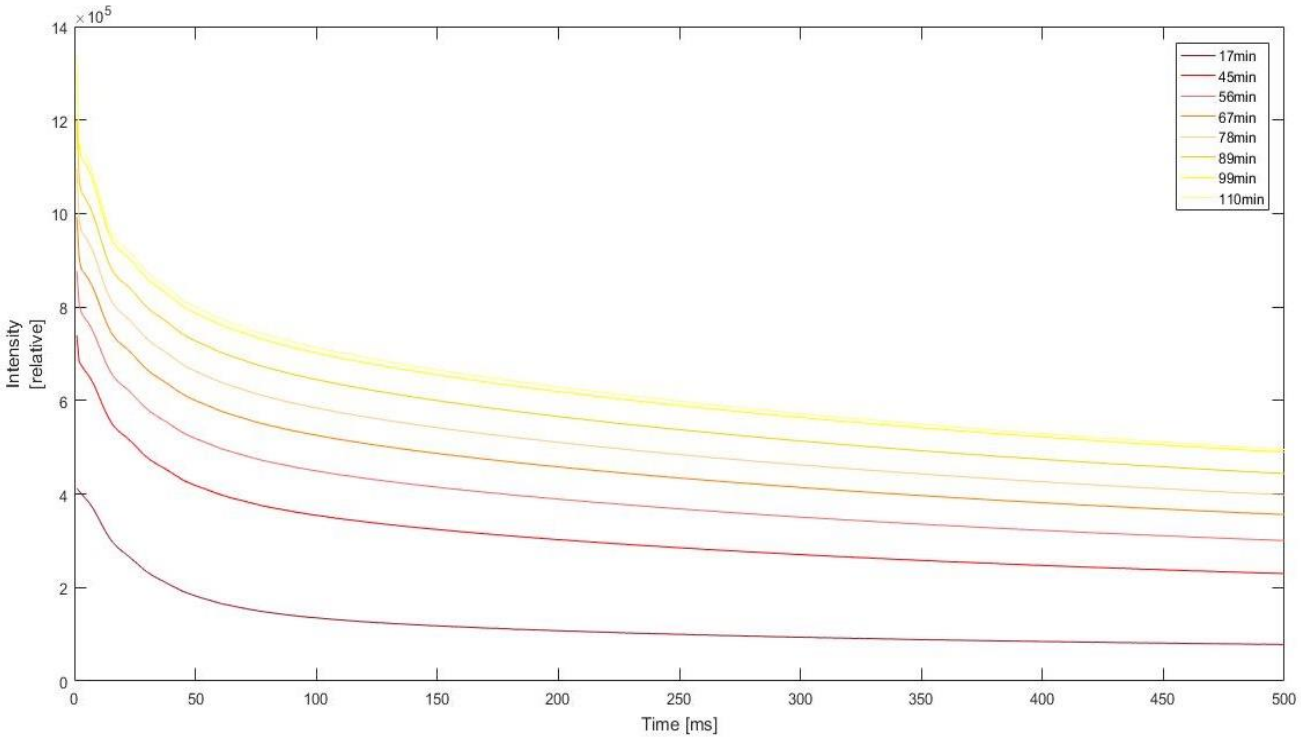

Figure A3.0.27 - Decay curves for sample 17, oil-wet sand with mixture THF:H2O 1:20 from CPMG scans.

These decay curves were used for further analysis through the inverse Laplace transformation to create T_2^a relaxation time distribution curves. To create a better fit for the data from these scans some data points had to be removed. The settings for the nnls-smoothing is given in table A3.0.3.

Table A3.0.3 - Parameters used for nnls smoothing for the inverse Laplace transformation performed on samples 14 to 17.

nnls smoothing parameters for ILT	
Alpha	1e7
T/D min	0,001
Tmax	10
Steps	150

Figure A3.0.28 displays the T_2^a relaxation time distribution for sample 14, water-wet sand with the hydrate mixture THF:H_2O 1:15.

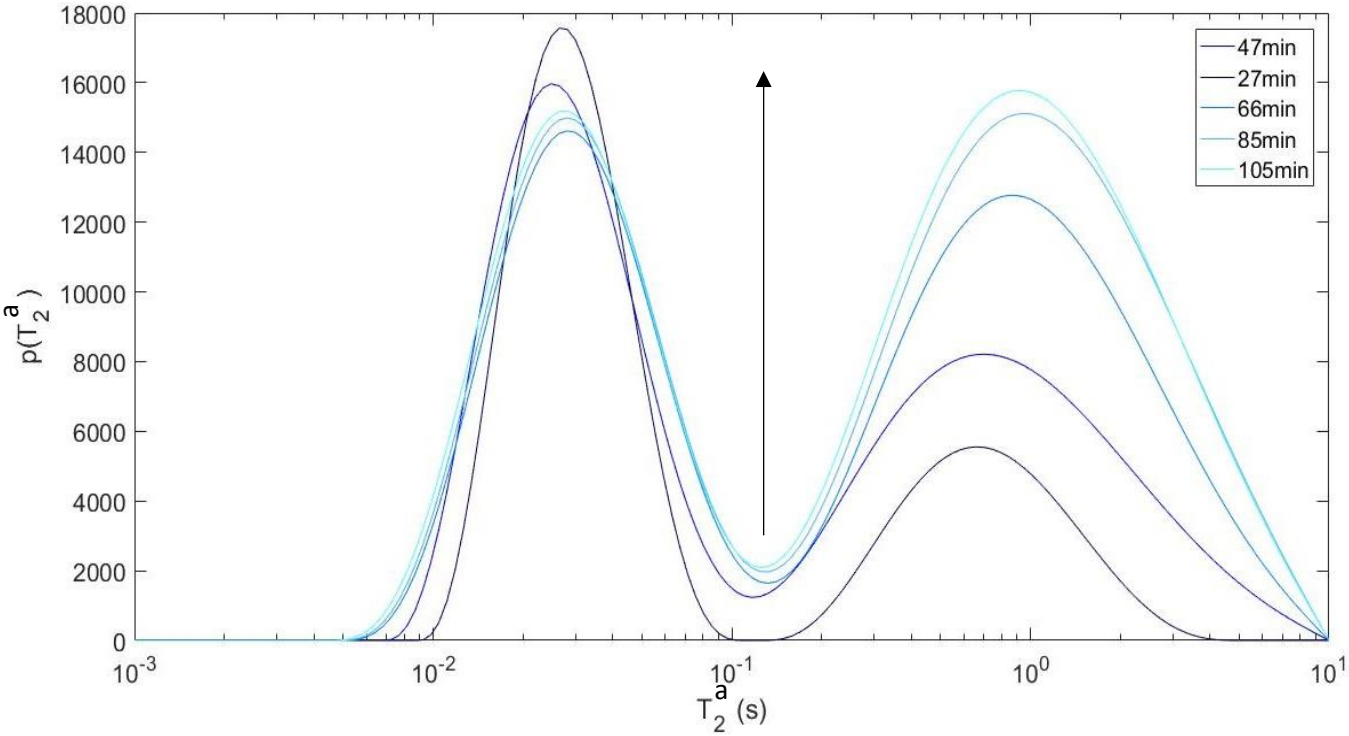

Figure A3.0.28 – T_2^a relaxation time distribution from CPMG data for sample 14, water-wet sand with a mixture THF:H2O 1:15. The development of the peaks follows the direction of the arrow.

Figure A3.0.29 displays the T_2^a relaxation time distribution for sample 16, water-wet sand with the hydrate mixture THF:H_2O 1:20.

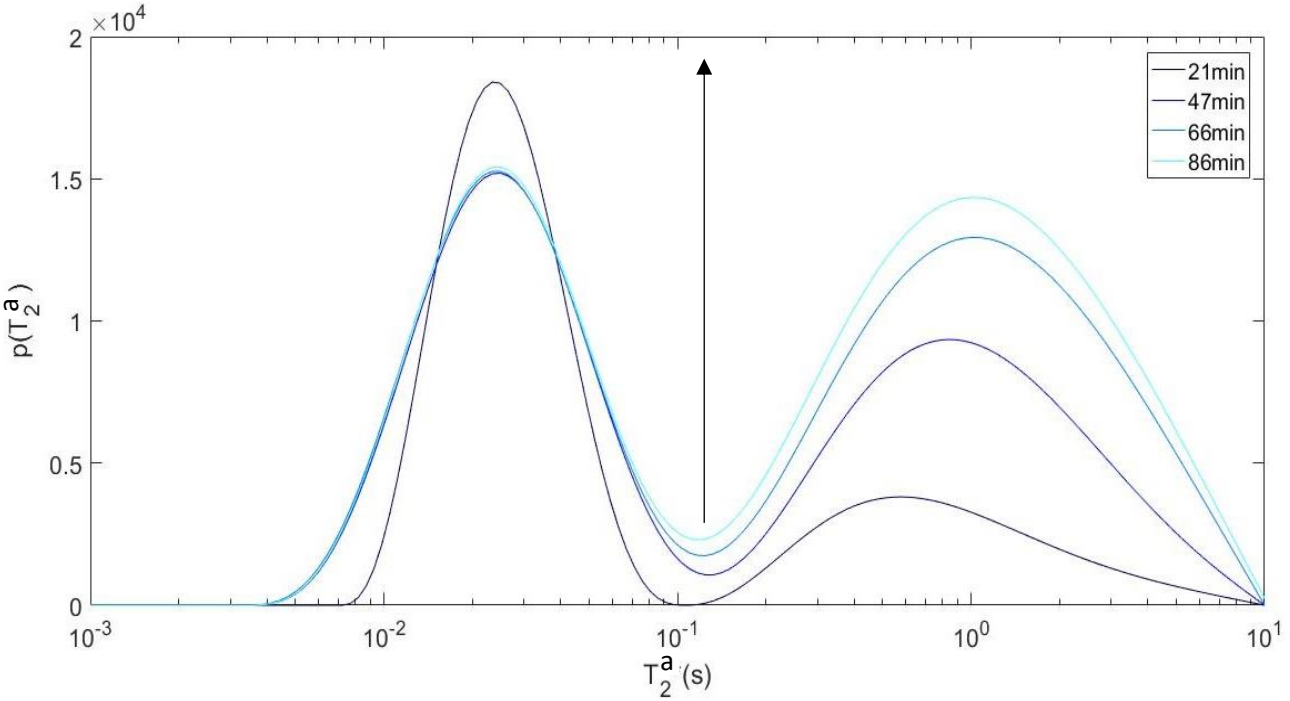

Figure A3.0.29 - T_2^a relaxation time distribution from CPMG data for sample 16, water-wet sand with a mixture THF:H2O 1:20. The development of the peaks follows the direction of the arrow.

Figure A3.0.30 displays the T_2^a relaxation time distribution for sample 14, water-wet sand with the hydrate mixture THF:H_2O 1:15, and for sample 16, water-wet sand with the hydrate mixture THF:H_2O 1:20.

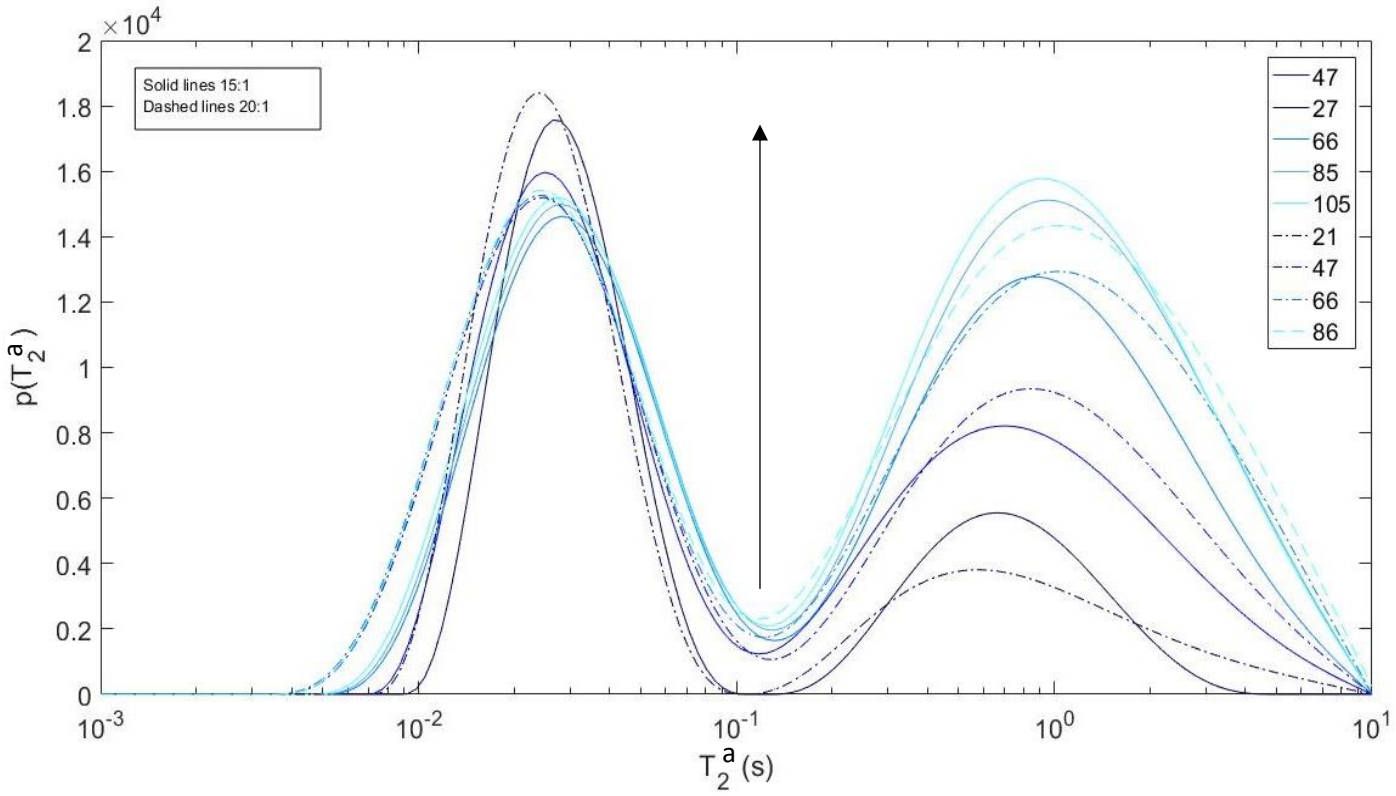

Figure A3.0.30 - T_2^a relaxation time distribution from CPMG data for sample 14, water-wet sand with a mixture THF:H2O 1:15, and for sample 16, water-wet sand with a mixture THF:H2O 1:20. The development of the peaks follows the direction of the arrow.

Table A3.0.4 displays the peak T_2^a distribution values from figure A3.0.30.

Table A3.0.4 - Peak values from the T_2^a relaxation time distribution for samples 14 and 16.

Water-wet sand 15:1 time [min]	peak one [ms]	peak two [ms]	Water-wet sand 20:1 time [min]	peak one [ms]	peak two [ms]
27 min	27,315	658,9	21 min	23,4	514,5
47 min	24,89	700,9	47 min	24,89	843,7
66 min	28,16	843,7	66 min	24,89	954,7
85 min	28,16	954,7	86 min	24,89	954,7
105 min	28,16	954,7	-	-	-

Figure A3.0.31 displays the T_2^a relaxation time distribution for sample 15, oil-wet sand with the hydrate mixture THF:H_2O 1:15.

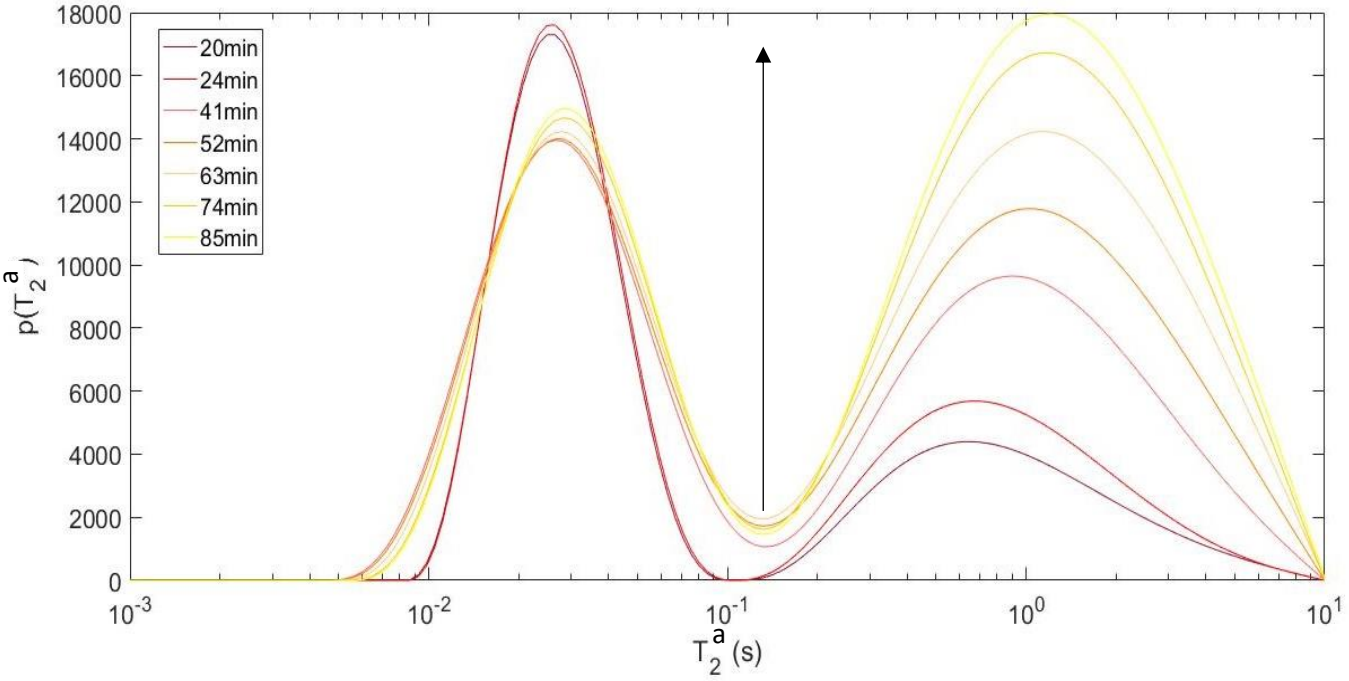

Figure A3.0.31 - T_2^a relaxation time distribution from CPMG data for sample 15, oil-wet sand with a mixture THF:H2O 1:15. The development of the peaks follows the direction of the arrow.

Figure A3.0.32 displays the T_2^a relaxation time distribution for sample 17, oil-wet sand with the hydrate mixture THF:H_2O 1:20.

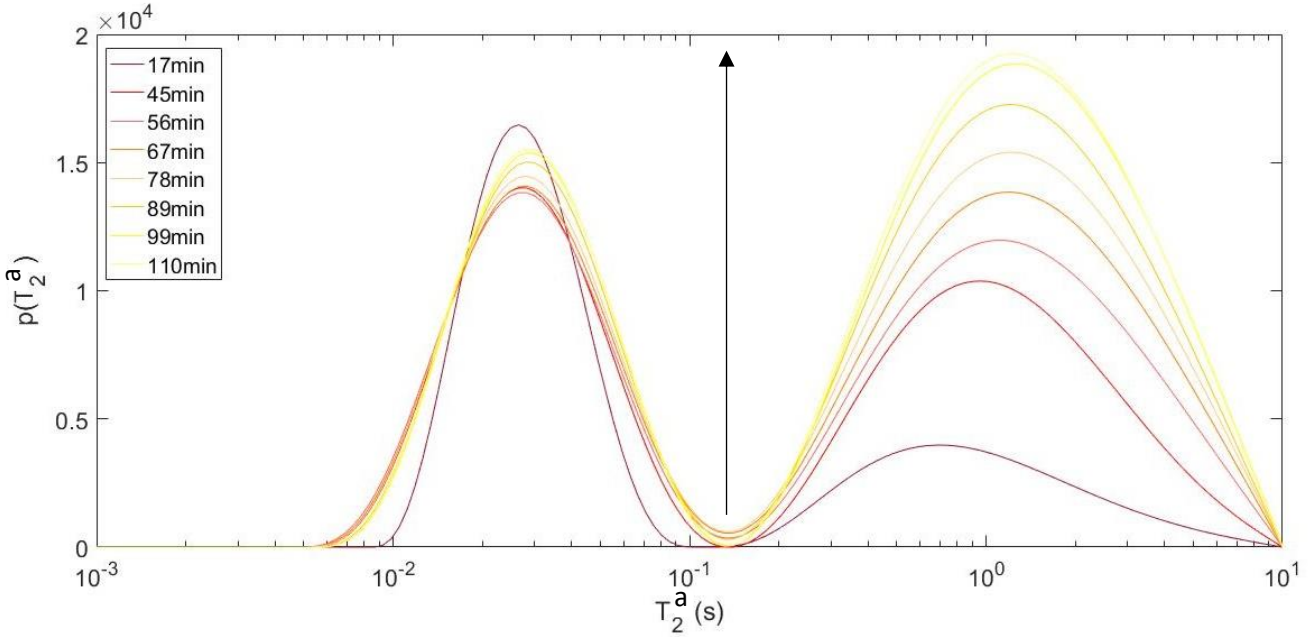

Figure A3.0.32 - T_2^a relaxation time distribution from CPMG data for sample 17, oil-wet sand with a mixture THF:H2O 1:20. The development of the peaks follows the direction of the arrow.

Figure A3.0.33 displays the $T_2{}^a$ relaxation time distribution for sample 15, oil-wet sand with the hydrate mixture THF:H_2O 1:15, and for sample 17, oil-wet sand with the hydrate mixture THF:H_2O 1:20.

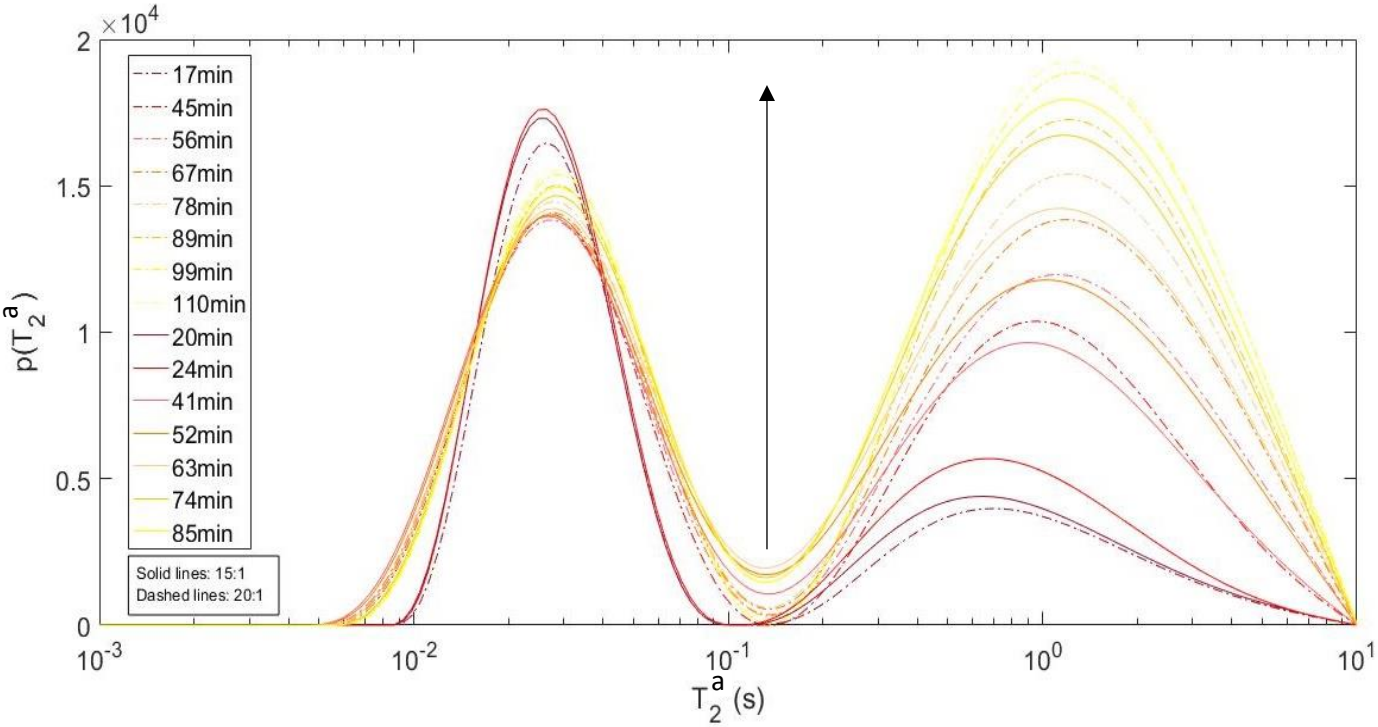

Figure A3.0.33 - $T_2{}^a$ relaxation time distribution from CPMG data for sample 15, oil-wet sand with a mixture THF:H2O 1:15, and for sample 17, oil-wet sand with a mixture THF:H2O 1:20. The development of the peaks follows the direction of the arrow.

Table A3.0.5 displays the peak $T_2{}^a$ distribution values from figure A3.0.33.

Table A3.0.5 - Peak values from the $T_2{}^a$ relaxation time distribution for samples 15 and 17.

Oil-wet sand 15:1 time	peak one [ms]	peak two [ms]	Oil-wet sand 20:1 time	peak one [ms]	peak two [ms]
20min	25,68	658,9	17 min	26,47	745,6
24 min	25,68	658,9	-	-	-
41 min	27,315	897,5	45 min	28,16	954,7
52 min	26,47	1016	56 min	26,47	1149
63 min	26,47	1149	67 min	28,16	1222
74 min	29,96	1149	78 min	28,16	1222
85 min	29,96	1222	89 min	29,06	1222
-	-	-	99 min	29,96	1222
-	-	-	110 min	29,96	1222

MSME Protocol

Figure A3.0.34 displays the settings used to acquire the MSME measurements of samples 14 to 17.

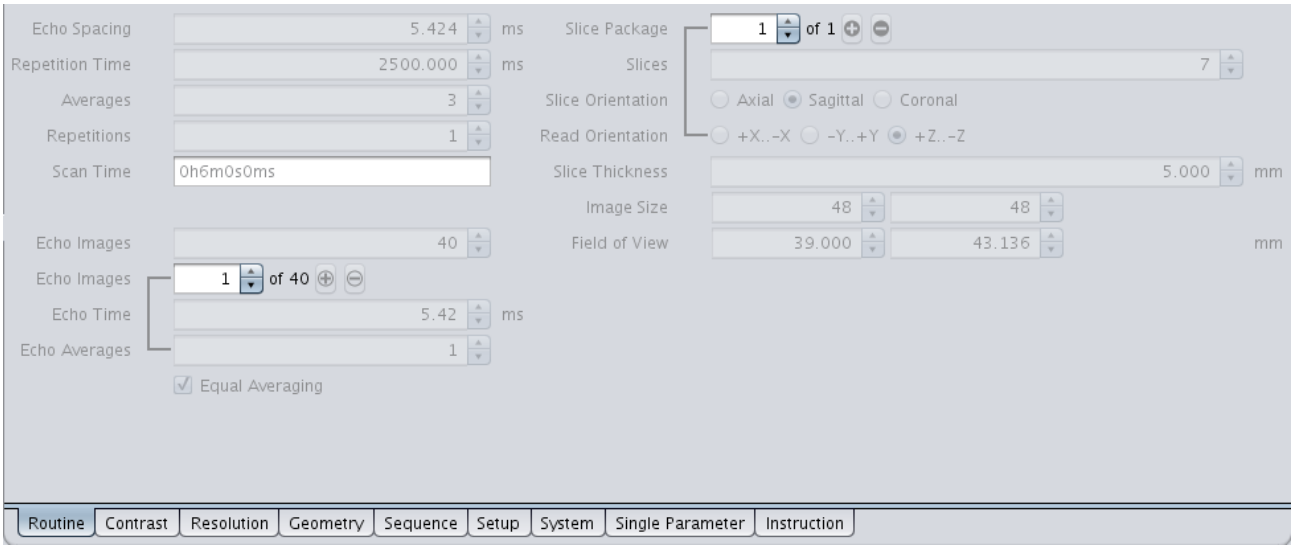

Figure A3.0.34 - Settings for the MSME scans used for samples 14 to 17.

Figures A3.0.35 to A3.0.38 display the region of interest chosen for samples 14 to 17. The same region of interest was chosen for all scans performed on the samples.

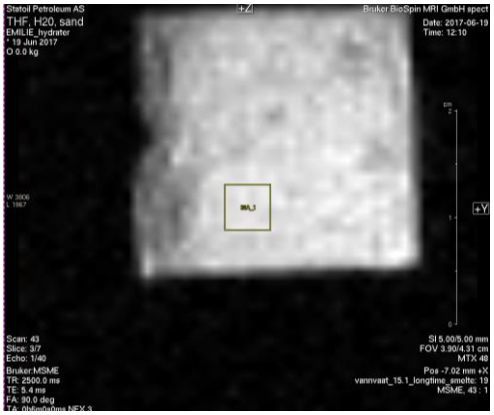

Figure A3.0.35 - Region of interest within slice 3 of sample 14.

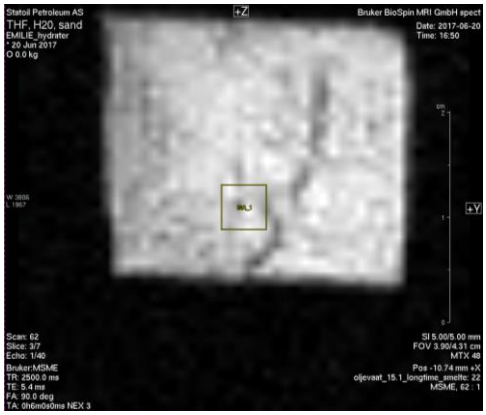

Figure A3.0.36 - Region of interest within slice 3 of sample 15.

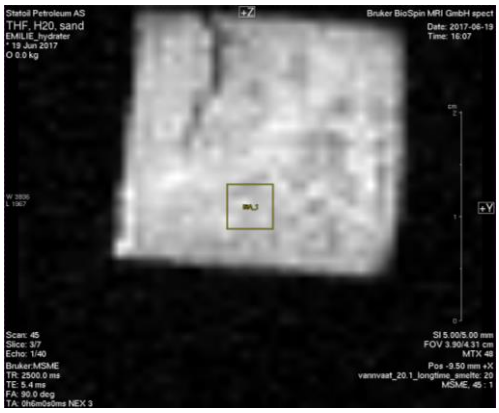

Figure A3.0.37 – Region of interest within slice 3 of sample 16.

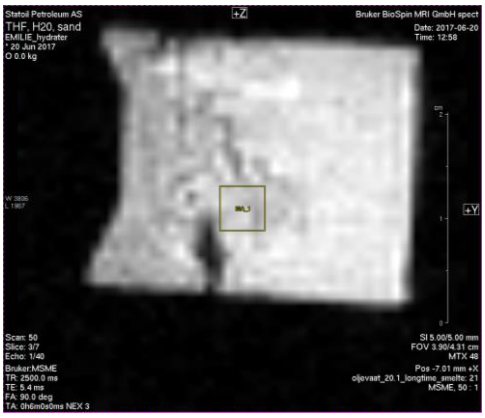

Figure A3.0.38 - Region of interest within slice 3 of sample 17.

The data acquired with the MSME scans were analyzed with the inverse Laplace transformation to create T_2^a relaxation time distribution curves. The settings for the nnls-smoothing is given in table A3.0.6.

Table A3.0.6 – Parameters used for nnls smoothing for the inverse Laplace transformation performed on the MSME data from samples 14 to 17.

nnls smoothing parameters for ILT	
Alpha	1e7
T/D min	0,001
Tmax	5
Steps	40

Figure A3.0.39 displays the T_2^a relaxation time distribution from MSME data for sample 14, water-wet sand with the hydrate mixture THF:H_2O 1:15.

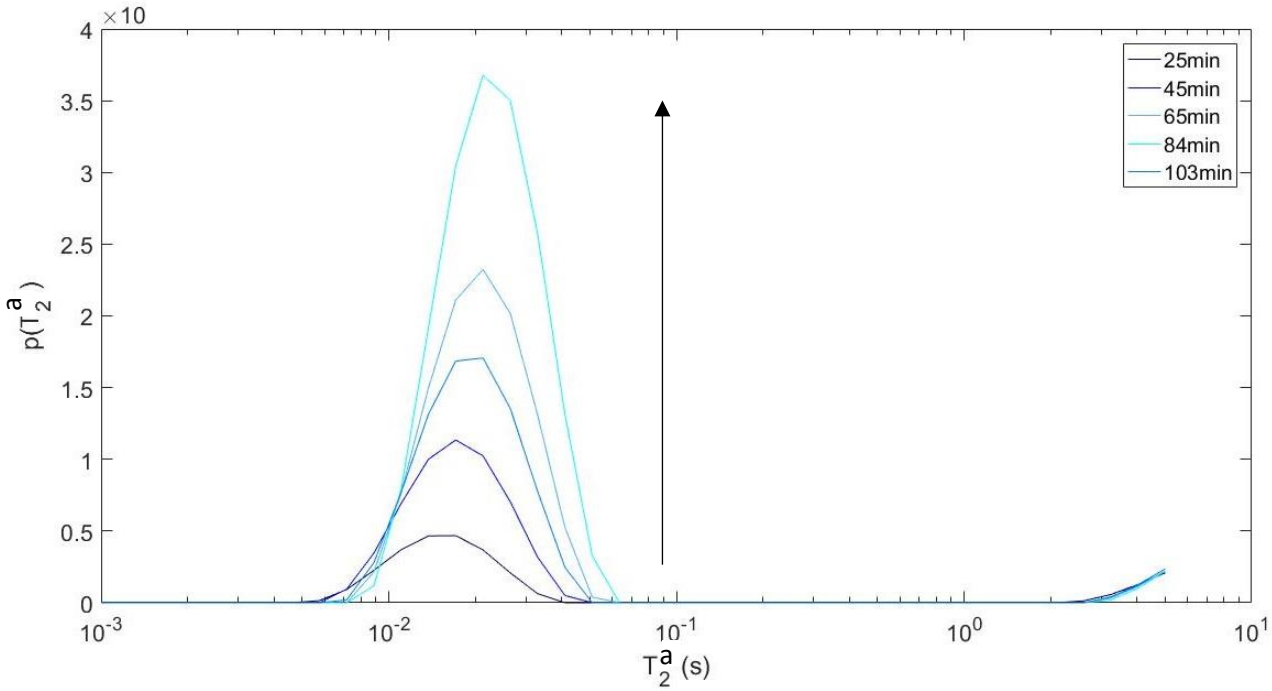

Figure A3.0.39 - T_2^a relaxation time distribution from MSME data for sample 14, water-wet sand with a mixture THF:H2O 1:15. The development of the peak follows the direction of the arrow.

Table A3.0.7 displays the peak values from the T_2^a relaxation time distribution for sample 14, water-wet sand with the hydrate mixture THF:H_2O 1:15.

Table A3.0.7 - Peak values for the T_2^a relaxation time distribution for sample 14, water-wet sand mixture THF:H2O 1:15, from MSME results from both ParaVision and ILT.

Time elapsed [min]	T2 relaxation time PARAVISION [ms]	std dev[ms]	T2 relaxation time ILT [ms]	ROI area [cm2]
25	16,7	1,2	15,4	0,26
45	18,5	0,7	17,1	0,26
65	21,9	0,5	21,3	0,26
84	23,8	0,7	21,3	0,26
103	20,5	0,6	21,3	0,26

Figure A3.0.40 displays the T_2^a relaxation time distribution from MSME data for sample 16, water-wet sand with the hydrate mixture THF:H2O 1:20.

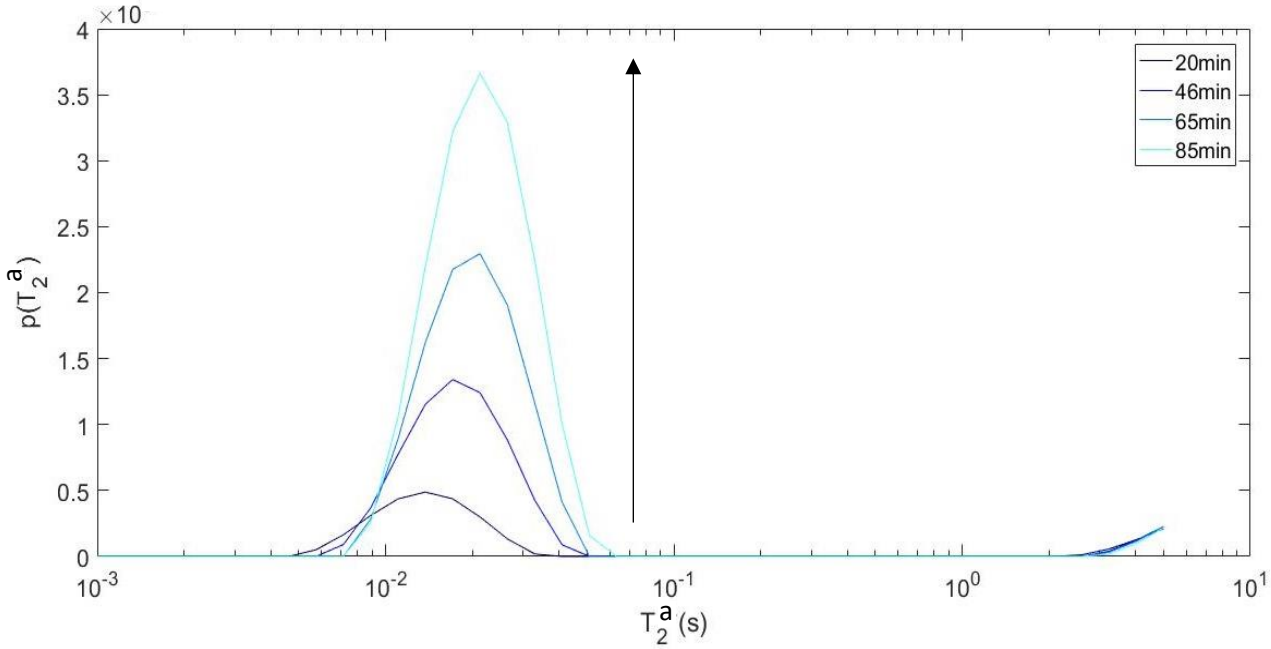

Figure A3.0.40 - T_2^a relaxation time distribution from MSME data for sample 16, water-wet sand with a mixture THF:H2O 1:20. The development of the peak follows the direction of the arrow.

Table A3.0.8 displays the peak values from the T_2^a relaxation time distribution for sample 16, water-wet sand with the hydrate mixture THF:H2O 1:20.

Table A3.0.8 - Peak values for the T_2^a relaxation time distribution for sample 16, water-wet sand mixture THF:H2O 1:20, from MSME results from both ParaVision and ILT.

Time elapsed [min]	T2 relaxation time PARAVISION [ms]	std dev[ms]	T2 relaxation time ILT [ms]	ROI area [cm2]
20	15,1	0,8	13,7	0,26
46	18,9	0,6	17,1	0,26
65	21,1	0,5	21,3	0,26
85	22,6	0,5	21,3	0,26

Figure A3.0.41 displays the T_2^a relaxation time distribution from MSME data for sample 15, oil-wet sand with the hydrate mixture THF:H2O 1:15.

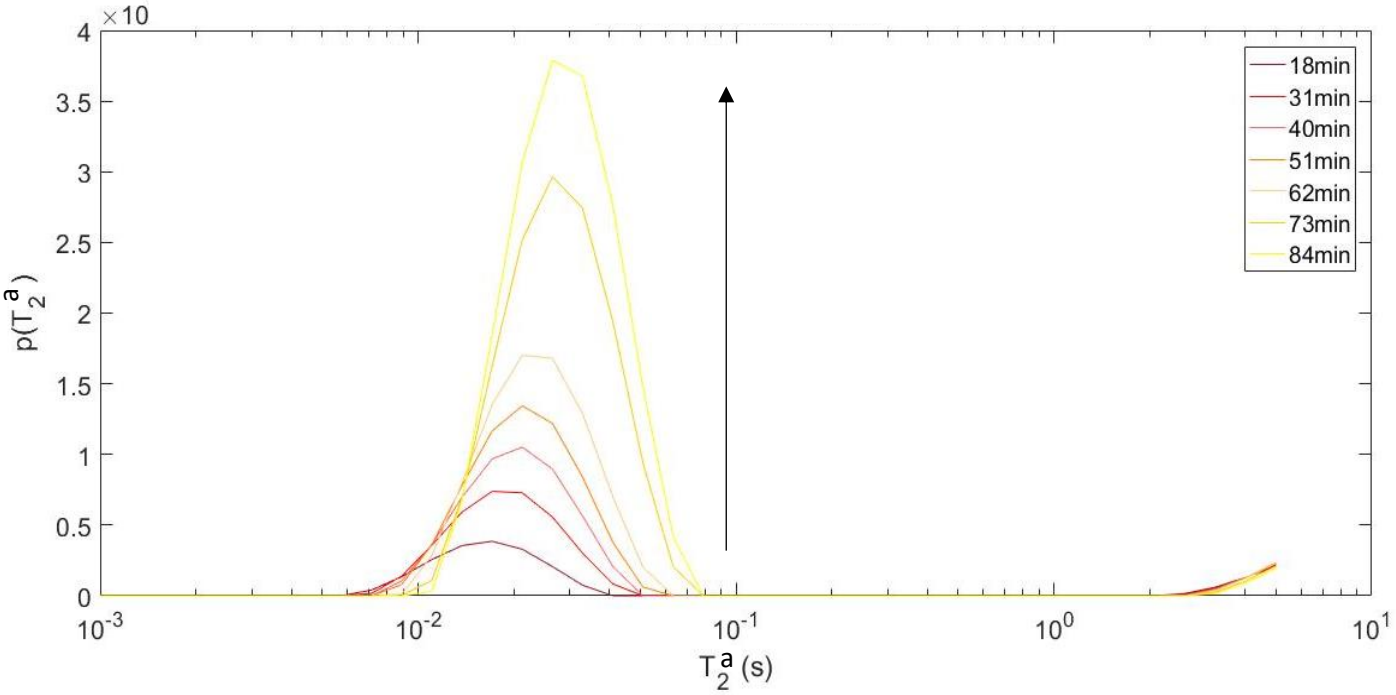

Figure A3.0.41 - T_2^a relaxation time distribution from MSME data for sample 15, oil-wet sand with a mixture THF:H2O 1:15. The development of the peak follows the direction of the arrow.

Table A3.0.9 displays the peak values from the T_2^a relaxation time distribution for sample 15, oil-wet sand with the hydrate mixture THF:H2O 1:15.

Table A3.0.9 - Peak values for the T_2^a relaxation time distribution for sample 15, oil-wet sand mixture THF:H2O 1:15, from MSME results from both ParaVision and ILT.

Time elapsed [min]	T2 relaxation time PARAVISION [ms]	1 std dev [ms]	T2 relaxation time ILT [ms]	ROI area [cm2]
18	17,9	1,4	17,1	0,26
31	20,1	1,1	19,2	0,26
40	21,7	0,9	21,3	0,26
51	22,9	0,8	21,3	0,26
62	24,7	0,6	23,9	0,26
73	28,6	0,6	26,5	0,26
84	29,9	0,6	26,5	0,26

Figure A3.0.42 displays the T_2^a relaxation time distribution from MSME data for sample 17, oil-wet sand with the hydrate mixture THF:H2O 1:20.

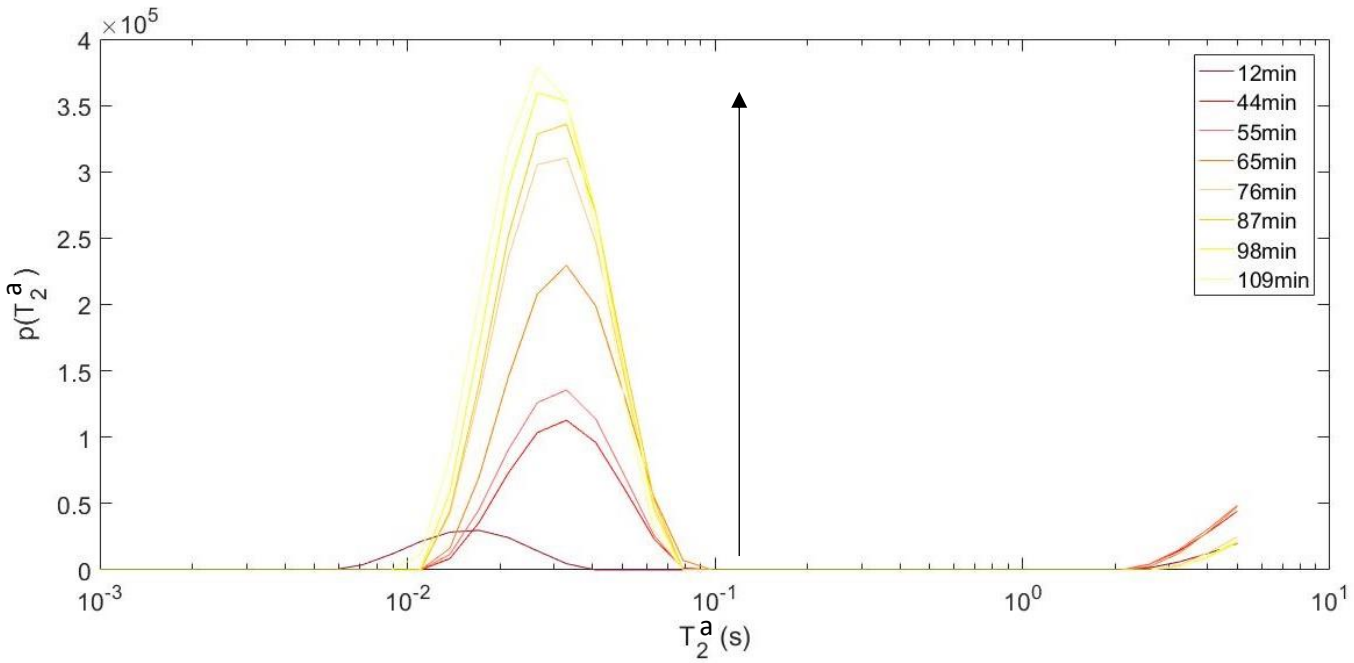

Figure A3.0.42 - T_2^a relaxation time distribution from MSME data for sample 17, oil-wet sand with a mixture THF:H2O 1:20. The development of the peak follows the direction of the arrow.

Table A3.0.10 displays the peak values from the T_2^a relaxation time distribution for sample 17, oil-wet sand with the hydrate mixture THF:H2O 1:20

Table A3.0.10 - Peak values for the T_2^a relaxation time distribution for sample 17, oil-wet sand mixture THF:H2O 1:20, from MSME results from both ParaVision and ILT.

Time elapsed [min]	T2 relaxation time PARAVISION [ms]	1 std dev[ms]	T2 relaxation time ILT [ms]	ROI area [cm2]
12	17,5	1,7	17,1	0,26
44	33,2	1,6	32,9	0,26
55	32,7	1,6	32,9	0,26
65	33,4	1,3	32,9	0,26
76	31,1	0,7	32,9	0,26
87	31,2	0,7	32,9	0,26
98	30,2	0,6	26,5	0,26
109	28,9	0,6	26,5	0,26

Figure A3.0.43 displays the T_2^a relaxation time distribution from MSME data for sample 15, water-wet sand with the hydrate mixture THF:H2O 1:15, and for sample 17, water-wet sand with the hydrate mixture THF:H2O 1:20.

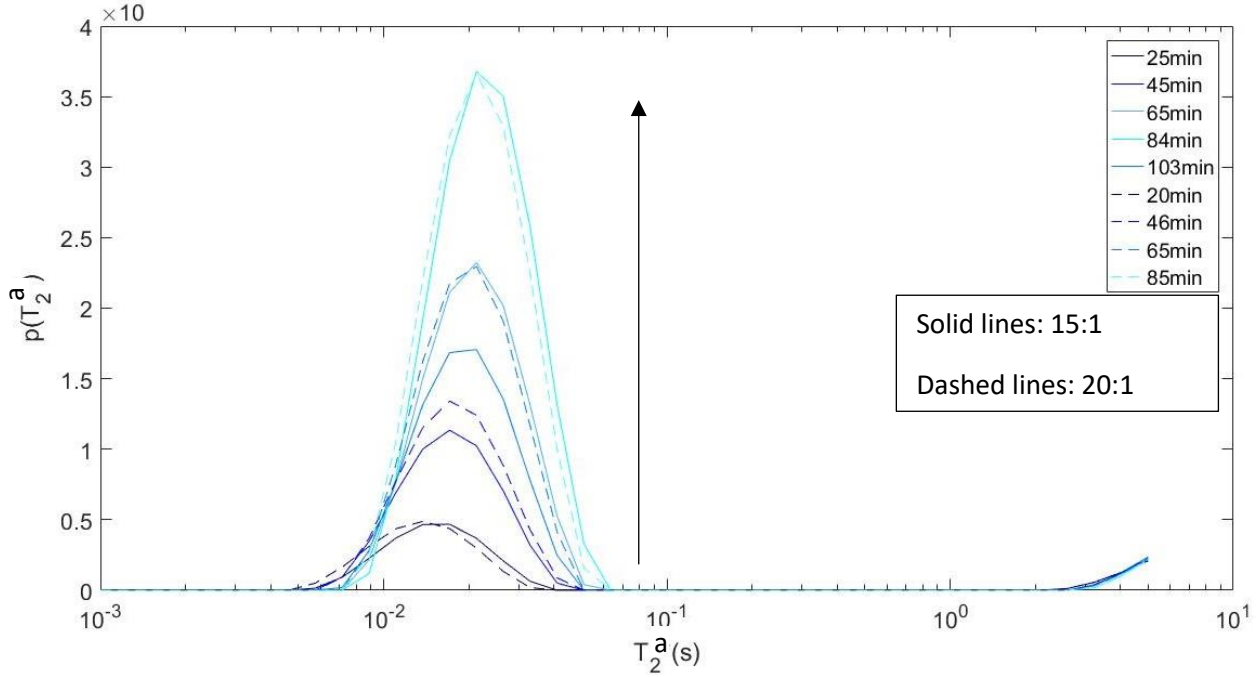

Figure A3.0.43 - T_2^a relaxation time distribution for water-wet sand with the mixtures THF:H2O 15:1, as the solid lines, and THF:H2O 20:1, as the dashed lines. The development of the peak follows the direction of the arrow.

Figure A3.0.44 displays the T_2^a relaxation time distribution from MSME data for sample 15, oil-wet sand with the hydrate mixture THF:H2O 1:15, and for sample 17, oil-wet sand with the hydrate mixture THF:H2O 1:20.

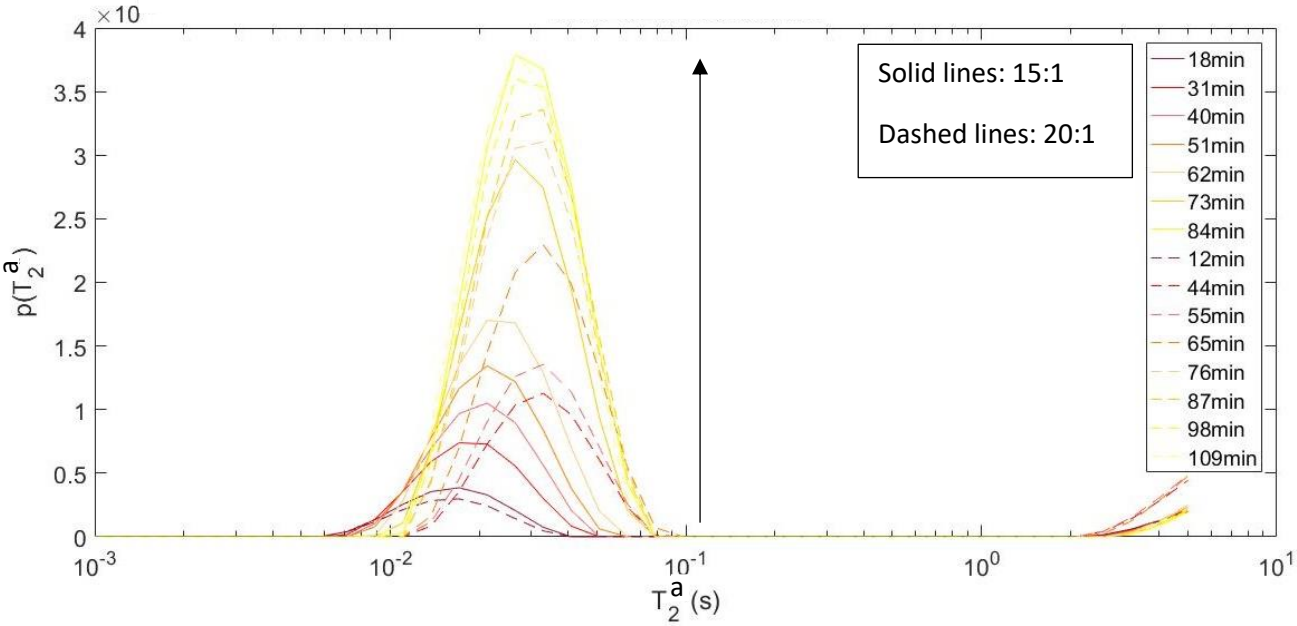

Figure A3.0.44 - T_2^a relaxation time distribution for oil-wet sand with the mixtures THF:H2O 15:1, as the solid lines, and THF:H2O 20:1, as the dashed lines. The development of the peak follows the direction of the arrow.

A4 Additional Information and Results, Cooling Experiments

Details about the samples

Sample 14 and 15 were also used for the cooling experiments. See the tables A3.0.1 and A3.0.2 for composition.

RAREst Protocol

Figure A4.0.1 displays the settings that was used for RAREst images of sample 14, water-wet sand with hydrate mixture THF:H2O 1:15. The same settings were used for the sagittal orientation, the only parameter that was changed was the field of view.

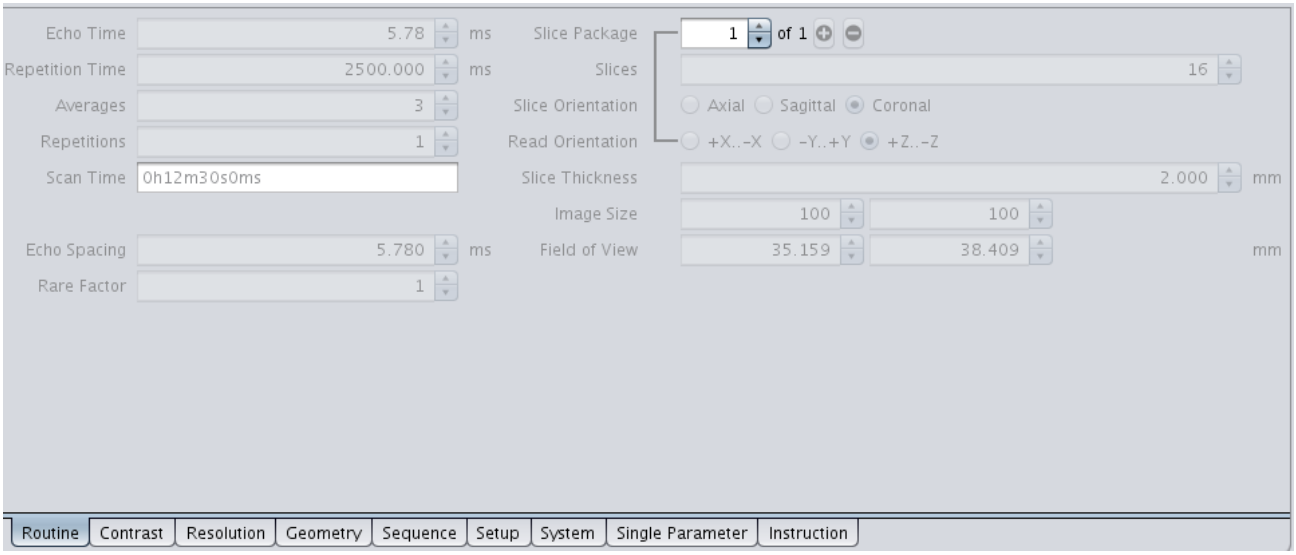

Figure A4.0.1 - Settings for RAREst scans of sample 14, water-wet sand with the mixture THF:H2O 1:15. The same were used for the sagittal orientation.

Figure A4.0.2 displays the dissociation process of slice 5 within sample 14 from the coronal orientation.

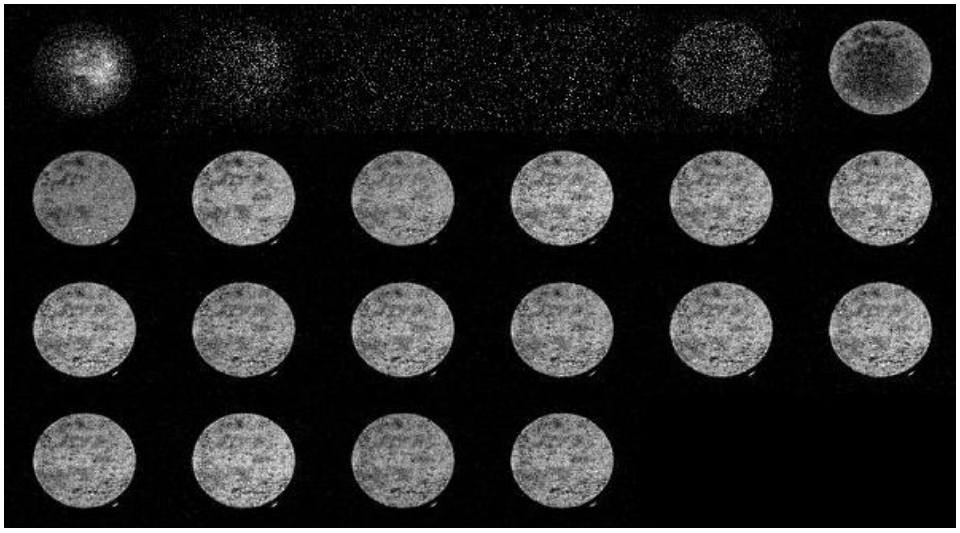

Figure A4.0.2 – RAREst images of the formation and dissociation process for slice 5 within sample 14, water-wet sand with the hydrate mixture THF:H2O 1:15.

Figure A4.0.3 displays the dissociation process of slice 7 within sample 14 from the coronal orientation.

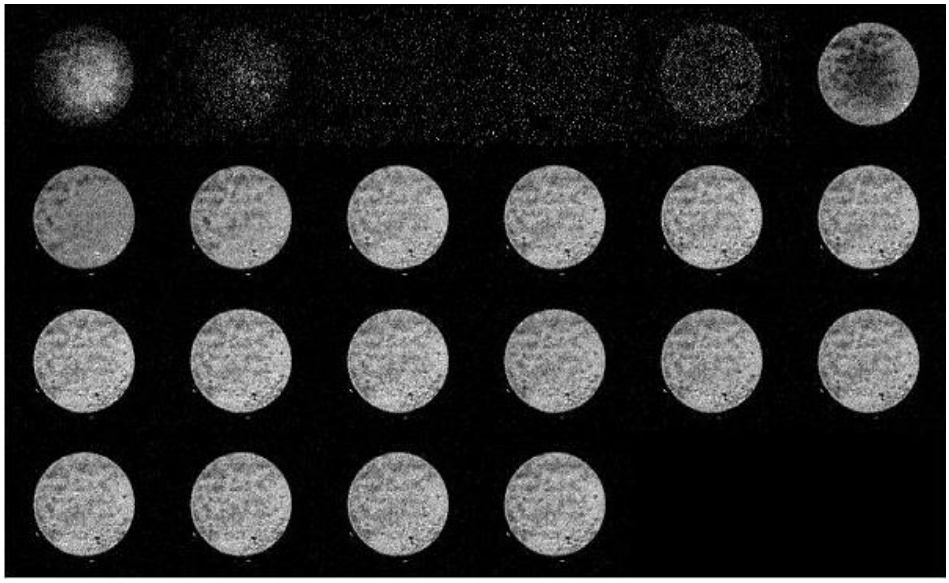

Figure A4.0.3 – RAREst images of the formation and dissociation process for slice 5 within sample 14, water-wet sand with the hydrate mixture THF:H2O 1:15.

Figure A4.0.4 displays the development of intensity for the dissociation process of THF hydrates in sample 14, water-wet sand with the mixture THF:H2O 1:15, where each line represents a point in time. The slice numbers are displayed on the x-axis. The slices are from the coronal orienation.

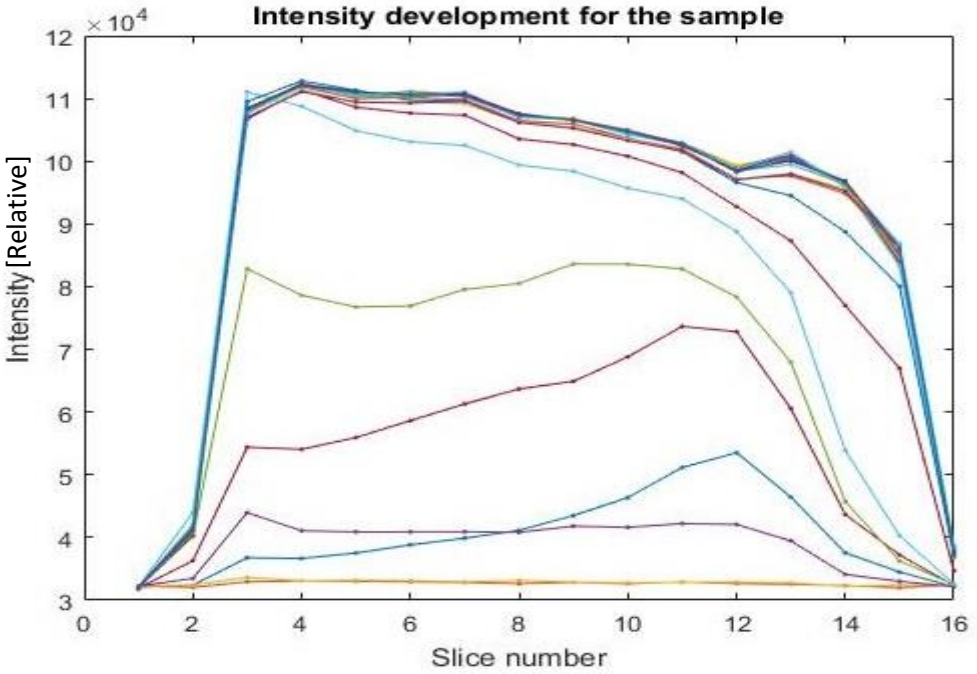

Figure A4.0.4 - Intensity development as a function of slice number for sample 14, water-wet sand with the mixture THF:H2O 1:15. Slices are displayed along the x-axis, each line represents a point in time. Slice 1 is the bottom of the sample, while slice 16 is the top of the sample.

Figure A4.0.5 displays how the slices are orientated in the intensity development plot from figure A4.0.4.

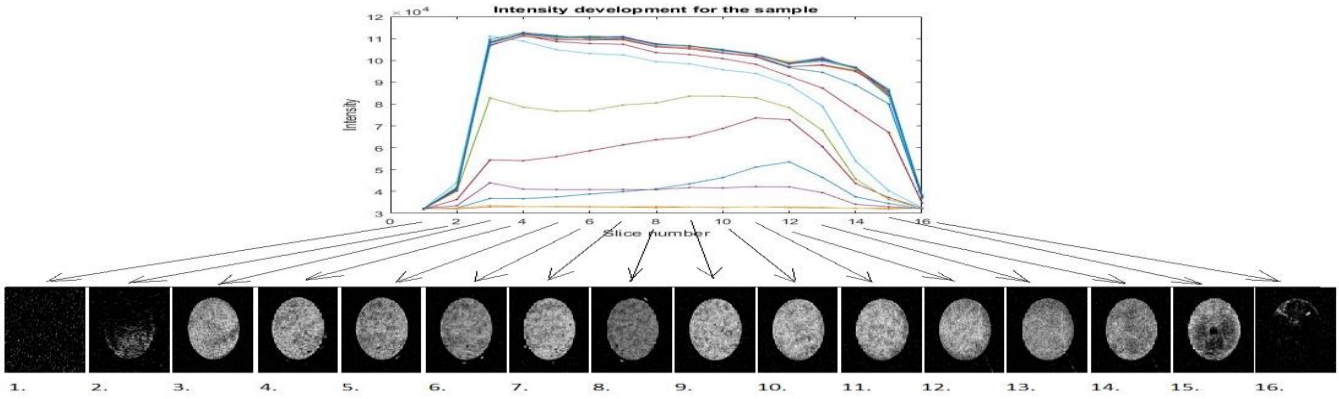

Figure A4.0.5 - Illustration of how the slices is displayed in the intensity plot from figure A4.0.4.

Figure A4.0.6 displays the intensity development for the dissociation process of THF hydrates in sample 14, water-wet sand with the mixture THF:H2O 1:15, where each line represents a slice. The time is displayed on the x-axis.

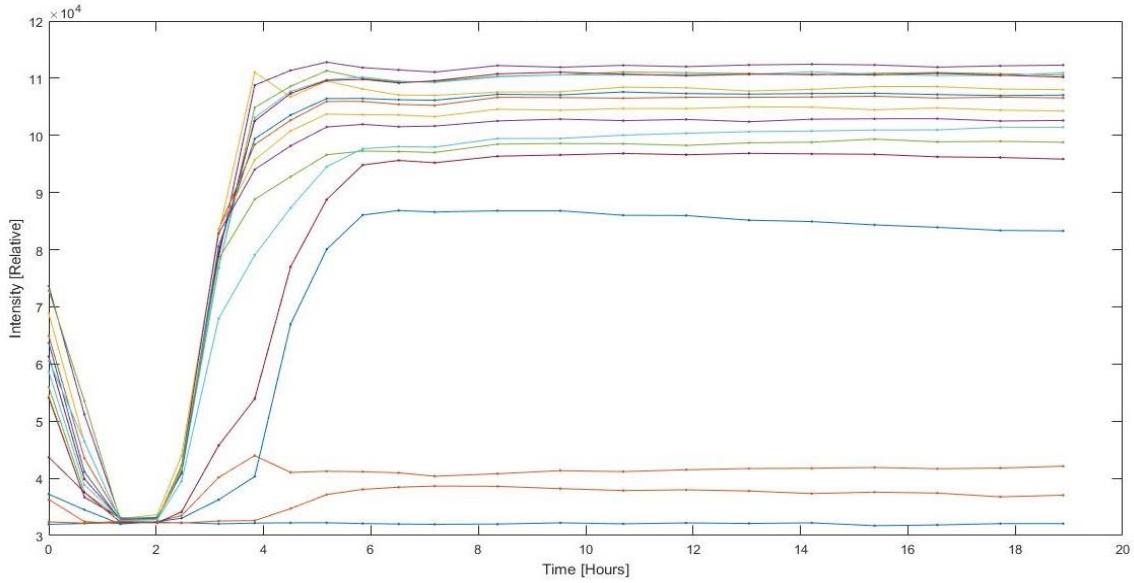

Figure A4.0.6 - Intensity development as a function of time for sample 14, water-wet sand with the mixture THF:H2O 1:15. Each line represents a slice. Coronal orientation.

Figure A3.0.7 displays the intensity development for the dissociation process of THF hydrates in sample 1, water-wet sand with the mixture THF:H2O 1:15. All the slices of sample 14 are now summarized to represent the total sample. The time is displayed on the x-axis.

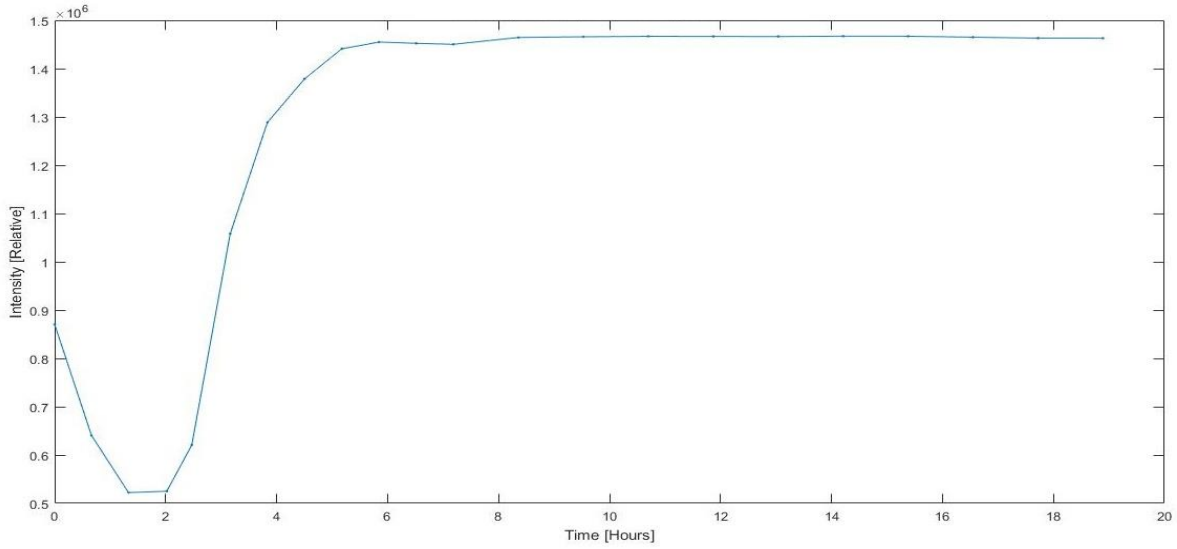

Figure A4.0.7 - Intensity development as a function of time for sample 14, water-wet sand with the mixture THF:H2O 1:15. All slices are summarized to one total value of intensity development. Coronal orientation.

Figure A4.0.8 displays the dissociation process of slice 5 within sample 14 from the sagittal orientation.

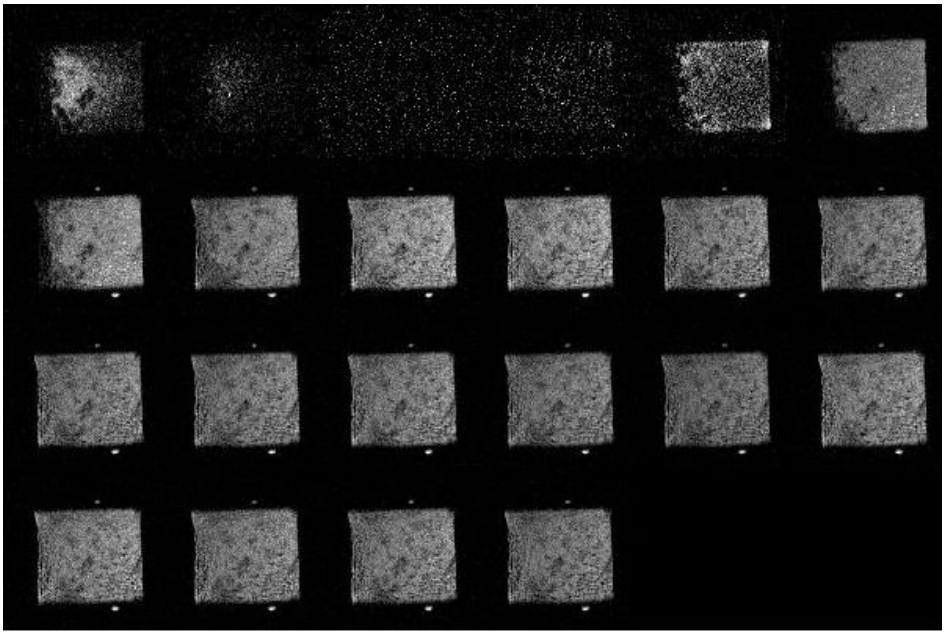

Figure A4.0.8 – Formation and dissociation process for slice 5 within sample 14, water-wet sand with the hydrate mixture THF:H2O 1:15.

Figure A4.0.9 displays the dissociation process of slice 8 within sample 14 from the sagittal orientation.

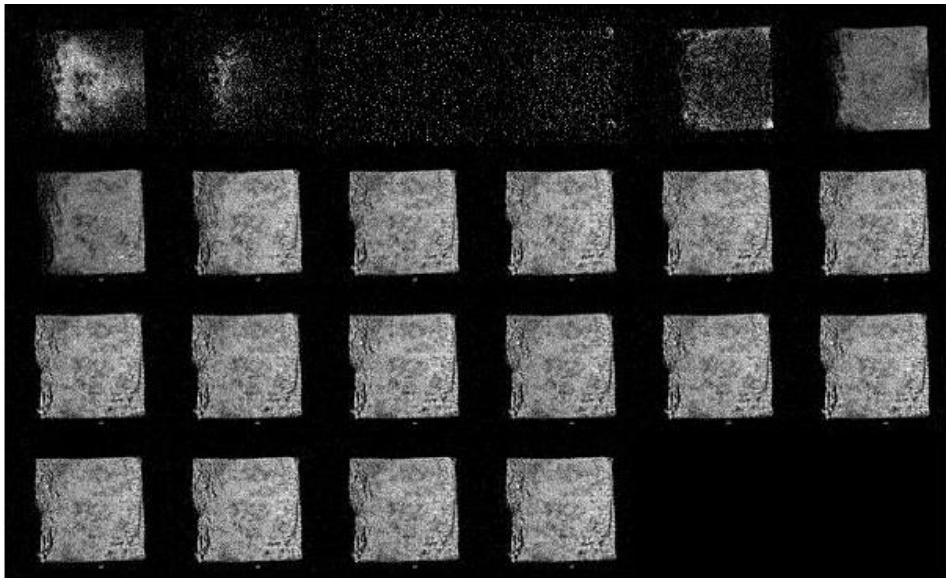

Figure A4.0.9 – RAREst images of formation and dissociation process for slice 8 within sample 14, water-wet sand with the hydrate mixture THF:H2O 1:15.

Figure A4.0.10 displays the development of intensity for the formation and dissociation process of THF hydrates in sample 14, water-wet sand with the mixture THF:H2O 1:15, where each line represents a point in time. The slice numbers are displayed on the x-axis. The slices are from the sagittal orienation.

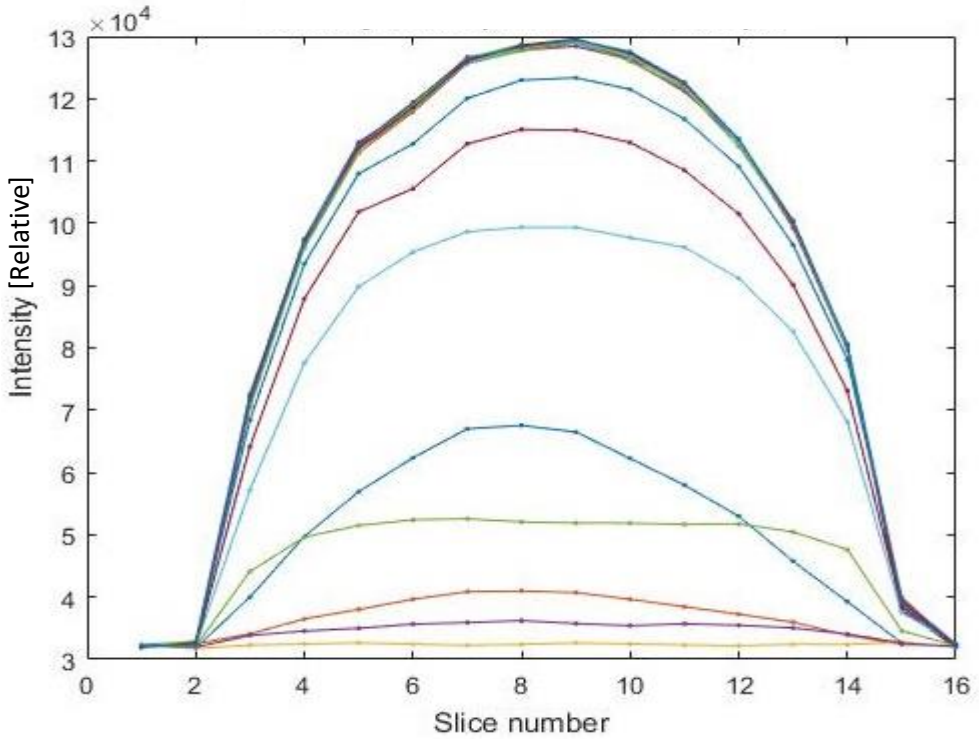

Figure A4.0.10 Intensity development as a function of slice number for sample 14, water-wet sand with the mixture THF:H2O 1:15. Each line represents a point in time.

Figure A4.0.12 displays the intensity development for the dissociation process of THF hydrates in sample 14, water-wet sand with the mixture THF:H2O 1:15, where each line represents a slice. The time is displayed on the x-axis.

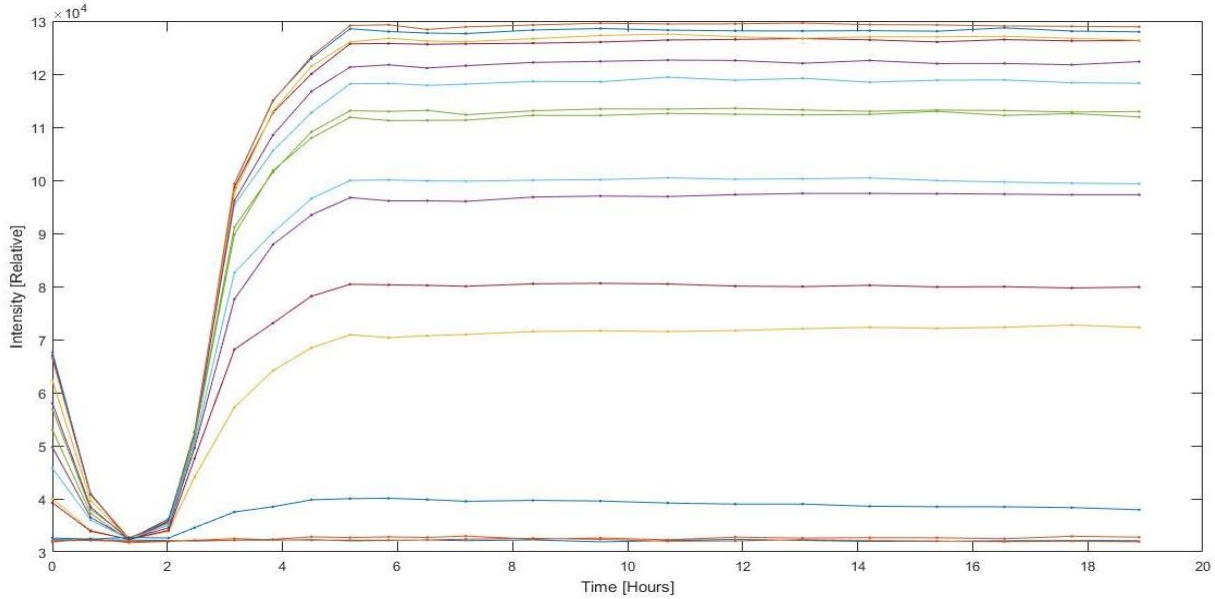

Figure A4.0.11 - Intensity development as a function of time for sample 14, water-wet sand with the mixture THF:H2O 1:15. Each line represents a slice. Sagittal orientation.

Figure A4.0.12 displays the settings that was used for RAREst images of sample 15, oil-wet sand with hydrate mixture THF:H2O 1:15.

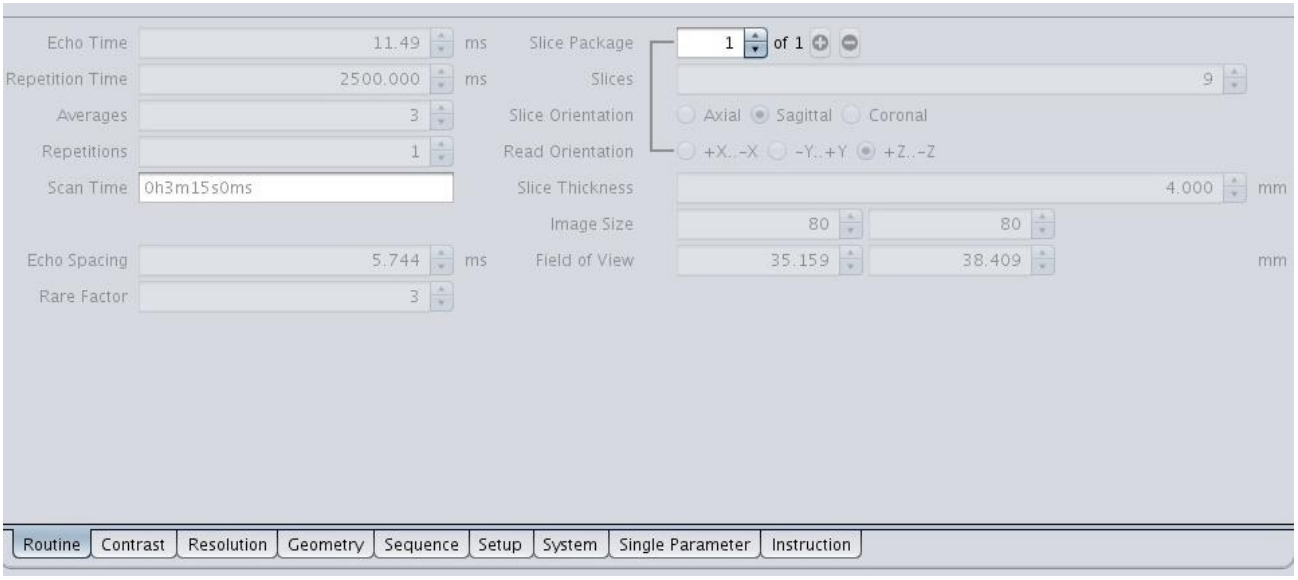

Figure A4.0.12 - Settings for RAREst scans of sample 15, oil-wet sand with the mixture THF:H2O 1:15.

Figure A4.0.13 displays the development of intensity for the dissociation process of THF hydrates in sample 15, oil-wet sand with the mixture THF:H2O 1:15, where each line represents a point in time. The slice numbers are displayed on the x-axis. The slices are from the sagittal orienation.

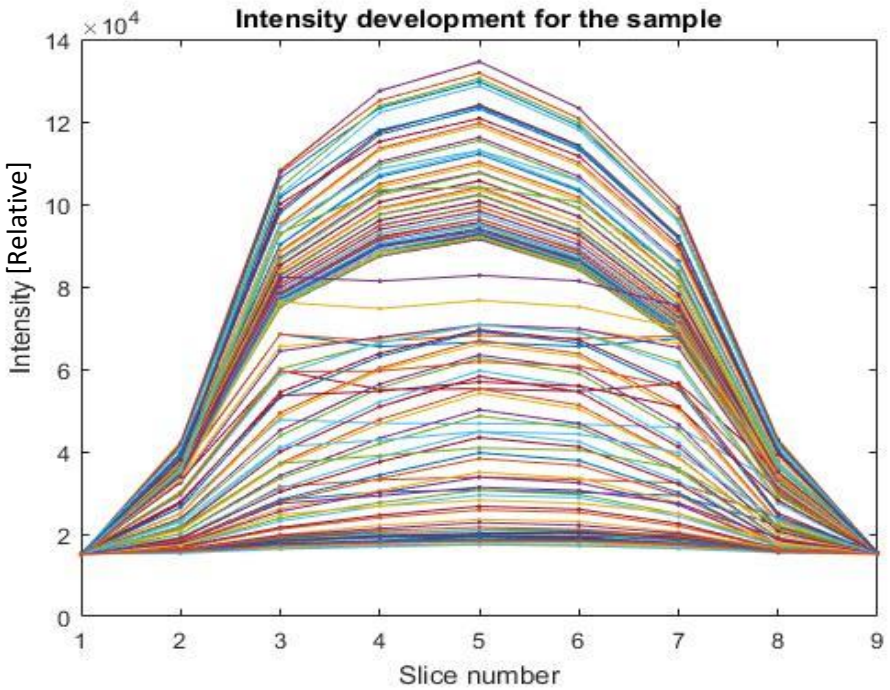

Figure A4.0.13 - Development of intensity as a function of slice number for oil-wet sand, THF:H2O 15:1. Each line represents a point in time, while each slice is marked on the x-axis.

Figure A4.0.14 displays the intensity development for the beginning of a dissociation process, before hydrate formation and a complete hydrate dissociation process of THF hydrates in sample 15, oil-wet sand with the mixture THF:H2O 1:15, where each line represents a slice. The time is displayed on the x-axis.

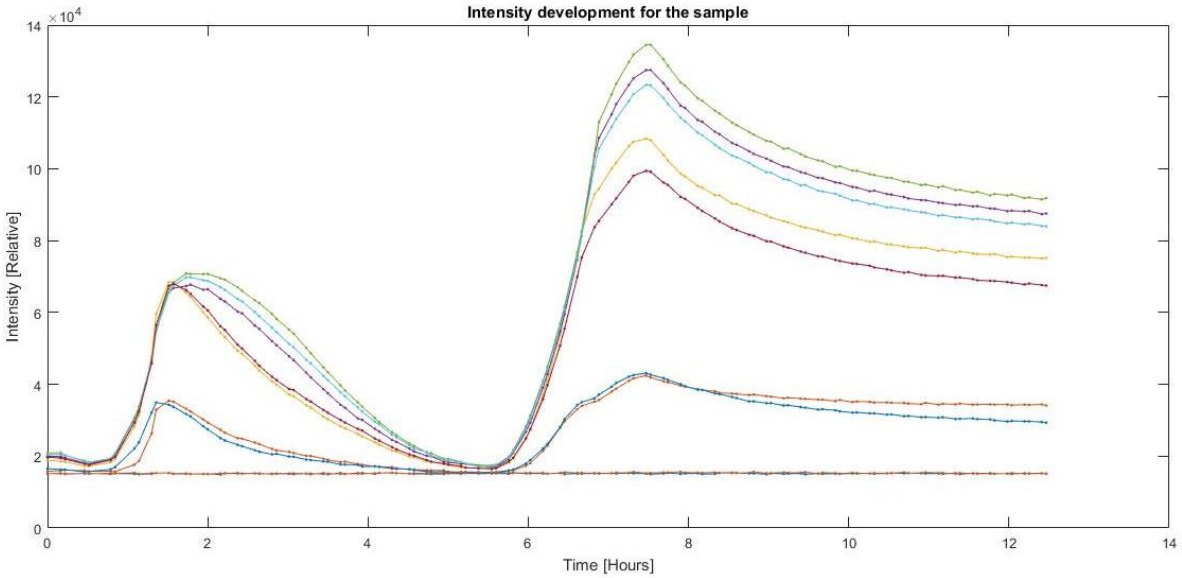

Figure A4.0.14 - Intensity development as a function of time for the sample over time. Each line represents one slice. Oil-wet sand. 15:1.

Figure A3.0.15 displays the intensity development for the beginning of a dissociation process, before hydrate formation and a complete hydrate dissociation process of THF hydrates in sample 15, oil-wet sand with the mixture THF:H2O 1:15. All the slices of sample 15 are now

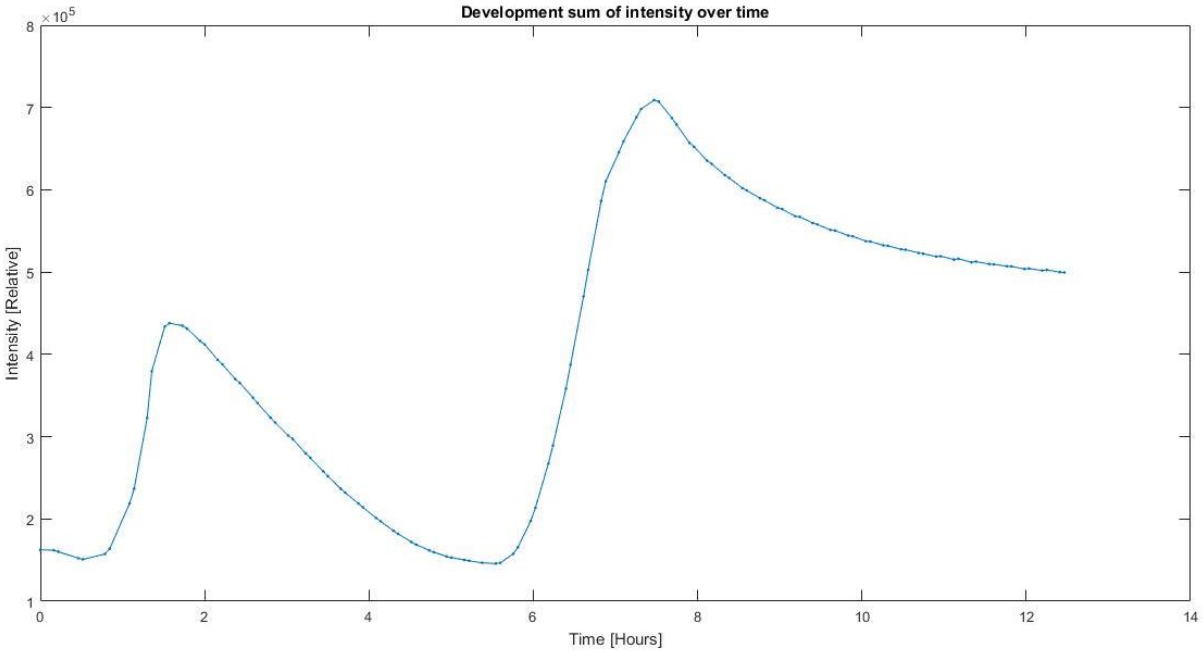

Figure A4.0.15 - Intensity development as a function of time for sample 15, oil-wet sand with the mixture THF:H2O 1:15. All slices are summarized to one total value of intensity development. Sagittal orientation.

summarized to represent the total sample. The time is displayed on the x-axis.

CPMG Protocol

Figure A4.0.16 displays the settings that was used for CPMG scans of sample 14, water-wet sand with hydrate mixture THF:H2O 1:15.

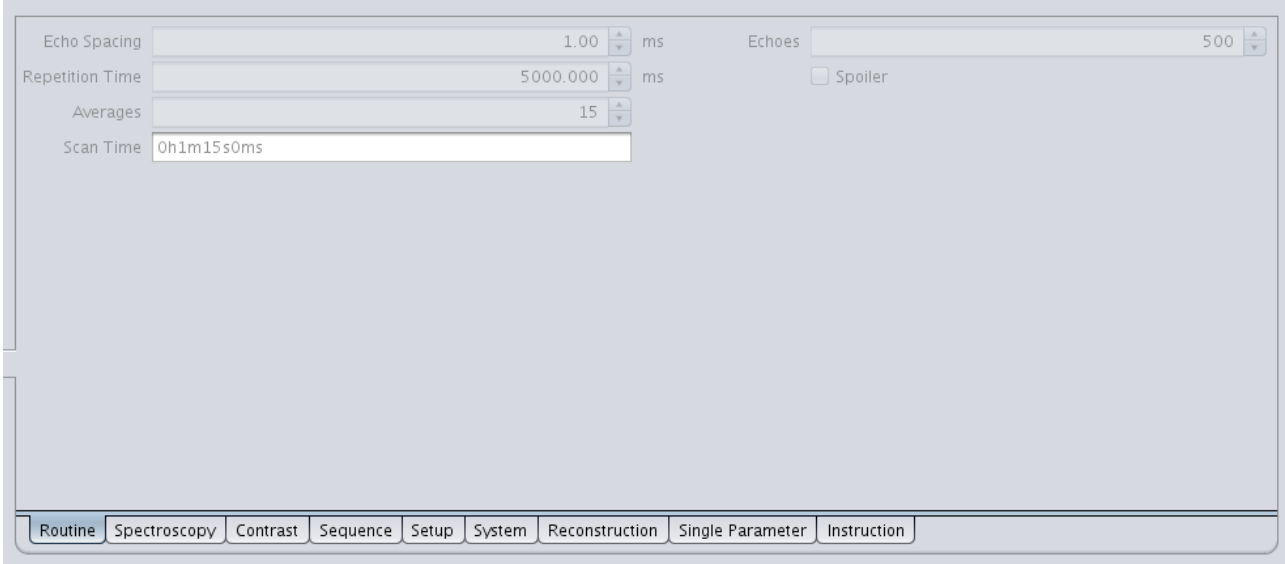

Figure A4.0.16 - Settings for the CPMG scans used for sample 14, water-wet sand with the hydrate mixture THF:H2O 1:15.

Figure A4.0.17 displays decay curves for sample 14, water-wet sand with the hydrate mixture THF:H2O 1:15, as hydrates are forming.

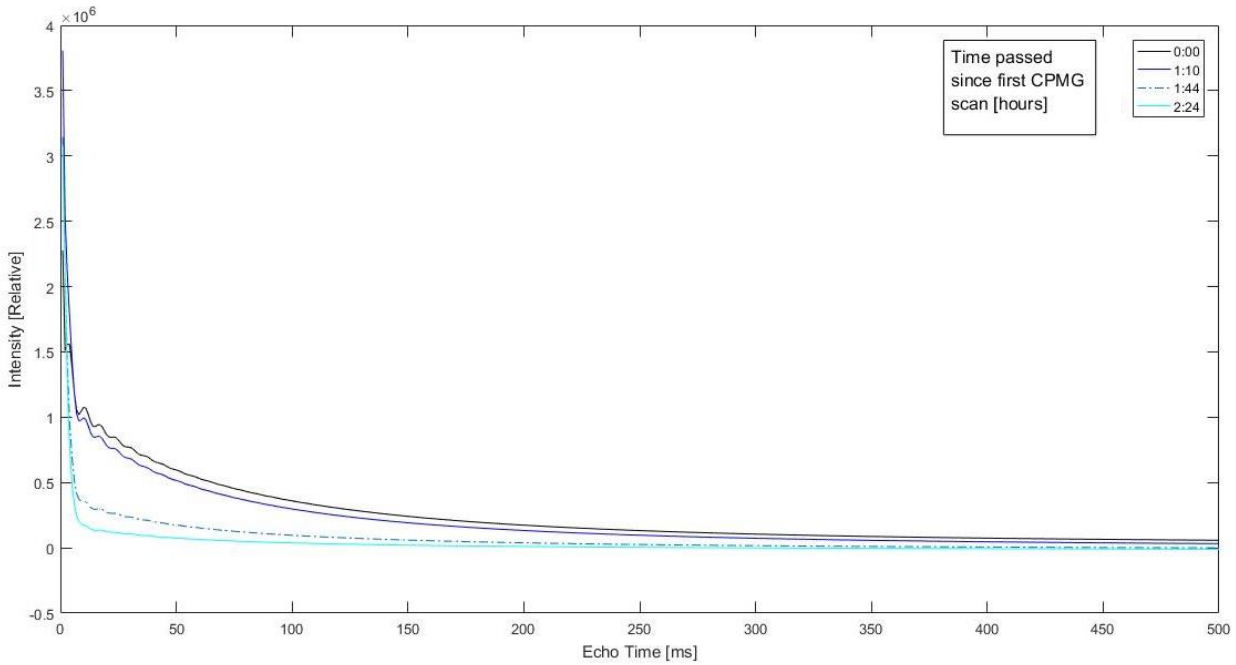

Figure A4.0.17 - Decay curves for sample 14, water-wet sand with mixture THF:H2O 1:15 from CPMG scans, as hydrates are forming.

Figure A4.0.18 displays decay curves for sample 14, water-wet sand with the hydrate mixture THF:H2O 1:15, as hydrates are dissociating.

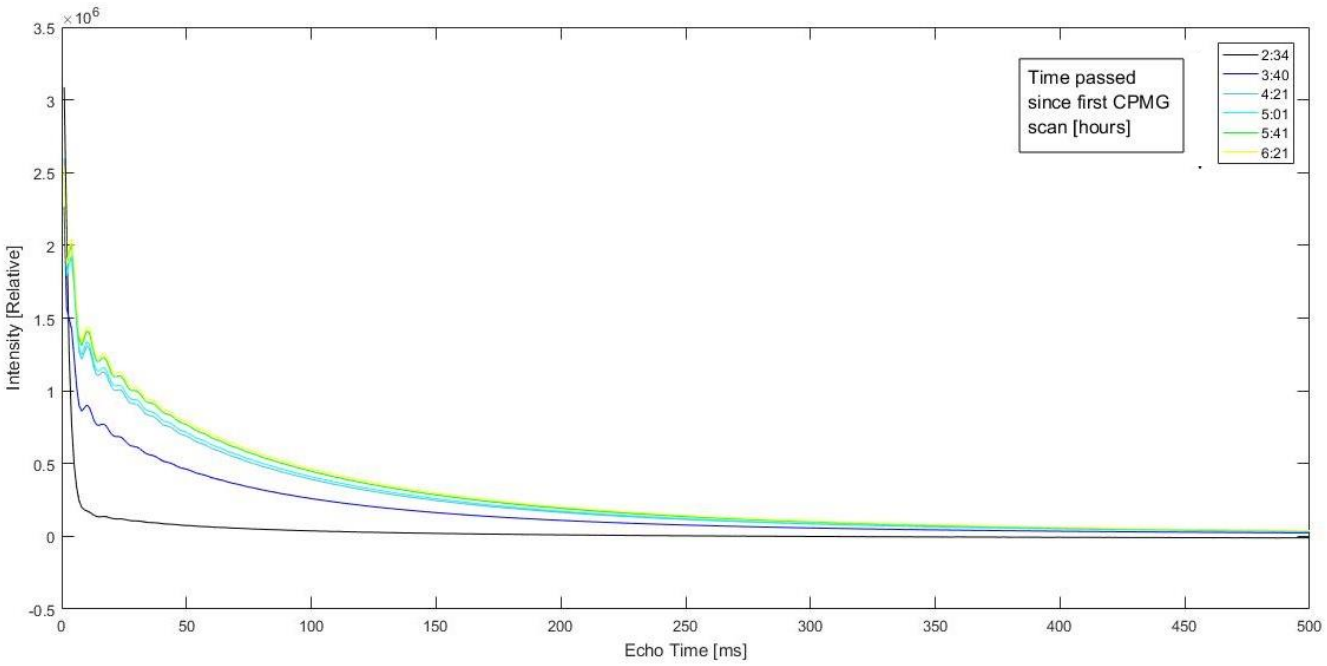

Figure A4.0.18 - Decay curves for sample 14, water-wet sand with mixture THF:H2O 1:15 from CPMG scans, as hydrates are dissociating.

These decay curves were used for further analysis through the inverse Laplace transformation to create T_2^a relaxation time distribution curves. To create a better fit for the data from these scans some data points had to be removed. The settings for the nnls-smoothing is given in table A4.0.1.

Table A4.0.1 - Parameters used for nnls smoothing for the inverse Laplace transformation performed on sample 14.

nnls smoothing parameters for ILT	
Alpha	1e9
T/D min	0,001
Tmax	10
Steps	150

MSME Protocol

Figure A4.0.19 displays the settings that was used for MSME scans of sample 14, water-wet sand with hydrate mixture THF:H2O 1:15.

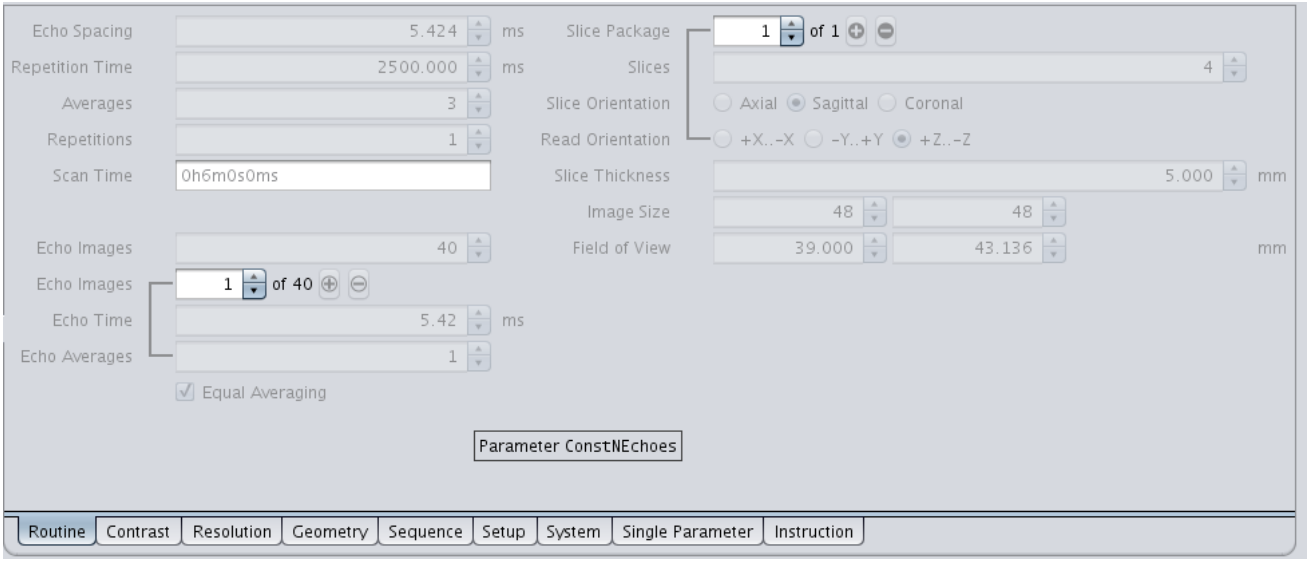

Figure A4.0.19 - Settings for the MSME scans used for sample 14, same settings are used for the sagittal orientation.

Figure A4.0.20 display the region of interest chosen for sample 14 in the sagittal orientation. The same region of interest was chosen for all scans performed on the sample.

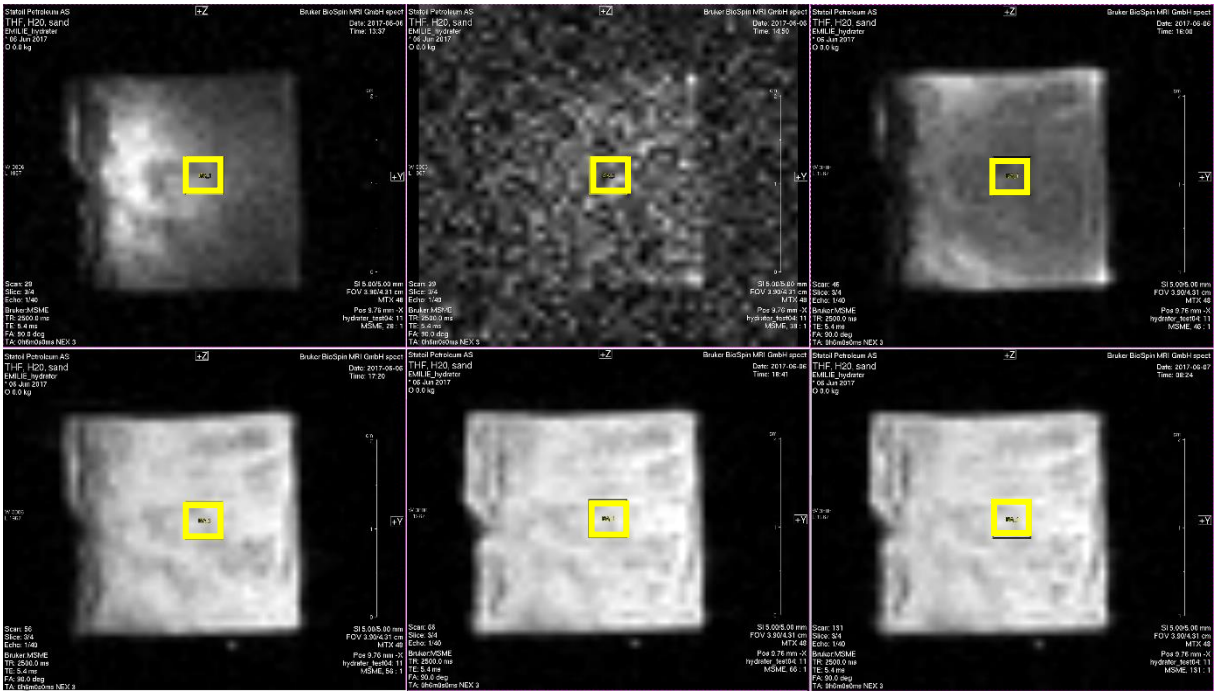

Figure A4.0.20 - Region of interest within slice 3 of sample 14, water-wet sand with the mixture THF:H2O 1:15. Sagittal orientation.

Figure A4.0.21 display the region of interest chosen for sample 14 in the coronal orientation. The same region of interest was chosen for all scans performed on the sample.

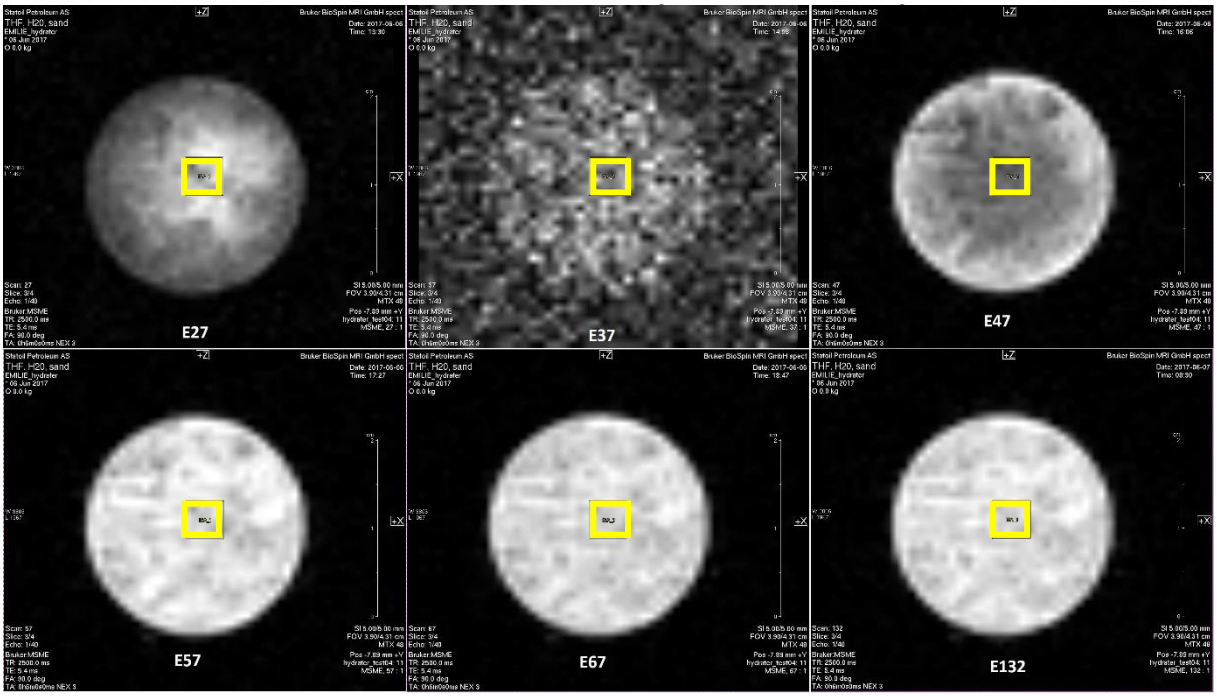

Figure A4.0.21 - Region of interest within slice 3 of sample 14, water-wet sand with the mixture THF:H2O 1:15. Coronal orientation.

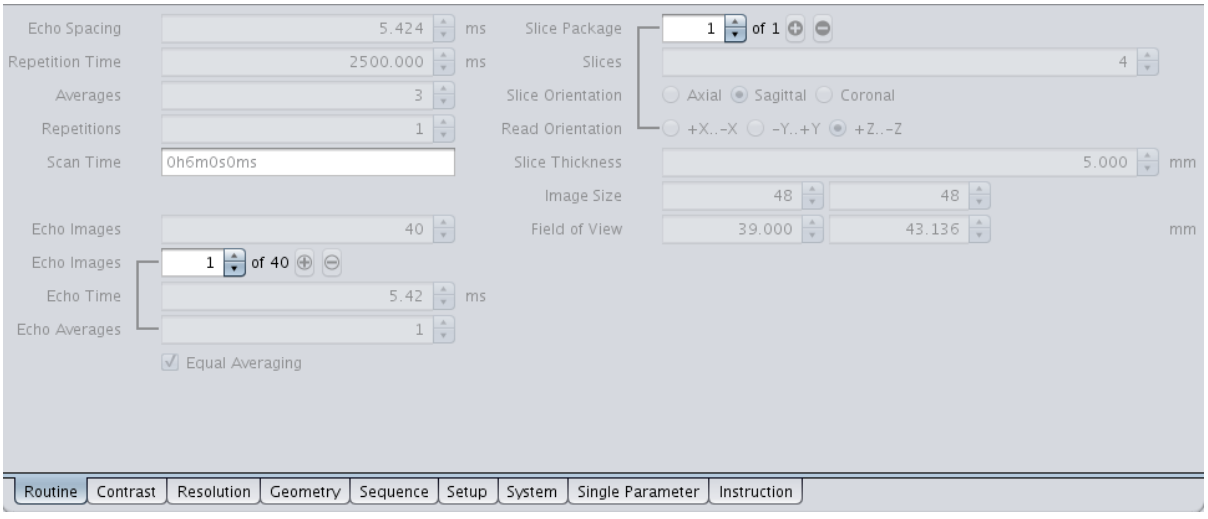

Figure A4.0.22 - Settings for the MSME scans used for sample 15.

Figure A4.0.23 display the region of interest chosen for sample 15 in the sagittal orientation. The same region of interest was chosen for all scans performed on the sample.

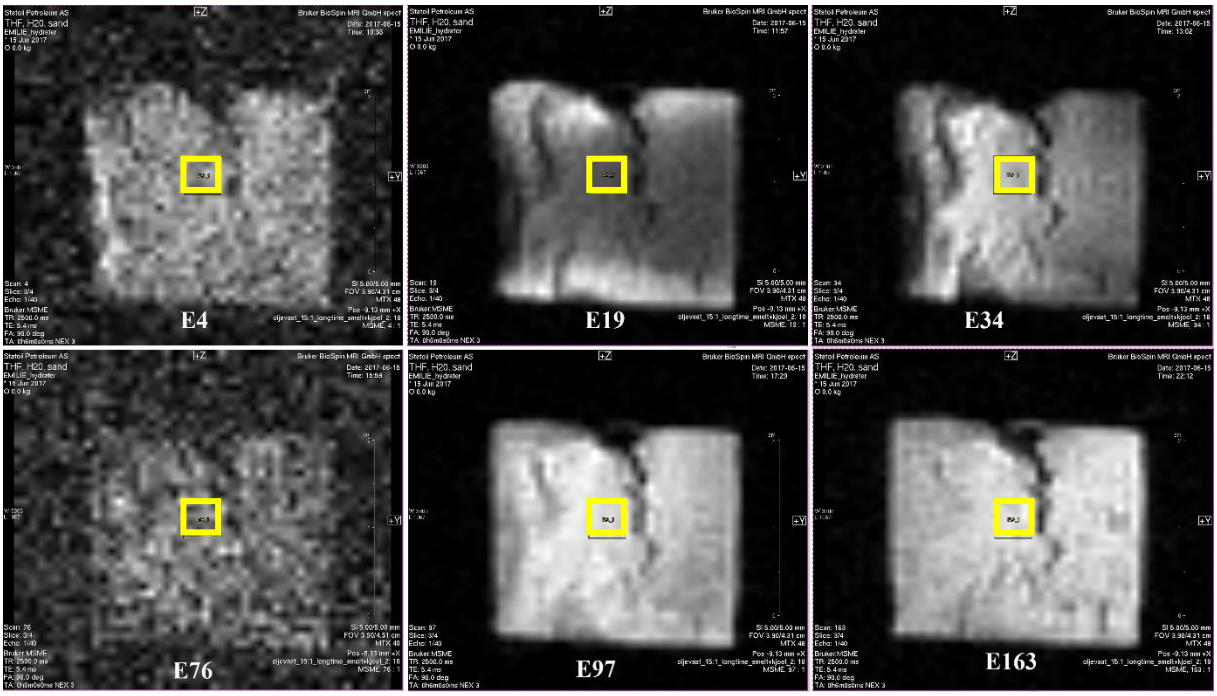

Figure A4.0.23 - Region of interest within slice 3 of sample 15, oil-wet sand with the mixture THF:H2O 1:15. Sagittal orientation.

The data acquired with the MSME scans were analyzed with the inverse Laplace transformation to create T_2^a relaxation time distribution curves. The settings for the nnls-smoothing is given in table A4.0.2.

Table A4.0.2 - Parameters used for nnls smoothing for the inverse Laplace transformation performed on the MSME data from samples 14 and 15.

nnls smoothing parameters for ILT	
Alpha	1e9
T/D min	0,001
Tmax	10
Steps	40

A5 Detailed composition of the sand

NC4X High Purity Quartz Sand [43]

The information below is directly copied from the data sheet regarding NC4X High Purity Quartz sand:

NC4X is manufactured from unique Quartz deposits in Spruce Pine, USA.

Spruce Pine quartz is the leading natural raw material for quartz glass products for the solar and semi-conductor industries globally. NC4X is an Ultra High Purity Quartz and is especially suited for use in applications with the highest requirements for purity and consistency.

NC4X is particularly suited for use in quartz glass for semiconductor applications and also for long service life Czochralski crucibles for both photovoltaic and semiconductor applications.

Chemical Content (ppm)

	Typical Value	Maximum
Al	14.0	18.0
B	≤0.1	0.1
Ca	0.5	1.0
Co	≤0.01	0.01
Cr	≤0.01	0.01
Cu	≤0.01	0.01
Fe	0.1	0.2
K	0.15	0.3
Li	0.4	1.0
Mg	≤0.1	0.1
Mn	≤0.05	0.05
Na	0.05	0.2
Ni	≤0.01	0.01
Ti	1.2	1.5

Particle size distribution (µm)

	Typical Value	Limit
D10	100	≥80
D50	220	170-320
D90	410	≤550

Cas No. 99439-28-8

References

1. *INTERNATIONAL ENERGY OUTLOOK 2017 - Executive Summary*. 2017 [cited 2017 15.10]; Available from: https://www.eia.gov/outlooks/ieo/exec_summ.php.
2. *GNS Science - Gas Hydrates* Available from: https://www.gns.cri.nz/Home/Our-Science/Energy-Resources/Gas-Hydrates.
3. Chatti, I., et al., *Benefits and drawbacks of clathrate hydrates: a review of their areas of interest.* Energy Conversion and Management, 2005. **46**(9): p. 1333-1343.
4. Max, M.D., *Natural gas hydrate : in oceanic and permafrost environments*. Coastal systems and continental margins. Vol. vol. 5. 2000, Dordrecht: Kluwer Academic Publishers.
5. *Los Alamos National Laboratory - Molecular Inclusion Compound R&D*. Available from: https://fehm.lanl.gov/source/orgs/ees/ees6/clathrates/index.shtml.
6. Sloan, E.D. and C.A. Koh, *Clathrate hydrates of natural gases*. 3rd ed. ed. Chemical industries. Vol. 119. 2008, Boca Raton, Fla: CRC Press.
7. Zhao, J., et al., *In situ observation of gas hydrates growth hosted in porous media.* Chemical Physics Letters, 2014. **612**: p. 124-128.
8. Baldwin, B.A., A. Moradi-Araghi, and J.C. Stevens, *Monitoring hydrate formation and dissociation in sandstone and bulk with magnetic resonance imaging.* Magnetic Resonance Imaging, 2003. **21**(9): p. 1061-1069.
9. Liu, Y., et al., *The detection of tetrahydrofuran hydrate formation and saturation using magnetic resonance imaging technique.* Journal of Natural Gas Chemistry, 2010. **19**(3): p. 224-228.
10. Di, L., et al., *Direct Observation of THF Hydrate Formation in Porous Microstructure Using Magnetic Resonance Imaging.* Energies, 2012. **5**(4): p. 898-910.
11. *Heriot Watt Institute of Petroleum Engineering - What are Hydrates*. [cited 2017 12.07]; Available from: http://www.pet.hw.ac.uk/research/hydrate/hydrates_what.cfm.
12. Abay, H.K., *Kinetics of gas hydrate nucleation and growth*. 2011, University of Stavanger, Faculty of Science and Technology, Department of Petroleum Engineering: Stavanger.
13. Fuel, O.o.F. *Methane Hydrate Production Feasibility*. Available from: https://energy.gov/fe/methane-hydrate-production-feasibility.
14. Wilson, P.W., D. Lester, and A.D.J. Haymet, *Heterogeneous nucleation of clathrates from supercooled tetrahydrofuran (THF)/water mixtures, and the effect of an added catalyst.* Chemical Engineering Science, 2005. **60**(11): p. 2937.
15. Semalka, M.A.B.a.R.C., *MRI Basic Principles And Applications*. Third edition ed. 2003, Hoboken, New Jersey: John Wiley and Sons, Inc.
16. Johannesen, E.B., *NMR characterization of wettability and how it impacts oil recovery in chalk*. 2008, University of Bergen, Department of Physics and Technology: Bergen.
17. Blink, E.J., *Basic MRI Physics - For anyone who does not have a degree in Physics*. 2004.
18. Heidenreich, M., *System Manual for Avanche III HD/MRI Instruments*. 2014, Bruker Corporation.
19. *How stuff works*. How MRI works; Available from: https://science.howstuffworks.com/mri1.htm.
20. Elster, A.D. *Questions and answers in MRI*. Available from: http://mriquestions.com/index.html.
21. HIDALGO-TOBON, S.S., *Theory of Gradient Coil Design Methods for Magnetic Resonance Imaging.* Wiley InterScience, 2009.
22. Hacein-Bey, T.A.G.A.J.N.L., *An Introduction to the Fourier Transform: Relationship to MRI.* American Roentgen Ray Society, 2007.
23. *XRayPhysics - Interactive Radiology Physics*. MRI Physics: Pulse sequences Available from: http://xrayphysics.com/sequences.html.

24. Mitchell, J., et al., *Magnetic resonance imaging in laboratory petrophysical core analysis.* Physics Reports, 2013. **526**(2): p. 165.
25. Carr, H.Y. and E.M. Purcell, *Effects of Diffusion on Free Precession in Nuclear Magnetic Resonance Experiments.* Physical Review, 1954. **94**(3): p. 630-638.
26. *Routine Core Analysis - Pore size distributions*. Available from: http://www.magritek.com/wp-content/uploads/2013/12/Magritek-App-Note-002-Pore-Size-Distribution-09-2013.pdf.
27. Zdravkov, B., et al., *Pore classification in the characterization of porous materials: A perspective.* Central European Journal of Chemistry, 2007. **5**(4): p. 1158-1158.
28. Berg, J.C., *An introduction to interfaces & colloids : the bridge to nanoscience*. 2010, Hackensack, N.J: World Scientific.
29. Fanchi, J.R. and R.L. Christiansen, *Introduction to Petroleum Engineering*. 2016: United States: John Wiley & Sons Inc.
30. Mahadik, D.B., et al., *Effect of concentration of trimethylchlorosilane (TMCS) and hexamethyldisilazane (HMDZ) silylating agents on surface free energy of silica aerogels.* Journal of Colloid And Interface Science, 2011. **356**(1): p. 298-302.
31. Syed, M.A., et al., *Basic Principles of Cardiovascular MRI : Physics and Imaging Techniques*. 1st ed. 2015. ed. Basic Principles of Cardiovascular MRI 2015. 2015: Springer International Publishing : Imprint: Springer.
32. *leticiateran*. Axial, sagittal and coronal images & magnetic field gradient (Part I); Available from: https://leticiateran.wordpress.com/2013/01/28/axial-sagittal-and-coronal-images-magnetic-field-gradient-part-i/.
33. *quartz*, in *Britannica Academic*. 2017.
34. Kleinhans, M.G., et al., *Magnetic Resonance Imaging of coarse sediment.* Sedimentary Geology, 2008. **208**(3): p. 69-78.
35. Zhao, J., et al., *In situ observations by magnetic resonance imaging for formation and dissociation of tetrahydrofuran hydrate in porous media.* Magnetic Resonance Imaging, 2011. **29**(2): p. 281-288.
36. Arns, C.H., *A comparison of pore size distributions derived by NMR and X-ray-CT techniques.* Physica A: Statistical Mechanics and its Applications, 2004. **339**(1): p. 159-165.
37. *Cyclopentane*

    Solvent Properties.

    [cited 2017 21.10]; Available from: http://macro.lsu.edu/HowTo/solvents/cyclopentane.htm.
38. Abdulkader, B.M.H. and i. Universitetet i Bergen Kjemisk, *Cyclopentane hydrate for hydrate wetting studies*. 2013, Department of Chemistry, University of Bergen: Bergen. Master thesis.
39. Dirdal, E.G., et al., *Can cyclopentane hydrate formation be used to rank the performance of kinetic hydrate inhibitors?* Chemical Engineering Science, 2012. **82**: p. 177-184.
40. Ben-Arye, T., et al., *Dielectrophoretic characterization of cells in a stationary nanoliter droplet array with generated chemical gradients.* BioMEMS and Biomedical Nanotechnology, 2015. **17**(5): p. 1-10.
41. Eriksen, C. and i. Universitetet i Bergen Kjemisk, *MRI method and development for hydrate studies*. 2017, Department of Chemistry, University of Bergen: Bergen. Master Thesis.
42. Sørgård, H.N., et al., *Crude Oil Adsorbates on Calcite and Quartz Surfaces Investigated by NMR Spectroscopy.* The Journal of Physical Chemistry C, 2017. **121**(38): p. 20892-20899.
43. *The QUARTZ Corp*. NC4X High Purity Quartz Sand; Available from: https://www.thequartzcorp.com/assets/file/140113%20NC4X.pdf.